ABSTRACT

Title of dissertation: CONTRIBUTIONS TOWARD UNDERSTANDING THE EFFECTS OF ROTOR AND AIRFRAME CONFIGURATIONS ON BROWNOUT DUST CLOUDS

Bharath Govindarajan, Doctor of Philosophy, 2014

Dissertation directed by: Dr. J. Gordon Leishman, Minta Martin Professor
Department of Aerospace Engineering

Brownout dust cloud simulations were conducted for rotorcraft undergoing representative landing maneuvers, primarily to examine the effects of different rotor placement and rotor/airframe configurations. The flow field generated by a helicopter rotor in ground effect operations was modeled by using an inviscid, incompressible, time-accurate Lagrangian free-vortex method, coupled to a semi-empirical approximation for the boundary layer flow near the ground. A surface singularity method was employed to represent the aerodynamic influence of a fuselage. A rigorous coupling strategy for the free-vortex method was developed to include the effects of rotors operating at different rotational speeds, such as a tail rotor. For the dispersed phase of the flow, particle tracking was used to model the dust cloud based on solutions to a decoupled form of the Basset–Boussinesq–Oseen equations appropriate to dilute gas particle suspensions of low Reynolds number Stokes flow. Important aspects of particle mobility and uplift in such vortically driven dust flows were modeled, which included a threshold-based model for sediment mobility and bombardment effects when previously suspended particles impact the bed and eject new particles. Various

techniques were employed to reduce the computational cost of the dust cloud simulations, such as particle clustering and parallel programming using graphics processing units. The predicted flow fields near the ground and resulting dust clouds during the landing maneuvers were analyzed to better understand the physics behind their development, and to examine differences produced by various rotor and airframe configurations. Metrics based on particle counts and particle velocities in the field of view were developed to help quantify the severity of the computed brownout dust clouds. The presence of both a tail rotor and the fuselage was shown to cause both local and global changes to the aerodynamic environment near the ground and also influenced the development of the resulting dust clouds. Studies were also performed to examine the accuracy of self-induced velocities of vortex filaments by augmenting the straight-line vortex segments with a curved filament correction term. It was found that while curved elements can accurately recover the self-induced velocity in the case of a vortex ring, there existed bounds of applicability when extended to three-dimensional rotor wakes. Finally, exploratory two-dimensional and three-dimensional studies were performed to examine the effects of blade/particle collisions. The loss in particle kinetic energy during the collision was adopted as a surrogate metric to quantify the extent of potential blade erosion.

Contributions Toward Understanding the Effects of Rotor and Airframe Configurations On Brownout Dust Clouds

by

Bharath Madapusi Govindarajan

Dissertation submitted to the Faculty of the Graduate School of the
University of Maryland, College Park in partial fulfillment
of the requirements for the degree of
Doctor of Philosophy
2014

Advisory Committee:

Professor J. Gordon Leishman, Chair/Advisor
Professor Inderjit Chopra
Professor Roberto Celi
Associate Professor James Baeder
Professor Ramani Duraiswami, Dean's Representative

Dedication

To
Amma and Appa

Acknowledgments

The last five years has been fun-filled, challenging, at at times trying. It has, however, undoubtedly been a memorable journey. I would like to take this opportunity to thank the people from the bottom of my heart who have made this dissertation a reality.

I have been fortunate to work under the guidance of Dr. J. Gordon Leishman, first towards my Masters, and then my doctoral degree, and I would like to express my deepest sense of gratitude towards him. Through his unique guiding style, he has honed me into a more complete and confident individual than I was when I stepped through his doors. Although I suspect he does not know it, Dr. Leishman has been more than a advisor over the years always lending a guiding hand, be it in the professional arena or regarding personal issues. In my opinion, he will always be the cool professor who pilots an airplane and restores vintage motorbikes for a hobby. I have and will always cherish the years I have worked under him. It has truly been a pleasure and a honour being his student.

I would also like to thank my committee Dr. James Baeder, Dr. Inderjit Chopra, Dr. Roberto Celi, and Dr. Ramani Duraiswami for guiding me along the way with their most valuable insights. I have had the wonderful opportunity of working on different projects with each of them and as a result, I been privy to their unique talents and abilities, all of which has helped me through this work. It must be said that they have always made me feel welcome and comfortable even in stressful situations like my defense or my oral examination. I could not have asked for a better committee.

There is not much I could possibly write that would begin to convey the extent of my parents

understanding and sacrifice towards my education. Despite my shortcomings, they have shown nothing but patience and have showered me with tender care and deep love. No amount of words will ever bring to bear the respect, appreciation, and admiration I have for them. I do hope that they will find some comfort and relief in knowing I have matured from a little boy who wanted to turn in his exam paper first, even if it were incomplete, to having the patience to stick through a PhD. To my parents, I dedicate this dissertation.

There are few special people without whom the last few years would have been nothing but shades of grey. In particular, I would like to thank Monica Syal for showing me ropes, making the lab a fun place and for always being a wonderful friend. My heartfelt thanks to Sandeep Menon, who always filled the apartment with sports, joy and a never ending source of some of the most tastiest delicacies I have feasted upon. Sufficient gratitude cannot be expressed towards Jaime Reel, who has made the last few years a truly unforgettable experience and from whom I have learnt a lot about life and cats. Her dynamism of life, open mind, and her never-ever give up attitude continue to be a source of inspiration for me.

Life in grad school would not have been as much fun if not for the "Team Leishman" spirit. The atmosphere in the lab would not have been the same without Anish Sydney and Joseph Milluzzo for their constant stream of jokes and for being my partners in crime. I would also like to acknowledge Ananth Sridharan, Sivaji Medida, and Sebastian Thomas for the laughs, advice, and constant support through grad school. I would like to thank my friends from undergrad, Amod, Deb, Hari, and Vaaruni, for their cheerful conversations and support in times of difficulty.

I would like to express my sincere gratitude towards my aunts (Anuradha, Vasanthi) and

uncles (Gopalan, Sarathy), who have viewed my journey as their and this little success fills all our hearts with joy.

Last but not least, I would like to thank my little sister Mathura for always keeping me young and never letting me grow up. If she were to ever realize that her name was not on my list of acknowledgments, I will never hear the end of it.

Table of Contents

List of Tables xii

List of Figures xii

Nomenclature xxviii

1 Introduction 1

1.1 The Problem of Rotorcraft Brownout 1

1.2 The Physics of Rotorcraft Brownout 8

1.2.1 Rotor Flow In Ground Effect 10

1.2.2 Effect of a Body on Rotor In Ground Effect 13

1.2.3 Sediment Physics Under the Action of Vortical Flows 16

1.3 Literature Survey of Brownout Related Research 22

1.3.1 Brownout Field Tests 23

1.3.2 Single-Phase and Dual-Phase Experiments on Isolated Rotors 26

1.3.3 Rotorcraft Interactional Aerodynamics 31

1.3.4 Computational Modeling of Rotorcraft Brownout 34

1.3.4.1 Modeling of the Aerodynamic Environment 35

1.3.4.2 Modeling of Particle Motion 39

1.3.5 Brownout Mitigation Studies 42

1.4 Objectives of the Present Dissertation 44

1.5 Organization of the Dissertation 45

2 Methodology 48

2.1 Introduction 48

2.2 Modeling of a Rotor Flow in Ground Effect 49

2.3 Blade Aerodynamic Solution 50

2.3.1 Calculation of the Bound Circulation Strength 52

2.3.2 Calculation of the Blade Loads 54

2.4 Computation of the Induced Velocity using the Biot–Savart Law 55

2.5 Free-Vortex Wake Modeling 58

2.5.1 Numerical Solution of the Wake Equation 62

2.5.2 Diffusion and Filament Straining 64

2.5.3 Rigid Blade Flapping Dynamics 69

2.5.4 Modeling of a Secondary Rotor 71

2.5.5 Ground Effect Modeling Using the Method of Images 74

2.5.6 Accuracy of the Induced Velocity Computations 76

2.6 Modeling of the Airframe 76

2.6.1 Coordinate Systems 84

2.7 Rotor Trim Methodology 87

2.7.1 Single Rotor Trim Methodology 87

2.7.2 Dual Rotor Trim Methodology 88

2.7.3 Tail Rotor Trim Methodology 91

2.8 Modeling of the Flow Near the Ground 92

2.8.1 Forces Acting on Stationary Particles on a Bed 98
2.8.2 Modeling of Threshold Friction Velocity 101
2.9 Particle Convection 104
2.9.1 Particle Equations of Motion 104
2.9.2 Solution to the Particle Equations of Motion 109
2.9.3 Accuracy of the Numerical Solution 111
2.10 Bombardment Ejection of Particles 113
2.10.1 Volume of Crater Formed by Bombardment Ejection 114
2.10.2 Initial Velocity of the Ejected Particles 115
2.11 Computational Considerations 119
2.12 Overall Methodology 120
2.12.1 Assumptions in the Methodology 123
2.13 Summary 125

3 Results and Discussion 129
3.1 Comparison with Measurements 130
3.1.1 Validation of Free Vortex Method 130
3.1.1.1 Laboratory-Scale Rotor 131
3.1.1.2 Full-Scale Rotor in Ground Effect 139
3.1.1.3 Comparison of Predicted Dust Clouds to Measurements 142
3.1.2 Validation of the Unsteady Panel Method 143
3.2 Effects of the Tail Rotor on Main Rotor 155

3.3 Effects of the Fuselage . . . 170
3.4 Grid Convergence Studies . . . 176
3.5 Brownout Dust Cloud Simulations . . . 187
3.5.1 Effects of the Fuselage . . . 193
3.5.1.1 UMD-AGARD Fuselage . . . 193
3.5.1.2 Cylindrical Fuselage . . . 196
3.5.1.3 Pilot's Field of View . . . 204
3.5.2 Effects of Rotor Configurations . . . 208
3.5.2.1 Single Main Rotor with Tail Rotor . . . 210
3.5.2.2 Coaxial Rotor Configuration . . . 213
3.5.2.3 Tandem Rotor Configuration . . . 216
3.5.2.4 Side-by-Side Rotor Configuration . . . 219
3.5.3 Brownout Severity . . . 231
3.5.4 Vection Illusions . . . 234
3.5.5 Dust Cloud Comparison with Field Observations . . . 238
3.6 Blade Erosion . . . 241
3.6.1 Two-Dimensional Flow Around an Airfoil . . . 243
3.6.2 Particle Collision . . . 245
3.6.3 Two-Dimensional Simulation . . . 247
3.6.4 Three-Dimensional Simulation . . . 252

4 Conclusions 258

4.1 Summary 258
4.2 Detailed Conclusions and Specific Contributions 259
4.2.1 Methodology 259
4.2.2 Effects of Fuselage 261
4.2.3 Effects of Multiple Rotors and Rotor Configurations 262
4.2.4 Blade Particle Collisions 264
4.2.5 Curved Filament Correction 265
4.3 Recommendation for Future Work 266

Appendix A: Curvature Correction 271
A.1 Introduction 271
A.1.1 Straight-Line Segmentation 273
A.1.2 Core Regularization 273
A.1.3 Curved Filament Correction 274
A.1.4 Numerical Implementation 278
A.1.5 Free-Vortex Method 283
A.1.6 Curvature Correction Term 286
A.1.7 Applicability to the Free-Vortex Method 289
A.1.7.1 Hovering Flight 289
A.1.7.2 Forward Flight 294

Appendix B: Utilization of Graphics Processing Units 298

Appendix C: Calculation of the Velocity Induced by a Quadrilateral Panel 305

C.1 Formation of a Plane Quadrilateral Surface Element 305

C.2 Induced Velocity from a Quadrilateral Source 309

C.3 Induced Velocity from a Quadrilateral Doublet 311

Appendix D: Coordinate Transformations 313

D.1 Main Rotor 313

D.2 Tail Rotor 316

Appendix E: Particle Clustering Algorithms 318

Appendix F: Helicopter Rotor Specifications 326

Bibliography 331

List of Tables

B.1 Comparison of rotor performance parameters between CPU and GPU for a rotor operating in hover. 303

B.2 Comparison of rotor performance parameters between CPU and GPU for a rotor operating in forward flight ($\mu = 0.1$). 304

F.1 Specifications of laboratory scale Rotor 1. 326

F.2 Specifications of laboratory scale Rotor 2. 326

F.3 Specifications of AGARD rotor. 327

F.4 Specifications of the CH-54 helicopter rotor. 327

F.5 Specifications of the UH-1 helicopter rotor. 327

F.6 Specifications of the Harrington coaxial rotor. 328

F.7 Specifications of full-scale isolated single main rotor. 328

F.8 Specifications of full-scale tail rotor. 328

F.9 Specifications of a representative coaxial rotor configurations. 329

F.10 Specifications of a representative tandem rotor configurations. 329

F.11 Specifications of a representative side-by-side rotor configuration. 330

F.12 Specifications of the AW-101 helicopter rotor. 330

List of Figures

1.1 A rotocraft encountering brownout conditions during a landing maneuver (courtesy of US Army AFDD). 2

1.2 Erosion damage on a rotor blade from encounters with brownout (Source: Warren [1]). 4

1.3 Brownout signatures produced in desert-like environments by: (a) Single main rotor (SMR) during landing, (b) SMR during hover, (c) Tandem rotor configuration, and (d) Side-by-side rotor configuration. 6

1.4 Brownout severity of different rotorcraft classified on the basis of average downwash and total wake strength [2]. 7

1.5 Schematic showing different modes of particle uplift and motion that can be generated by a helicopter operating in ground effect. 9

1.6 Flow visualization of a 2-bladed rotor operating under: (a) out of ground effect, and (b) in ground effect [3]. 11

1.7 Flow characteristics for a rotor as it transitions from forward flight to hover near the ground: (a) high speed forward flight, (b) lower speed forward flight, (c) transition to hover, (d) hover taxi. Adapted from Leishman [4]. 12

1.8 Schematic and smoke flow visualization showing the interaction of the wake of a rotor and body when operating in ground effect (Source: Sydney and Leishman [5]). 14

1.9 Concentration and percent mass density of particles of different diameters in a dust cloud [6, 7]: (a) average particle concentration, i.e., number of particles per cubic meter, and (b) percentage of the mass fraction of the dispersed phase to the carrier phase. 19

1.10 Schematic showing important particle mobilization and transport proceses in rotor flows [8]. 20
1.11 Instantaneous renditions showing the development of a brownout dust cloud (Source: Optical Air Data Systems). 21
1.12 Timeline of brownout related research. 24

2.1 Weissinger-L lifting surface model for the rotor blade. 51
2.2 Velocity induced at a point P from: (a) a curved vortex filament, and (b) a straight vortex segment. 57
2.3 Schematic showing the coordinate system and the Lagrangian description of the vortex filaments trailing from the blade tips. 59
2.4 The convection of an element on a trailed tip vortex filament. 61
2.5 Schematic showing the numerical stencil for PC2B algorithm. 62
2.6 Principle of splitting the free-vortex wake solution into separate, sequential treatment of convection, viscous and stretching terms over one time step. 65
2.7 Schematic showing stretching of individual vortex filaments and vorticity intensification that results in an increase in swirl velocity surrounding the filament core. . 68
2.8 Computational stencil showing the implementation of the numerical coupling methodology, in this case between the more slowly turning main and the faster turning tail rotor. 73
2.9 A representative free-vortex wake solution obtained using the method of images for a rotor operating in ground effect. 75

2.10 Panel representation of a fuselage coupled with the FVM. 81

2.11 Illustration of the prescribed wake displacement rules. 84

2.12 Helicopter and blade coordinate systems. 85

2.13 Representative measurements of the flow on the ground below a hovering rotor at several downstream distances from a point below the rotational axis of the rotor r. The distance is normalized with the rotor radius R and the wall velocity is normalized with rotor tip speed ΩR 93

2.14 Schematic showing the inviscid-viscous matching of the velocity field in the near-wall region. 95

2.15 Representative computed velocity profiles made by the FVM below the rotor at the ground. 96

2.16 Near-wall boundary layer measurements in the flow below the rotor showing that a logarithmic boundary layer profile is a reasonable approximation. (Source of experiments: Milluzzo et al. [9]) 98

2.17 Forces acting on sediment particles at the surface of a particle bed. 99

2.18 Forces acting on an airborne sediment particle. 105

2.19 Schematic of a sediment particle impacting the ground, forming a crater, and ejecting new particles. 114

2.20 Flowchart showing the overall methodology used in the present work. 121

3.1 FVM and CFD predictions for the: (a) radial displacement, (b) vertical displacement, and (c) wake boundary, of the tip vortices with wake age for the laboratory-scale rotor hovering in ground effect at $z/R = 1$. 132

3.2 FVM and CFD predictions for the normalized: (a) tip vortex strength, and (b) core radius, versus wake age for a rotor hovering in ground effect at $z/R = 1$. 133

3.3 Variation of the time-averaged radial velocity profiles at: (a) r/R = 0.8, (b) r/R = 1.0, (c) r/R = 1.25, (d) r/R = 1.5, (e) r/R = 1.75, and (f) r/R = 2.0, versus normalized height above the ground, as obtained from experiments, CFD, and the FVM. 135

3.4 Predictions of the power requirements of for a coaxial rotor configuration as a function of the system thrust. 137

3.5 Wake geometry of the coaxial rotor. 138

3.6 Variation of time-averaged groundwash velocity at 0.3 ft above the ground for a CH-54 helicopter hovering at: (a) 40 ft along the lateral axis, (b) 40 ft along longitudinal axis, (c) 80 ft along the lateral axis, and (d) 80 ft along longitudinal axis. 140

3.7 Variation of time-averaged groundwash velocity at 0.3 ft above the ground for a CH-54 helicopter hovering at 44 ft along the: (a) 40 ft along the lateral axis, and (b) 40 ft along longitudinal axis. 141

3.8 Processed image of the brownout cloud obtained through photogrammetry technique highlighting the structures and the envelope of the cloud (Source: Tanner [10]). 142

3.9 Comparison of the predicted dust clouds for weights of 14,500 lbs (shown in red) and 16,300 lbs (shown in green) with photogrammetric measurements (shown in blue) for the taxi-pass maneuver at t = 0, 4, 10, and 22 s. 144

3.10 Pressure distribution on the surface of a sphere. 145

3.11 Time history of unsteady force on an osciallating sphere. 146

3.12 Deviation of the: (a) amplitude, and (b) phase, of the apparent force over a sphere at different oscillating frequencies. 148

3.13 Panel representation of the slender body AGARD fuselage. 149

3.14 Comparison of surface pressure measurements of the time-averaged pressure distribution on the AGARD fuselage. 149

3.15 Validation of the surface singularity method for the AGARD fuselage. Steady pressure distribution on the: (a) Retreating side; (b) Top surface. 151

3.16 Variation of the figure of merit of the rotor with and without the presence of a fuselage. Source of experiments: Bagai & Leishman [11]. 152

3.17 Spanwise variation of: (a) Inflow, (b) Lift coefficient, (c) Blade bound circulation, and (d) Thrust, with and without the presence of fuselage. 153

3.18 A schematic of the position of the rotor, the body and the ground plane used in the experimental setup of Hance [12]. 154

3.19 Top and side cross-section views of the rectangular body. 155

3.20 Experimental measurements and FVM predictions for the: (a) radial displacement, and (b) vertical displacement of the tip vortices with wake age ahead of the fuselage for the laboratory-scale rotor hovering in ground effect at $z/R = 1$ with and without the presence of a rectangular body. 156

3.21 Longitudinal and lateral wake geometries for (a) an isolated SMR and (b) SMR with a TR operating in hover out of ground effect. 158

3.22 Total velocity contours showing the: (a) instantanoues, and (b) time-averaged velocity profile along the longitudinal plane for a SMR with TR operating out of ground effect. 159

3.23 Total velocity contours showing the: (a) instantanoues, and (b) time-averaged velocity profile along the lateral plane for a SMR with TR operating out of ground effect. 159

3.24 Comparison of the radial and axial displacements of the tip vortex filaments versus wake age for a single main rotor with and without the presence of a tail rotor operating in hover out of ground effect. Results from a single blade are shown for clarity. 161

3.25 Time averaged out of plane velocity at the rotor plane ($z/R = 0$) for (a) isolated SMR, and (b) SMR with TR, operating in hover out of ground effect. 162

3.26 Variation of non-dimensional thrust and power for a single main rotor in hover with and without the presence of a tail rotor operating in hover out of ground effect. 163

3.27 Longitudinal and lateral wake geometries for (a) an isolated SMR and (b) SMR with a TR hovering above the ground at $z/R = 1$. 165

3.28 Total velocity contours showing the instantanoues and time-averaged velocity profile along the: (a) longitudinal, and (b) lateral plane for a SMR with TR hovering above the ground at $z/R = 1$. 166

3.29 Total inplane velocity on the ground for (a) isolated SMR, and (b) SMR with TR hovering above the ground at $z/R = 1$. 167

3.30 Longitudinal and lateral wake geometries for (a) an isolated SMR and (b) SMR with a TR operating at an advance ratio of $\mu = 0.1$ out of ground effect. 168

3.31 Time averaged inplane velocity at the rotor plane ($z/R = 0$) for (a) isolated SMR, and (b) SMR with TR operating at an advance ratio of $\mu = 0.1$ out of ground effect. 169

3.32 Comparison of the rotor inflow in hover in the presence of a fuselage. 171

3.33 Comparison of the angle of attack across the rotor in hover in the presence of a fuselage. 171

3.34 Panel representation of the UMD-AGARD and cylindrical fuselage shapes. 172

3.35 Comparison of the rotor wake geometries in ground effect operation for the: (a) isolated SMR, (b) SMR with the UMD-AGARD body, and (c) SMR with the cylindrical body. 174

3.36 Comparison of the total velocity contours at $z/R = 0.02$ for the: (a) isolated SMR, (b) SMR with the UMD-AGARD body, and (c) SMR with the cylindrical body. . . 175

3.37 Comparison of the rotor wake geometries in ground effect operation for the: (a) isolated SMR, (b) SMR with the UMD-AGARD body, and (c) SMR with the cylindrical body. 177

3.38 Numerical solution from the FVM for different discretization showing grid independence for finer resolution: (a) Radial displacements, r/R, and (b) Vertical displacements, z/R, as a function of wake age. 178

3.39 Variation of the total induced velocity along a longitudinal axis at $z/R = 0.02$ for a rotor hovering at $z/R = 1$. 179

3.40 Forward flight wake geometries in: (a) Top view, and (b) Side view, for 5° and 10° azimuthal discretization. 180

3.41 Predicted wake positions from the FVM for a rotor operating in forward flight for different discretization: (a) Radial displacements, r/R, and (b) Vertical displacements, z/R, as a function of wake age. 181

3.42 Schematic showing the planes of interest where induced velocities were extracted. . 182

3.43 Time-averaged total induced velocity contours induced at the planes $x/R = 1$, $x/R = 3$, and $x/R = 5$ for: (a) $\Delta\psi = 5°$, and (b) $\Delta\psi = 10°$ 183

3.44 Time-averaged total induced velocity contours induced at the planes $z/R = 1$, $z/R = 2$, and $z/R = 3$ for: (a) $\Delta\psi = 5°$, and (b) $\Delta\psi = 10°$ 184

3.45 Instantaneous wake geometries at six instances during a representative landing maneuver with: (a) 5° and (b) 10°, azimuthal discretization. 186

3.46 Minerology study and particle distribution of a sample from the test range used for full-scale brownout field tests. 189
3.47 Assumed approach profile for landing: (a) Rotor hub center positions; (b) Shaft tilt angles; (c) Overall maneuver. 190
3.48 Representative variation of: (a) Rotor thrust; (b) Pilot control inputs; (c) Rotor flap response, during the prescribed trajectory. 191
3.49 Development of the dust cloud when using the UMD-AGARD fuselage configuration at time t = 4 and 6 s of the landing maneuver. 194
3.50 Development of the dust cloud when using the UMD-AGARD fuselage configuration at time t = 10 and 22 s of the landing maneuver. 195
3.51 Development of the dust cloud when using the cylindrical fuselage configuration at time t = 4 and 6 s of the landing maneuver. 198
3.52 Development of the dust cloud when using the cylindrical fuselage configuration at time t = 10 and 22 s of the landing maneuver. 199
3.53 Simulated dust cloud profiles for the (a) Isolated rotor; (b) Rotor and UMD-AGARD fuselage; and (c) Rotor and cylindrical fuselage. 200
3.54 Time-history of the total number of particle clusters entrained during the maneuver for different fuselage configurations. 202
3.55 Time-history of the least squares error of the particle density in the visual field of between different fuselage configurations and the isolated rotor. 203

3.56 Schematic of the coordinate system for projecting the cloud in the pilots FOV. Adpated from Tritschler [13]. 205
3.57 Representation of the spherical map centered around the pilot. 206
3.58 Differences in particle count in the pilot's FOV for the rotor with the cylindrical fuselage versus the isolated rotor configuration. 207
3.59 Representative wake geometries of the SMR (with TR), coaxial, tandem, and side-by-side rotor configurations. 209
3.60 Development of the dust cloud for the SMR with TR configuration at time t = 4 and 6 s of the landing maneuver. 211
3.61 Development of the dust cloud for the SMR with TR configuration at time t = 10 and 22 s of the landing maneuver. 212
3.62 Development of the dust cloud for the coaxial rotor configuration at time t = 4 and 6 s of the landing maneuver. 214
3.63 Development of the dust cloud for the coaxial rotor configuration at time t = 10 and 22 s of the landing maneuver. 215
3.64 Development of the dust cloud for the tandem rotor configuration at time t = 4 and 6 s of the landing maneuver. 217
3.65 Development of the dust cloud for the tandem rotor configuration at time t = 10 and 22 s of the landing maneuver. 218
3.66 Development of the dust cloud for the side-by-side rotor configuration at time t = 4 and 6 s of the landing maneuver. 220

3.67 Development of the dust cloud for the side-by-side rotor configuration at time t = 10 and 22 s of the landing maneuver. 221
3.68 Development of the ground vortex dust cloud in hover for a side-by-side rotor configuration. 224
3.69 Development of the dust cloud in hover for a side-by-side rotor configuration. . . . 225
3.70 Dust clouds formed by a SMR (with TR), coaxial, tandem, and side-by-side rotors at the end of the simulated landing maneuvers. 226
3.71 Relative particle count in the pilot's field of view for the tandem configuration versus the SMR configuration. 228
3.72 Relative particle count in the pilot's field of view for the tandem configuration versus the SMR configuration. 229
3.73 Comparative levels of brownout severity for different rotor configurations. 233
3.74 Particle convection velocities along the ground for the different rotor configurations. 235
3.75 Top-view and side-view of the different rotor configurations with the reference axes (highlighted in red). 236
3.76 "Donut" dust cloud brownout signature of Rotorcraft A. 238
3.77 Representative fuselage shape of Rotorcraft A. 239
3.78 Dust cloud development at: (a) t = 4 s, (a) t = 6 s, (a) t = 10 s, and (a) t = 22 s, of the prescribed landing maneuver for Rotorcraft A. 239
3.79 Schematic representation of the source-vortex panel of an airfoil. 242
3.80 Kutta condition at the trailing edge of the airfoil. 243

3.81 Schematic representation of a particle colliding with the surface of an airfoil. . . . 246

3.82 Comparison of the variation of non-dimensional pressure on the upper and lower surfaces of a NACA 4412 airfoil between the two-dimensional panel method and experiments (Source: Stack et al. [14]). 247

3.83 Trajectories of particles colliding with a NACA 0015 airfoil at 0° for particles sizes of (a) 10 μm, (b) 20 μm, (c) 50 μm, and (d) 70 μm. 248

3.84 Trajectories of particles colliding with a NACA 0015 airfoil at 10° for particles sizes of (a) 10 μm, (b) 20 μm, (c) 50 μm, and (d) 70 μm. 249

3.85 Variation of loss of kinetic energy per particle versus particle diameter upon colliding with a NACA 0015 for different freestream velocities. 251

3.86 Schematic representation of a particle colliding with a solid boundary. 251

3.87 Comparison of the predicted brownout dust clouds in hover for different particle sizes. 254

3.88 Total number of particles versus particle diameter entrained through the rotor disk for brownout clouds in hover. 255

3.89 Total number of particles versus particle diameter entrained through the rotor disk for brownout clouds in hover. 256

A.1 Comparison of the self-induced velocity produced by a vortex ring calculated analytically and numerically by using a discretization $\Delta\theta$ with a traditional core regularization with $n \to \infty$ [15]. 275

A.2 Schematic of a discretized vortex ring [16]. 277

A.3 Self-induced velocity of a thin-cored vortex ring as calculated numerically using the traditional core regularization (Eq. A.2) with $n \to \infty$, and the curvature correction by using Eq. A.3 with $\Delta\theta_c = 2r_c/R$ [16]. 279
A.4 Schematic illustrating the use of different global ($\Delta\theta_c$) and local discretizations ($\Delta\theta$). 279
A.5 Evaluation of the subtended angles of the straight-line segments at the circumcenter. 280
A.6 Total self-induced velocity at a vortex collocation point (blue) arises from Biot–Savart computations (line-segments) and adjacent curved filaments (red). 284
A.7 Schematic illustrating the deviation of the curved filament (red) from the original tip vortex trajectory (dashed-black). 286
A.8 Variation of the self-induced velocity correction term with: (a) $\Delta\theta_c$, (b) r_c, and (c) R. 287
A.9 Side-view of the wake geometry for a rotor hovering with the inclusion of the curvature correction term for azimuthal discretizations of (a) 10°, and (b) 5°. 290
A.10 Variation of $\Delta\theta - (\Delta\theta_c)_{\text{min}}$ against wakeage for rotor azimuthal discretizations of (a) 10°, and (b) 5°. 291
A.11 Variation of r_c/R against wakeage for rotor azimuthal discretizations of (a) 10°, and (b) 5°. 291
A.12 Comparison of hover wake geometries with and without the curvature correction term. The wake geometry from a single blade is shown for clarity. 293
A.13 Inflow distribution hover with and without the curvature correction term. 293
A.14 Wake geometries for a rotor operating in forward flight with the inclusion of the curvature correction term. 295

A.15 Variation of r_c/R against wakeage for a rotor operating in forward flight. 296

A.16 Comparison of forward flight wake geometries with and without the curvature correction. The wake geometry from a single blade is shown for clarity. 297

B.1 Internal memory architecture on a representative CPU and GPU. 299

B.2 L_2 norm of the error in the wake position after one time step between the CPU and GPU [17]. 300

B.3 L_2 norm of the error in the wake position after 100 time step between the CPU and GPU for the case of (a) hover, and (b) forward flight. 301

B.4 Isometric view of predicted brownout dust cloud at the end of a landing maneuver computed using (a) CPU, and (b) GPU. 302

C.1 Illustration of the transfer of origin from the average point to the centroid of a plane quadrilateral element. 307

C.2 Quadrilateral constant strength source element. 310

C.3 Quadrilateral doublet element and its vortex ring equivalent. 312

D.1 Schematic representationg of the fixed frame and hub rotating frame coordinate systems for the: (a) Main rotor, and (b) Tail rotor. 314

E.1 Schematic showing the Gaussian method of particle clustering. 319

E.2 An example of Gaussian solution obtained from Govindarajan [18]: Total number of clusters cluster = 1,125, total number of particles per cluster = 5, i.e., total number of particles in the clustered solution = 5,625. 322

E.3 A solution obtained from brownout dust field computations when using the Gaussian clustering method. 323

E.4 Actual and clustered solution during a landing maneuver using the Gaussian distribution method. Source Govindarajan [18] 324

Nomenclature

C_d	Drag coefficient
A	Cross-sectional (frontal) area of suspended particle
A	Influence coefficient matrix of the panels
c	Blade chord
C_d	Drag coefficient of suspended particle
C_d	Sectional drag coefficient
C_l	Sectional lift coefficient
C_{l_α}	Sectional lift-curve slope
C_P	Rotor power coefficient, $= P/\rho A\Omega^3 R^3$
C_{P_i}	Rotor induced power coefficient, $= P_i/\rho A\Omega^3 R^3$
C_{P_0}	Rotor profile power coefficient, $= P_0/\rho A\Omega^3 R^3$
C_Q	Rotor torque coefficient, $= Q/\rho A\Omega^2 R^3$
C_T	Rotor thrust coefficient, $= T/\rho A\Omega^2 R^2$
$C_{T_{\text{req}}}$	Target thrust coefficient, $= T_{\text{req}}/\rho A\omega^2 R^2$
d_p	Particle diameter
D	Rotor diameter
e	Coefficient of restitution
e	Flapping hinge offset as a fraction of rotor radius
E_c	Kinetic energy of a cluster
E_R	Kinetic energy of a rebounding particle

$\mathbf{F}$	Total force acting on a particle
$\mathbf{F}_{\text{am}}$	Apparent mass force
$\mathbf{F}_b$	Buoyancy force
$\mathbf{F}_{\text{basset}}$	Basset force
$\mathbf{F}_d$	Drag force from viscous shear effects on a stationary particle
$\mathbf{F}_D$	Fluid drag force on a suspended particle
$\mathbf{F}_g$	Gravitational force
$\mathbf{F}_i$	Inter-particle force
$\mathbf{F}_l$	Lift force from viscous shear effects on a stationary particle
$\mathbf{F}_L$	Lift force on a suspended particle
$\mathbf{F}_m$	Force produced by moments
$\mathbf{F}_{\Delta P}$	Lift force from unsteady pressure on a stationary particle
g	Acceleration under gravity
h	Perpendicular distance between a vortex element and an evaluation point
h	Rotor plane height above the ground
Δt	Time step size
$\mathbf{i}$, $\mathbf{j}$, $\mathbf{k}$	Unit vectors along x, y, and z directions, repectively
I	Influence coefficient matrix
I_B	Influence coefficient matrix for the bound circulation
I_{NW}	Influence coefficient matrix for the near-wake circulation
$\mathbf{J}$	Jacobian matrix

k	Von Karman's constant (= 0.4)
k_r	Roughness height
m	Mass of a particle
m_n	Mass of the n^{th} ejected particle
m_R	Mass of a rebounding particle
m_0	Mass of an impacting particle
M	Aerodynamic moment
M_A	Aerodynamic moment about the flapping hinge
M_I	Inertial moment about the flapping hinge
n	Index used for time steps
n	Index of particles ejected by bombardment
$\mathbf{n}$	Panel outward unit normal vector
N	Total number of particles in the brownout simulation
N_b	Number of blades
N_b	Number of particles ejected from the bed by bombardment
N_r	Number of rotors
N_s	Number of spanwise blade segments
N_{pan}	Number of panels
N_v	Total number of vortex elements in the flow field
N_2	Particles associated with a cluster in the Gaussian clustering method
$p,\ q, r$	Roll, pitch, and yaw rates along x, y, and z directions, repectively

P_∞	Free-stream static pressure
P	Rotor power
P_i	Rotor induced power
P_0	Rotor profile power
Q	Rotor torque
r	Non-dimensional blade spanwise distance
r	Radial distance of a point on the ground measured from rotor shaft axis
$\mathbf{r}$	Position vector of an evaluation point relative to a vortex filament
r_c	Core radius of a vortex filament
r_{c_0}	Initial core radius of a vortex filament
r_d	Moment arm of drag force $\mathbf{F}_d$ about the point of particle mobility
r_i	Moment arm of interparticle force $\mathbf{F}_i$ about the point of particle mobility
r_l	Moment arm of lift force $\mathbf{F}_l$ about the point of particle mobility
R	Rotor radius
Re_p	Particle Reynolds number
Re_v	Vortex Reynolds number, $= \Gamma_v/\nu$
S	Cross-sectional area of a vortex filament
t	Time
T	Main rotor thrust
T_{TR}	Tail rotor thrust
T_{req}	Target rotor thrust

u_*	Friction velocity, $= \sqrt{\tau/\rho}$
u_{*_t}	Threshold friction velocity
v_h	Hover inflow velocity, $= \sqrt{T/2\rho A}$
v_i	Inflow velocity
V_{px}, V_{py}, V_{pz}	Components of particle velocity along the x, y and z directions, respectively
V_{tip}	Rotor hover tip speed, $= \Omega R$
V_x, V_y, V_z	Components of flow velocity along the x, y and z directions, respectively
$\mathbf{V}$	Flow velocity
$\mathbf{V}_B$	Velocity induced by the bound vortices
$\mathbf{V}_{\text{FW}}$	Velocity induced by the free-wake trailers
$\mathbf{V}_i$	Total velocity at a control point
$\mathbf{V}_{\text{ind}}$	Total induced velocity at a Lagrangian marker
$\mathbf{V}_{\text{fus}}$	Velocity induced by the panels
$\mathbf{V}_{\text{man}}$	Velocity induced by maneuvering effects
$\mathbf{V}_n$	Velocity of the n^{th} ejected particle
$\mathbf{V}_{\text{NW}}$	Velocity induced by the near-wake vortices
$\mathbf{V}_p$	Particle velocity
$\mathbf{V}_P$	Velocity induced at panel control point
$\mathbf{V}_R$	Velocity of a rebounding particle
$\mathbf{V}_s$	Velocity of the singularity
$\mathbf{V}_0$	Velocity of an impacting particle

$\mathbf{V}_\infty$	Freestream velocity
$x,\ y,\ z$	Cartesian coordinate system

Greek Symbols

α	Lamb-Oseens constant, = 1.25643
α	Angle of attack
α_0	Incident angle of an impacting particle
β	Blade flapping angle
β_p	Blade precone angle
β_{1c}	Longitudinal flapping angle
β_{1s}	Lateral flapping angle
Γ	Strength of a vortex filament
Γ_b	Strength of a bound vortex
Γ_{NW}	Strength of a near-wake trailer
Γ_v	Strength of a finite length filament
Γ_w	Total wake strength, = $N_r N_b \Gamma_V$
δ	Boundary layer thickness
δ	Turbulent or eddy viscosity parameter
$\Delta\mathbf{l}$	Change in the length of a vortex filament
ΔP	Unsteady pressure difference relative to ambient, = PP_∞

Δr_c	Change in the core radius of a vortex filament
Δt	Time step size
$\Delta\zeta$	Discretization along the spatial direction
$\Delta\psi$	Discretization along the azimuthal or temporal direction
ε	Strain rate, $= \Delta l/l$
ζ	Wake age
θ, ϕ, ρ	Elevation, eccentricity, and distance in a spherical coordinate system, respectively
θ_0	Collective pitch angle
θ_{1c}	Lateral cyclic pitch angle
θ_{1s}	Longitudinal cyclic pitch angle
θ_{tw}	Linear blade twist rate
υ	Volume of crater formed on the sediment bed
λ	Eigenvalue of an ODE
λ	Non-dimensional inflow velocity, $= v_i/\Omega R$
μ	Rotor advance ratio
μ	Mean vector for the Gaussian distribution
μ_c	Mean vector for clustering
μ^*	Normalized advance ratio, $= \mu/\sqrt{C_T/2}$
ν	Kinematic viscosity coefficient
μ_β	Non-dimensional rotating blade flap frequency
ρ	Flow density

ρ_p	Particle density
σ	Rotor solidity, $= N_b c/\pi R$
σ	Root of the characteristic equation
σ_S	Source singularity strength
Σ_B	Covariance matrix for the Gaussian distribution
Σ_C	Covariance matrix for clustering
τ	Shear stress
τ_{st}	Threshold shear stress
τ_p	Particle response time
τ_{p_s}	Particle response time in Stokes flow
ϕ	Sectional inflow angle
Φ	Velocity potential
ψ	Azimuth angle
$\overline{\omega}$	Vorticity vector
ω_β	Rotating blade flapping frequency
Ω	Rotational angular speed of the rotor
Ω_s	Frequency of vortical wake shedding, = $N_r N_b \Omega$

List of Abbreviations

BBO	Basset–Boussinesq–Oseen

CFD	Computational Fluid Dynamics
CPU	Central Processing Unit
GPU	Graphics Processing Unit
HUD	Head-Up Display
FMM	Fast Multipole Method
FOV	Field of View
FVM	Free Vortex Method
MTF	Modulation Transfer Function
PC2B	Predictor-Corrector 2nd-order Backward difference
PIV	Particle Image Velocimetry
PTV	Particle Tracking Velocimetry
RANS	Reynolds-Averaged Navier–Stokes
SMR	Single Main Rotor
TR	Tail Rotor
VTM	Vorticity Transport Method

Chapter 1

Introduction

1.1 The Problem of Rotorcraft Brownout

Brownout is a phenomenon that often occurs when rotorcraft operate over ground surfaces covered with mobile sediment material, such as loose soil, gravel or sand. Through a series of complex fluid dynamic uplift and sediment mobilization mechanisms, the rotor wake stirs up a dust cloud that can quickly engulf the rotorcraft. Photographs of a rotorcraft encountering brownout conditions during a landing in the desert are shown in Fig. 1.1. The equivalent phenomenon under snowy conditions is referred to as whiteout.

The main concern during brownout occurrences is that the pilot loses visibility of the take-off or landing zone and may also experience spurious sensory cues from the relative motion of the dust cloud. From a broader perspective, brownout is an example of operating in a Degraded Visual Environment (DVE) wherein the dust cloud can develop to sufficient concentrations such that it degrades or completely eliminates the optical cues, thereby posing a safety of flight issue. Pilots commonly rely on the surrounding macrotexture (buildings, trees) and microtexture (blades of grass, rocks on the ground) to help determine the spatial orientation and motion of the rotorcraft. In the absence of these visual cues, the relative motion between the rotorcraft and the motion of the dust cloud can produce vection illusions, which can lead to the pilot experiencing spatial disorientation. In some cases, the pilot may lose control of the rotorcraft and may drift into obstacles,

Figure 1.1: A rotocraft encountering brownout conditions during a landing maneuver (courtesy of US Army AFDD).

which can lead to serious mishaps. The significance of brownout encounters is such that it is the leading cause of human factor-related mishaps in military operations [19, 20].

The suspended dust particles in a brownout dust cloud can also cause rapid abrasion of the rotor blades as well as engine components, driving up maintenance costs and reducing mission readiness. The leading edge of the rotor blades are covered with metallic strips (usually composed of titanium alloys) to prevent abrasion. These strips, however, can become quickly eroded by the repeated impact of dust particles [1] when the rotocraft operates in brownout conditions, as shown in Fig. 1.2. The consequences of blade erosion are shortening in the life of the rotor blades, loss in rotor aerodynamic performance, and compromised blade structural properties.

Brownout is a complex physical phenomenon, and a better understanding of the fundamental processes involved necessitates a multidisciplinary approach. Key technical disciplines involved in the brownout phenomenon include:

1. Fluid dynamics: The interaction between the flow field produced by the rotocraft and the ground is responsible for the mobilization and uplift of the dust particles, which is ultimately responsible for the resulting structure of the dust cloud.

2. Sedimentology: The composition and characteristics of the sediment bed covering the ground can influence the development of the dust cloud. For example, the quantity of particles entrained into the flow is dependent on the particle size and weight. The subsequent motion of these particles under the action of the carrier phase is also dependent on their aerodynamic and inertial characteristics.

3. Flight dynamics: The flight path of a rotorcraft during an approach to landing or take off

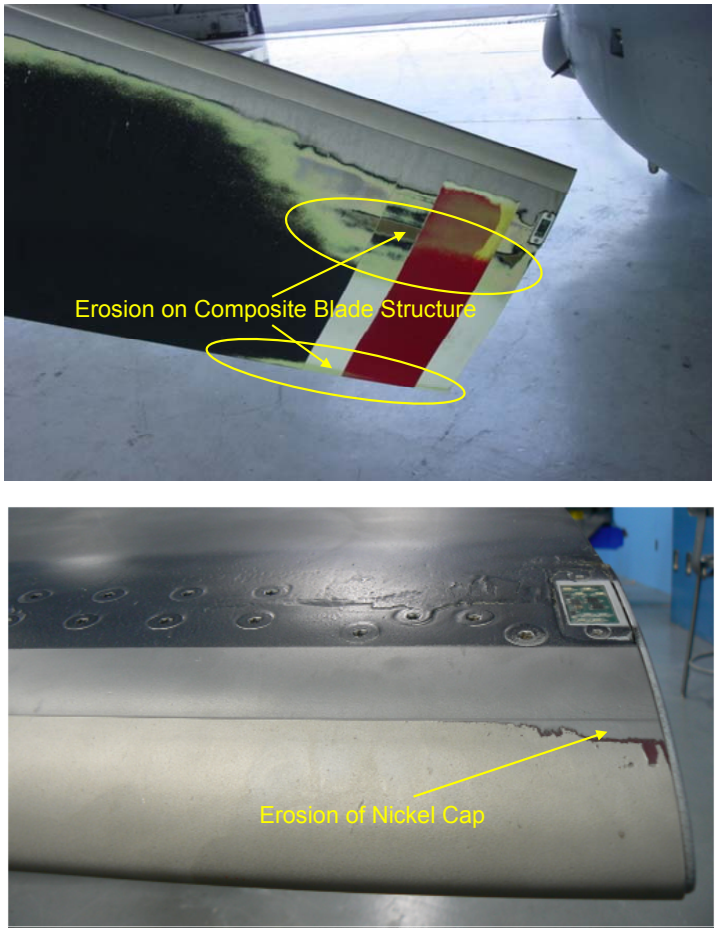

Figure 1.2: Erosion damage on a rotor blade from encounters with brownout (Source: Warren [1]).

maneuver can affect the rate of formation and the severity of the dust clouds. Operational tactics, widely adopted by pilots, involve specialized flight path profiles that minimize the effects of brownout. One such example is flying faster near the ground before landing to outpace the evolving dust cloud.

4. Human related factors: With the knowledge that the visual obscuration produced by the uplifted dust during brownout is likely to affect piloting, it is important to understand the processes through which sensory information (mostly visual) is perceived by humans, which is vital to reducing the operational risks associated with brownout.

5. Physics of light scattering: The primary mechanism by which a brownout cloud obscures the pilot's field of view is through the compounded effect of scattering and absorption of light by the particles in the dust cloud.

An improved understanding of the factors that influence the occurrence of brownout and an informed exploration of strategies to mitigate it are of great practical importance for safe and cost-effective rotorcraft operations. However, a permanent solution to the mitigation of brownout poses many challenges.

One technique currently being pursued is the development of sensors, that allow pilots to see through the dust cloud [6, 7, 21]. These sensors project flight parameter values or sensory cues onto displays, e.g., pilot helmet mounted. The most recent work on the development of tactical displays [21] focuses on providing pilots with visual references of the landing zone, as well as the crucial "feeling" of the speed and attitude of the helicopter, to counter effects such as vection illusions. These visual augmentation systems have been reasonably effective in improving safety

(a) SMR – Landing

(b) SMR – Hover

(c) Tandem

(d) Side-by-side

Figure 1.3: Brownout signatures produced in desert-like environments by: (a) Single main rotor (SMR) during landing, (b) SMR during hover, (c) Tandem rotor configuration, and (d) Side-by-side rotor configuration.

of flight when they are combined with certain operational tactics involving flight path management.

While sensors technologies and operational tactics offer the promise of increased flight safety, the root cause of the brownout problem is the interaction of the fluid flow with the sediment bed when the rotorcraft is operating close to the ground. Comparative videographic observations [2] suggest that rotorcraft can produce different dust clouds in terms of their spatial extent, particle concentration, and rapidity of their development, for reasons that are not yet fully understood. On one hand, during landing some helicopters appear to produce radially expanding,

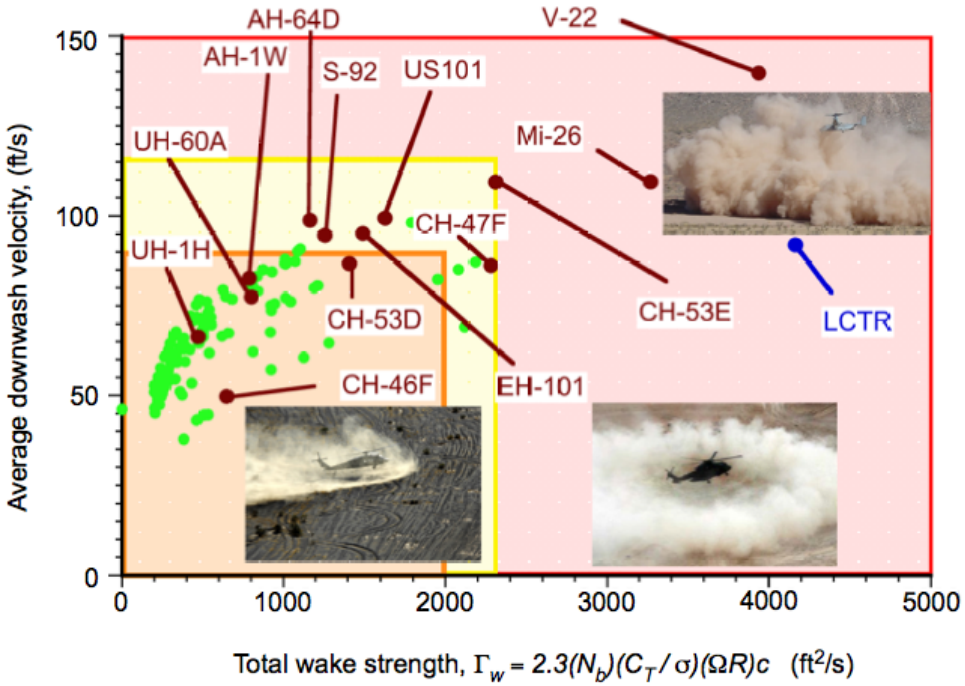

Figure 1.4: Brownout severity of different rotorcraft classified on the basis of average downwash and total wake strength [2].

toroidal-type dust clouds that can allow the pilot to more easily see the ground. On the other hand, some other helicopters produce large, dome-shaped dust clouds that recirculate through the rotor disk and can engulf the entire helicopter, significantly reducing the pilot's visibility of the ground; see Fig. 1.3. Even with the same rotorcraft performing the same landing/takeoff maneuver, the characteristics of the sediment bed, such as the size of particles, moisture content, mineralogy, etc. can influence the formation of the dust cloud.

Milluzzo and Leishman analyzed photographs of different rotorcraft landing in brownout conditions and hypothesized rotor parameters that are likely to play an important part in brownout. It was argued that brownout severity depends on several parameters such as disk loading, total wake strength, average downwash, and reduced frequency of convection of rotor wake. A tentative

ranking of the severity of the brownout clouds produced by different rotorcraft was proposed, as shown in Fig. 1.4. Each of the three rectangles correspond to a subjective level of brownout severity. Level 1 (orange) brownout severity has high ground visibility with little sediment accumulation in the air around the rotorcraft. Level 2 (yellow) severity has sufficient ground visibility, with a higher sediment accumulation in the air around the rotorcraft and a denser cloud formation. Level 3 (pink) severity has little to no ground visibility with large columns of sediment that surround or engulf the rotorcraft. Such observations show that understanding of the fundamental physical processes involved in the formation and development of brownout clouds is critical to attempt to mitigate this problem.

1.2 The Physics of Rotorcraft Brownout

A brownout dust cloud forms through a series of complex fluid dynamic mechanisms that are associated with the flow velocities, vorticity and turbulence embedded in the rotor wake, which can mobilize and uplift large quantities of dust particles from the ground; a schematic conveying the general complexity of the problem is shown in Fig. 1.5. Fundamentally, brownout is a two-phase fluid dynamics problem: (a) the fluid phase (i.e., the carrier phase), which is driven by the flow induced by the rotor(s) and the interactions of the flow with the surface of the particle bed, and (b) the dust particle phase (i.e., the dispersed phase), which comprises of the nonuniform concentration of sediment particles that are mobilized, uplifted and convected under the influence of this fairly complex flow. This multiphase aspect of the problem drastically increases the complexity of quantifying, understanding, and modeling brownout because the carrier and dispersed phases are

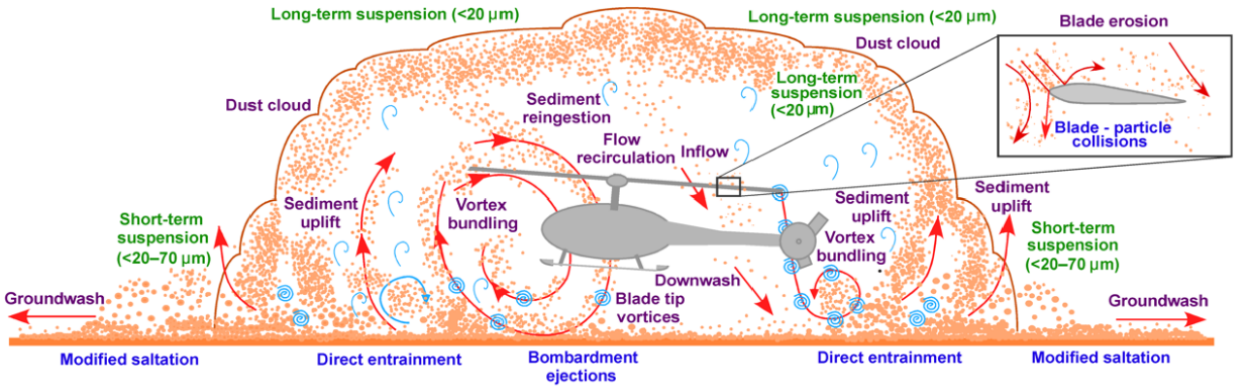

Figure 1.5: Schematic showing different modes of particle uplift and motion that can be generated by a helicopter operating in ground effect.

intrinsically coupled.

Figure 1.5 identifies some of the fluid mechanics and sedimentology processes involved in brownout. The combined downwash from the rotor and the vortical wake to the sediment bed induces an unsteady velocity field, that when sufficiently intense, causes incipient motion of loose sediment from the bed. Interactions of the rotor wake with the airframe may also affect this problem, which can not only create separated flows and turbulence, but also distort the main rotor wake and so influence the three-dimensional unsteady flow that evolves at the ground. Depending on the vertical velocities close to the bed, mobilized sediment particles can either settle back on the bed, or can be picked up and carried off into the flow. Some of these particles can reach the plane of the rotor and collide with the rotor blades, as shown in the inset in Fig. 1.5. Energy transfer can occur during the blade-particle collisions, where the kinetic energy of the colliding particles can abrade the surface of the rotor blades, which drastically reduces the operational life of the rotor blades and other rotating components.

1.2.1 Rotor Flow In Ground Effect

The rotor wake contains vortical flows, turbulence, and other secondary flow structures [8, 22] that not only interact with each other, but are also influenced by the presence of the ground plane. Many experimental studies have been conducted for rotors operating in ground effect to document performance [23–29], generally exploring the advantages of operating a rotor in ground effect in terms of reducing power requirements for a given rotor thrust. This reduction in power is primarily attributed to the decrease in the induced velocity for a rotor hovering in ground effect as compared to that operating out of ground effect. Profile power also reduces because the individual blade sections on the rotor blades operate at lower angles of attack in ground effect to produce the same rotor thrust.

Figures 1.6(a) and (b) show flow visualization images of a 2-bladed rotor operating out of ground effect and in ground effect, respectively. In these images, the flow was seeded with smoke and is illuminated by a laser light sheer in a radial plane. As the rotor passes through the imaging plane, helicoidal vortex filaments are trailed from the blade tips, which can be identified by the seed voids in Fig. 1.6. Under out of ground effect conditions (see Fig. 1.6(a)), the vortex filaments undergo radial contraction close to the plane of the rotor disk. Coherent seed voids observed close to the rotor plane show that these vortices have primarily laminar cores, devoid of small eddies and turbulence that are present in the surrounding area of the rotor flow. After about 2–3 rotor revolutions, the tip vortices start to diffuse under the influence of turbulence and viscosity. Instabilities in the wake further downstream also become more apparent, in part because of pairing of adjacent turns of the helical vortices as they reach older wake ages.

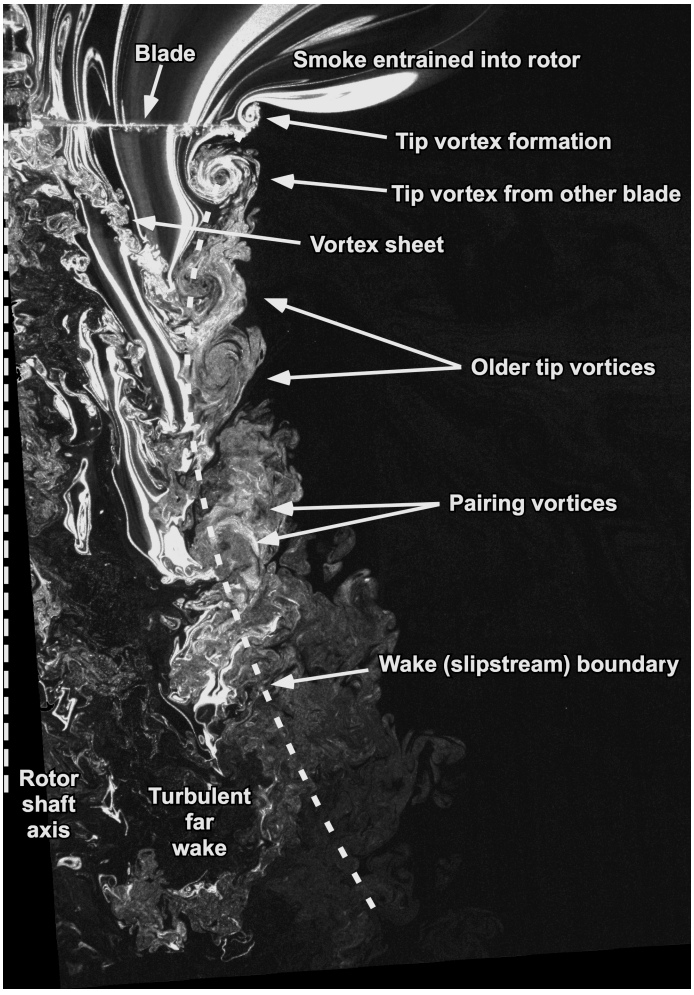

(a) Out of ground effect

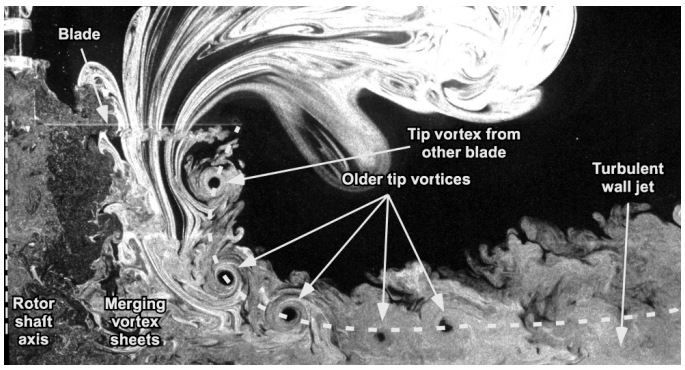

(b) In ground effect

Figure 1.6: Flow visualization of a 2-bladed rotor operating under: (a) out of ground effect, and (b) in ground effect [3].

(a) High speed forward flight

(b) Lower speed forward flight

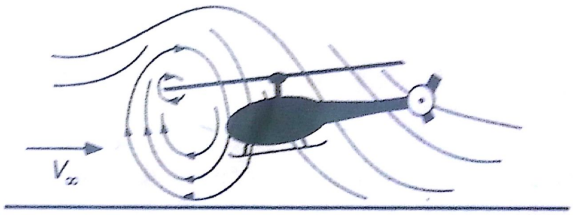

(c) Transition to hover

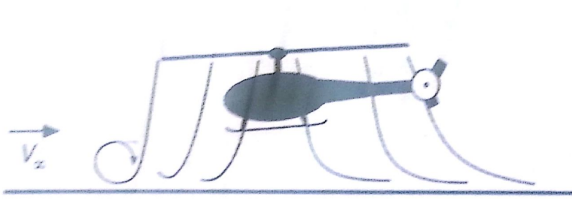

(d) Hover taxi

Figure 1.7: Flow characteristics for a rotor as it transitions from forward flight to hover near the ground: (a) high speed forward flight, (b) lower speed forward flight, (c) transition to hover, (d) hover taxi. Adapted from Leishman [4].

When operating in ground effect (see Fig. 1.6(b)), the wake initially contracts similar to the out of ground effect case, but then the presence of the ground forces the wake to expand radially away from the rotor and almost parallel to the ground. The radial expansion of the wake close to the ground results in the stretching of the vortex filaments, which results in a reduction in the vortex core size [9, 22, 30]. This process effectively reintensifies the vortices and increases the swirl velocity, in effect countering their normal diffusive action and causing them to persist in the flow to much older wake ages [30].

A helicopter primarily encounters brownout conditions during landing and takeoff operations, for which the flow field is even more complex when compared to that found under hover conditions. The transient changes in rotor height and velocity close to the ground can produce localized regions of the flow that affect sediment mobilization and uplift from the ground. Two such

distinct regimes are “recirculation” at very low advance radio, and the formation of the “ground vortex” at higher advance ratios [27,31]. A helicopter approaching the ground in a landing maneuver first encounters the formation of a ground vortex, which is then followed by the recirculation region as the helicopter further decelerates into hover [32], as shown in Fig. 1.7.

The recirculation regime is usually observed at low advance ratios, wherein the wake recirculates through the upstream of the rotor disk with significant unsteadiness and aperiodicity. This operating condition is particularly unfavorable from the brownout perspective because it can result in the reingestion of many sediment particles through the front of the rotor disk, which can obstruct pilot’s field of view (FOV) and can lead to blade abrasion. As the advance ratio of the helicopter increases, the recirculation region weakens and the flow passes under the leading edge of the rotor disk, forming a distinct vortical flow region called the “ground vortex”, as shown in Fig. 1.7(c). As advance ratio increases further, the ground vortex becomes weaker and passes rearwards under the rotor, and ultimately disappears at higher advance ratios [27]. Experiments conducted by Nathan and Green [31] also showed that the regions where the ground vortex and recirculation form can affect particle uplift.

1.2.2 Effect of a Body on Rotor In Ground Effect

Prior work [8, 22, 33] has shown the wake below a rotor to be complicated, in part, because of the presence of various vortical structures and turbulence; see Fig. 1.6. The presence of a body beneath a rotor, therefore, can further significantly alter the development of the flow. Figure 1.8(a) shows a schematic of the aerodynamic environment beneath a rotor in the presence of a body. At

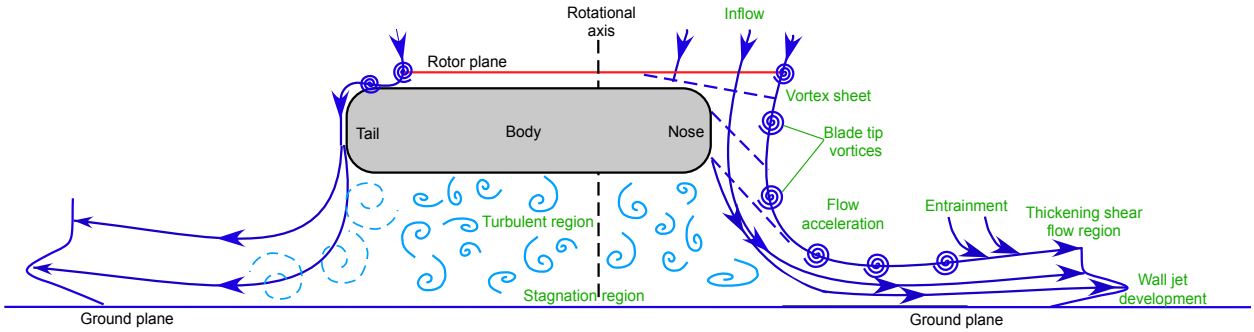

(a) Schematic of rotor/body interaction

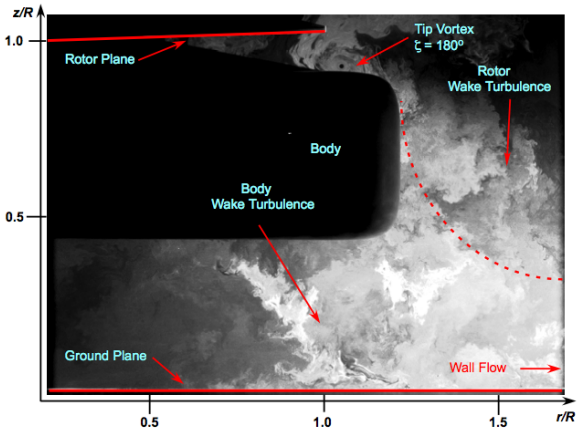

(b) Smoke flow visualization of the tail region

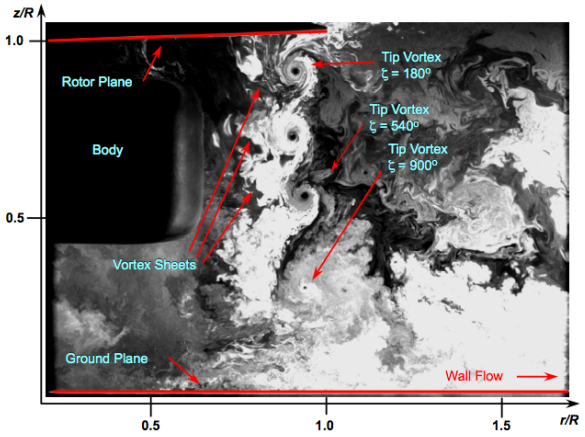

(c) Smoke flow visualization of the nose region

Figure 1.8: Schematic and smoke flow visualization showing the interaction of the wake of a rotor and body when operating in ground effect (Source: Sydney and Leishman [5]).

the nose end of the fuselage (right end of the schematic), the vortical structures trailed from the rotor blade are only slightly affected by the presence of the fuselage and the flow develops similar to that without the presence of a body. At the tail end of the fuselage (left end of the schematic), the body extends beyond the edge of the rotor. In this case, the slipstream boundary is significantly distorted and the blade tip vortices impinge directly upon the body. The wake of the body also creates regions of eddies and turbulence of greater intensity than those produced by the rotor itself.

The aerodynamic environment around the body is determined in part by the interaction of the rotor wake sheet and tip vortices with the body. Figure 1.8(b) shows the interaction of the wake sheet and the tip vortex at the tail end of the body. In this case, the blade tip vortices impinge on the body, and undergo significant stretching as it is wrapped around contour of the body. These filaments may ultimately burst and lead to a rapid diffusion of the vorticity and redistributed in the form of small eddies. These eddies follow the contour of the body and mixes with the boundary layer and are convected downstream towards the ground introducing a significant amount of turbulence in the near-wall region. Figure 1.8(c) shows the dynamics of the impingement process at the nose end of the body. The inboard sections of the wake sheet impinges directly onto the body, distorts and undergoes a shearing process. The outboard section, which is relatively unaffected by the presence of the body, convects downward. The vortical eddies in the sheet diffuse rapidly when they impinge on the body surface and produce turbulence.

The presence of a body beneath a rotor are known to cause localized region of increased flow velocity [5]. This local flow is a consequence of the interaction between the rotor-induced flow and the body where the magnitude and direction of the flow depends on the geometric shape

of the fuselage. Furthermore, the local flow can significantly alter the shear stresses of the flow along the ground, which can affect the entrainment of particles from the sediment bed and produce the uplift of more sediment.

Fradenburgh [24] compared the performance of rotors operating in ground effect with and without the presence of a body (in this case, a circular disk) beneath the rotor. These studies showed that the presence of an object in the rotor wake can augment the benefits of ground effect through the "thrust recovery effect." When a rotor and body are operated out of ground effect, the vertical drag on the body produces a net downforce that counters the thrust of the rotor. However, at lower heights in the presence of the ground, the body will begin to produce a net upward thrust or thrust recovery effect that can augment the thrust produced by the rotor itself. Hance [12] however showed that this thrust recovery effect is not a general effect and depends on the body cross-sectional shape. Hance [12] also found that bodies with the circular and elliptical cross-sections showed evidence of the Fradenburgh thrust recovery effect [24] at higher blade loading coefficients, while the rectangular cross-section showed no evidence of the thrust recovery effect.

1.2.3 Sediment Physics Under the Action of Vortical Flows

The flow induced by the rotor and its interaction with the airframe and the ground is the root cause for the mobilization and entrainment of sediment that forms the dust cloud. Therefore, a good understanding of the sediment transport physics is also required. Sediment transport is broadly classified into two regimes: (a) Aeolian flows, or wind-driven particle transport, and (b) Riverine flows, or hydrodynamic particle transport, common in coastal environment. Sediment

motion by the action of air is of primary interest to the problem of brownout and has been discussed in some detail in the present work.

Particle motion in brownout dust clouds can be influenced by various factors, that include rotor parameters (e.g., disk loading, blade loading), rotor configurations (e.g., coaxial, tandem), interference from the fuselage, flight path followed by the rotor, soil properties (e.g., moisture content, hardness), and topology of the surface. All these factors can influence, and to varying degrees, the severity of the dust clouds that are formed.

The DARPA "Sandblaster" program [6,7], performed full-scale brownout field tests, to characterize and quantify dust clouds. These tests extracted particle concentration and particle size distributions around helicopters performing hover-taxi maneuvers at various heights above the ground. Figure 1.9(a) shows the particle concentration in dust clouds with sizes varying from 1 μm to 1,000 μm. These dust clouds contained very high concentrations of small-size dust particles (1 μm–10 μm), which tend to remain suspended in the air for extended periods of time, and are primarily responsible for much of the visual obscurations produced inside the dust cloud. In comparison, dust particles of larger sizes (100 μm–1,000 μm) are many orders of magnitude lower in concentration because these particles tend to quickly settle back on the ground under gravity.

Figure 1.9(b) shows the equivalent mass fraction of the dispersed phase (i.e., particle present in the rotor flow) to the carrier phase (i.e., the rotor flow). On an average, the mass fraction of the dispersed to the carrier phase is $< 0.1\%$, which implies that the brownout problem can probably be modeled as one-way coupled with only the carrier phase influencing the dispersed phase, at least away from the immediate region of the ground. If such a simplification can be justified,

computational costs of modeling brownout can be significantly reduced.

Figure 1.10 shows a detailed schematic of the primary mobilization and transport mechanisms of particles found below a rotor. Three main process of particle motion under the action of the carrier flow has been identified in previous studies [8, 22]: (a) Mobilization, which is where the particles just start to become mobilized by the external flow, (b) Entrainment, which involves processes responsible for pickup of particles from the bed under the influence of the external flow, and (c) Transport, which governs the trajectories of these entrained particles in the flow field.

The initial mobilization and entrainment of the particles from the sediment bed is governed by the forces acting on them when they are stationary. These forces include aerodynamic (shearing action of the boundary layer flow), pressure forces (from the passage of vortices), gravitational forces, and inter-particle forces. Particles can be entrained when the aerodynamic and pressure forces exceed the gravitational and inter-particle forces. Rotor flows and its interaction with the airframe can significantly affect the velocity and pressure fields at the ground, which can produce sediment mobilization and uplift [33].

Once a particle in mobilized, the resulting forces acting on the particle govern its motion. The initial motion of the particle can be categorizes as: (a) creep, (b) saltation, and (c) suspension; see Figs. 1.5 and 1.10. Creep is characterized by the rolling of mobilized particles along the ground. This process occurs either because the particles are heavy or the local flow gradients are not large enough and the forces in the vertical direction are insufficient to uplift the particles [22]. Saltation is the bouncing of particles along the surface of the sediment bed and is typically the principal mechanism of transport of sand particles in unidirectional flows. However, in vortical

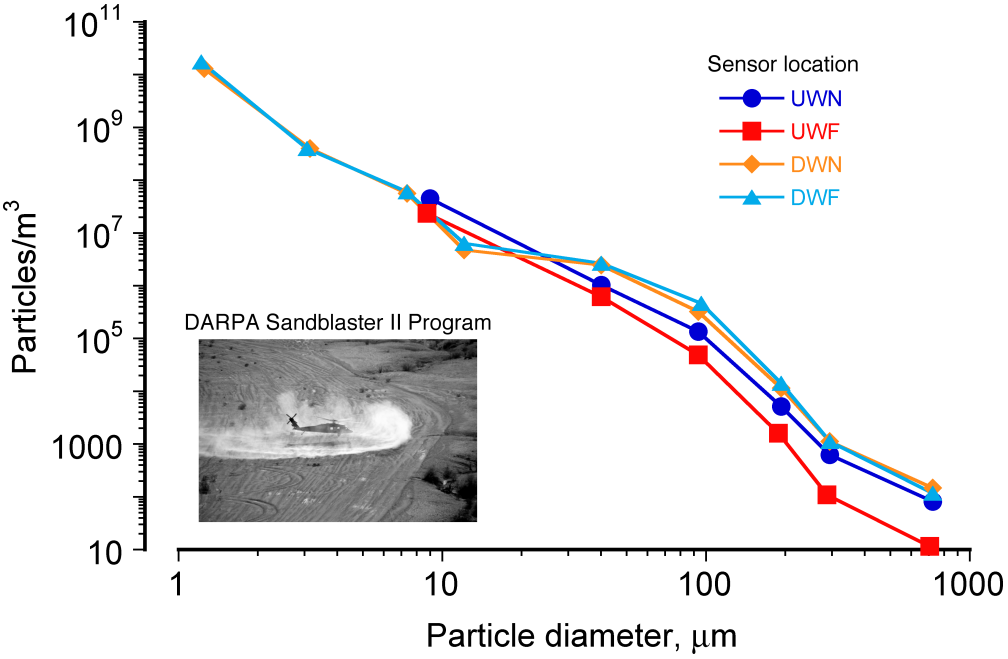

(a) Average particle concentration

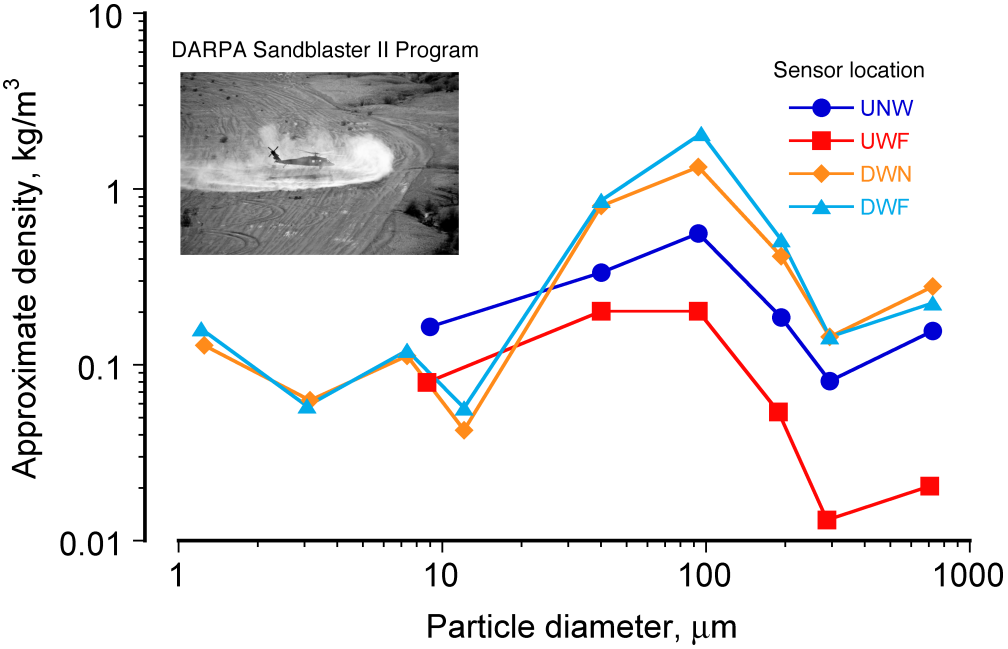

(b) Percentage of the mass density of particles to air

Figure 1.9: Concentration and percent mass density of particles of different diameters in a dust cloud [6, 7]: (a) average particle concentration, i.e., number of particles per cubic meter, and (b) percentage of the mass fraction of the dispersed phase to the carrier phase.

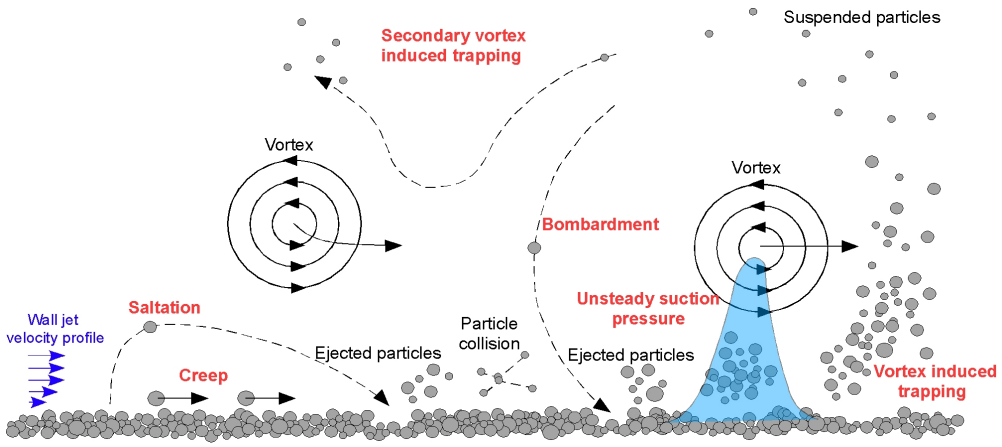

Figure 1.10: Schematic showing important particle mobilization and transport proceses in rotor flows [8].

flows, a modified trajectory is followed by these particles when compared to unidirectional flows. Finally, suspension is the motion of dust particles in which these particles remain in the air for longer durations because of their very small terminal velocities, i.e., high settling times.

Another mechanism of sediment entrainment responsible for uplifting large quantities of dust is bombardment ejection [8,34], where previously suspended particles can impact the bed with high momentum under the action of the local vortical flow, and so eject many more particles into the flow. This mechanism of bombardment ejection has been observed in actual brownout dust clouds, and also has been measured and quantified in laboratory experiments [8, 22]. A variation of the bombardment mechanism is reingestion bombardment, where suspended particles recirculate in the rotor wake flow and bombard back onto the underlying sediment bed, ejecting large quantities of particles into the flow from the resulting impacts [8, 35].

An example of the formation and evolution of the dust cloud is shown in Fig. 1.11. As the helicopter approaches the ground, the action of the rotor wake is sufficient to mobilized and entrain loose sediment particles from the bed. Some of the suspended particles are reingested through the

Figure 1.11: Instantaneous renditions showing the development of a brownout dust cloud (Source: Optical Air Data Systems).

rotor disk and impact the bed at a relatively high velocity, quickly mobilizing large volumes of dust, as shown in Figs 1.11(b) to 1.11(e). The strong vortical flows generated by the rotor create local regions of upwash and downwash that trap and recirculate the particle, and the global recirculation flow through the rotor can also occur and can be a major contributor to the brownout problem; see also Fig. 1.5. Notice that the helicopter is quickly engulfed by the dust cloud (Fig. 1.11(f)) and it is during this stage of cloud development that the pilot loses the necessary visual cues that can compromise flight safely. The dust is also uplifted to the plane of the rotor and can collide with the blade, resulting in the abrasion of the blades.

1.3 Literature Survey of Brownout Related Research

The understanding of the problem of brownout requires a multidisciplinary approach, which involves at a minimum, fluid dynamics (rotor in ground effect and interactional aerodynamics), particle dynamics (sediment mobilization and transport), and flight mechanics (handling qualities and visual perception). From the perspective of the present research work, the primary areas of interest are the fluid dynamics and sedimentology aspects of brownout. Figure. 1.12 shows research works that have been performed to understand brownout, and has been categorized into work that focus on: (a) the rotor flow development in ground effect, (b) the combined dual-phase flow over a mobile sediment bed, and (c) interactional aerodynamics, i.e., between rotor/airframe and main rotor/tail rotor. This research work has also been color coded to identify them as experimental studies, computational studies or field tests. The complexity of the brownout problem and the cost involved is highlighted in the limited number of full-scale field tests, with much of the foundational

research being focused on laboratory-scale experiments and numerical simulations. The present section discusses the relevant previous work performed to better understand the various aspects of the brownout problem.

1.3.1 Brownout Field Tests

Brownout dust clouds generated by actual rotorcraft operating in desert-like environments are important to better characterize the dust clouds, as well as explore the sensitivity of the cloud to rotor configuration and rotor parameters. While the quantitative measurements of the flow field and dust cloud that can be made during field tests are relatively limited, they can be useful for validating brownout simulation methodologies.

Rodgers [36] conducted field tests of single rotor and tandem rotor helicopter configurations as a function of the rotor type and rotor height above the ground to measure the concentration of particles in the dust cloud. The concentration of particles were measured using 25 dust collectors attached to the fuselage of the helicopter. It was found that for both rotor configurations, the concentration of dust was lowest close to the rotor hub and increased away from the rotor. For the tandem configuration, the concentration of dust was higher in the region of rotor overlap. Also, the maximum size of particles decreased as the rotor height above the ground was increased. Furthermore, dust concentration was seen to be increased by a factor of three during landing and takeoff maneuvers as compared to hovering flight.

DARPA's "Sandblaster" program was undertaken to examine aspects of the brownout problem for helicopters in a desert-like environment [6, 7], primarily with single main rotor helicopters.

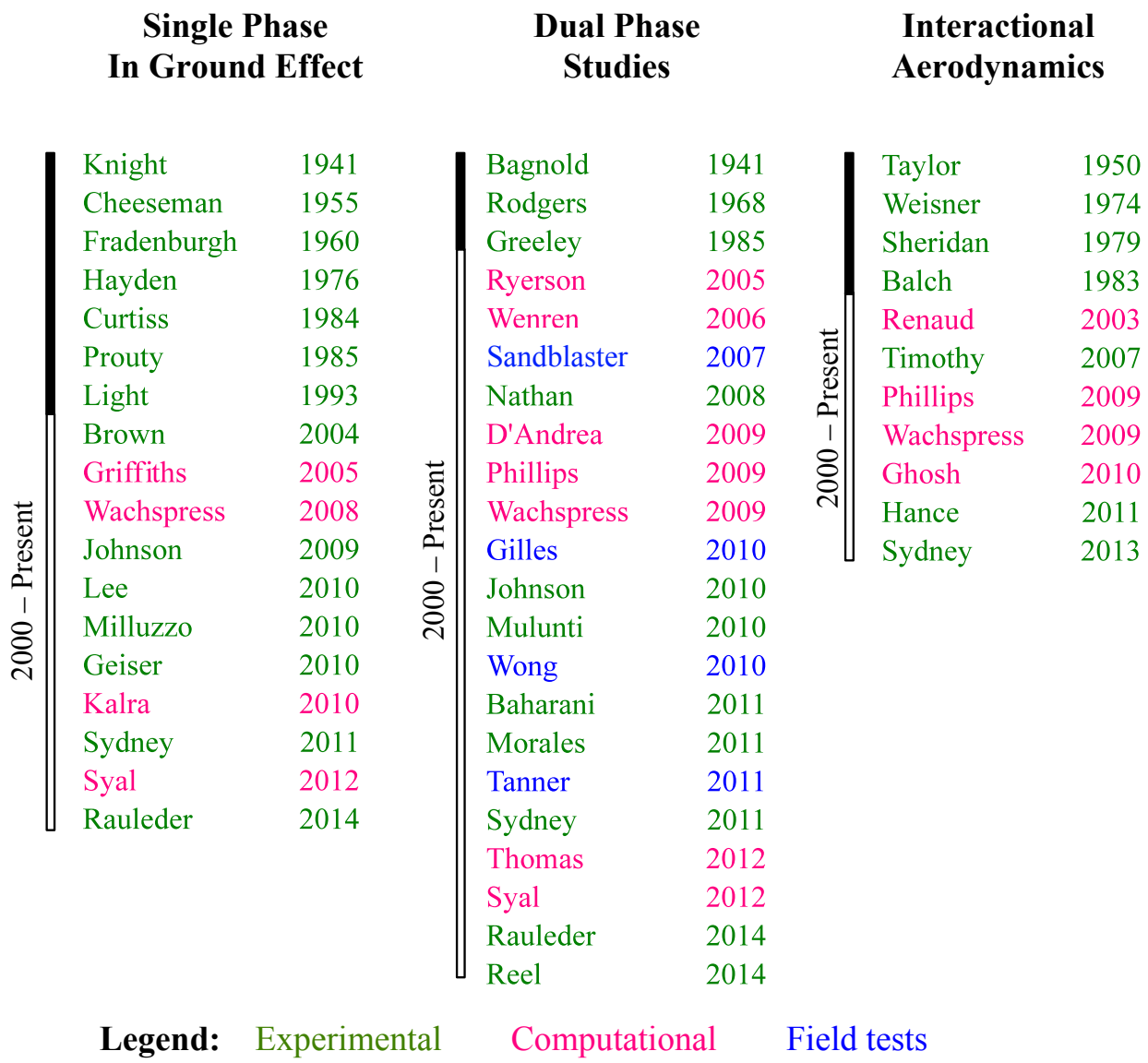

Figure 1.12: Timeline of brownout related research.

The goal of these field tests were to characterize the dust cloud developments during hover-taxi maneuvers flown at different heights above the ground, and during takeoff and landing maneuvers. Particle concentrations were recorded in containers (bins) at various locations and heights above the ground. Again, the results showed that the dust cloud comprised primarily of small-sized particles (see Fig. 1.9(a)), with the larger particles quickly settling back to the ground. The measurements showed that helicopters with higher disk loadings generated dust clouds with higher particle concentrations, which can be attributed, in part, to the higher average flow velocities induced at the ground.

Gilles et al. [37] conducted field tests to measure the dust emission generated by low flying helicopter at different operating conditions over both undisturbed and previously disturbed desert surfaces. These measurements showed that the dust emissions decreased with increased forward airspeed of the aircraft, which decreases the residence time of the aircraft over any region and, therefore, reduces the interaction of the helicopter downwash with the mobile surface. The measurements further showed that dust emissions over previously disturbed surfaces were an order of magnitude greater than for the undisturbed surfaces.

While the field tests [6, 7, 36, 37] have focused more on the concentration and distribution of the particles in the dust cloud, Wong and Tanner [38] and Tanner [10] attempted to better quantify the structure of the dust clouds. A photogrammetry technique was used in which photographs of the dust clouds were taken using several synchronous cameras, and then analyzed using triangulation methods to find the coordinates of different features on the cloud. Wong and Tanner [38] measured the location, size and average convective velocity of the dust cloud, along with the characteristics

of defined structures within the cloud. These measurements have been used to compare the dust clouds predicted by the methodology that was developed in the present research.

1.3.2 Single-Phase and Dual-Phase Experiments on Isolated Rotors

While the aforementioned studies have helped provide some insight into the phenomenon of brownout on full-scale rotorcraft, it is difficult to study the details of the fluid dynamic mechanisms involved in the actual entrainment of the particles. Therefore, several experimental studies have focused on studying single-phase and dual-phase flow fields produced by laboratory-sized rotors to better understand the physics of brownout. Unlike full-scale field tests, such experiments allow for better control of the flow environment and can be useful in isolating the different features that contribute to the problem of brownout.

The earliest studies of rotor in ground effect operations have focused on quantifying the rotor performance [23–29]. Some studies were conducted to quantify changes to the wake geometry using flow visualization techniques. Taylor [39] conducted flow visualization studies using balsa dust as seeding material to qualitatively study flow patterns in ground effect produced by single rotor and coaxial rotor systems. Light [29] conducted flow visualization by using the wide-field shadowgraph method to measure the positions of the rotor tip vortices produced under a hovering rotor in ground effect.

Curtiss et al. [27] conducted experimental and analytical studies to investigate the aerodynamic characteristics of an isolated rotor in ground effect at low advance ratios. These experiments showed that the favorable effect on performance of ground proximity in hover disappears rapidly

with small increases in advance ratio. Two flow regimes were shown to occur: (a) recirculation of the rotor wake at the low advance ratios, and (b) formation of a ground vortex as the advance ratio was increased. Hot wire measurements of the flow field under the rotor in ground effect were analyzed to determine the strength of the rolled-up ground vortex, which was found to be much stronger than the individual tip vortices.

Single-phase flow studies in forward flight (at low advance ratios) were also made by Nathan and Green [31] for a range of rotor heights above the ground. Traditional two-component and three-component stereoscopic particle image velocimetry (PIV) was used to investigate the single-phase flow characteristics, and the formation of a recirculation region at low advance ratios and the ground vortex at higher advance ratios were shown. Fine talcum powder was used to represent the material of the sediment bed, and it was observed that the talcum powder could get trapped and accumulate in the regions of high vorticity ahead of the rotor disk. However, the tracking of sediment particles were not performed in unison with the measurement of the flow field and, therefore, these studies were limited to single-phase studies.

Lee et al. [40] used high-speed flow visualization and PIV techniques to study the flow field around a hovering laboratory-scale rotor positioned at various heights above a ground plane. Time-averaged and phase-averaged velocity profiles close to the ground were measured as part of this study. Mechanisms such as vortex diffusion, vortex stretching, and turbulence generation were identified, and their characteristics in ground effect were studies. For example, as the vortex filaments approach the ground, vortex stretching and straining was shown to increase the swirl velocities within the vortex cores, leading to a reintensification of vorticity. Furthermore, it was

found that these stretching effects were largest when the rotor hovered at an intermediate height above the ground. Away from this height, the effects of vortex diffusion became more significant than vortex stretching.

Johnson and Leishman [22] used an experimental setup similar to that of Lee, and performed both single-phase and dual-phase measurements of the flow environment induced by a small-scale rotor hovering above a sediment bed. High-resolution, near-wall, PIV measurements showed large excursions in the boundary layer velocity profiles as a result of the convecting vortices. The highest sediment entrainment levels were seen to occur at regions where the vortices were closest to the ground because this resulted in increased groundwash and wall shear in those regions. In addition, this study observed the highly aperioidic phenomena of vortex pairing and merging of adjacent turns of the blade tip vortices. These phenomena were found to play a key role in increasing local induced velocities, and consequently shear stresses at the ground plane, which in turn increased initial mobilization and uplift of particles from the bed. Secondary vortical structures and the presence of a separation bubble just downstream of the vortex impingement zone was also observed. In the dispersed phase, the mechanisms of saltation, saltation bombardment, reingestion bombardment and vortex induced trapping were observed using high-speed flow visualization.

Milluzzo et al. [9] conducted rotor wake measurements in ground effect for rotors with various blade planforms and tip shapes (i.e., rectangular, swept, BERP-like, and slotted-tip). The core size and swirl characteristics of the tip vortices for the different blades were measured. A significant finding from this study was the effectiveness of the slotted-tip blade in reducing the strength of the tip-vortices through the injection of turbulence and vorticity into the tips of the blade, which

accelerated the diffusion of the tip vortices. This reduction in strength of the tip vortex had the effect of reducing groundwash velocities (mean and instantaneous) at later wake ages which could play a key role in minimizing particle mobilization and entrainment.

Extending the work of Johnson and Leishman [22], Sydney et al. [8] conducted further time-resolved flow visualization, PIV, and particle tracking velocimetry (PTV) experiments to study the flow fields produced by one-bladed and two-bladed rotors operating in ground effect. A comparison of the rotor flow fields was conducted at the same rotor blade loading coefficient. The analysis showed that the 2-bladed rotor system was more susceptible to the creation of aperiodicity in the flow, which was caused by vortex merging and pairing and was shown to be a significant factor influencing sediment uplift. The 2-bladed rotor system also changed significantly the bed topology from erosion, which altered the trajectories followed by the older tip vortices and increased the susceptibility to producing vortex-vortex interactions, thereby further increasing the aperiodicity in the flow. Several fundamental processes of sediment uplift and mobilization were identified: (a) creep, (b) modified saltation and saltation bombardment, (c) vortex induced trapping, (d) reingestion bombardment, and (e) secondary suspension; see Fig. 1.10.

The unsteady pressures induced on the bed as it affected particle uplift and motion under a hovering rotor was experimentally investigated by Reel [41]. These experiments involved time-resolved flow visualization and particle PIV measurements of the rotor wake, which were related to time-histories of the unsteady pressure field measured over a ground plane. Distinctive pressure signatures were identified that corresponded to three regimes on the ground plane as they were affected by the vortices in the rotor wake. Particle tracking velocimetry was used to measure

the motion of the sediment particles, and measurements of the particle displacements and their local concentrations were found to be related to the location of the vortices and the corresponding unsteady pressures that were produced over the ground plane.

The turbulence in the flow under a hovering rotor in ground effect was studied by Rauleder et al. [33,42]. The flow field measurements were obtained from the single-phase and dual-phase flow experiments of Sydney et al. [3, 8]. The quantification of turbulence under a rotor is challenging, in part because of the highly aperiodic nature of the flow and the difficulty in collocating the tip vortices for analysis. The study showed that a general two-way coupling between the flow phases were produced near the ground, with the coupling being very significant under certain conditions. For example, it was also shown that the uplifted particles altered the carrier flow near the sediment bed, leading to an earlier distortion of the external flow induced by the blade tip vortices and the accelerated diffusion of the vorticity they contained. Furthermore, the anisotropy of the turbulence in the flow was found to increase because of the uplifted particles in the region closer to the ground.

Mulinti and Kiger [43] and Geiser and Kiger [44] used a simplified experiment to simulate the representative flowfield beneath hovering rotors and study the sediment dynamics. These studies allowed a relatively simpler analysis of the rotor flow by decomposing it into its constituent parts, i.e., a vortical flow in the form of vortex rings superimposed upon an axial jet-like flow. Phase-locked flow visualization techniques and PIV were used to characterize these flows and to track the motion of the sediment particles. It was found that the secondary vortical structures were formed on the interaction of the vortex rings with the ground plane, which also influenced the particle motion.

Haehnel and Dade [45] conducted videography experiments to understand sediment dynamics near the ground under the action of an axisymmetric jet flow. Measurements of sediment bed profile were made to quantify the rate of erosion of the bed. It was found that the turbulent shear stresses, and not the average stresses on the surface, drive the mobilization of sediment particles. The study further exposed the role of the instantaneous velocity field and turbulent fluctuations in particle uplift.

1.3.3 Rotorcraft Interactional Aerodynamics

The mobilization and uplift of dust particles is primarily caused by the action of the flow induced by the main rotor wake, especially the localized effects produced by blade tip vortices, as discussed previously.. However, there can be a variety of possible other explanations for apparent differences in the dust clouds, including the effects of the tail rotor (if used) and flow distortions caused by the airframe (size, shape, of the fuselage, sponsons, empennage, etc.), although the individual effects may be difficult to isolate.

The problem of aerodynamic interactions between the rotor and airframe have been studied for several decades, both experiments and simulations having helped in the understanding of this very difficult problem; see Chapter 11 of Leishman [4] for a review. However, studies to quantify the role of the rotor/airframe interactions as they might affect the flow at the ground have been more limited. There have been a number of experimental and theoretical studies that have investigated these interactional aerodynamic effects. Early studies included wind-tunnel experiments [46–49] have shown that substantial pressure loads are induced on the fuselage by the main rotor wake, and

the influence of the rotor wake(s) on the airframe also affects the performance of the rotor.

Bi et al. [50, 51] performed wind-tunnel experiments on a model scale representative rotor/airframe configuration. Results from this study showed that the interaction of a rotor wake with a body is an extremely complicated and highly unsteady process. The amplitude of the unsteady pressures on the body were found to be relatively large and significantly exceeded the mean pressures. Therefore, any theoretical analysis of the interactional flow field must include unsteady effects to account for these effects.

Wide-field shadowgraphy techniques were used by Bagai et al. [11] to visualize the blade tip vortices in the rotor wake in the presence of a body. The study showed that the presence of the body significantly affected both the contraction and axial convection velocities of the tip vortex filaments. The tip vortex geometry was also shown to locally distort in close proximity to the body, and appeared to loop over and around the body, stretching significantly in the process. In some cases, the tip vortices burst, resulting in locally increased levels of turbulence after the diffusion of the tip vortex.

More recently, Hance [12] performed a study on the flow field of a hovering rotor in ground effect in the presence of a body. Videographic flow visualization and two-component PIV measurements were performed to examine the developing vortical wake produced by a laboratory scale two-bladed rotor. The bodies examined had circular, elliptical, and rectangular cross-sections. The results showed that the flow over the nose of each of the bodies (which was not obstructed by the body) was similar to that of the isolated rotor, but with some minor differences in the flow at the ground. The slipstream boundary was shown to be severely disrupted by the tail of each body, and

showed larger variations in the flow velocities from those produced by the isolated rotor. Wake impingement on the body was shown to cause the bursting of the tip vortices. Furthermore, the different body shapes caused substantial changes to the flow field beneath the rotor. For example, the rectangular cross-section shaped body produced significantly higher Reynolds stress in the wall region compared to the other bodies. Therefore, it is likely that the resulting boundary layer flow over the ground would have some effect on the mobilization and uplift of dust.

In an extension of the work on quantifying the flow field under a hovering rotor in ground effect [8], Sydney and Leishman [5] performed single-phase and dual-phase PIV and PTV measurements with three different bodies placed in the rotor wake over a mobile sediment bed. The bodies examined were similar to that used by Hance [12], i.e., of circular, elliptical, and rectangular cross-sections. The study found that the continuous helicoidal filament formed a hairpin loop around the surface of the body, reintensifying first the vorticity and then bursting and causing rapid diffusion of vorticity. A localized flow with a relatively high velocity was observed at the tail region of each of the bodies as a consequence of the interaction between the rotor-induced flow and the body. This region was found to vary both in magnitude and direction for each of the three bodies. The three-dimensional variations in the flow at the ground produced by the bodies manifested as non-uniform concentrations of particles compared to case of the isolated rotor. The study also found that the particle concentrations produced by the flow in the presence of bodies to be radially asymmetric, and that the distribution of particles depended on the variations of the flow on the ground produced by the individual body shapes.

Experiments examining the aerodynamic interactions of multi-rotor systems (e.g., main ro-

tor/tail rotor, coaxial rotor system, etc.) have been limited, in part, because of the experimental challenges involved in measuring the flow field in the wake. Various aspects of the main rotor/tail rotor interactions, primarily related to rotor performance and blade-vortex interaction noise have been studied [46, 52–54]. While the individual wakes from the tail rotor are much weaker than those of the main rotor, the effect of the tail rotor on the structure of the main rotor wake has not been quantified. Changes to the structure and strength of the main rotor wake because of the presence of the tail rotor may affect the flow at the ground and therefore, affect the process of sediment entrainment and uplift.

1.3.4 Computational Modeling of Rotorcraft Brownout

While good experiments and analysis of the measurements are critical to understanding the key features of the underlying physics of the brownout problem, it can be very difficult and time consuming to conduct exhaustive parametric studies in the laboratory. The number of interdependent factors involved in the brownout problem suggests that computational modeling of the dust clouds can offer better insight into the fundamental parameters that influence the intensity of the dust clouds. Such models have much value for the brownout problem, not only for their potential predictive capability but also for their ability to help understand the individual contributing mechanisms of sediment mobility. These simulation techniques are not limited by the same constraints of geometric scale and dual-phase flow scaling issues that are faced with most laboratory experiments. A difficulty in simulating the resulting two-phase dusty flow is that the mathematical models must predict the vortically dominated flow at the ground, as well as being able to model

the various mechanisms that lead to the mobilization, uplift and convection of potentially billions upon billions of small particles.

1.3.4.1 Modeling of the Aerodynamic Environment

Previous models for the simulation of rotor in ground effect flows have focused on developing theoretical and relatively simple numerical models. Betz [55] developed analytical methods to study the effect of the ground on a lifting propeller, which showed that the power required by the propeller decreased at heights lower than the propeller radius for a constant thrust. Knight and Hefner [25] developed a vortex cylinder method to model rotor performance in ground effect using the method of images to represent the ground plane.

Eulerian grid-based methods have been used to model the complex, unsteady, three-dimensional flow field produced by a rotor in ground effect. Kalra et al. [56] used an overset, compressible, Reynolds-Averaged Navier–Stokes (RANS) solver to simulate the hovering micro-rotor setup of Lee et al. [40], as described earlier. This methodology was initially developed by Lakshminarayan and Baeder [57,58]. The numerical results obtained were validated by comparison of the predicted integrated thrust and power coefficients with experimental measurements. The tip-vortex trajectories and time-averaged jet-flows predicted by the RANS simulations were also found to give good correlation with the measurements. The primary disadvantage with RANS models, however, is the computational expense. For example, a large number of mesh points are required to: (a) accurately capture complex viscous phenomena such as boundary layer growth and vortex ground interactions, and (b) to minimize artificial dissipation and allow for long term preservation of vorticity

in the flow. Furthermore, the number of mesh points required for viscous, turbulent RANS simulations is known to scale linearly with Reynolds number, making full-scale, realistic simulations exceedingly expensive.

Another method, based on the incompressible RANS equations to model the rotor flow, was developed by Rajagopalan [59]. Although this model captured viscous effect close to the walls, the rotor blades themselves were modeled using a momentum-source representation. A limitation of this approach is that it did not model the localized effect of the blade tip vortices, which are now known to play a critical role in sediment uplift and mobilization below a rotor.

Phillips and Brown [32, 60, 61] used a vorticity transport model (VTM) to solve for rotor flows in ground effect. The VTM is a finite-volume based method that solved for the evolution of vorticity by solving the incompressible Navier–Stokes equation expressed in an equivalent velocity-vorticity form. By nature of the VTM formulation, vorticity is inherently preserved in the solution and the breakdown of larger vortical structures into secondary structures are properly resolved. The study showed that an increase in the advance ratio of the ratio increased the strength of the tip vortices, which played a key role in the development of the dust cloud.

Wenren et al. [62] used a vorticity confinement method inside an incompressible flow solver to better resolve the tip vortices generated by a hovering rotor. This study showed that the tip vortices tend to roll along the ground plane, creating concentric rings of increased particle concentration. The vorticity confinement method convects concentrated vortices without artificial diffusion when using relatively coarse meshes. However, this technique requires the use of empirical factors to resolve the boundary layer at the ground.

A Direct Numerical Simulation (DNS) was performed by Morales and Squires [63] to gain insight into the fluid-particle dynamics near a sediment bed under the influence of a train of coherent vortical structures. Most computational studies on brownout have neglected certain sediment processes like particle-particle collisions. However in this work, the competing effects of vortex-vortex interactions, inter-particle collisions, and gravitational effects on particle transport were studied in detail, albeit on a simplified problem. A key finding in this study was the increased effects of inter-particle collisions near the boundary layer because of the larger dispersed-phase concentrations caused by gravitational settling.

An alternate to the Eulerian grid-based approaches adopted for modeling rotors in ground effect is to use Lagrangian-based flow field solvers. One such method is the free-vortex analysis, which has been used extensively over many decades to predict rotor performance, wake geometries, and induced velocity fields under a variety of flight conditions; see Chapter 10 of Leishman [4] for a comprehensive review. Syal et al. [64–67] and Wachspress et al. [68, 69] have performed computational analyses of full-scale rotorcraft in ground effect using a time-accurate free vortex method (FVM). The FVM is a very efficient numerical scheme for the preservation of far-wake vortical structures, but must employ an empirical model for the growth of the core size as the vortex core diffuses; this vortex diffusion with wake age is a function of vortex Reynolds number. The FVM is used to model rotor flows in the present study and discussed in detail later; see Section 2.2.

Fletcher and Brown [70] used a VTM to study the aerodynamic interactions between the main and tail rotor in hover and at a range of forward flight speeds. While this study was focused on the implications of the main rotor/tail rotor interaction on the directional control of the helicopter,

the wake structure was examined in different flight conditions. This study showed that in hover the tail rotor wake undergoes a distinct change in geometry when exposed to the flow field of the main rotor, wherein some or all of the vorticity in the tail rotor in entrained into the wake of the main rotor. This interaction of the two rotor wakes was found to be a highly unsteady process and was found to depend, to some extent, on the direction of rotation of the rotor. As the forward flight speed was increased, both the entrainment of the tail rotor wake into the main rotor wake and the perturbation to the main rotor loading from the tail rotor were reduced.

Phillips and Brown [60] used the VTM coupled to a particle transport model, to examine the brownout dust cloud uplifted by a tandem rotor configuration. The effect of blade twist on the development of the dust clouds were also explored. This study showed that the severity of the dust clouds produced is intricately linked to the ground vortex formed by the aerodynamic interaction of the forward and rear rotors. The strength and location of the ground vortex was found to depend on the forward flight speed of the helicopter. At higher advance ratios, a strong ground vortex was created by the rear rotor, while at lower advance ratios the ground vortex of the rear rotor is replaced by a strong vortex that lies just below the leading edge of the front rotor. This ground vortex was found to be responsible for mobilizing significant amounts of dust from the sediment bed, and also caused the recirculation of dust through the front rotor, exacerbating the problem of brownout.

Ghosh et al. [71] used an incompressible RANS solver to predict the flow field in ground effect produced by a single, tandem, side-by-side, and quad rotor configurations. The rotor was modeled as momentum-sources and so was unable to capture the effects of the discrete tip vortices.

Studies were performed in hover at various heights about the ground. Although the aerodynamics modeling of the rotor wake was insufficient because of the lack of concentrated vorticity, the study showed that the flow field produced were unique to the rotor configuration.

Thomas et al. [72] used a Lagrangian-Eulerian hybrid methodology to better understand the two-phase flow field close to the ground in hover. The methodology coupled a numerical efficient FVM far away from the ground to a relatively high-fidelity three-dimensional RANS based CFD methodology to capture the viscous phenomena present at the ground. The work also utilized the use of graphics processing units (GPU) to expedite the computational process and achieve an order of magnitude speed up when compared to traditional CPU clusters.

1.3.4.2 Modeling of Particle Motion

Two methods have been used previously to model the dispersed particle phase. In an Eulerian grid-based formulation, the particle in the cloud are represented by their concentrations on the grid and changes in the particle concentration are based on the governing particle transport equations. A Lagrangian-based methodology models the individual particles directly and there particles are tracked through space and time based on the net forces acting on each of the individual particles.

Ryerson et al. [73] developed an Eulerian-based particle entrainment and dispersion (PED) methodology. The particle concentration in space and time were solved using the advection-diffusion equations, which represents changes in the particle concentration as a function of the computed velocity gradients in the three spatial dimensions. Entrainment of the dispersed phase was modeled as an equilibrium boundary flux [74], which is based on the threshold friction veloc-

ity. A one way coupling was assumed wherein only the carrier phase affects the dispersed phase. This carrier phase (i.e., the flow field) in ground effect was solved using an Eulerian based inviscid, incompressible approach of Rajagopalan [59], which, as discussed previously, solves the RANS equations using a momentum-source representation of the rotor blades and cannot model the effects of the discrete vortices in the flow. The PED methodology of Ryerson et al. [73] was also coupled to other Eulerian grid-based solvers [62, 75, 76], the key assumptions in the modeling of the dispersed phase being the same. The important effects of bombardment ejections and particle-ground interactions, however, were not modeled.

Phillips and Brown [32] developed an Eulerian particle transport method that was based on the particle concentrations. This model was based on the assumption that away from the ground the suspended particles remain in near-equilibrium under the action of the aerodynamic forces. Near the ground, a source model in the sublayer of the boundary later profile was used, in which particles were entrained by the mechanism of saltation. The initiation of particle mobility was modeled by using an empirical flux model [77], which uses the threshold friction velocity expression developed by Shao and Lu [78]. The resulting particle transport equations were expressed in a mathematically similar manner to the vorticity transport equation, and therefore, the evolution of vorticity in the VTM convected both the vorticity and the particle concentration fields. The mechanism of bombardment-based ejections were not modeled in this work.

Wachspress et al. [79] developed a Lagrangian-based methodology to simulated the entrainment and subsequent motion of the particles in the dust cloud. The entrainment of particles were based on a threshold friction velocity model, based on the model developed by Shao and Lu [78].

Because brownout dust clouds contain large concentrations of small size particles (see Fig. 1.9(a)) and the Shao and Lu model predicts higher threshold velocities for particles of smaller size, Wachspress et al. [79] altered the empirical constants in the model to "tune" them to rotor flows. The threshold friction velocity was compared to the friction velocity obtained from a logarithmic boundary layer assumption, as the flow field was solved using an inviscid methodology [69]. A similar method for modeling the dispersed phase was developed by D'Andrea [80–82].

A comprehensive review of the modeling of the particle motions in rotorcraft brownout was conducted by Syal [83]. The study showed that while dual-phase rotor experiments [8, 22] exposed the significant sediment mechanism likely to participate in rotorcraft brownout, previous models [32, 79, 80] accounted only for particle mobilization mechanism through boundary layer shear effects. Syal et al. [64,66] developed sediment entrainment models that accounted for effects such as the gravity on the particle-fluid dynamics, and the unsteady pressure forces produced by vortices convecting close to the sediment bed. The mechanism of particle bombardments, which have been identified as being responsible for ejecting large quantities of dust, have were modeled using a probabilistic approach based on the conservation of energy of the impacting and ejected particles [66]. This particle still assumed a one-way coupling between the carrier and dispersed phases, in which particles were influenced by flow velocities, but not vice-versa. Monodispersed particles were considered and sediment mechanisms such as particle-particle collisions were ignored, as their inclusion increased the computational costs required by many orders of magnitude. The methodology developed by Syal et al. [64] is used in the present work, and is discussed in detail in Section 2.8.

1.3.5 Brownout Mitigation Studies

The severity of a brownout cloud can be broadly classified to depend on the: (a) quantity of dust particles uplifted, (b) spatial and temporal distribution of particles in the cloud, and (c) rapidity at which the particles are uplifted. The severity of the cloud potentially depends upon many dependent and interdependent parameters, such as the rotor disk loading, blade loading, rotor tip speed, number of blades, blade tip shapes, rotor configuration, fuselage shape, empennage configuration, and flight profile of the aircraft near the ground. Because most of these parameters might have interdependent influences and their individual effects are hard to isolate.

Milluzzo and Leishman [2] analyzed photographs of videography of different rotorcraft landing in brownout conditions and hypothesized that certain rotor parameters are likely to play a key role in brownout severity based on their geometry and operating conditions. It was shown that severity may depend on parameters such as the total wake strength, disk loading, and reduced frequency of the convection of the vortex wake. A tentative ranking of the brownout severity for different rotorcraft was proposed, as shown previously in Fig. 1.4.

Tritschler et al. [84, 85] conducted a formal optimization study that explored the potential sensitivity of brownout to rotor design parameters of a single main rotor (SMR) configuration. The design variables chosen were the blade radius, blade chord, and linear twist rate. The objective function used in the study was a simplified surrogate metric to the Modulation Transfer Function (MTF) [86], which is based on the optical attenuation of light through the dust clouds. This metric allowed for a comparison of different brownout clouds for different rotor blade designs, as "good" (i.e., allows "perfect" visibility) or "bad" (i.e., completely eliminates visual cues) from the pilot's

perspective. In general, the study found that the optimizer favored rotor designs that resulted in a high disk loading. While a higher disk loading would result in a higher downwash velocity that could potentially uplift more dust from the sediment bed, this higher downwash would also convect the dust cloud away from the rotorcraft, thereby granting the pilot better visibility of the ground.

Previous studies have identified the tip vortex to be one of the primary drivers of sediment entrainment [8, 22]. Milluzzo et al. [9] studies the effect of four different blade tip shapes on the structure of the tip vortices as they interacted with the ground plane. The measurements concluded that the blade tip shape could likely be an important aspect of the blade design for altering the flow velocities near the ground and, therefore, having the potential for altering the development of brownout conditions. In particular, the slotted tip, which diffuses the tip vortices by injecting part of the incoming air into the tip vortex, was shown to produce much lower shear stresses on the ground compared to all the other blade shapes tested.

Along with experiments, computational studies have been conducted to explore the possibilities of mitigating brownout. Syal et al. [65] conducted brownout studies to study the effect of tip shape, especially the rectangular and slotted tips [9]. The slotted tip blade was modeled within the context of a FVM methodology using a modified vortex core growth. Analysis of the dust clouds showed that the rotor wake produced by the slotted tip uplifted lower quantities of dust and potentially would have allowed to the pilot to see through the cloud better compared to the rectangular blade. Whitehouse et al. [87] have utilized simulations and experiments to examine the potential for aerodynamic mitigation of brownout using retrofittable concepts to more rapidly diffuse the tip vortex. Phillips et al. [32, 60] have also examined the potential for aerodynamic mitigation using

simulations, examining configurational effects as well as the sensitivity of brownout to rotor design parameters such as blade twist and tip shape. Each of these approaches has contributed much to developing a better understanding of the problem of rotorcraft brownout, and the growing body of research lends confidence that aerodynamic methods for brownout mitigation may eventually be feasible.

1.4 Objectives of the Present Dissertation

The objectives of this dissertation is to better understand the role of fuselage and rotor configurations on the developments of brownout dust cloud. A longer term goal was to better understand aspects of how brownout may be mitigated, either at source or by appropriate flight path management, or by the synergistic use of both approaches. The specific objectives of this dissertation are:

1. To use a Lagrangian-based FVM to model the aerodynamic environment around a rotor to better understand brownout dust cloud, especially during representative landing maneuvers. The methodology, therefore, must be capable of representing the effects associated with maneuvering flight conditions. Furthermore, the methodology must also be capable of conserving vorticity to older wake ages where they interact with the ground.

2. Extend the FVM to include the effects of a rotor operating at a different rotational frequency, such as the tail rotor. To use the extended FVM to study the effect of a tail rotor on the airloads and wake structure of the main rotor, and ultimately on the development of the brownout dust cloud.

3. Couple the above FVM with a model that represents the aerodynamic effects of the fuselage. The proposed fuselage model must be capable of capturing the key effects of rotor/fuselage interactions, such as the interaction of the tip vortices with the fuselage and the unsteady pressure effects of the rotor.

4. Extend the coupling of the aerodynamic and particle simulation models within a computationally practical framework that is suitable for routine parametric studies. This includes the use of hardware acceleration techniques and algorithmic routines to reduce the computational times by an order of magnitude.

5. To use the proposed numerical framework to study the predicted brownout dust clouds produced by different rotor configurations, main rotor/tail rotor, and rotor/fuselage configurations during a simulated landing maneuver.

6. Propose metrics to characterize the severity of brownout dust clouds, including the intensity and rapidity with which the dust clouds form. To use the proposed metrics to grade the relative severity of brownout dust clouds produced by the different rotor and airframe configurations.

1.5 Organization of the Dissertation

The problem of rotorcraft brownout has been introduced in the present chapter. A general discussion of the different aspects of this problem was presented, i.e., of the rotor flow in ground effect operation, dust particle motion under the action of an external flow, and potential conse-

quences the dust cloud has on visual obscuration, piloting safety, and rotor component abrasion. A detailed survey of previous work performed on the brownout problem was also discussed. The methodologies of previously developed brownout simulations have been discussed and their limitations outlined. The need to overcome these limitations, and to develop brownout simulation methodology of much higher fidelity that are representative of rotorcraft that encounter such conditions, was the primary motivation for the present work.

The remainder of the dissertation is organized into three chapters. The mathematical and algorithmic details of the methodology that was developed to simulate the aerodynamic flow and the brownout dust clouds are discussed in Chapter 2. This chapter first explains the modeling of the rotor flow field in ground effect using the FVM, followed by the viscous flow approximation used to model the flow near the ground. Modeling of a secondary rotor in conjunction with the existing free-vortex method is also discussed. The methodology used to model the airframe using a surface singularity technique is then discussed. The methods that were developed to simulate the mobilization, uplift, and convection of the dust particles in the flow is then discussed. The numerical methods developed to solve the particle equations of motion are also described in detail, along with the application of graphics processing units and clustering methods.

Chapter 3 discusses in detail the results obtained using the various modeling approaches that were developed in the present research, including the free-vortex wake model, the near-ground flow model, the tail rotor, the addition of a fuselage and the sediment mobility model. First, the outcomes from the validation study are presented, where available measurements were used to establish the credibility of the various modeling approaches being used. Then, an analysis of the

development of the rotor wake and the corresponding dust clouds produced during a simulated landing configuration for different fuselage configurations are discussed. Brownout clouds simulated for different rotor configurations are discussed along with an assessment of their relative severity. It is here that the role of the wakes from the interacting rotors in uplifting and mobilizing sediment is better exposed.

Chapter 4 presents two exploratory studies performed that are extensions of the work performed in this dissertation. The details of the methodology and the results are for these studies are presented in this chapter. A study was conducted to quantify the potential effect of blade/particle collisions on blade erosion using representative two-dimensional and three-dimensional simulations. The potential use of curved vortex elements instead of the straight-line segments to represent vortex filaments of a rotor wake was also explored. Their use was extended to realistic three-dimensional rotor wakes computed using the free-vortex method.

Finally, Chapter 5 presents the detailed conclusions obtained from the present work, and also provides recommendations for future work. It is clear, however, that much further work is needed before simulations can reach the high confidence levels needed for optimization and mitigation studies.

Chapter 2

Methodology

2.1 Introduction

This chapter describes in detail the overall methodology developed in the present work to study the problem of brownout. The computational model developed for the prediction of the dust clouds is made up of individual sub-components, each dealing with a different part of the problem. The aerodynamic flow produced by the rotors operating in ground effect, aerodynamic interactions of multiple rotors operating at different rotational frequencies, aerodynamic influence of the airframe, mobilization and entrainment of the sediment particles from the bed and their subsequent motion, and various particle interactions with the ground (i.e., bombardment), are aspects of the problem that are all considered. The development of a comprehensive methodology of brownout is difficult in that it must: (1) predict the flow over long time-scales, (2) contain enough dust particles to represent the essential features and physical characteristics of the brownout cloud, (3) track the position of the particles in space in practically feasible computational times.

A prerequisite in modeling rotorcraft brownout is to accurately model the time-dependent flow generated by the rotor close to the ground. In the present work, the rotor flow in ground effect was modeled using a free-vortex method (FVM), which is discussed first. A new coupling strategy for the FVM was developed to include the effects of more than one rotor operating at different rotational speeds, such as a main and tail rotor. The airframe was modeled using a surface

singularity method, which represents the surface of the fuselage as discrete control points on which flow tangency is satisfied. An inviscid-viscous method was used to predict the flow field arising from a combination of the rotor flow (modeled as an inviscid potential flow using the FVM) and the resulting (viscous) flow in the boundary layer region at the ground. Different models of particle mobility and entrainment are discussed, along with the particular solution to the particle equations of motion. Furthermore, suspended particles can bombard back onto the sediment bed, ejecting more particles in a process known as bombardment ejection. A probabilistic model to represent this latter effect has been discussed to better help represent the physics of brownout. Finally, computational techniques that were used to expedite the computational solution of both the FVM and the particle equations of motion are discussed.

2.2 Modeling of a Rotor Flow in Ground Effect

This section discusses the free-vortex method (FVM) [11, 88, 89], which was configured to predict the flow produced by a rotor in ground effect in arbitrary maneuvering flight conditions. The FVM is a Lagrangian-based methodology that solves for the evolution of the rotor wake geometry in time and space. This process occurs under the influence of the total velocity induced by all the elements in the flow, i.e., the vortical elements comprising the rotor wake and the sources representing the fuselage. The strength of the vortex filaments are obtained from a blade aerodynamic solution that is coupled with the individual blade flapping motion. The vortical elements comprise of the bound vortices on the rotor blade, the trailing near-wake representing the wake sheet at early wake ages, and the rolled-up far-wake filaments. It is assumed that all the vorticity

in the flow is confined to these vortex elements, and the flow outside is inviscid, incompressible and irrotational. The velocity induced the vortex elements are calculated from the application of the Biot–Savart law (discussed in Section 2.4) and those from the individual panels representing the fuselage are calculated using the classic "panel method" approach of Hess and Smith [90]. The rotor flow in the presence of the ground can be modeled in the FVM either by means of an image system or a surface singularity technique [89], although in the present work an image system is used.

2.3 Blade Aerodynamic Solution

The rotor in the present study is modeled as N_b rigid blades, which can execute time-accurate, flapping motion. Aerodynamically, each blade was modeled as a distribution of vortex singularities (bound vortices) in the flow field using a Weissinger-L lifting surface model [91]. In this formulation, the blades are divided into N_s spanwise segments, with each segment basically representing a horseshoe vortex, as shown in Fig. 2.1. The bound vortices were located at 1/4-chord, and the flow tangency condition was satisfied at the 3/4-chord, as in the classical thin airfoil theory [92]. The bound vortex strength was constant along each blade segment and could vary between the different segments. Therefore, in accordance with Helmholtz laws of conservation of vorticity [93], circulation must be trailed at the ends of each segment. The strengths of the trailer at the end of j^{th} blade segment (see Fig. 2.1) is

$$\Gamma_t\big|_j = \Gamma_b\big|_j - \Gamma_b\big|_{j+1} \tag{2.1}$$

In general, the vortex wake from a rotor blade comprises of a vortex sheet and a concentrated

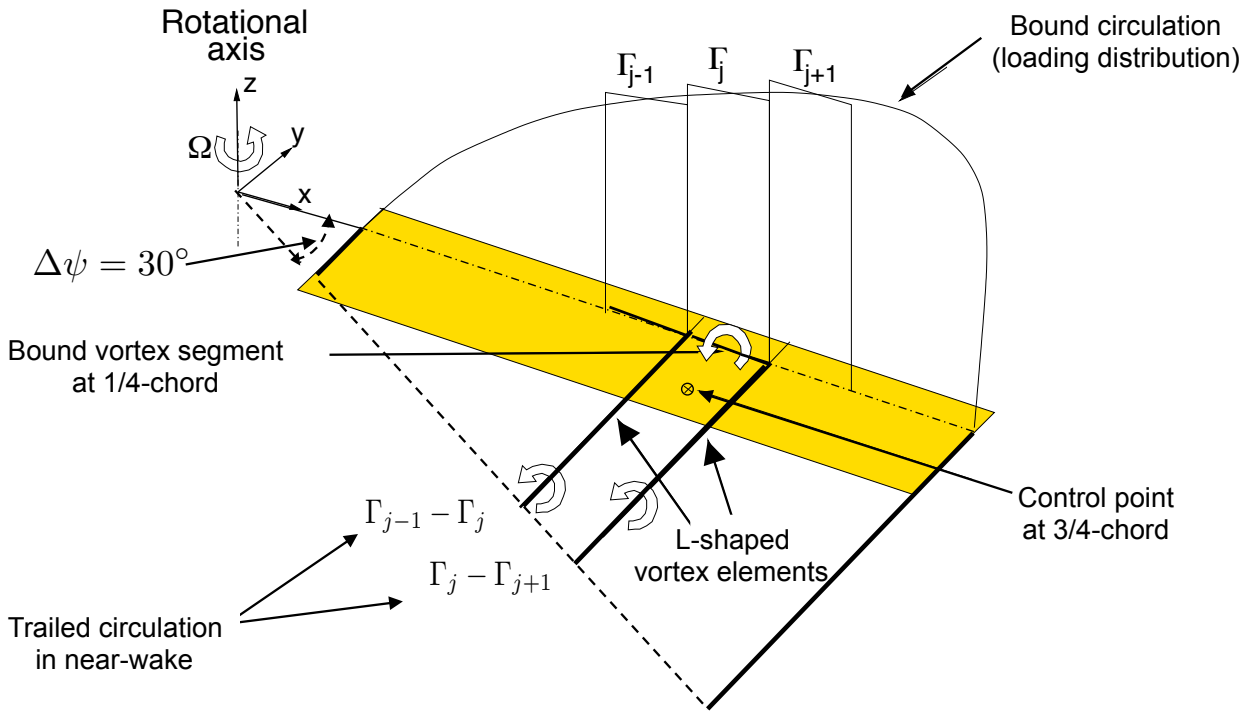

Figure 2.1: Weissinger-L lifting surface model for the rotor blade.

vortex trailed from the blade tip. The trailing line vortices from the Weissinger-L model (Eq. 2.1) comprise the near-wake of the rotor blade. In the present work, the near-wake was assumed to be rigid and tails off smoothly from the trailing edge of the blades. These near-wake trailers are truncated after a short distance, typically $\Delta\psi = 30°$, where $\Delta\psi$ is the azimuthal distance. Further downstream, it is assumed that the near-wake has completely rolled up and all the circulation on the blade is concentrated in the free trailers (typically only a tip vortex is considered), which comprises the far-wake. The strength of the tip vortex was assumed to be equal to the maximum bound circulation along the blade span [94].

2.3.1 Calculation of the Bound Circulation Strength

The strength of the bound circulation along the blade span was calculated by enforcing flow tangency at the blade control points located at 3/4-chord positions. This means that the component of the local incident velocity, which was perpendicular to the i^{th} blade segment at the blade control point, must be exactly zero, i.e.,

$$\mathbf{V}_i \cdot \mathbf{n}_i = 0 \quad i = 1, 2, \cdots, N_s \tag{2.2}$$

where $\mathbf{V}_i$ is the total velocity induced at the i^{th} control point. Notice that $\mathbf{V}_i$ comprises of the contributions from the free-stream velocity $\mathbf{V}_\infty$, the velocities induced by the near-wake $\mathbf{V}_{\text{NW}}$, the bound vortices $\mathbf{V}_B$, the far-wake $\mathbf{V}_{\text{FW}}$, the panels of the fuselage $\mathbf{V}_{\text{fus}}$, and by the effects caused by flight maneuvers $\mathbf{V}_{\text{man}}$. Therefore, Eq. 2.2 can be rewritten as

$$(\mathbf{V}_\infty + \mathbf{V}_B + \mathbf{V}_{\text{NW}} + \mathbf{V}_{\text{FW}} + \mathbf{V}_{\text{fus}} + \mathbf{V}_{\text{man}}) \cdot \mathbf{n}_i = 0 \quad i = 1, 2, \cdots, N_s \tag{2.3}$$

Because the blade and its immediate near-wake are both assumed to be rigid, $\mathbf{V}_B$ and $\mathbf{V}_{\text{NW}}$ can be expressed as

$$\mathbf{V}_{B_i} = \sum_{j=1}^{N_s} I_{B_{ij}} \Gamma_j \tag{2.4}$$

$$\mathbf{V}_{\text{NW}_i} = \sum_{j=1}^{N_s} I_{\text{NW}_{ij}} \Gamma_j \tag{2.5}$$

where I_B and I_{NW} are the influence coefficient matrices that depend upon the blade and near-wake geometry.

Substituting Eqs. 2.4 and 2.5 in Eq. 2.3, an expression for the bound circulation can be obtained, which can now be rewritten as a linear system of equations

$$[I_{ij}\mathbf{n}_i]\Gamma_j = (\mathbf{V}_\infty + \mathbf{V}_{\mathrm{FW}} + \mathbf{V}_{\mathrm{fus}} + \mathbf{V}_{\mathrm{man}}) \cdot \mathbf{n}_i \qquad i, j = 1, 2, \cdots, N_s \tag{2.6}$$

where $I = I_B + I_{\mathrm{NW}}$. The bound circulation is obtained by the inversion of the influence coefficient matrix, i.e.,

$$\Gamma_j = [I_{ij}\mathbf{n}_i]^{-1}(\mathbf{V}_\infty + \mathbf{V}_{\mathrm{FW}} + \mathbf{V}_{\mathrm{fus}} + \mathbf{V}_{\mathrm{man}}) \cdot \mathbf{n}_i \tag{2.7}$$

The blade and the near-wake are assumed to be rigid, therefore the influence coefficient matrix, I, and the normal vectors, $\mathbf{n}_i$, remain constant in the blade-fixed frame of reference. Therefore, the matrix inversion for the solution of the bound circulation needs to be performed just once, which is a benefit of the rigid near-wake assumption. The additional velocities introduced by a maneuver are a function of the angular roll p, pitch q and yaw r rates along the x, y, and z axes respectively, i.e.,

$$\boldsymbol{\omega} = p\mathbf{i} + q\mathbf{j} + r\mathbf{k} \tag{2.8}$$

and so $\mathbf{V}_{\mathrm{man}}$ is given by

$$\mathbf{V}_{\mathrm{man}} = \boldsymbol{\omega} \times \mathbf{r} \tag{2.9}$$

where $\mathbf{r}$ is the position vector of the point of interest in the body-fixed frame of reference.

2.3.2 Calculation of the Blade Loads

The strength of the bound vortices, Γ_j, as calculated using Eq. 2.7, varies along the blade span as well as the azimuthal direction around the rotor disk. In the far-wake, the strength of the blade tip vortex at any azimuthal location is the maximum value of Γ_j along the blade span, as discussed in Section 2.3. The tip vortex attachment point on the blade is determined through the blade flapping response, which is discussed later in Section 2.5.3. The positions of the Lagrangian filament markers are obtained by solving the governing vorticity transport equation, which will be discussed next in detail in Section 2.5.

Once the position and strength of all singularity elements (rotor wake vortices and fuselage source panels) are known, the velocities induced at the blade control points can be calculated by using the Biot–Savart law. These velocities along with the orientation of the rotor blade can then be used to calculate the sectional angles of attack. The effects of unsteady aerodynamics on the blade angles of attack are then calculated using the indicial response method, as proposed by Leishman and Beddoes [95]. The nonlinear lift and drag characteristics are calculated based on the Beddoes two-dimensional, nonlinear airfoil model for the NACA 0012 airfoil [96]. Alternatively, airfoil tables can also be integrated with the FVM to calculate the airfoil sectional characteristics.

Finally, the sectional airloads can then be integrated to obtain rotor thrust, C_T, and torque, C_Q, by using

$$C_T = \frac{1}{2\pi}\int_0^{2\pi}\int_e^1 \frac{\sigma}{2}\left(\frac{U}{\Omega R}\right)^2 (C_l\cos\phi - C_d\sin\phi)\,dr\,d\psi \tag{2.10}$$

$$C_Q = \frac{1}{2\pi}\int_0^{2\pi}\int_e^1 \frac{\sigma}{2}\left(\frac{U}{\Omega R}\right)^2 (C_l\sin\phi + C_d\cos\phi)\,r\,dr\,d\psi \tag{2.11}$$

where σ is the local solidity, e is the non-dimensional flapping hinge offset, C_l and C_d are the sectional lift and drag coefficients, respectively, ψ is the azimuthal location of the reference rotor blade (see Fig. 2.3), r is the non-dimensional radial distance, U is the total velocity at the blade cross-section, and ϕ is the inflow angle.

2.4 Computation of the Induced Velocity using the Biot–Savart Law

The velocity induced at any point in the flow field from vortical elements can be evaluated by the application of the Biot–Savart law (see Krishnamurthy [92], pp. 226–227, and Batchelor [97], pp. 93–94). The Biot–Savart law gives the flow velocity $d\mathbf{V}$ at a point $\mathbf{r}$ induced by an infinitesimally small vortex element $d\mathbf{l}$ of strength Γ (Fig. 2.2(a)) as

$$d\mathbf{V} = \frac{\Gamma}{4\pi}\frac{d\mathbf{l}\times\mathbf{r}}{|\mathbf{r}|^3} \tag{2.12}$$

which can then be numerically integrated along the total length of the vortical element to obtain the total induced velocity, and can be expressed as

$$\mathbf{V} = \int d\mathbf{V} = \int_l \frac{\Gamma}{4\pi}\frac{d\mathbf{l}\times\mathbf{r}}{|\mathbf{r}|^3} \tag{2.13}$$

In the present formulation of the FVM, the general curved vortex filaments are discretized into straight-line segments, which give a second-order reconstruction of the induced velocity field [15, 16, 98]. A detailed study of the application of curvature correction terms to the induced velocity of straight-line vortex filaments is also presented in Appendix A, both for an idealized two-

dimensional vortex ring and for more general three-dimensional rotor wakes. Because the regions of applicability of this curvature correction term are not universal, it was not used in the present work; see Appendix A for further details. For a straight-line vortex with constant circulation Γ along its length (see Fig. 2.2(b)), an exact form of Eq. 2.12 is

$$\mathbf{V} = \frac{\Gamma}{4\pi h}(\cos\theta_1 - \cos\theta_2)\frac{\mathbf{a}\times\mathbf{r}}{|\mathbf{a}\times\mathbf{r}|} \tag{2.14}$$

where h is the perpendicular distance between the evaluation point and the vortex element, θ_1 and θ_2 are the angles subtended between the vortex element and the position vector of the evaluation point relative to the two end points of the vortex element, respectively. However, the numerical solution of Eq. 2.14 involves trigonometric functions, which requires a higher number of processor cycles to evaluate. Therefore, an alternative algebraic form of Eq. 2.14 is given by

$$\mathbf{V} = \frac{\Gamma}{4\pi h}\left[\mathbf{a}\cdot\left(\frac{\mathbf{r}_1}{|\mathbf{r}_1|} - \frac{\mathbf{r}_2}{|\mathbf{r}_2|}\right)\frac{\mathbf{a}\times\mathbf{r}}{|\mathbf{a}\times\mathbf{r}|^2}\right] \tag{2.15}$$

which is based on the vector algebra of floating point numbers and comprises of vector manipulations that are very efficient on modern computers. This latter implementation of the Biot–Savart law is also more efficient on the graphics processing units (GPUs), as discussed in Appendix B.

Therefore, a curvilinear vortex filament is approximated using straight-line segments and the net velocity induced is obtained through numerical integration along the length of the vortex filament. This latter process is equivalent to the use of the trapezoidal method of integration. The errors associated with the approximation can be assessed using a Taylor series analysis. It has been

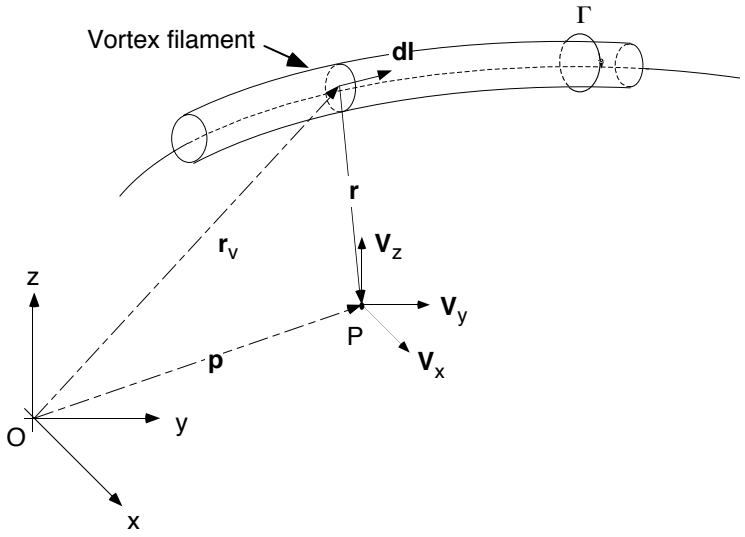

(a) Velocity induced by a curved vortex filament

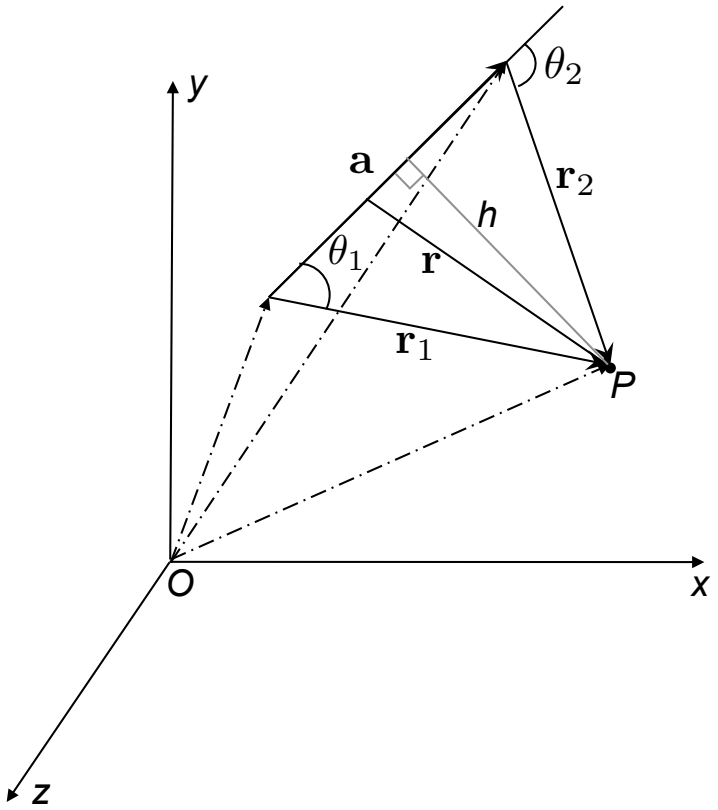

(b) Velocity induced by a straight vortex filament

Figure 2.2: Velocity induced at a point P from: (a) a curved vortex filament, and (b) a straight vortex segment.

shown in the work by Bhagwat and Leishman [99] that the leading error term becomes

$$\mathbf{V}_{\text{discrete}} = \mathbf{V}_{\text{exact}} + \frac{1}{12}\frac{d^2\mathbf{V}}{d\zeta^2}\Delta\zeta^2 + \text{higher order terms} \tag{2.16}$$

which is $O(\Delta\zeta^2)$, i.e., second-order accurate in the filament discretization.

2.5 Free-Vortex Wake Modeling

The crux of a free-vortex method (FVM) is to model the convection of vorticity in the rotor wake as physically accurately as possible. This goal is achieved by tracking the Lagrangian markers in a time-accurate manner, which are placed along a series of contiguous vortex filaments trailing from the ends of the blades. Successive markers on the vortex filament are linked together thought a piecewise linear reconstruction, as shown in Fig. 2.3.

Unlike the bound vortices, whose position is determined by the blade position, the wake vortices are free to convect under the influence of the local velocity field. Fundamentally, the movement of these Lagrangian markers is governed by the three-dimensional, incompressible Navier-Stokes equations, which can be written in the velocity-vorticity form as

$$\frac{D}{Dt}\boldsymbol{\omega} = (\boldsymbol{\omega}\cdot\nabla)\mathbf{V} + \nu\Delta\cdot\boldsymbol{\omega} \tag{2.17}$$

This equation defines the change in vorticity associated with a fluid element moving in the flow in terms of the instantaneous value of vorticity $\boldsymbol{\omega}$ and the local velocity $\mathbf{V}$. The left-hand side of Eq. 2.17 is the material derivative of vorticity, which represents both the time rate of change

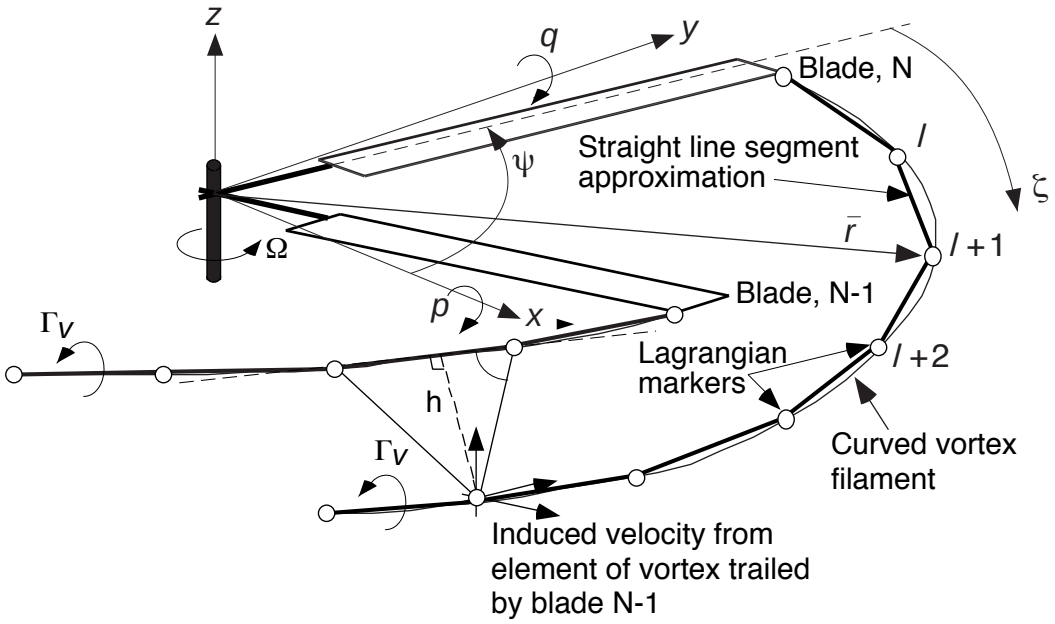

Figure 2.3: Schematic showing the coordinate system and the Lagrangian description of the vortex filaments trailing from the blade tips.

of vorticity and the convection term. The right-hand side of Eq. 2.17 has two terms. The first term represents the strain and rotation effects on the vortex filament. It represents two phenomena as the vorticity is convected along the flow: (1) the change in the length of the vortex filaments (strain effect), and (2) the change in the orientation of the vorticity vector (rotation effect). The second term represents the diffusion of vorticity as a result of the viscosity of the fluid. In most practical problems, the viscous effects will be confined to much smaller length scales compared to the potential flow phenomena, and so the remainder of the flow field can be considered essentially inviscid.

In the FVM modeling, the vorticity is confined to the vortices themselves and the flow outside is assumed to be inviscid. Under the conditions of inviscid, incompressible and irrotational flow,

Helmholtz's law [93] states that the vortex lines move as material lines at the local flow velocities whose motion is described by the motion of the Lagrangian fluid markers. Thus, the problem of tracking vortex filaments reduces to a convection (advection) equation of the form

$$\frac{d}{dt}\mathbf{r} = \mathbf{V}(\mathbf{r}), \quad \mathbf{r}(t=0) = \mathbf{r}_0 \tag{2.18}$$

where the vector $\mathbf{r}$ represents the position of the Lagrangian markers in the vortical wake and $\mathbf{r}_0$ is the initial position vector.

In case of a helicopter rotor blade rotating with a constant angular velocity Ω, the position vector $\mathbf{r}$ of a wake element can be expressed as a function of the azimuthal position ψ of the blade and the age of the filament ζ relative to the blade when it was trailed into the wake, as shown in Fig. 2.4. This representation of the governing equations based on the principles of CFD was first used by Crouse [100]. Therefore, in a non-rotating, hub fixed coordinate system, the left-hand side of Eq. 2.18 can be expressed as

$$\frac{\partial \mathbf{r}}{\partial \psi} + \frac{\partial \mathbf{r}}{\partial \zeta} = \frac{\mathbf{V}(\mathbf{r})}{\Omega} \tag{2.19}$$

where the velocity $\mathbf{V}$ has contributions from the free-stream, self and mutually induced velocities from the vortex wake structure, panels representing the fuselage, and the additional velocities imposed during the maneuver.

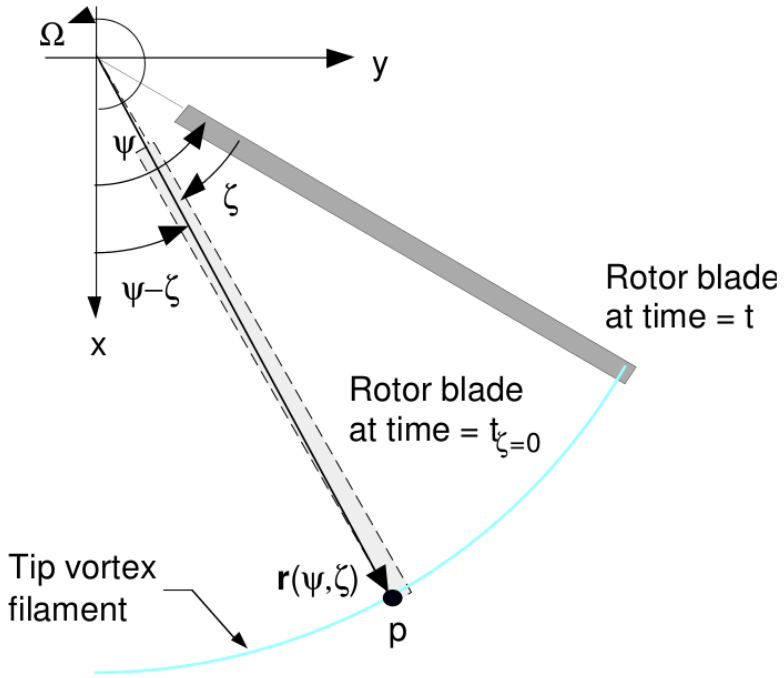

Figure 2.4: The convection of an element on a trailed tip vortex filament.

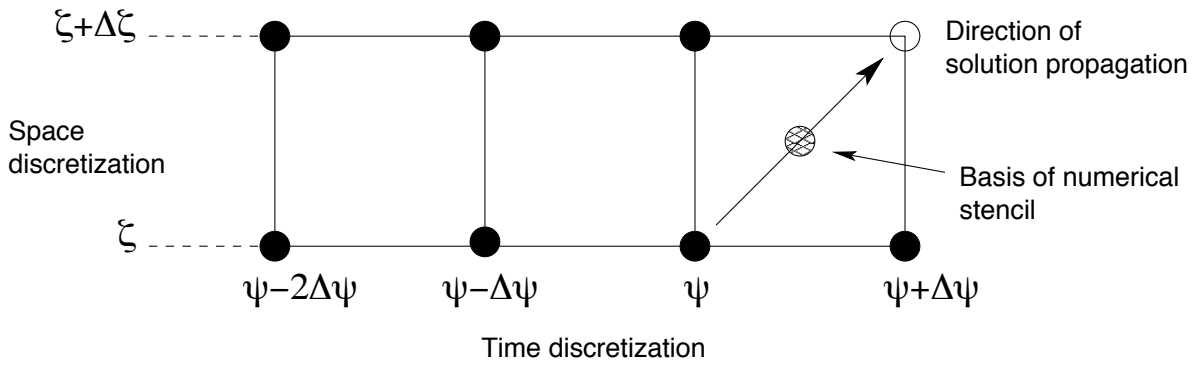

Figure 2.5: Schematic showing the numerical stencil for PC2B algorithm.

2.5.1 Numerical Solution of the Wake Equation

The terms on the left-hand side of Eq. 2.19 represent the derivatives in the temporal direction, ψ, and spatial direction, ζ. These equations can be solved using finite differences. To this end, the vortex filed is discretized in space and time with step sizes of $\Delta\zeta$ and $\Delta\psi$, respectively. The finite difference equation can be written in the form

$$D_{\psi}(\mathbf{r}) + D_{\zeta}(\mathbf{r}) = \frac{\mathbf{V}_{\infty}}{\Omega} + \frac{1}{\Omega}\sum_{j=1}^{N_v} \Delta\mathbf{V}_{\mathrm{ind}_j} \tag{2.20}$$

where $\mathbf{V}_{\infty}$ and $\mathbf{V}_{\mathrm{ind}_j}$ comprise the free-stream and induced effects, respectively, at any point in the flow.

Equation 2.20 was solved using the time-accurate, two-step backward, predictor-corrector scheme (PC2B) proposed by Bhagwat and Leishman [88]. The computational domain is divided into a grid with steps of $\Delta\psi$ and $\Delta\zeta$. The governing equations are solved at the midpoints $(\psi + \Delta\psi/2, \zeta + \Delta\zeta/2)$ of the grid cell, as shown in Fig. 2.5. This algorithm uses a five-point central

discretization in space and two-point backwards discretization in time, i.e.,

$$\begin{aligned}
\frac{\partial \mathbf{r}}{\partial \psi} &\approx D_{\psi}(\mathbf{r})\Big|_{\psi+\Delta\psi/2,\zeta} \\
&= \frac{3\mathbf{r}(\psi+\Delta\psi,\zeta)-\mathbf{r}(\psi,\zeta)-3\mathbf{r}(\psi-\Delta\psi,\zeta)+\mathbf{r}(\psi-2\Delta\psi,\zeta)}{4\Delta\psi} \qquad (2.21) \\
\frac{\partial \mathbf{r}}{\partial \zeta} &\approx D_{\zeta}(\mathbf{r})\Big|_{\psi+\Delta\psi/2,\zeta+\Delta\zeta/2} \\
&= \frac{\mathbf{r}(\psi+\Delta\psi,\zeta+\Delta\zeta)+\mathbf{r}(\psi,\zeta+\Delta\zeta)-\mathbf{r}(\psi+\Delta\psi,\zeta)-\mathbf{r}(\psi,\zeta)}{2\Delta\zeta} \qquad (2.22)
\end{aligned}$$

The left-hand-side of the governing equation (Eq. 2.20) can be obtained from Eqs. 2.21 and 2.22 as

$$\begin{aligned}
D_{\psi}(\mathbf{r})+D_{\zeta}(\mathbf{r}) = \frac{\partial \mathbf{r}}{\partial \psi}+\frac{\partial \mathbf{r}}{\partial \zeta} &+ \left(-\frac{5}{24}\frac{\partial^3 \mathbf{r}}{\partial \psi^3}+\frac{1}{8}\frac{\partial^3 \mathbf{r}}{\partial \psi^2 \partial \zeta}\right)\Delta\psi^2 \\
&+ \left(\frac{1}{24}\frac{\partial^3 \mathbf{r}}{\partial \zeta^3}+\frac{1}{8}\frac{\partial \mathbf{r}}{\partial \psi \partial \zeta^2}\right)\Delta\zeta^2 \\
&+ \frac{1}{4}\frac{\partial^4 \mathbf{r}}{\partial \psi^4}\Delta\psi^3+\cdots \qquad (2.23)
\end{aligned}$$

The leading error terms in Eq. 2.23 are second-order accurate in both space and time, which confirms the overall second-order accuracy of the finite difference approximations to the derivatives.

The self-induced and mutually induced velocities on the right-hand-side of Eq. 2.20 from the N_v vortex filaments are approximated by using the Biot–Savart law; see Section 2.4. Furthermore, the approximation at the mid-point of each grid cell is further approximated by averaging the velocities at the four surrounding grid points. The leading error terms from the velocity averaging

can be written as [101]

$$\mathbf{V}_{\text{discrete}} = \mathbf{V}_{\text{exact}} + \frac{5}{24}\frac{\partial^2 \mathbf{V}}{\partial \zeta^2}\Delta\zeta^2 + \frac{1}{8}\frac{\partial^2 \mathbf{V}}{\partial \psi^2}\Delta\psi^2 + O(\Delta\zeta^4) \tag{2.24}$$

which are also second-order accurate so providing the overall second-order accuracy for the induced velocity computations at the mid-point of each grid cell. The modified equation can then be obtained by combining Eqs. 2.23 and 2.24, i.e.,

$$\begin{aligned} \frac{\partial \mathbf{r}}{\partial \psi} + \frac{\partial \mathbf{r}}{\partial \zeta} = \frac{\mathbf{V(r)}}{\Omega} \quad &+ \quad \frac{\Delta\zeta^2}{\Omega}\left[\frac{5}{24}\frac{\partial^2 \mathbf{V}}{\partial \zeta^2} + \frac{1}{8}\frac{\partial^2 \mathbf{V}}{\partial \psi^2} - \left(-\frac{5}{24}\frac{\partial^3 \mathbf{r}}{\partial \psi^3} + \frac{1}{8}\frac{\partial^3 \mathbf{r}}{\partial \psi^2 \partial \zeta}\right)\right] \\ &- \quad \frac{\Delta\zeta^2}{\Omega}\left[\left(\frac{1}{24}\frac{\partial^3 \mathbf{r}}{\partial \zeta^3} + \frac{1}{8}\frac{\partial^3 \mathbf{r}}{\partial \psi \partial \zeta^2}\right) + \underline{\frac{1}{4}\frac{\partial^4 \mathbf{r}}{\partial \psi^4}\Delta\zeta}\right] \\ &+ \quad O(\Delta\zeta^4) \end{aligned} \tag{2.25}$$

The above equation assumes equal spacing of $\Delta\psi$ and $\Delta\zeta$. Notice that the leading truncation error terms are not dependent on the gradient of the local velocity field, therefore, the numerical scheme is essentially problem independent. The underlined term in Eq. 2.25 is a fourth-order dissipative term, and this implicit artificial dissipation makes the numerical scheme stable. Furthermore, this term is $O(\Delta\zeta^3)$ and so the overall solution is still second-order accurate.

2.5.2 Diffusion and Filament Straining

The diffusion and filament straining effects are neglected in the development of Eq. 2.20 because they are active over much smaller scales (within the scale of the vortex cores) as compared to the scales associated with the overall development of the wake. However, for several flight con-

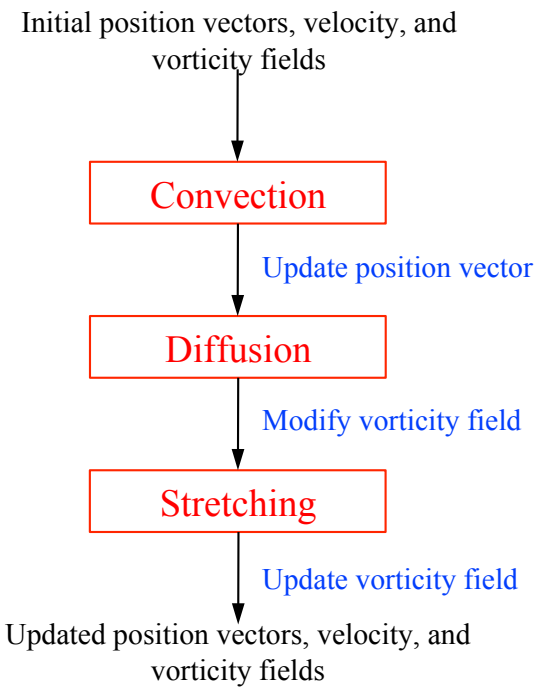

Figure 2.6: Principle of splitting the free-vortex wake solution into separate, sequential treatment of convection, viscous and stretching terms over one time step.

ditions, e.g., rotor flow in ground effect and during maneuvering flight, the vortex wake undergoes significant deformations, including stretching. Such effects play an important role in determining the flow induced near the rotor as well as at the ground [22].

In the FVM, these latter effects are modeled using a sub-step approach as shown in Fig. 2.6, where the convection, diffusion and stretching effects are considered sequentially. The vortex filaments are first convected to their new positions under the action of the local flow velocity. Then, the viscous effects associated with the diffusion of vorticity in the filament core are calculated based on the age of the filament relative to the time they were originated in the flow. The third sub-step implements filament strain or stretching effects, which uses the position vectors from the first sub-step. Combined with the new position vectors defined by the first sub-step, the second

and third sub-steps allow the new velocity and vorticity fields to be calculated at the next time step. In the present application, the entire process has been implemented as a predictor-corrector sequence (discussed in Section 2.5.1), so that the three sub-step updates are performed twice at each time-step, thereby improving the net accuracy and numerical stability of the solution process.

The effects of viscous diffusion of the vortex filaments are included in the FVM by incorporating a viscous core into the vortex model. In the present work, the Vatistas [102] vortex model was used, where the tangential (swirl) component of the velocity in the two-dimensional cross-section plane of the vortex can be written as

$$V_\theta(r) = \frac{\Gamma_V}{2\pi}\left(\frac{r}{(r^{2n}+r_c^{2n})^{1/n}}\right) \tag{2.26}$$

where r_c is the vortex core radius and Γ_v is the strength of the vortex. The value of $n = 1$ gives the "Scully" vortex profile. However, it has been found that $n = 2$, i.e., the algebraic form of the Lamb–Oseen vortex, generally provides better correlation with velocity profile measurements for rotor-generated tip vortices [103].

A model for the growth of the vortex core radius, r_c, with time, t, can be obtained starting from the Lamb–Oseen laminar result, as given by

$$r_c(t) = \sqrt{4\alpha\nu t} \tag{2.27}$$

where $\alpha = 1.25643$ and ν is the kinematic viscosity of the fluid. Because $\psi \equiv \zeta = \Omega t$, Eq. 2.27 can be expressed in terms of wake age. Because of the laminar flow assumptions, the vortex core size

predicted by Eq. 2.27 gives a much slower diffusion of the tip vortex than has been measured in experiments. The tip vortex exhibits laminar behavior initially, but then becomes turbulent because of the roll up of the vortex sheet and the presence of small-scale eddies in the flow [4].

Squire [104] proposed the inclusion of an average apparent or turbulent "eddy" viscosity parameter δ to account for the natural effects of turbulence on the net rate of viscous diffusion, which effectively increases the viscous core growth. However, at $t = t_0$, the vortex core model given by Eq. 2.27 predicts a zero core radius, which results in a singular vortex and predicts much higher velocities compared to experimental measurements. Bhagwat and Leishman [88, 105] developed a semi-empirical model, which is a modification to Squire's approach, i.e.,

$$r_c(\zeta) = \sqrt{4\alpha\delta\nu\left(\frac{\zeta+\zeta_0}{\Omega}\right)} \equiv \sqrt{r_{c_0}^2 + \frac{4\alpha\delta\nu\zeta}{\Omega}} \tag{2.28}$$

where ζ is the wake age and r_{c_0} is the initial core radius. The coefficients in this model, r_{c_0} and δ, were defined empirically using vortex tip-growth measurements [106]. Following Squire, the effective eddy viscosity coefficient, δ, is a function of the vortex Reynolds number Γ_v/ν, and is given by

$$\delta = 1 + a_1\left(\frac{\Gamma_v}{\nu}\right) = 1 + a_1 \mathrm{Re}_v \tag{2.29}$$

Based on experimental correlation of full-scale and model-scale rotors, the average value of a_1 was estimated to be 2×10^{-4} [4].

The filament strain or "stretching" effects were modeled using the methodology developed by Ananthan and Leishman [107]. Under the assumptions of a predominantly incompressible flow

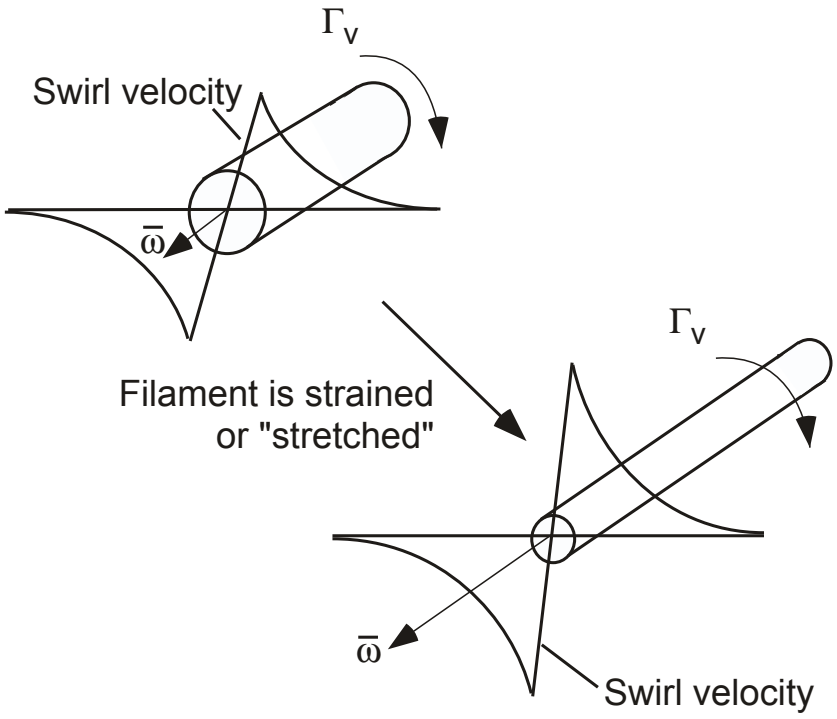

Figure 2.7: Schematic showing stretching of individual vortex filaments and vorticity intensification that results in an increase in swirl velocity surrounding the filament core.

and that any local changes in density are small, Helmholtz's third law [92] requires that the net circulation strength of any vortex filament remains constant, i.e.,

$$\Gamma = \int_S \boldsymbol{\omega} \cdot d\mathbf{S} \tag{2.30}$$

Therefore, any change in the length of a vortex filament will result in a change in the vorticity confined within the vortex core. This effect occurs because in an incompressible flowfield an increase in the length of the cylindrical filament must be accompanied with a corresponding decrease in the cross-sectional area of the filament.

Assuming that the net vorticity is confined with a cylinder of radius r_c and length l, an

increase in the length of the cylinder will result in a decrease in the core radius. Because the flow is considered to be incompressible, the principle of conservation of mass can be used to compute the effective change in core radius as a result of filament straining, $\varepsilon = \Delta l/l$, i.e.,

$$\pi r_c^2 l = \pi(r_c - \Delta r_c)^2(l + \Delta l) \tag{2.31}$$

$$\left(\frac{r_c - \Delta r_c}{r_c}\right)^2 = \frac{l}{l + \Delta l} \tag{2.32}$$

$$\Delta r_c = r_c\left(1 - \frac{1}{\sqrt{1+\varepsilon}}\right) \tag{2.33}$$

Combining Eqs. 2.29 and 2.33, the expression for the core radius at a given wake age, ζ, can be written as

$$r_c(\zeta, \varepsilon) = \sqrt{r_{c_0}^2 + \frac{4\alpha\delta(\mathrm{Re}_v)\nu}{\Omega}\int_0^{\zeta}(1+\varepsilon)^{-1}d\zeta} \tag{2.34}$$

The core radius calculated at any time includes the integral effects of the strain field from the point of the origin of the vortex as it was convected through the flow field.

2.5.3 Rigid Blade Flapping Dynamics

Blade flapping dynamics plays an important role in determining the airloads on the helicopter rotor blade, especially in maneuvering flight. Because the flapping response depends on the local induced velocity, the blade flapping response is dictated by the wake solution. Furthermore, the wake attachment point to the blade depends on the flapping response, which necessitates the tight coupling of the blade flapping response to the wake solution.

The governing equation for the blade flapping response is formulated by considering the

aerodynamic and inertial moments about the blade flapping hinge. In maneuvering flight, the contributions of helicopter dynamics to the aerodynamic and inertial moments must also be considered. Furthermore, the blade flapping equations must be solved independently for each rotor blade because the aerodynamic environment can be different for each rotor blade at different times, i.e., it is not periodic.

For a hinged blade, the sum of the applied moments must be equal to zero, i.e.,

$$M_A + M_I = 0 \tag{2.35}$$

where M_A and M_I are the aerodynamic and inertial flap moments about the blade flap hinge, respectively. A general form of the flapping equation for a blade with a flap hinge offset of eR, where R is the rotor radius, can be written as

$$\overset{**}{\beta} + \nu_\beta^2 \beta = \frac{M_A}{I_b \Omega^2} \frac{1}{(1-e)^3} + M_I' \tag{2.36}$$

where I_b is the moment of inertia of the blade, ν_β is the non-dimensional flapping frequency, and M_I' are the additional inertial terms introduced the rolling and pitching motion of the hub about the helicopter center of mass. For given pitch and roll rates, p and q, respectively, the flapping

equation can be expressed as

$$\begin{aligned}\overset{**}{\beta}+\nu_\beta^2\beta &= \frac{M_A}{I_b\Omega^2}\frac{1}{(1-e)^3} \\ &- 2\left(1+\frac{3}{2}\frac{e}{1-e}\right)\frac{q}{\Omega}\sin\psi+2\left(1+\frac{3}{4}\frac{e}{1-e}\right)\frac{p}{\Omega}\cos\psi \\ &+ \left(1+\frac{3}{2}\frac{e}{1-e}\right)\frac{\overset{*}{q}}{\Omega}\cos\psi+\frac{3}{2}\left(1+\frac{3}{2}\frac{e}{1-e}\right)\frac{\overset{*}{p}}{\Omega}\sin\psi \end{aligned} \tag{2.37}$$

The coordinate system used for blade flapping is presented in Section 2.6.1 and a detailed derivation of the above equation is given by Ananthan [108]. The above formulation can be extended to include a root spring and other degrees of freedom, such as the yaw rate of the helicopter. Equation 2.36 can be rewritten as a set of two first-order ordinary differential equations (ODEs) in $\overset{**}{\beta}$ and β as

$$\frac{\partial}{\partial\psi}\begin{Bmatrix}\overset{*}{\beta}\\ \beta\end{Bmatrix}+\begin{bmatrix}0 & \nu_\beta^2\\ -1 & 0\end{bmatrix}\begin{Bmatrix}\overset{*}{\beta}\\ \beta\end{Bmatrix}=\begin{Bmatrix}\frac{M_A}{I_b\Omega^2}\frac{1}{(1-e)^3}+M_I'\\ 0\end{Bmatrix} \tag{2.38}$$

Equation 2.38 is similar in form to Eq. 2.19, and, therefore, it can be solved by using the PC2B scheme (see Section 2.5.1) to give a consistent second-order accurate solution.

2.5.4 Modeling of a Secondary Rotor

The formulation of the FVM (see Eqn. 2.19) is based on the use of rotor time (ψ) rather than physical time (t). As a consequence, rotors operating at different rotational frequencies (such as the main and tail rotor) can advance in the numerical solution by different physical times (as time-step for each rotor is, $\Delta t = \Delta\Psi/\Omega$). To ensure that the solutions from the two rotors are

synchronized in physical time, the rotor with the smaller solution time step will need to be marched through an additional number of steps (referred to as sub-time steps, denoted by n). The induced velocity field produced by the main rotor on the collocation points of the secondary rotor wake at these sub-time steps have not been previously computed, so an interpolation of the main rotor vortex positions or the vortex induced velocity needs to be performed. If the main rotor vortex positions are interpolated, these interpolated positions can then be used to compute the induced velocity field at the wake collocation points from the second rotor. However, if the interpolation were to be performed on the induced velocity field itself, then the main rotor induced velocity field will have to be interpolated onto a known grid and then interpolated again from that grid to the collocation points of the secondary rotor wake, which are not known a priori. The latter type of strategy will result in two level of interpolations, increasing significantly the computational time and also the errors in the computed induced velocity compared to a strategy where the wake positions themselves are interpolated.

In the present formulation, the flow solutions for the two rotors are coupled by exchanging information across their respective computational grids, as shown in Fig. 2.8. The main rotor solution (i.e., the vortex filament positions and corresponding strengths) across one simulation time step (denoted by solid circles) is linearly interpolated at each of the n secondary rotor solution time steps (denoted by open circles), which is then used to compute the induced velocity field produced by the main rotor at the collocation points defining the positions of the secondary rotor wake (hashed solid circles). The linear interpolation process can be formalized as

$$\mathbf{r}(\psi_{t+\alpha_i\Delta t}, \zeta_{t+\alpha_i\Delta t}) = \mathbf{r}(\psi_t, \zeta_t) + \alpha_i \mathbf{r}(\psi_{t+\Delta t}, \zeta_{t+\Delta t}) \tag{2.39}$$

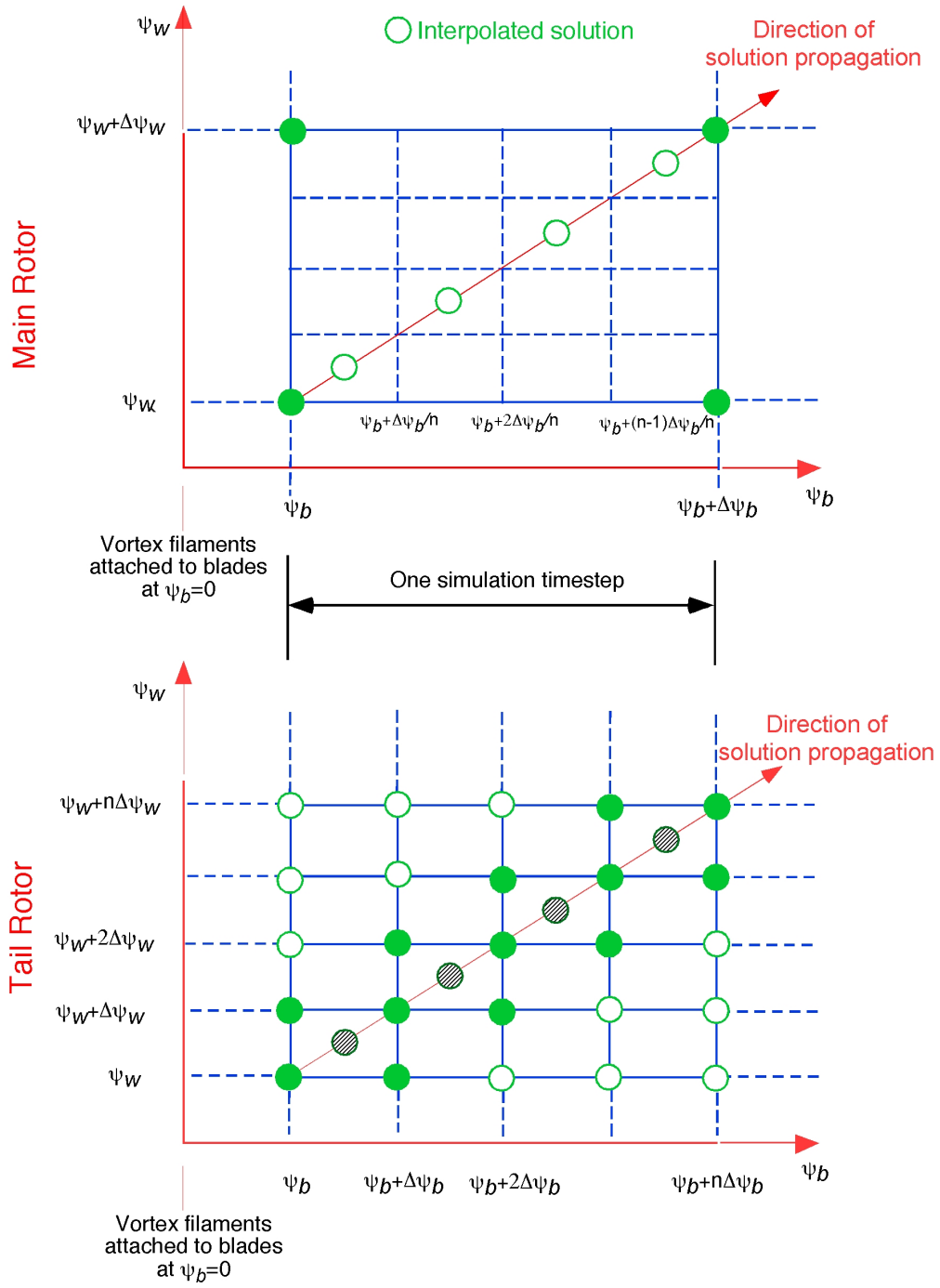

Figure 2.8: Computational stencil showing the implementation of the numerical coupling methodology, in this case between the more slowly turning main and the faster turning tail rotor.

where α_i denotes the fraction of the time step, i.e.,

$$\alpha_i = (i-1)/n, \quad i = 1,2,..,n \tag{2.40}$$

Therefore, the methodology for the modeling of the tail rotor is based on the PC2B scheme, which gives a second-order accurate solution. Furthermore, the coupling strategy developed ensures that the solutions from the two rotors are marched through equal in physical time although they operate at different rotational frequencies.

2.5.5 Ground Effect Modeling Using the Method of Images

The aerodynamic effect of the presence of the ground can be modeled in the FVM using either an image system or a surface singularity method; see [89]. In the present work, the image system approach has been used, not only for its significantly better computational efficiency but also that this type of formulation guarantees flow tangency at all points on the ground plane rather than at a discrete control points.

In this method, an image of the "real" rotor system and its wake (above the ground) are used to simulate the ground plane, as shown in Fig. 2.9. An image is also created of the panels that comprise the fuselage. The strength of the vortex filaments and the panel singularities from the image and the "real" rotor system are equal and opposite to each other. The Lagrangian markers of the "real" rotor system are convected under the influence of all the elements present in the flow field, including those from the image rotor system. Consequently, the total normal component of velocity at the ground is identically zero, which implicitly satisfies the flow tangency condition at all

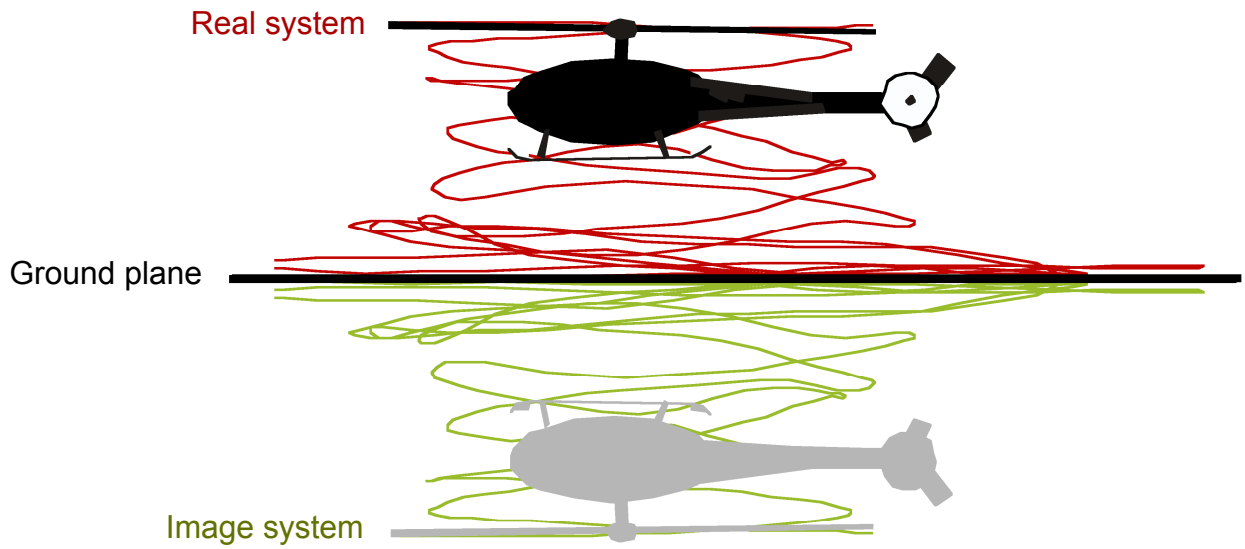

Figure 2.9: A representative free-vortex wake solution obtained using the method of images for a rotor operating in ground effect.

points over the ground plane. With the singularity method, many panels must be used to explicitly satisfy flow tangency conditions over the ground plane, which can incur very high computational overheads. Nevertheless, the panel method approach lends itself more readily to the modeling of non-planar surfaces.

The total cost of the induced velocity computations is $O(N_v(N_v+N_p))+O(N_pN_v)$, where N_v and N_p are the number of Lagrangian wake markers and panels, respectively, from the "real" system. Because the total number of Lagrangian markers and panels for modeling the ground effect problem become twice than that of those in out of ground effect, the cost of the induced velocity computations increase by a factor of four. To save the computational cost of updating the positions of the image system, these positions are obtained as the mirror images of the real rotor system about the ground plane at each time step. This approach also saves on the computer memory requirements because no extra memory is required to store the positions and strengths of

the vortex filaments and panels of the image rotor system.

2.5.6 Accuracy of the Induced Velocity Computations

The velocities induced by the rotor wake at a suspended dust particle can be computed by using the Biot–Savart law, as previously discussed in Section 2.4. The accuracy of this velocity computation depends upon the accuracy of the solution of the rotor wake obtained from the FVM. This rotor wake solution is obtained by discretizing the wake vortex filaments into straight-line segments, which are convected in space and time by solving the vorticity transport equations under the assumptions of incompressible and inviscid flow fields; see Section 2.5.

The governing EOMs in this case were solved by using the PC2B scheme [99, 101] which is second-order accurate in both space ζ and time ψ; see Eq. 2.22. Notice that the representation of the temporal coordinate ψ in the FVM is equivalent to time t used in the tracking of the particles such that $\Delta t = \Delta\psi/\Omega$, where Ω is the rotational frequency of the rotor. The velocity at the midpoint of the computational domain was solved by averaging the velocity at four neighboring points, which is also second-order accurate; see Eq. 2.23. Therefore, the rotor wake solution from the FVM is second-order accurate.

2.6 Modeling of the Airframe

This section discusses the modeling of an airframe and its aerodynamic coupling with the FVM. The flow over a helicopter fuselage is rather complicated because it often behaves in a manner similar to a bluff body, and may have regions of separated flow and vorticity production,

especially in regions of high surface curvature. Furthermore, the flow over the fuselage can be unsteady because of the periodic passage of the blade and other effects such as localized interactions of the vortices in the rotor wake.

Although surface singularity techniques or panel methods are not easily adaptable to model flow features typical of bluff body shapes such as flow separation over helicopter fuselages, they are computationally efficient and can give reasonable assessments of the perturbations produced by the fuselage on the wake developments, especially in forward flight and/or in descending flight where there are shallower cross-flow angles and fewer rotor wake/body surface impingements.

Panel methods may employ a variety of flow elements, each of which are fundamental solutions to the governing Laplace's equation (Eq 2.41), to represent the aerodynamics around a surface; see Chapter 7 of Katz and Plotkin [109] for a detailed and comprehensive analysis. The panels may be composed of flow elements such as sources, doublets, vortices, vortex blobs, and can be broadly classified into lifting and non-lifting elements. Lifting elements (e.g., doublets and vortices) are capable of generating circulation essential in the production of lift, while non-lifting elements (e.g., sources) are incapable of producing lift. Within the context of panel methods, for lift to be produced over a surface, points of flow separation have to be specified. These separation points are relatively simpler to specify for an airfoil/wing (the trailing edge) as compared to bluff body shapes of helicopter fuselages, which may vary depending on the surrounding flow conditions. Therefore, in the present work, only panel of sources have been considered in the modeling of the fuselage.

Surface singularity methods are based on the assumptions of incompressible, irrotational

flow, with the governing equation being the Laplace's equation for velocity potential, Φ, i.e,

$$\nabla^2\Phi = 0 \tag{2.41}$$

and the flow velocity at any point, $\mathbf{V}$, can be expressed as a gradient of the velocity potential, i.e.,

$$\mathbf{V} = \nabla\Phi \tag{2.42}$$

Panels of unknown singularity strengths are used to mathematically represent the aerodynamic influence of the fuselage, the strengths being solved for by imposing flow tangency at the panel control points. A schematic of a panel representation of a fuselage coupled with the FVM is shown in Fig. 2.10. Planar quadrilateral and/or triangular panels are used, and being essentially non-lifting bodies, only panels with constant source strengths are needed. The formulation of the panel method is also consistent with the formulation and other assumptions of the FVM.

The source strengths are computed by enforcing the flow tangency condition at the panel control points, i.e.,

$$\mathbf{V}_{P_i} \cdot \mathbf{n}_i = 0 \quad \text{for } i = 1, 2, \cdots, N_p \tag{2.43}$$

where N_p is the total number of panels, $\mathbf{V}_{P_i}$ is the total velocity induced at a panel control point from other panels and the vortex elements in the rotor wake, and $\mathbf{n}_i$ is the unit outward normal vector of the i^{th} panel, respectively. The total velocity at the panel control point is given by,

$$\mathbf{V}_{P_i} = \mathbf{V}_\infty + \sum_{j=1}^{N_{\text{pan}}} \mathbf{V}_{ij}\sigma_{s_j} \tag{2.44}$$

where $\mathbf{V}_{ij}$ represents the velocity induced at the i^{th} panel by the j^{th} panel of unit strength, and $\mathbf{V}_\infty$ contains the influence of the freestream and the rotor wake. Equation 2.43 in conjunction with Eq. 2.44 can be reduced to a set of linear simultaneous equations to solve for the singularity strengths, σ_{si}, i.e.,

$$\mathbf{A}_{ij}\sigma_{sj} = -\mathbf{V}_\infty \cdot n_i \quad \text{for } i = 1,2,...,N_p \tag{2.45}$$

The matrix inversion of A is performed using a LU decomposition technique. For a $N \times N$ square matrix A, the cost of solving for σ_s scales as $O(N^2)$ as opposed to $O(N^3)$ when using other inversion techniques such as Gauss elimination. Therefore, A can be factorized into a lower triangular matrix L and an upper triangular matrix U, i.e.,

$$A = L\,U \tag{2.46}$$

In the lower triangular matrix, L, all elements in the matrix above the diagonal are zero, and in the upper triangular matrix, U, all elements below the diagonal are zero. Therefore, to solve the system of linear equations in Eq. 2.45 for σ_s, Eq. 2.46 can be used in conjunction with Eq. 2.45 to obtain

$$L\,U\sigma_s = b \tag{2.47}$$

where $b = -\mathbf{V}_\infty \cdot n$. The solution for σ_s in Eq. 2.47 can then be obtained in two steps

$$L\, y = b \tag{2.48}$$

$$U\, \sigma_s = y \tag{2.49}$$

Equations 2.48 and 2.49 can be solved directly through forward and backward substitutions, respectively. Direct matrix inversions are computationally expensive and are $O(n^3)$ where n is the size of the square matrix. Once the lower and upper diagonal matrices are computed, which needs to be performed only once, the LU decomposition technique to evaluate σ_s is $O(n)$, which saves on computational time.

The unsteady nature of the rotor-wake interactions is also included in the formulation, with the panel surface pressure being obtained using the unsteady Bernoulli's equation, i.e.,

$$p_\infty + \frac{1}{2}\rho \mathbf{V}_\infty^2 = p + \frac{1}{2}\rho \mathbf{V}_P^2 + \rho \frac{\partial \Phi}{\partial t} \tag{2.50}$$

where Φ is the velocity potential, p_∞ and $\mathbf{V}_\infty$ represent the freestream pressure and velocity respectively, p, $\mathbf{V}_P$, and ρ represented the local pressure, velocity, and air density respectively.

The unsteady term in the equations, $\partial\Phi/\partial t$, is the time rate-of-change of the velocity potential. This term accounts for the energy changes in the unsteady flow-field. The importance of this term has been recognized [110, 111], where it is the source of noncirculatory or apparent mass forces. The unsteady term can be calculated by considering the effect of each singularity individually and summing the results.

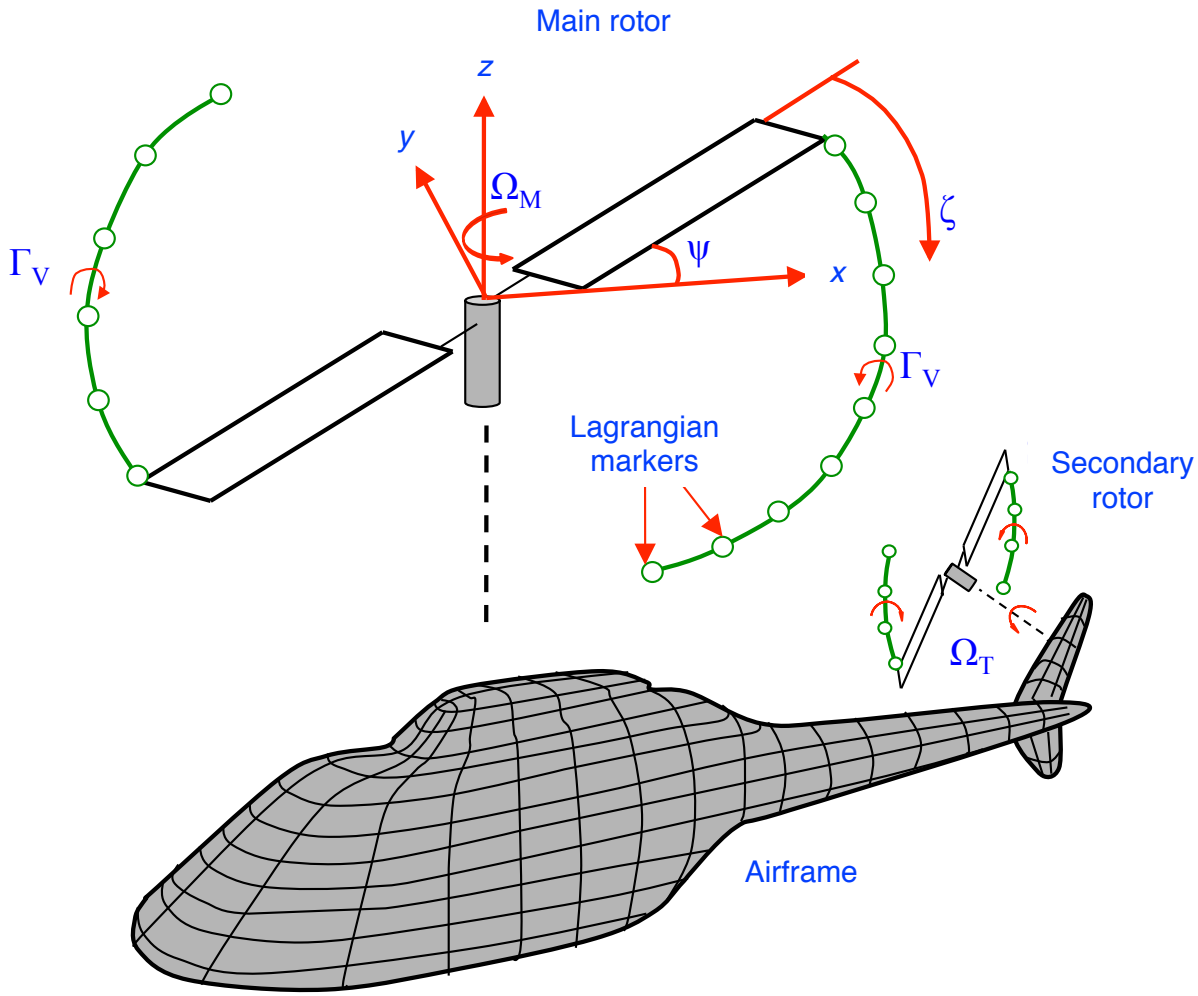

Figure 2.10: Panel representation of a fuselage coupled with the FVM.

To calculate the unsteady effect of one singularity, consider a reference system moving with the singularity. A point moving with the singularity, i.e., stationary in the moving reference system, will experience no changes in potential as a result of the movement of the singularity. Any changes in the velocity potential at that point is because of the changes in the strength of the singularity, which can be expressed as

$$\frac{D\Phi}{Dt} = \frac{\partial\Phi}{\partial\sigma}\frac{\partial\sigma}{\partial t} \tag{2.51}$$

where $D\Phi/Dt$ represents the derivative of the potential with respect to the moving reference system, and σ represents the strength of the singularity. The definition of $D\Phi/Dt$ with regard to the fixed reference frame is very similar to the definition of the substantial derivative [112] and can be expressed as

$$\frac{D\Phi}{Dt} = \frac{\partial\Phi}{\partial t} + \mathbf{V}_s \cdot \nabla\Phi \tag{2.52}$$

where $\mathbf{V}_s$ is the velocity of the singularity (and thus the coordinate system). By combining Eqs. 2.51 and 2.52, an equation for $\partial\Phi/\partial t$ can be derived, i.e.,

$$\frac{\partial\Phi}{\partial t} = -\mathbf{V}_s \cdot \nabla\Phi + \frac{\partial\Phi}{\partial\sigma}\frac{\partial\sigma}{\partial t} \tag{2.53}$$

which can be further simplified by noting that the velocity induced by the singularity is $\mathbf{V}_{\text{ind}} = \nabla\Phi$ and thus the final equation for $\partial\Phi/\partial t$ is

$$\frac{\partial\Phi}{\partial t} = -\mathbf{V}_s \cdot \mathbf{V}_{\text{ind}} + \frac{\partial\Phi}{\partial\sigma}\frac{\partial\sigma}{\partial t} \tag{2.54}$$

The unsteady pressure term for the i^{th} panel can be represented as

$$\frac{\partial \Phi_i}{\partial t} = \left.\frac{\partial \Phi_i}{\partial t}\right|_{\text{rotor+wake}} + \left.\frac{\partial \Phi_i}{\partial t}\right|_{\text{panels}} \tag{2.55}$$

with the unsteady term from the rotor and wake given by

$$\left.\frac{\partial \Phi_i}{\partial t}\right|_{\text{rotor+wake}} = -\mathbf{V}_{\text{ind}} \cdot \mathbf{V}_s \tag{2.56}$$

where $\mathbf{V}_{\text{ind}}$ is the induced velocity from the vortical elements on the wake and rotor (bound and free vortices) onto the panel control point, and $\mathbf{V}_s$ is the velocity of these vortices, respectively. The unsteady potential from the panels can be expressed as,

$$\left.\frac{\partial \Phi_i}{\partial t}\right|_{\text{panels}} = \sum_{j=1}^{N_{\text{pan}}} \frac{\partial \Phi_i}{\partial \sigma_j}\frac{\partial \sigma_j}{\partial t} = \sum_{j=1}^{N_{\text{pan}}} \Phi_{\text{ij}}\frac{\partial \sigma_j}{\partial t} \tag{2.57}$$

where Φ_{ij} is the potential at panel i induced by panel j of unit source strength. The influence coefficients for the potential and the velocity components can be calculated at the same time influence coefficients for the velocity components are calculated without any significant increase in computational cost. Algorithmic details of this classic implementation are given in Appendix C.

In the panel method, flow tangency is ensured only at the panel control points and, therefore, the vortex filaments may penetrate the fuselage during the time marching procedure, a numerical artifact that has often been seen in panel methods when applied to rotorcraft problems [100, 113, 114]. In the present study, prescribed displacement rules are used after each convection step to ensure that vortex filaments always remain outside of the body. If markers are projected to enter

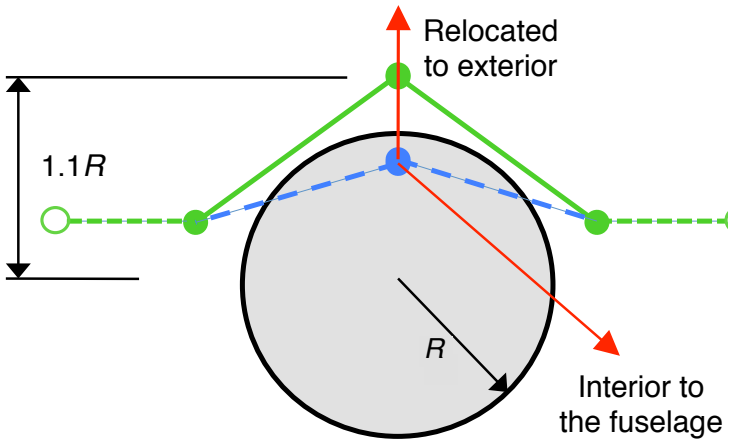

Figure 2.11: Illustration of the prescribed wake displacement rules.

the interior of the fuselage, the position is relocated to a specified distance of 10% of the fuselage cross-sectional radius above the surface, along the radially outward direction, as shown in Fig. 2.11.

2.6.1 Coordinate Systems

The following right-handed coordinate systems are used in the present work: (a) body axes, (b) non-rotating hub axes (for the main and tail rotor), and (c) rotating blade fixed axes. Figure 2.12 shows a schematic of the coordinate system for the different components of the helicopter.

Consider a helicopter executing arbitrary pitch and roll motions about the body-fixed axes with the rates p and q, respectively. The rotor is rotating about the z axis with a rotational speed Ω. The blade flapping equations of motion (Eq. 2.37) are derived in the body fixed coordinate system $(x,y,z)_B$. The helicopter rolls and pitches about this axis. The $(x,y,z)_{\text{MR}}$ frame of reference is the hub-fixed, non-rotating frame of reference of the main rotor. The main rotor is at a distance $\mathbf{R}_H$ from the helicopter center of gravity. The frame (x,y,z) is the rotating coordinate system, with z axis along the axis of rotation of the rotor blades. The frame $(x,y,z)'$ is the blade-fixed coordinate

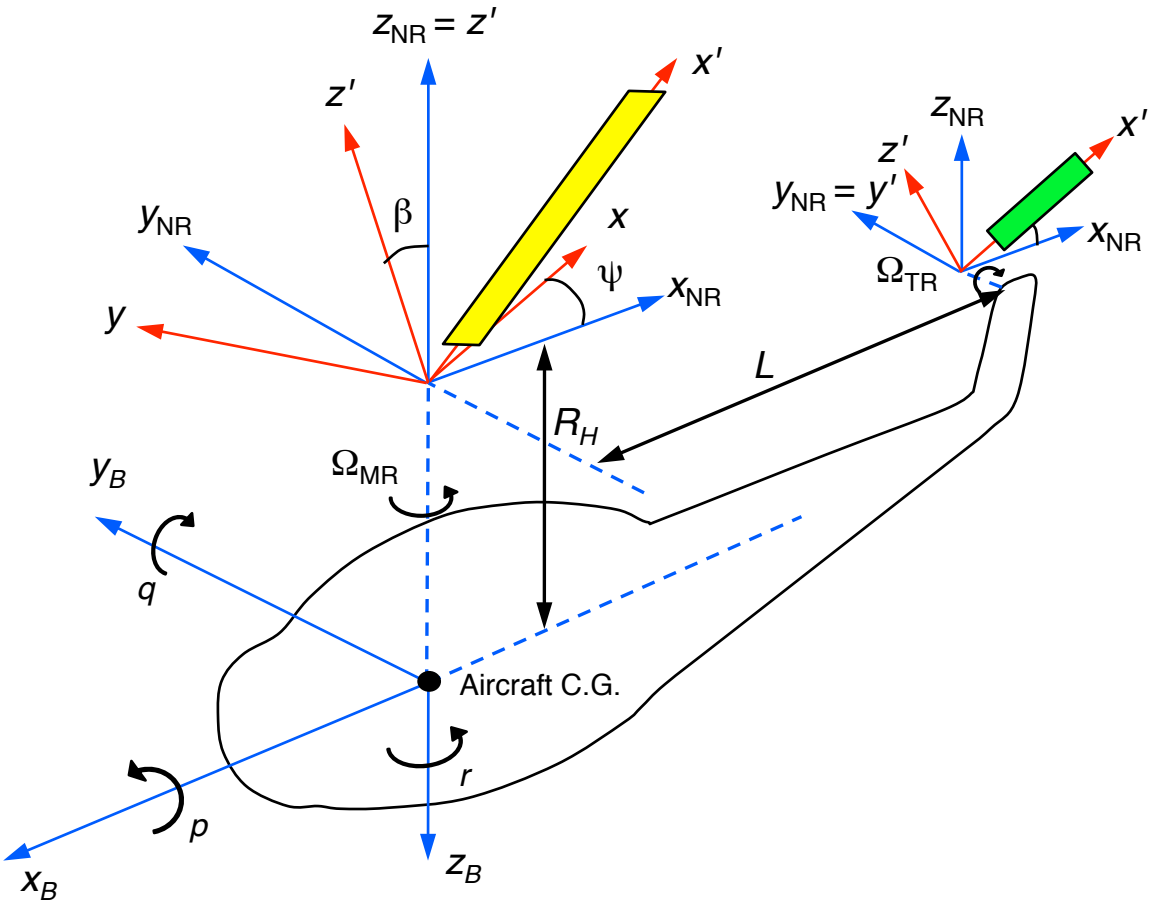

Figure 2.12: Helicopter and blade coordinate systems.

system whose xy plane is at an angle, β, to the rotating frame of reference.

The governing equations of the Lagrangian-based FVM (Eq. 2.20) are expressed in the non-rotating rotor hub frame with the origin of the coordinate frame located at the rotor hub. The z axis points along the axis of rotation of the rotor. The x axis points towards the tail of the helicopter and the y axis points towards starboard. Notice that the orientation of x_B and x axes are opposite to each other. The sectional characteristics of the airfoil are based on the rotating, blade-fixed coordinate system, which has the x_b axis along the span of the rotor blade. The y axis is along the chord pointing towards the leading edge of the blade, and the z axis is normal to the blade. The integrated sectional loads (as described in Section 2.3.2) are generally three-dimensional vectors in space, with components along each of the three body axes. More specifically, the rotor thrust is defined as the force along the rotor shaft axis.

The methodology involved in the modeling of the tail rotor mirrors that of the main rotor and the information between the two rotors is exchanged according to the coupling scheme outlined in Section 2.5.4. The frame $(x, y, z)_{\mathrm{TR}}$ is the non-rotating hub frame with its origin centered where the blades of the tail rotor are attached to its hub. The tail rotor hub is at a distance of $\mathbf{L}$ from the main rotor hub, but the axes maintain the same orientation as those of the main rotor axes. Because of the convention adopted in the present work, the tail rotor operates in a clockwise fashion when viewed along the positive y_{TR} axis as compared to the main rotor, which operates in a counter-clockwise manner when viewed along the positive z_{MR} axis. The coordinate transformation matrices between the different frames of reference for the main and tail rotor are given in Appendix D.

2.7 Rotor Trim Methodology

The aerodynamic response of a rotor is a coupled function of the blade control angles and the resulting aerodynamic environment. The positions and strengths of the tip vortex filaments highly depends on the rotor operating conditions. Therefore, to obtain the aerodynamic response for a given flight condition, the rotor must be trimmed to obtain the necessary control angles to produce the required thrust and orientation of the rotor disk plane. For the case of the rotor in ground effect operation, the trimming process is the same as that for the isolated "real" rotor system. The only difference is that the aerodynamic response of the real rotor system is calculated by considering the influence of all the vortical elements of the image rotor system.

2.7.1 Single Rotor Trim Methodology

The rotor control input vector, $\mathbf{x}$, comprising of the blade collective θ_0, lateral cyclic θ_{1c}, and longitudinal cyclic θ_{1s} angles (i.e., $\mathbf{x} = \{\theta_0, \theta_{1c}, \theta_{1s}\}^T$), is updated in the trim procedure using a Newton–Raphson approach [108] to solve the rotor aerodynamic environment such that the desired response vector $\mathbf{y}$ comprising of the thrust and orientation of the rotor TPP (i.e., $\mathbf{y} = \{C_T, \beta_{1c}, \beta_{1s}\}^T$) is obtained.

The change in the response vector $\mathbf{y}(\mathbf{x}+\Delta\mathbf{x})$ is approximated using the Taylor series expansion, as given by

$$\mathbf{y}(\mathbf{x}+\Delta\mathbf{x}) = \mathbf{y} + [\mathbf{J}]\Delta\mathbf{x} + \cdots \tag{2.58}$$

The trim Jacobian matrix, $\mathbf{J}$ is expressed as

$$\mathbf{J} = \frac{\partial \mathbf{y}}{\partial \mathbf{x}} = \begin{bmatrix} \frac{\partial C_T}{\partial \theta_0} & \frac{\partial C_T}{\partial \theta_{1c}} & \frac{\partial C_T}{\partial \theta_{1s}} \\ \frac{\partial \beta_{1c}}{\partial \theta_0} & \frac{\partial \beta_{1c}}{\partial \theta_{1c}} & \frac{\partial \beta_{1c}}{\partial \theta_{1s}} \\ \frac{\partial \beta_{1s}}{\partial \theta_0} & \frac{\partial \beta_{1s}}{\partial \theta_{1c}} & \frac{\partial \beta_{1s}}{\partial \theta_{1s}} \end{bmatrix} \tag{2.59}$$

The updated perturbation is then obtained by re-arranging Eq. 2.58 to give

$$\Delta \mathbf{x} = \mathbf{J}^{-1} \begin{Bmatrix} C_T - C_{T_{\text{req}}} \\ \beta_{1c} \\ \beta_{1s} \end{Bmatrix} \rightarrow 0 \tag{2.60}$$

where $C_{T_{\text{req}}}$ is the target total thrust coefficient of the rotor system.

The trim is performed by using an initial guess of the input control vector, which is then updated by solving Eq. 2.60. The Jacobian matrix is calculated using a first-order forward difference approximation. This approximation is performed by first calculating the initial response vector based on the initial guess of the input vector. The input vector is then perturbed, and the response vector is recalculated to find the Jacobian matrix.

2.7.2 Dual Rotor Trim Methodology

The single rotor trim approach can be extended to dual rotor configurations (such as a coaxial, tandem, or a side-by-side) with two sets of collectives and cyclic pitch angles, and these will be coupled because of the interference between the aerodynamics of the two rotors. Because of the

interfering flow fields, both rotors may operate at different conditions and different disk loading in a torque balanced condition. Therefore, the system of two rotors must be trimmed to satisfy the following two conditions:

1. Thrust balance: The net rotor thrust obtained must counter-balance the components of weight and drag forces of the system. It is assumed that the presence of the airframe (if any) results in a zero contribution to the overall lift. Therefore, it is reasonable to assume that the net rotor thrust equals the weight of the rotorcraft.

2. Torque balance: The net yaw moment on the rotorcraft as a system must be zero. If the contributions other than that of the rotor are neglected, then the torque produced by one rotor must be counter-balanced by the other rotor.

For dual rotor systems, the control input vector and the response vector can be defined using

$$\mathbf{x} = \begin{Bmatrix} \theta_0^1 \\ \theta_{1c}^1 \\ \theta_{1s}^1 \\ \theta_0^2 \\ \theta_{1c}^2 \\ \theta_{1s}^2 \end{Bmatrix} \quad \text{and} \quad \mathbf{y} = \begin{Bmatrix} \sum C_T \\ \sum C_Q \\ \beta_{1c}^1 \\ \beta_{1s}^1 \\ \beta_{1c}^2 \\ \beta_{1s}^2 \end{Bmatrix} \tag{2.61}$$

where the superscript represents the two rotors of the system. The Jacobian matrix for the dual rotor system can then be defined as

$$\mathbf{J} = \frac{\partial \mathbf{y}}{\partial \mathbf{x}} = \begin{bmatrix} \frac{\partial \sum C_T}{\partial \theta_0^1} & \frac{\partial \sum C_T}{\partial \theta_{1c}^1} & \frac{\partial \sum C_T}{\partial \theta_{1s}^1} & \frac{\partial \sum C_T}{\partial \theta_0^2} & \frac{\partial \sum C_T}{\partial \theta_{1c}^2} & \frac{\partial \sum C_T}{\partial \theta_{1s}^2} \\ \frac{\partial \sum C_Q}{\partial \theta_0^1} & \frac{\partial \sum C_Q}{\partial \theta_{1c}^1} & \frac{\partial \sum C_Q}{\partial \theta_{1s}^1} & \frac{\partial \sum C_Q}{\partial \theta_0^2} & \frac{\partial \sum C_Q}{\partial \theta_{1c}^2} & \frac{\partial \sum C_Q}{\partial \theta_{1s}^2} \\ \frac{\partial \beta_{1c}^1}{\partial \theta_0^1} & \frac{\partial \beta_{1c}^1}{\partial \theta_{1c}^1} & \frac{\partial \beta_{1c}^1}{\partial \theta_{1s}^1} & \frac{\partial \beta_{1c}^1}{\partial \theta_0^2} & \frac{\partial \beta_{1c}^1}{\partial \theta_{1c}^2} & \frac{\partial \beta_{1c}^1}{\partial \theta_{1s}^2} \\ \frac{\partial \beta_{1s}^1}{\partial \theta_0^1} & \frac{\partial \beta_{1s}^1}{\partial \theta_{1c}^1} & \frac{\partial \beta_{1s}^1}{\partial \theta_{1s}^1} & \frac{\partial \beta_{1s}^1}{\partial \theta_0^2} & \frac{\partial \beta_{1s}^1}{\partial \theta_{1c}^2} & \frac{\partial \beta_{1s}^1}{\partial \theta_{1s}^2} \\ \frac{\partial \beta_{1c}^2}{\partial \theta_0^1} & \frac{\partial \beta_{1c}^2}{\partial \theta_{1c}^1} & \frac{\partial \beta_{1c}^2}{\partial \theta_{1s}^1} & \frac{\partial \beta_{1c}^2}{\partial \theta_0^2} & \frac{\partial \beta_{1c}^2}{\partial \theta_{1c}^2} & \frac{\partial \beta_{1c}^2}{\partial \theta_{1s}^2} \\ \frac{\partial \beta_{1s}^2}{\partial \theta_0^1} & \frac{\partial \beta_{1s}^2}{\partial \theta_{1c}^1} & \frac{\partial \beta_{1s}^2}{\partial \theta_{1s}^1} & \frac{\partial \beta_{1s}^2}{\partial \theta_0^2} & \frac{\partial \beta_{1s}^2}{\partial \theta_{1c}^2} & \frac{\partial \beta_{1s}^2}{\partial \theta_{1s}^2} \end{bmatrix} \tag{2.62}$$

Finally, the updated perturbation vector can be written as

$$\Delta \mathbf{x} = \mathbf{J}^{-1} \begin{Bmatrix} \sum C_T - C_{T_{\text{req}}} \\ \sum C_Q \\ \beta_{1c}^1 \\ \beta_{1s}^1 \\ \beta_{1c}^2 \\ \beta_{1s}^2 \end{Bmatrix} \rightarrow 0 \tag{2.63}$$

2.7.3 Tail Rotor Trim Methodology

A free-flight trim (i.e., propulsive trim) would have to be performed to accurately calculate the pilot control inputs for the main and tail rotor. The trim targets would be the force and moment equilibrium of the rotorcraft along each of the three axes. The control input vector, $\mathbf{x}$, would be the main rotor collective θ_0, lateral cyclic θ_{1c}, longitudinal cyclic θ_{1s}, tail rotor collective θ_t, the aerodynamic incidence of the fuselage α_f, and fuselage sideslip angle β_f.

While the inclusion of a detailed flight dynamics model can alter the orientation of the tip path plane and affect the sediment uplift at the ground [115], a prescribed flight path is used in the present work to describe the trajectory of the rotorcraft, which provides a good approximation to the overall development of the flow field and the dust cloud [84]. Consequently, a relatively simpler trim methodology is used where a sequential trim procedure is performed for the main and tail rotors. The main rotor is trimmed in accordance with the procedure described in Section 2.7.1, with the main rotor trimmed to a given rotor thrust and zero cyclic flapping angles. The tail rotor control angles are then obtained based on the forces and moments produced by the already trimmed main rotor. The presence of a tail rotor introduces an extra control variable θ_t, i.e., the collective pitch control. Tail rotors do not require cyclic pitch control. The collective pitch of the tail rotor, θ_t, is trimmed to counter the yaw moment produced by the main rotor. It is assumed that in trim, the main rotor flow field affects that of the tail rotor, but not vice versa.

If $\mathbf{L}$ represents the vector from center of the main rotor hub to the center of the tail rotor hub,

and the net thrust force produced by the tail rotor is $\mathbf{T}_{\mathrm{TR}}$, the torque balance can be expressed as

$$\mathbf{Q} = \mathbf{L} \times \mathbf{T}_{\mathrm{TR}} \tag{2.64}$$

where $\mathbf{Q}$ is the torque produced by the main rotor about its shaft axis. The tail rotor collective pitch in conjunction with the local aerodynamic environment is used to obtain the sectional blade loads, which are then integrated along the rotor span and azimuth to obtain the net thrust; see Eq. 2.10. The main rotor is trimmed using the procedure for trimming a single rotor, as described in Section 2.7.1, with the trim targets being C_T, β_{1c} and β_{1s}. The weight of the helicopter is now balanced by the main rotor thrust and the vertical component of the tail rotor, if any (e.g., from a canted tail rotor).

2.8 Modeling of the Flow Near the Ground

The presence of an impervious ground plane below the rotor significantly alters its developing wake structure; see Fig. 2.9. Representative flow velocity measurements [9] on the ground below an isolated rotor at several downstream distances are shown in Fig. 2.13, where the developing wall-jet and boundary layer region are evident. The threshold entrainment models (discussed in Section 2.8.2) are based on the calculation of the friction velocities in the near wall region at the edge of the boundary layer, which means that the details of the flow close to the ground must be well represented if sediment entrainment conditions are to be predicted. The challenge is to be able to predict the near-wall flow using the current methodology with results essentially equivalent to those that would be obtained using a viscous solution.

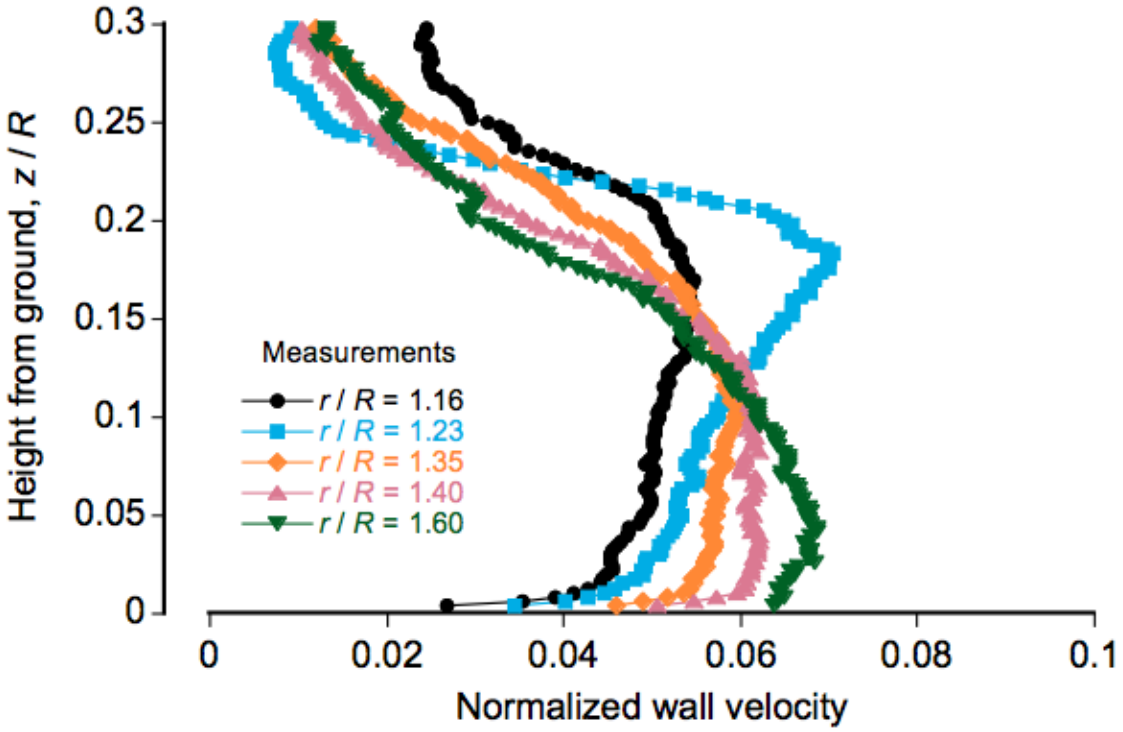

Figure 2.13: Representative measurements of the flow on the ground below a hovering rotor at several downstream distances from a point below the rotational axis of the rotor r. The distance is normalized with the rotor radius R and the wall velocity is normalized with rotor tip speed ΩR

The flow field predicted using the FVM is fundamentally inviscid, as a result of which non-zero wall parallel velocities are predicted at the ground violating the physical no-slip condition. An example of this behavior is shown in Fig. 2.15 in terms of the component of velocity parallel to the wall at several downstream distances. Therefore, another model must be used to represent the flow in the region near the ground.

In the present work, an inviscid-viscous method was developed to predict the flow arising from a combination of the rotor flow (modeled through the FVM, an inviscid potential flow methodology) and the resulting (viscous) flow in the boundary layer region at the ground. A schematic of the approach used is shown in Fig. 2.14. In this model, the effect of the rotor wake solution (obtained from the FVM) and the airframe (obtained from the panel method) provides the induced velocity at a computational interface that is located a small distance above the ground (of the order of the boundary layer thickness, δ). The flow parameters in the viscous region are then matched to the inviscid solution at the interface by using a semi-empirical boundary layer profile. In the present work, the boundary layer regions was modeled using a self-similar logarithmic velocity profile of the form

$$u(z) = \frac{u_*}{k} \log\left(\frac{z}{k_r}\right) \tag{2.65}$$

where k_r is the assumed equivalent roughness height of the ground surface, $k = 0.4$ is Von Kármán's constant, z is the height above the ground within the boundary layer region, and u_* (Eq. 2.66) is the friction velocity. The velocity field $u(z)$ within the boundary layer region can be obtained from Eq. 2.65, if the values of k_r and u_* are known apriori. The value of k_r can be approximated as $3.33 \times 10^{-2} d_p$, as given by Bagnold [116], where d_p is the diameter of the particle. In general,

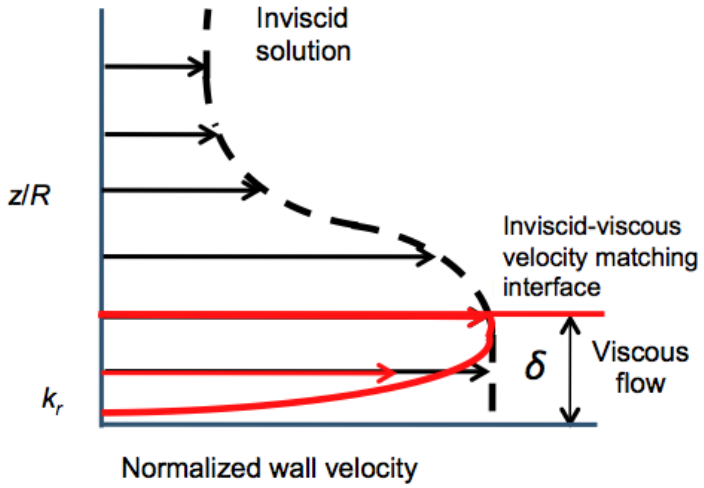

Figure 2.14: Schematic showing the inviscid-viscous matching of the velocity field in the near-wall region.

however, k_r is not a constant and increases as the particles are uplifted [34]. This variation in k_r is not well understood and therefore, a constant value is assumed in the present work.

The friction velocity, u_*, is a representation of the shear stress on the ground and is expressed conventionally as

$$u_* = \sqrt{\tau/\rho} \tag{2.66}$$

where τ is the boundary layer shear stress at the wall. Most particle uplift models are based on the attainment of a critical friction threshold velocity, u_{*t}, to determine the mobilization of the particles from the sediment bed. The values of u_{*t} are obtained from particle mobility observations in uniform flows passing over sediment beds of certain known (or estimated) characteristics [116]. An increase in the flow velocity near the wall increases the friction velocity, and where the friction velocity reaches the threshold, i.e., $u_* > u_{*t}$, particles that are stationary move downstream in saltation.

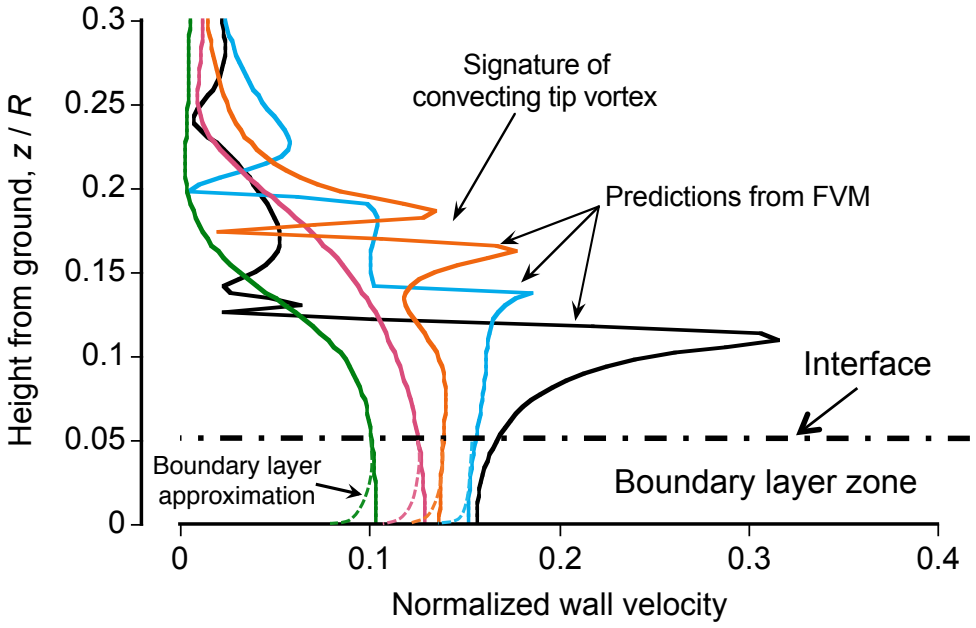

Figure 2.15: Representative computed velocity profiles made by the FVM below the rotor at the ground.

The process of finding u_* also requires the assumption of a nominal boundary layer thickness, δ. At the edge of the boundary layer, the friction velocity can be expressed using Eq. 2.65 as

$$u_* = \frac{u(\delta)k_r}{\log(\delta/k_r)} \tag{2.67}$$

where $u(\delta)$ is the flow velocity at the edge of the boundary layer, which in the current formulation, is assumed to be velocity predicted by the FVM at the ground. The boundary layer profile below a rotor is not a constant and varies spatially and temporally based on the rotor operating conditions and the local vortical aerodynamic environment in the near-wall region. Experimental studies [8,9,33] of the flow close to the ground have shown that the boundary layer profile is dependent on the breakdown and merging of vortices, and the formation of counter-rotating secondary vortical structures. Because the foregoing effects cannot be predicted within the context of the FVM, an average boundary layer profile is used in the present work. Laboratory experiments [9,22,30] have shown that the average thickness of the boundary layer in the fully developed wall-jet flow on the ground below a rotor is of the order of 5% of the rotor radius. Therefore, the value of u_* can be calculated by using Eq. 2.67, which can then be compared against the threshold friction velocity to determine particle mobility.

Validation of the assumed logarithmic profile in the near-wall region was obtained by using the near-wall velocity measurements of Milluzzo et al. [9] in comparison with the wall-parallel velocities obtained using Eq. 2.65. The results are shown in Fig. 2.16, which confirms that the logarithmic approximation is reasonable in the modeling of the boundary layer flow.

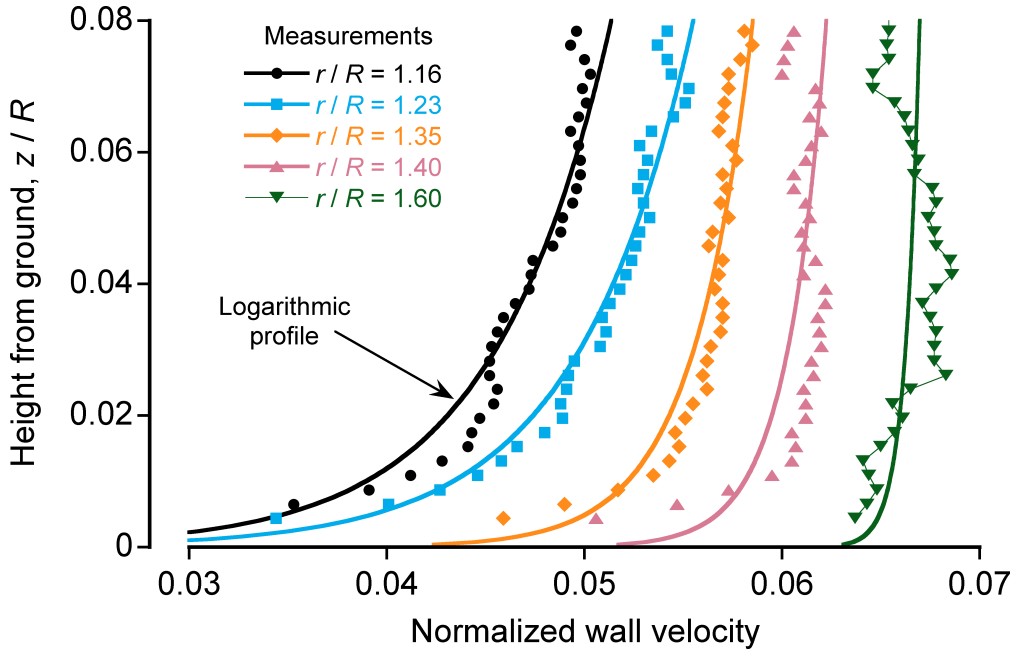

Figure 2.16: Near-wall boundary layer measurements in the flow below the rotor showing that a logarithmic boundary layer profile is a reasonable approximation. (Source of experiments: Milluzzo et al. [9])

2.8.1 Forces Acting on Stationary Particles on a Bed

Stationary particles on a bed below the rotor can experience several types of forces such as shear, pressure, inter-particle and gravitational, as shown in Fig. 2.17. Shear forces on the stationary particles arise because of the velocity gradients produced by the boundary layer on the sediment bed, as previously discussed. The components of the shear force along and perpendicular to the wind direction are referred to as the drag force $\mathbf{F}_d$, and the lift force $\mathbf{F}_l$, respectively. Significant unsteady pressures may also be produced in the vorticity-laden flow field below the rotor and have the potential to produce forces, $\mathbf{F}_{\Delta P}$, that can affect onset of sediment motion [83]. Besides these forces, a particle on the bed also experiences gravitational forces $\mathbf{F}_g$ and inter-particle forces $\mathbf{F}_i$. Inter-particle forces comprise of Van der Waals's forces, electrostatic forces, cohesive

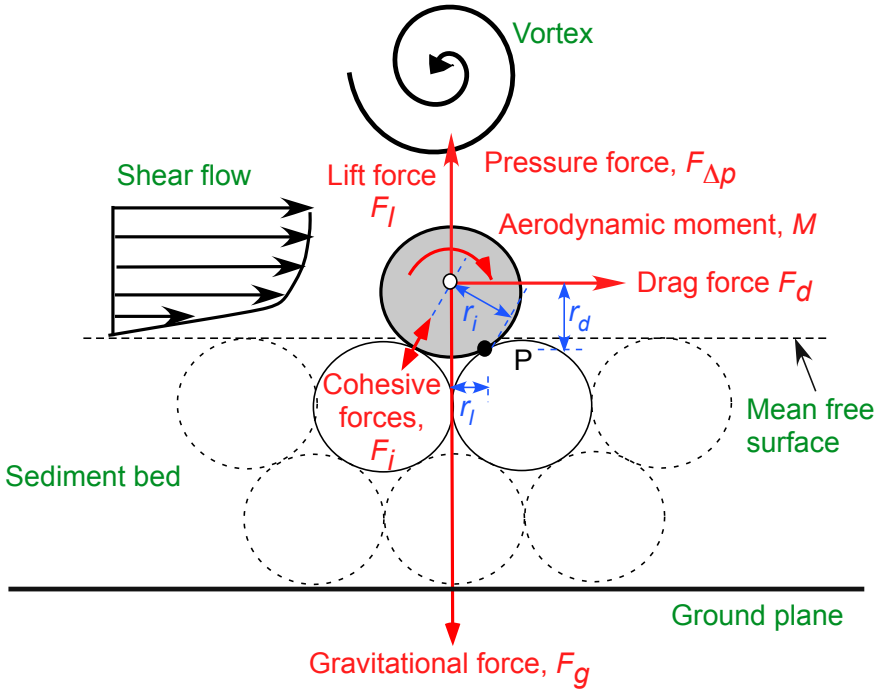

Figure 2.17: Forces acting on sediment particles at the surface of a particle bed.

forces, etc. [34]. These forces are the most difficult to measure or calculate, and can only be approximated in the development of mathematical models. A particle subjected to these forces will be mobilized about a point P, as shown in Fig. 2.17, if the moments created by the forces in the flow (aerodynamic and shear) are greater than the moments created by the gravitational and the inter-particle forces. This mechanism of entrainment is referred to as direct aerodynamic entrainment.

Another significant mobilization mechanism in a rotor induced flow field is that of bombardment ejections. This latter process occurs when previously suspended sediment particles in the flow impact the sediment bed with significant downward momentum, and then eject more particles. Previous work in aeolian sciences [35] has shown that this particular mechanism can be a major contributor to the mobilization and ejection of small-sized particles. The numerical model-

ing of this mechanism is discussed in Section 2.10.

In the case of a rotor, the presence of blade tip vortices, vortex sheets, and secondary vortical structures near the bed can produce eddies and turbulence on the bed that may affect the behavior of the inter-particle forces. The interaction of the fluid and dust phases can further alter the flow field close to the ground and affect the forces on the acting on a particle on the sediment bed [42]. These complex processes need further understanding, and are challenging to represent using mathematical models.

In the present study, only mono-dispersed spherical particles were considered, i.e., all the particles were assumed to be of uniform density and were represented as spheres. However, a typical sediment bed contains particles of different sizes [117], which occur because of the mineralogy of the bed and the packing of the smaller sized particles within the boundary adjacent to the bigger particles. Particle collisions and bombardment mechanisms can result in the disintegration of larger particles, and may be another contributor to the liberation of smaller sized particles. These latter mechanisms are obviously difficult to accurately model and represent, especially in a computationally efficient manner, and are not considered in the present work. It is however clear that sediment entrainment in a highly vortical flow field, such as that below a rotor, is a very complex behavior and the current level of understanding of the physical principles is insufficient to model all of the various effects.

2.8.2 Modeling of Threshold Friction Velocity

Previous models for the entrainment of particles from the sediment bed is based on empirical determination of u_{*t}, by considering the balance of forces acting on the particles. In the present work, an entrainment model has been developed based on the previous research of Bagnold [116], Greeley and Iverson [118], and Shao [78].

The various forces acting on a particle on the sediment bed is shown in Fig. 2.17. The moment balance of the different forces on the particle at the point P can be expressed as

$$(F_l + F_{\Delta P} - F_g)r_l + F_d r_d + F_m r_m - F_i r_i = 0 \tag{2.68}$$

where the magnitude of the forces are written as $F_x = |\mathbf{F}_x|$, and r_l, r_d, r_m, r_i are the respective moment arms. Although the moment depend on the distribution of particles on the bed, they are assumed to be proportional to the particle diameter, d_p, in the present model [116, 118]. Therefore, the moment arms can be expressed as $r = ad_p$, where a is the associated constant of proportionality, and so Eq. 2.68 becomes

$$(F_l + F_{\Delta P} - F_g)a_l + F_d a_d + F_m a_m - F_i a_i = 0 \tag{2.69}$$

The drag force, F_d, on the particle was approximated using

$$F_d = \frac{1}{2} C_{d_s} \rho A_s U_s^2 \tag{2.70}$$

where C_{d_s} is the drag coefficient of the particle when it is stationary on the bed, A_s is the particle frontal area, and U_s is the characteristic flow velocity.

The calculation of F_d is difficult because behavior of C_{d_s} is not well understood [78, 116], and the choice of U_s is difficult near the particle bed where the effect of turbulence dominates the flow. However, the mean value of the drag force depends upon the velocity in the boundary layer region and, therefore, depends on the shear force. Therefore, Bagnold expressed the drag force (Eq. 2.70) as

$$F_d = K_d \rho d_p^2 u_*^2 \tag{2.71}$$

where u_* is the friction velocity and K_d is a non-dimensional coefficient.

Greeley and Iverson [118] represented the other aerodynamic viscous forces as

$$F_l = K_l \rho d_p^2 u_*^2 \tag{2.72}$$

$$F_m = K_m \rho d_p^2 u_*^2 \tag{2.73}$$

where K_l and K_m are the non-dimensional lift and moment coefficients, respectively.

The pressure force, $F_{\Delta P}$, was modeled by using several assumptions. Firstly, it was assumed that the top half surface of the stationary particle on the bed is acted upon by uniform pressure, which is created by the presence of vortices in the flow field. Secondly, it was assumed that the bottom half surface of the particle is acted upon by the ambient pressure, p_∞. The resulting pressure

force acting on the particle can then be written as

$$F_{\Delta P} = -K_P \Delta P \, d_p^2 \tag{2.74}$$

where K_P is the non-dimensional constant that depends upon the fraction of the particle cross-sectional area affected by the pressure forces; the value of K_P in the present work was $\pi/4$.

The gravitational force, F_g, with buoyancy effects can be written as

$$F_g = \frac{\pi}{6}(\rho_p - \rho) g d_p^3 \tag{2.75}$$

Substituting into Eq. 2.69 the expression for forces from Eq. 2.71–2.75, the moment balance can be expressed as

$$a_t K_t \rho u_{*t}^2 d_p^2 - a_l K_P \Delta P d_p^2 = a_l \frac{\pi}{6}(\rho_P - \rho) g d_p^3 + a_i F_i \tag{2.76}$$

where $a_t K_t = a_l K_l + A_d K_d + a_m K_m$. Further simplification of the foregoing equation gives

$$\rho u_{*t}^2 = \frac{a_l K_p}{a_t K_t} \Delta P + \frac{a_l}{a_t K_t} \frac{\pi}{6}(\rho_p - \rho) g d_p + \frac{a_i}{a_t K_t} \frac{F_i}{d_p^2} \tag{2.77}$$

Using the value of $K_p = \pi/4$, the expression for the threshold friction velocity, u_{*t}, can then be written as

$$u_{*t} = A \sqrt{\frac{6}{\pi} \frac{K_p}{\rho} \Delta P + \frac{\rho_p - \rho}{\rho} g d_p + \frac{6}{\pi} \frac{a_i}{a_l} \frac{F_i}{\rho d_p^2}} \tag{2.78}$$

where $A = \sqrt{a_l \pi / 6 a_t K_t}$.

2.9 Particle Convection

After the particles are entrained into the flow field based on the threshold conditions, the resulting forces acting upon the particle govern their convective motion. The present section discusses the forces acting on the particles after they become airborne. The development of the particle equations of motions (EOMs) are also discussed, along with the mathematical approximations involved in their formulation.

2.9.1 Particle Equations of Motion

Brownout is a problem of coupled phases in that the carrier phase affects the motion of the individual particles and the dispersed phase may also affect the convection of the fluid. Figure 1.9(a) shows that the typical ratio of the mass fraction of the dispersed to the carrier phases in a brownout dust cloud is $< 0.1\%$ everywhere except close to the ground. Two-phase laboratory experiments [42] have showed that the presence of uplifted particle in the dual-phase flow serve to diffuse the concentrated tip vortex close to the ground and influence the turbulence characteristics. However, it is assumed in the present work that the resulting two-phase flow is lightly loaded by the particle in that the particle motion is driven by the fluid phase but not vice-versa, i.e., an assumption of one-way coupling. Therefore, the aerodynamic flow is first calculated followed by the tracking of the individual particles over time.

The forces acting on an airborne particle is shown in Fig. 2.18 and include a drag force $\mathbf{F}_D$, a lift force $\mathbf{F}_L$, gravity force $\mathbf{F}_g$, buoyancy force $\mathbf{F}_b$, apparent mass forces $\mathbf{F}_{\text{am}}$, Basset forces $\mathbf{F}_{\text{Basset}}$. The Basset force, which depends on the time-history of the particle motion, manifests as

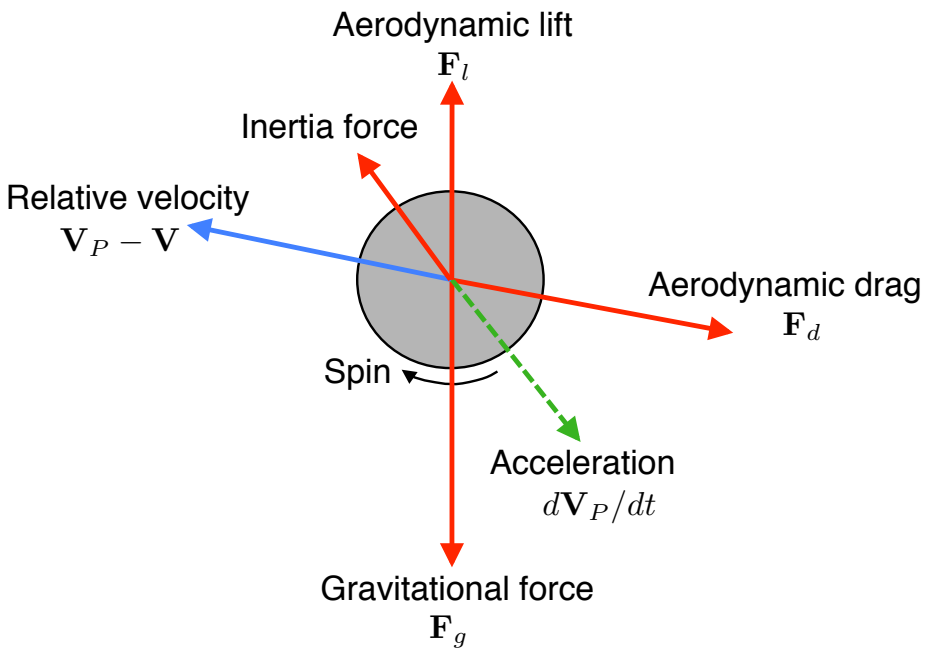

Figure 2.18: Forces acting on an airborne sediment particle.

an apparent drag force. However, it can be neglected because it is important only in flows with very light particles and very steep velocity gradients.

The Basset–Boussinesq–Oseen (BBO) equation governs the resulting dynamic behavior of the particles, which under the assumptions of dilute gas-particle suspensions at low Reynolds numbers of the relative particle motion, can be decoupled in the three spatial dimensions. Therefore, apart from the drag and gravitational forces, all other forces vary proportionally to the ratio of the gas to particle density, which is of the order of 10^{-3} in air [119].

The equations of motion (the BBO equations) can then be expressed as

$$\begin{aligned} m\frac{d\mathbf{V}_p}{dt} &= \sum \mathbf{F} \\ &= \mathbf{F}_d + \mathbf{F}_L + \mathbf{F}_g + \mathbf{F}_b + \mathbf{F}_m + \mathbf{F}_{\text{Basset}} \\ &\approx \mathbf{F}_d + \mathbf{F}_g \\ &= -\frac{1}{2}\rho C_d A|\mathbf{V}_p - \mathbf{U}|(\mathbf{V}_p - \mathbf{U}) + m\mathbf{g} \end{aligned} \tag{2.79}$$

where $\mathbf{V}_p$ and $\mathbf{U}$ are the particle and flow velocities. The quantities C_d and A are the particle drag coefficient and its cross-sectional area, respectively, m is the mass of the particle, and g is the acceleration under gravity. In the present model, mono-dispersed spherical particles with a diameter of d_p were assumed, so $A = \pi d_p^2/4$.

The drag coefficient of the particle, C_d, is a function of the particle Reynolds number, Re_p, [120] i.e.,

$$C_d(Re_p) = \frac{24}{Re_p}\left(1 + 0.15Re_p^{0.687}\right) \tag{2.80}$$

where

$$Re_p = \frac{|\mathbf{V}_p - \mathbf{U}|d_p}{\nu} \tag{2.81}$$

Combining Eqs. 2.79 and 2.80, the EOMs for the particle can be expressed as

$$\begin{aligned} \frac{d\mathbf{V}_p}{dt} &= -\frac{(\mathbf{V}_p - \mathbf{U})}{\tau_p} + \mathbf{g} \\ \frac{d\mathbf{X}_p}{dt} &= \mathbf{V}_p \end{aligned} \tag{2.82}$$

where $\mathbf{X}_p$ is the particle position at time t, and τ_p is the particle response time given by

$$\tau_p = \frac{m}{\frac{1}{2}\rho C_d(Re_p)A|\mathbf{V}_p - \mathbf{U}|} \tag{2.83}$$

which indicates the time taken by a particle to respond to changes in local fluid velocity. Higher the response time, longer the time it takes the particle to match its velocity with the surrounding fluid. Notice that the particle response time is a function of the particle and flow properties. Using Eqs. 2.80 and 2.81, τ_p can be written as

$$\tau_p = \frac{\tau_{p_s}}{1 + 0.15Re_p^{0.687}} \tag{2.84}$$

where τ_{p_s} is the particle response time under Stokes flow (i.e., $Re_p \ll 1$) conditions, and can be expressed as

$$\tau_{p_s} = \frac{\rho_p d_p^2}{18\mu} \tag{2.85}$$

Inserting the value of τ_p from Eq. 2.84 into Eq. 2.83, the particle EOMs become

$$\begin{aligned} \frac{d\mathbf{V}_p}{dt} &= -\frac{(1 + 0.15Re_p^{0.687})}{\tau_{p_s}}(\mathbf{V}_p - \mathbf{U}) + \mathbf{g} \\ \frac{d\mathbf{X}_p}{dt} &= \mathbf{V}_p \end{aligned} \tag{2.86}$$

which is a nonlinear ordinary differential equation and, therefore, must be solved by using iterative methods.

In the present work, Stokes flow assumptions ($Re_p \ll 1$) were used to further linearize

Eq. 2.86 with respect to the particle velocity, $\mathbf{V}_p$. Therefore, the particle EOMs can be written as

$$\begin{aligned} \frac{d\mathbf{V}_p}{dt} &= -\frac{(\mathbf{V}_p - \mathbf{U})}{\tau_{p_s}} + \mathbf{g} \\ \frac{d\mathbf{X}_p}{dt} &= \mathbf{V}_p \end{aligned} \tag{2.87}$$

Under the additional assumption of dilute gas-particle suspensions, Eq. 2.88 can be decoupled in the three spatial dimensions. The resulting EOMs then become two sets of first-order ODEs. The components of particle velocities are determined by solving the set

$$\begin{aligned} \frac{dV_{p_x}}{dt} &= -\frac{(\mathbf{V}_{p_x} - \mathbf{U}_x)}{\tau_{p_s}} \\ \frac{dV_{p_y}}{dt} &= -\frac{(\mathbf{V}_{p_y} - \mathbf{U}_y)}{\tau_{p_s}} \\ \frac{dV_{p_z}}{dt} &= -\frac{(\mathbf{V}_{p_z} - \mathbf{U}_z)}{\tau_{p_s}} + \mathbf{g} \end{aligned} \tag{2.88}$$

and the particle displacements by solving the subsequent set

$$\begin{aligned} \frac{dX_{p_x}}{dt} &= V_{p_x} \\ \frac{dX_{p_y}}{dt} &= V_{p_y} \\ \frac{dX_{p_z}}{dt} &= V_{p_z} \end{aligned} \tag{2.89}$$

2.9.2 Solution to the Particle Equations of Motion

The decoupled particle EOMs (Eq. 2.89) can be expressed in a simplified mathematical form as

$$\frac{dV_{p_i}(X_{p_i},t)}{dt} = -\frac{V_{p_i}(X_{p_i},t) - f_i(X_{p_i},t)}{\tau_{p_s}} \tag{2.90}$$

$$\frac{dX_{p_i}(t)}{dt} = V_{p_i}(X_{p_i},t) \tag{2.91}$$

where $i = x,y,z$ and $\mathbf{f}$ is the forcing function containing contributions from the flow velocity $\mathbf{U}$ and the gravitational force, and can be written as

$$\begin{aligned} f_x &= U_x \\ f_y &= U_y \\ f_z &= U_z - g\tau_{p_s} \end{aligned} \tag{2.92}$$

Equations 2.90 and 2.91 are three sets of ODEs, where each set can be written as

$$\frac{d}{dt}\begin{Bmatrix} V_{p_i} \\ X_{p_i} \end{Bmatrix} - \begin{bmatrix} -1/\tau_{p_s} & 0 \\ 1 & 0 \end{bmatrix} \begin{Bmatrix} V_{p_i} \\ X_{p_i} \end{Bmatrix} = \begin{Bmatrix} f_i \\ 0 \end{Bmatrix} \tag{2.93}$$

These ODE sets in Eq. 2.93 are solved together to compute the positions of the particles, $\mathbf{X}_p$, at different times. First, the particle velocities $\mathbf{V}_p$ are determined using Eq. 2.90 under the influence of rotor flow velocities $\mathbf{U}$, which appear in the forcing function, $\mathbf{f}$, in Eq. 2.92. These velocities

include the induced velocities from all of the vortex elements in the flow field, the maneuver velocities, the free-stream velocities, effects of the fuselage, etc. The computed particle velocities, $\mathbf{V}_p$, are then used to convect the particles to new positions in time, $\mathbf{X}_p$, using Eq. 2.91.

Because the forcing function on the right-hand side of Eq. 2.92 also contains the wake induced velocities $\mathbf{U}$, which is a nonlinear function of the particle positions, $\mathbf{X}_p$, an exact analytical solution to Eqs. 2.90 and 2.91 is permissible only for simplified flow conditions. Therefore, these ODEs must be solved numerically by using time-marching schemes. The left-hand-side can be discretized by using the most suitable time-marching algorithm. The components of the forcing function $\mathbf{f}$ (see Eq. 2.92) is computed by using the Biot–Savart law [15] as an integral along the length of each vortex segment. This integral cannot be evaluated exactly, therefore, it is approximated using numerical quadrature and straight-line vortex segmentation [15], as discussed previously in Section 2.5.

The time-marching schemes must be chosen such that ensure stability of the solution and preserve its accuracy over long time durations. Several time-marching schemes were analyzed such as first-order Euler explicit, first-order Euler implicit, explicit second-order Adams–Bashforth method, implicit second-order BDF2, and the implicit third-order BDF3 [83], for tracking the trajectory of the particles. The two point backward difference formula, BDF2, was used in the present work and the numerical implementation of this scheme requires a knowledge of the particle velocities and position from the two previous time steps. Because this information is not available at the first time step of the BDF2 scheme, an Euler-explicit scheme is used for the initial time step.

Notice that the BDF2 scheme is an implicit scheme and, therefore, requires a knowledge of

the forcing function as given by Eq. 2.92, at $(n+1)^{\text{th}}$ time step. Because f_i is a function of the flow velocity $U_i(X_{p_i},t)$, it is not known in the $(n+1)^{\text{th}}$ time step unless X_{p_i} is also known at this time step. In the present implementation of the BDF2 scheme, f_i is approximated at the n^{th} time step. The numerical solution of $V_{p_i}^{n+1}$ and $X_{p_i}^{n+1}$ can be written as

$$V_{p_i}^{n+1} = \frac{1}{\left(1+\frac{\Delta t}{\tau_{p_s}}\right)}\left(V_{p_i}^{n}+\frac{\Delta t}{\tau_{p_s}}f_i^n\right) \quad \text{for} \quad n=1 \tag{2.94}$$

$$V_{p_i}^{n+1} = \frac{1}{3\left(1+\frac{2\Delta t}{3\tau_{p_s}}\right)}\left(4V_{p_i}^{n}-V_{p_i}^{n-1}+2\frac{\Delta t}{\tau_{p_s}}f_i^n\right) \quad \text{for} \quad n>1 \tag{2.95}$$

and

$$X_{p_i}^{n+1} = X_{p_i}^{n}+\Delta t\ V_{p_i}^{n+1} \quad \text{for} \quad n=1 \tag{2.96}$$

$$X_{p_i}^{n+1} = \frac{1}{3}\left(4X_{p_i}^{n}-X_{p_i}^{n-1}+2\Delta t\ V_{p_i}^{n+1}\right) \quad \text{for} \quad n>1 \tag{2.97}$$

2.9.3 Accuracy of the Numerical Solution

Numerical solutions are approximations to the exact solutions of the ODEs, and can consequently introduce several types of errors. These errors include truncation or discretization errors and round-off errors. Discretization errors, as the name suggests, are introduced while discretizing the original ODE. As the discretization size approaches zero, the approximate solutions should approach the exact solution. Discretization errors can arise from two reasons: the use of a particular numerical scheme and by the approximation to the induced velocity field. These errors depend upon the discretization time step size Δt, and the numerical scheme chosen, and are usually es-

timated by using a Taylor-type of error analysis [121]. The round-off errors arise because of the result of non-exact representation of real numbers on finite-precision computers. The computations in the present work were performed in double-precision with round-off errors of magnitude about 10^{-16}. In the present study, the use of Graphics Processing Units (GPU) can also introduce round-off errors, which is an issue discussed later in Appendix B.

The sources of discretization errors can be examined by writing the discretized equations in the form

$$\underline{\frac{\Delta V_p}{\Delta t}} + \frac{V_p}{\tau_{p_s}} = \frac{1}{\tau_{p_s}} \underline{f(X_p)} \tag{2.98}$$

$$\underline{\frac{\Delta X_p}{\Delta t}} = \underline{V_p} \tag{2.99}$$

The subscript i indicating the three spatial coordinates has been omitted from the previous equations for simplicity. The underlined terms are approximated by discretization and, therefore, can produce numerical errors. The two sources of discretization errors in the numerical solution of the particle EOMs are: (a) calculation of the forcing function f_i on the RHS of the Eq. 2.92 by using the Biot–Savart integral, and (b) use of the time-marching schemes to solve these equations. The global error incurred in the numerical solution of the multi-step schemes also depends upon the lower-order time-marching schemes used at the initial time steps.

2.10 Bombardment Ejection of Particles

Bombardment ejection is a key sediment mobilization mechanism in the formation of brownout dust clouds. Modeling this process is challenging, in part because of the difficulty in representing the mechanical characteristics of the sediment bed and the effects arising from inter-particle forces. The present section explains a simplified model that has been developed to simulate the process of bombardment ejections in the modeling of rotorcraft brownout problem.

Shao [35] has shown that the mechanism of bombardment ejections is primarily responsible for the uplift of smaller-sized dust particles, for which the inter-particle forces are strong enough to prevent them from being dislodged otherwise by the external flow. Recent dual-phase experiments conducted by Sydney et al. [3] also showed that bombardment ejections may be an important contributor to sediment mobilization and uplift under the action of rotor wake flows. Different forms of bombardment have been observed in this case; see Fig. 1.10. For example, particles saltating on the bed follow ballistic-like trajectories and if they gain sufficient velocity can bombard on the bed, ejecting more particles through bombardments. These ejected particles can then become uplifted by the upwash region of a vortical flow, recirculated through the downwash region, and bombarded back onto the bed to eject even more particles. This form of bombardment is called localized reingestion bombardment.

Another form of reingestion bombardment occurs when particles are suspended high enough from the ground to be recirculated through the rotor disk. In this case, the particles can also bombard the bed and eject more particles in a process called global bombardment; see Fig. 2.19. During all of these bombardment processes, small-sized craters are left on the bed. In some cases,

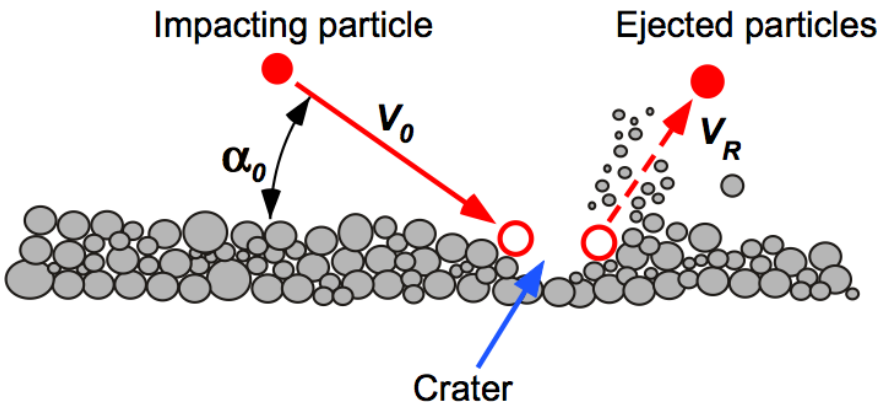

Figure 2.19: Schematic of a sediment particle impacting the ground, forming a crater, and ejecting new particles.

such craters may be big enough to change the topology of the bed and affect the flow, but for a full-scale rotorcraft deviations in the original nominally flat bed topology are generally small compared to the overall linear dimensions of the problem.

In the present work, the process of bombardment ejection was modeled using a probabilistic approach. The two main components of the model were: (a) finding the volume of crater formed by the impacting particles, and (b) approximating the initial velocities of the ejected particles.

2.10.1 Volume of Crater Formed by Bombardment Ejection

Several assumptions are needed to develop the bombardment ejection model. First, it was assumed that a particle impacting the bed can excavate void-shaped craters, as shown in Fig. 2.19. This latter assumption is justified based on experimental observations of the mechanism of bombardment ejections seen in dual-phase rotor flows [8, 22, 30]. The volume of particles ejected from the bed was assumed to be equal to the volume of the crater formed by the impacting particle. It was further assumed that a constant plastic pressure acts upon the particle impacting the bed, and

that the particled do not shatter during the impact. The ratio of the vertical to the horizontal force acting on the particle during its impact with the bed was considered constant, which has a value of about 2 for abrasive grains [122].

Under these assumptions, Lu and Shao [122] solved the EOMs of each particle that impacts the bed and creates a crater. The resulting volume of the crater, θ, was expressed as a function of the velocity $\mathbf{V}_0$, diameter d_p, and mass m_0 of the impacting particle, as well as of plastic pressure exerted by the bed, i.e.,

$$\vartheta = \frac{\pi \rho_p d_p^3 |\mathbf{V}_0|^2}{12 P_s} \left(\sin 2\alpha_0 - 4\sin^2 \alpha_0 + \frac{7.5\pi |\mathbf{V}_0| \sin^3 \alpha_0}{\beta_v d_p} \right) \tag{2.100}$$

where $\beta_v = \sqrt{2P_s d_p / m_0}$ and P_s is the horizontal component of the plastic pressure of the bed exerted on the particle. The plastic pressure P_s is a measure of soil erodibility, which depends upon the mechanical properties of the soil such as its cohesion, tensile strength, modulus of elasticity, and aggregate content. While the measurement of such properties is rather difficult, In general, Lu and Shao [35] have estimated the range of P_s to lie between 10 to 25×10^5 Nm^2 for sandy to loamy beds. For the present analysis, P_s was considered to be 1,000 Nm^2, which was the value also used by Lu and Shao [122] for smooth and fine grained unaggregated particle beds.

2.10.2 Initial Velocity of the Ejected Particles

Several assumptions must also be made to compute the initial velocities of the particles that are ejected during the process of bombardment. In the present work, it was assumed that the particles removed from the bed were tightly packed into the crater volume. All of the ejected

particles were assumed to be of the same size as that of the impacting particle. It is recognized, however, that in practice, particles of different sizes could be ejected from the bed, but this is a much more difficult problem to model and is left for future work.

The initial velocities and positions of the ejected particles were determined from the particle rebound velocity, $\mathbf{V}_R$, by using a probabilistic approach while conserving momentum and energy of the rebounding particle. The rebound velocity of impacting particles can be computed by using a hard-sphere model after integrating the EOMs and assuming a coefficient of restitution [119]. The coefficient of restitution of the particles was assumed to be 0.6 for the present studies [123].

The positions and velocities of the ejected particles are probabilistically distributed using the principles of energy and momentum conservation with the velocity, $\mathbf{V}_i(\mu_B, \Sigma_B)$, of the ejected particles being distributed using

$$\phi = \frac{1}{2\pi^{k/2}|\Sigma_B|^{k/2}} \exp\left(-\frac{1}{2}\left(\mathbf{V}_i - \mu_B\right)^T \Sigma_B^{-1}\left(\mathbf{V}_i - \mu_B\right)\right) \tag{2.101}$$

where μ_B and Σ_B are the mean and covariance matrices of the normal distribution, respectively, as given by

$$\mu_B = \frac{1}{N_B}\sum_{i=1}^{N_B} \mathbf{V}_i \tag{2.102}$$

and

$$\Sigma_B = \begin{bmatrix} \sigma_{xx}^2 & \sigma_{xy}^2 & \sigma_{xz}^2 \\ \sigma_{yx}^2 & \sigma_{yy}^2 & \sigma_{yz}^2 \\ \sigma_{xz}^2 & \sigma_{yz}^2 & \sigma_{zz}^2 \end{bmatrix} \tag{2.103}$$

where

$$\sigma_{ij}^2 = \frac{1}{N_B+1}\sum_{i=1}^{N_B+1}(\mathbf{V}_i-\mu_B)(\mathbf{V}_j-\mu_B)^T \tag{2.104}$$

is the variance of the i^{th} dimension with j and N_B is the total number of bombarded particles [66].

The mean and covariance matrices can be estimated using momentum and energy conservation of both the rebounding particle and the ejected particles. Using momentum conservation, the momentum of the particle rebounding with velocity $\mathbf{V}_R$ will be equal to the momentum gained by N_B particles that are ejected through bombardment, i.e.,

$$m_R\mathbf{V}_R = \sum_{n=1}^{N_B+1} m_n\mathbf{V}_n \tag{2.105}$$

where V_n is the velocity of the n^{th} bombardment particle, and m_R and m_n are the masses of the rebounding and bombarded particles, respectively. In the present study, all particles were considered to have the same mass, i.e., $m_R = m_n$.

Using Eqs. 2.102 and 2.105, the mean μ_B of the velocity distribution can be written as

$$\mu_B = \frac{1}{N_B+1}\sum_{n=1}^{N_B+1}\mathbf{V}_n = \frac{\mathbf{V}_R}{N_B+1} \tag{2.106}$$

Furthermore, the conservation of the total kinetic energy of the rebounding particles gives

$$E_R = \frac{1}{2}m_R|\mathbf{V}_R|^2 = \frac{1}{2}\sum_{n=1}^{N_B+1} m_n|\mathbf{V}_n|^2 \tag{2.107}$$

where E_R is the total kinetic energy of the rebounding particle. Considering the covariance matrix

to be diagonal (i.e., neglecting the coupling between different dimensions in Eq. 2.103, then it can be written as

$$\Sigma_B = \begin{bmatrix} \sigma_{xx}^2 & 0 & 0 \\ 0 & \sigma_{yy}^2 & 0 \\ 0 & 0 & \sigma_{zz}^2 \end{bmatrix} \tag{2.108}$$

where σ_{xx}, σ_{yy}, and σ_{zz} are the variances along the x, y, and z directions, respectively. Using Eq 2.104, the variance along the x-direction becomes

$$\sigma_{xx}^2 = \frac{1}{N_B+1} \sum_{n=1}^{N_B+1} (V_{n_x} - \mu_{B_x})^2 = \frac{1}{N_B+1} \left(\sum_{n=1}^{N_B+1} V_{n_x}^2 - 2\mu_{B_x} \sum_{n=1}^{N_B+1} V_{n_x} + \mu_{B_x}^2 \right) \tag{2.109}$$

The first term in Eq. 2.109 can be assumed to be equal to the fraction of the total rebound kinetic energy (as given by Eq. 2.107) along the x-direction, which can be written as

$$\sum_{n=1}^{N_B+1} V_{n_x}^2 = E_R \frac{V_{R_x}^2}{V_{R_x}^2 + V_{R_y}^2 + V_{R_z}^2} \tag{2.110}$$

Similar expressions can be derived for the y and z dimensions. Using Eqs. 2.106 and 2.110 with Eq. 2.109 gives

$$\begin{aligned} \sigma_{xx}^2 &= \left(\frac{E_R}{N_B+1} \right) \frac{V_{R_x}^2}{V_{R_x}^2 + V_{R_y}^2 + V_{R_z}^2} - \frac{V_{R_x}^2}{(N_B+1)^2} \\ \sigma_{yy}^2 &= \left(\frac{E_R}{N_B+1} \right) \frac{V_{R_x}^2}{V_{R_x}^2 + V_{R_y}^2 + V_{R_z}^2} - \frac{V_{R_y}^2}{(N_B+1)^2} \\ \sigma_{zz}^2 &= \left(\frac{E_R}{N_B+1} \right) \frac{V_{R_x}^2}{V_{R_x}^2 + V_{R_y}^2 + V_{R_z}^2} - \frac{V_{R_z}^2}{(N_B+1)^2} \end{aligned} \tag{2.111}$$

Therefore, using the mean velocity, μ_B, given by Eq. 2.106 and the covariance matrix, Σ_B, given by terms of Eq. 2.111, the initial velocities of the bombarded particles can be found by using Eq. 2.101. In the present formulation, the initial position of the newly ejected particles are co-located at the point of impact, i.e., where the impacting particle interacts with the sediment bed.

2.11 Computational Considerations

One of the primary challenges in the numerical modeling of brownout clouds is the tracking of a very large number of suspended particles over the time scales characteristic of the actual flight maneuvers. A rotorcraft landing or takeoff maneuver can involve time scales that are measured in tens of seconds or hundreds of rotor revolutions. The most computationally expensive part of a brownout simulation is the computation of the induced velocity field. The cost of the induced velocity calculations is $O(N_v^2 + N_v N)$, where N_v is the total number of vortex elements, and N is the total number of particles in the brownout simulation. This cost may translate into weeks or months of computational time, depending upon the time scales of the maneuvers. To contain this cost, two approaches were considered in the present work, namely: (1) utilization of parallel hardware for high-performance computing, and (2) development of efficient algorithms to reduce computational costs.

In the first approach, the dust cloud simulation methodology was implemented in double-precision on graphic processor units (GPUs) by dividing and assigning particle data to each GPU thread and spawning a large number of similar threads. In this approach, the resulting CPU-GPU computations were nearly found to be 50 times faster without any loss of accuracy. Further details

on the specific implementation are given in Appendix B.

In the second approach, particle clustering [124] was used to reduce the high computational costs of convecting the particles. In this form of particle clustering, each cluster center is associated with a specified number of particles that have surrounding positions that are determined from a multi-variate Gaussian distribution relative to the velocity of the center of the cluster. Further details on clustering techniques are given in Appendix E.

2.12 Overall Methodology

The present work required the coupling of multiple models and techniques to represent various aspects of the brownout simulation. Figure 2.20 shows the various components of the overall methodology used in the present work. The methodology is are broadly classified into the techniques required to: 1. model the aerodynamic environment (blue), 2. mobilize and convect the sediment particles (yellow), and 3. expedite computations (orange). The sequence of steps in the simulation is as follows:

1. The fluid phase (i.e., carrier phase) of the flow field is first computed using the FVM and surface singularity method for the airframe.

    (a) The FVM computes the induced velocities on the rotor blades and wake from different sources in the flow field through repeated application of Biot–Savart law. The wake solution is then marched in space and time according to the PC2B scheme outlined previously in Section 2.5.1.

    (b) If a rotor operating at a different rotational speed is included in the simulation, such as

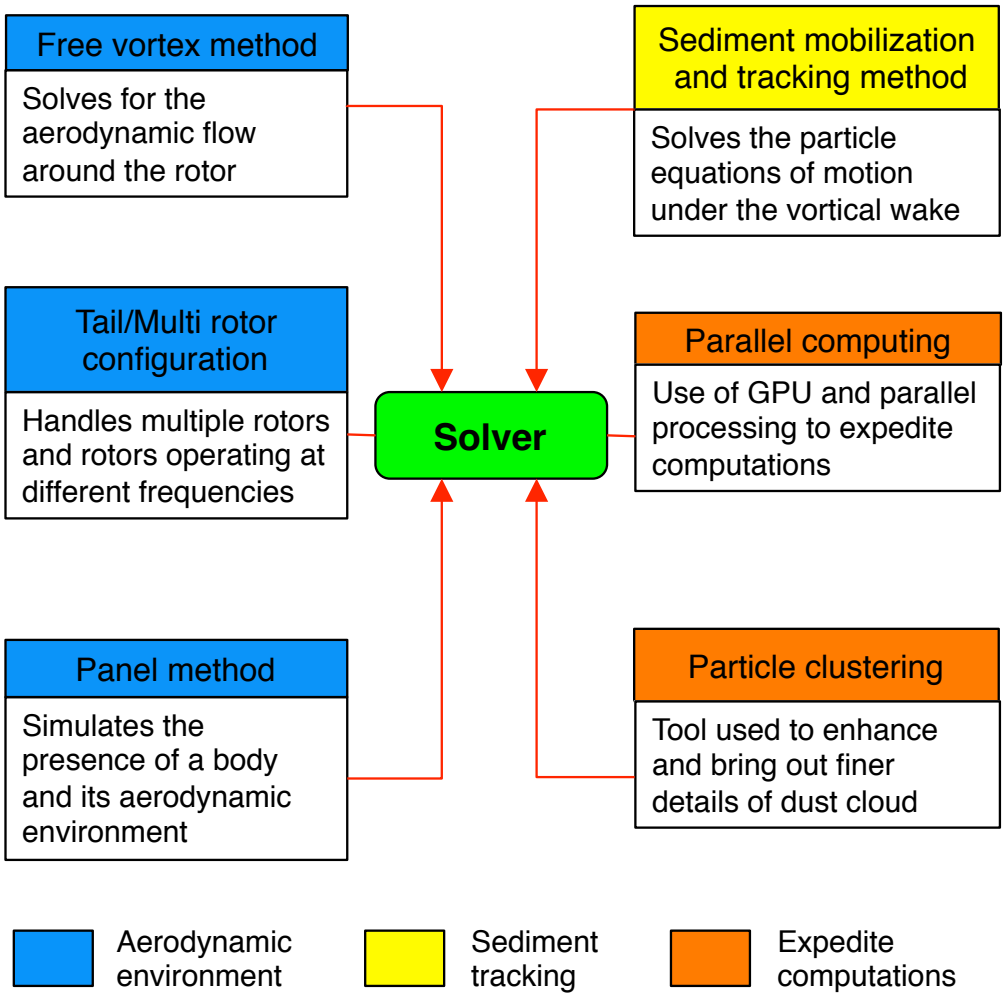

Figure 2.20: Flowchart showing the overall methodology used in the present work.

a tail rotor, the mutually induced effects of the two rotors are included and the wake solution is marched in time using the using the coupling strategy discussed previously in Section 2.5.4. This strategy ensures that the solutions from the main and tail rotor march equally in time.

(c) If a fuselage is included in the simulation, the aerodynamic effects of the fuselage are represented by the surface singularity method described previously in Section 2.6. The influence of the fuselage and the solution from the FVM is tightly coupled such that the mutually induced velocities are updated at every time step of the aerodynamic solution.

(d) The induced velocity computations of the vortex filaments rotor wakes and the panels of the fuselage are parallelized using GPUs. This hardware acceleration reduced the computational cost by an order of magnitude compared to serial processing on a CPU.

2. The dust phase (i.e., the carrier phase) is simulated based on the carrier phase solution previously computed. Notice that because a one-way coupling is assumed (i.e., only the fluid phase affects the carrier phase), Steps 1(a)–1(d) can be performed independent of the dust phase computations.

(a) The sediment tracking methodology described previously in Section 2.9 evaluates the sediment mobility conditions based on the velocity and pressure field at the surface of the sediment bed. The particles are then convected under the action of the vortical wake according to the BBO equations. Further particles may be entrained into the flow as a result of particle bombardment ejections.

(b) Because the number of sediment particles entrained into the flow are of the order of millions, the sediment code is executed in parallel on GPUs to reduce the computational time.

3. After the fluid and dust phases are computed, particle clustering techniques (discussed in Section E) are used to enchance the features of the dust cloud and bring out the finer details in the cloud. The clustering is performed as a post-processing procedure.

2.12.1 Assumptions in the Methodology

The following assumptions and simplifications have been made in the modeling of the different components of the methodology to facilitate the study of an inherently complex problem such as rotorcraft brownout. Throughout the present work, the use of these assumptions have been justified and it has been shown that the overall methodology retains the key features and physics of the problem. Extensive validation against available experimental data of the different components of the methodology are presented in Chapter 3, which lends confidence in the techniques used in the present work.

1. Rotor and airframe modeling:

   (a) The rotor comprises of rigid blades and do not account for elastic deformations.

   (b) The blade flapping dynamics and the associated rotor responses are incorporated, while lag and torsional dynamics of the rotor blades are not represented.

   (c) The flow remains attached over the surface of the fuselage and the current formulation

of the panel method does not include flow separation effects.

2. Trim solution:

   (a) A sequential trim procedure is performed for the single main rotor and tail rotor with the trim for the main rotor being performed such that the rotor tip path plane is perpendicular to the rotor shaft axis. The rigid body dynamics of the body are not represented and a fully coupled free-flight trim is not performed.

   (b) The tail rotor thrust is determined based on yawing moment balance.

   (c) The landing trajectory is prescribed to the rotor hub and not the aircraft center of gravity.

3. Dust cloud modeling:

   (a) A one-way coupling strategy was assumed, i.e., the carrier phase affects the dispersed phase but not vice versa.

   (b) The near-wall flow was approximated using a logarithmic boundary layer profile to provide a better representation of the flow velocities at the ground.

   (c) Spherical particles were assumed, which do not rotate, deform, or disintegrate.

   (d) Effects of particle/particle collision and blade/particle collisions were not modeled.

2.13 Summary

The present chapter has focussed on the development and integration of various methodologies to predict the aerodynamic environment and the resulting dust clouds produced by different rotor and rotor/airframe configuration when operating in ground effect over a mobile sediment bed. The main components of the methodology included: modeling of rotor flows from multiple rotors in ground effect, modeling of a secondary rotor (tail rotor) that operates at a different rotational frequency to that of the main rotor, representing the aerodynamic influence of the fuselage using surface singularity techniques, representation of the viscous flow near the ground, modeling the onset of particle mobility, and modeling other particle entrainment mechanisms, such as bombardment that is known to occur in brownout conditions.

The rotor flow field was modeled using a time-accurate free-vortex method (FVM) based on the assumptions of a inviscid and incompressible flow, which was discussed in Section 2.5. In this method, the blade aerodynamics were modeled using a Weissinger-L model, which solved for the bound vortex circulation strengths by enforcing flow tangency at the blade control point. The trailed circulation from the blade was modeled as a full span planar near-wake that rolled up into a single tip vortex filament at the blade tip. The strength of the tip vortices were calculated, which is related to the maximum spanwise circulation on the blade. The curved tip vortex filaments were approximated using straight-line segments of uniform vortex strength and the induced velocity at a target point was evaluated using repeated computation of the Biot–Savart law. Effects of filament diffusion and stretching were accounted for using a semi-empirical viscous core growth model. The governing convection equation was numerically solved using an implicit, second-order,

predictor-correction backward scheme; this scheme contained a fourth-order artificial dissipation term to improve numerical stability and convergence. The aerodynamic influence of the ground was modeled using an image system, which universally enforces flow tangency along the ground plane.

The modeling of a secondary rotor, i.e., operating at a rotational frequency different to that of the main rotor was performed using the FVM, as discussed in Section 2.5.4. Because the governing equations of the FVM are expressed in rotor time, the solutions for two rotors (main and tail) could potentially march through time at different time steps. Therefore, to synchronize in time the solutions of the two rotors, a coupling strategy was developed that allowed for information (i.e., vortex strengths and positions) to be exchanged between the two rotors at pre-determined intervals. The vortex positions and strengths were interpolated as opposed to the interpolation of the induced velocities because the former strategy results in lower errors. The collective pitch on the tail rotor was trimmed such that the torque produced by the tail rotor thrust about the main rotor hub counteracted the main rotor torque.

A surface singularity techniques was used to model the fuselage, which has been discussed previously in Section 2.6. Quadrilateral panels of constant source strengths were used to represent the surface of the fuselage and the strengths of these panels were evaluated by enforcing flow tangency conditions on the panel control point. Because the no-penetration condition was enforced on discrete points on the fuselage surface, prescribed rules were also used to prevent vortex filaments from convecting into the interior of the fuselage. An unsteady panel formulation was also included to more accurately represent the unsteady and aperiodic flow environment; the unsteady changes

in surface pressure accounted for convection of vortices and the change in panel strength by using the unsteady Bernoulli equation.

The overall flow computed by the FVM is inviscid and violated the no-slip boundary condition at the ground plane. Therefore, flow conditions near the ground were computed using certain approximations. An inviscid-viscous matching technique was discussed in Section 2.8, in which the inviscid flow predicted by the FVM is coupled at the interface, and the flow from the edge of the interface to the ground was approximated by using a logarithmic boundary layer profile. This inviscid-viscous approach was then used to estimate the friction velocity on the bed, which in turn was used to predict the onset of sediment mobility.

The mobilization of particles from the sediment bed under the action of shear, gravitational, pressure and inter-particle forces was discussed previously in Section 2.9. The particles are mobilized when the aerodynamic forces acting on them exceed the gravitational and inter-particle forces. A sediment mobility model was developed by solving for the moment equilibrium at each particle from all the forces acting upon it. The motion of the uplifted particles was tracked by solving the particle equations of the motion. The two-phase problem was assumed to be one-way coupled, i.e., the position and convection of sediment particles did not affect the flow. These assumptions were used to decouple the equations of motion along the three spatial directions, which were then solved using an implicit, second-order, backward difference time marching scheme under the assumptions of a Stokes-like flow.

Previously suspended particles can impact the bed, lose part of its kinetic energy, which can then eject many more particles from the sediment bed. This process, known as bombardment

ejection, was discussed in Section 2.10. In this model, the volume of the crater formed on the bed was used to approximate the quantity of ejected particles. The spatial positioning of the ejected particles was determined by using a multi-variate Gaussian distribution. The mean and variance of the distribution were calculated by solving for the conservation of momentum and energy of the impacting and the ejected particles.

Because of the very large number of particles required to model the brownout dust clouds, the present methodology was designed to be implemented on GPUs, as discussed previously in Section 2.11. A Gaussian-based particle clustering techniques was used to contain the computational costs of the simulation and to enhance the features of the dust cloud without any loss in the accuracy of the actual solution.

Chapter 3

Results and Discussion

The free-vortex methodology (FVM), as described in the previous chapter, has been developed to handle arbitrary, non-steady flight conditions and fairly general rotor geometries. It has been extended in the present research to simulate the aerodynamic environment around sets of rotors that are operating at different rotational frequencies, e.g., a main rotor and a tail rotor. Furthermore, an unsteady surface singularity method has been coupled to the FVM to model fuselage shapes so as to provide a more comprehensive overall modeling tool that can potentially aid in further understanding the problem of rotorcraft brownout. The brownout dust cloud methodology used in the present work has made advancements over existing methodologies, and includes detailed numerical models to simulate the processes of sediment mobilization and uplift as well as particle bombardment. The modeling of these physical processes also increases significantly the numerical complexity of the methodology, and techniques have been adopted to minimize these computational costs.

The first part of the present chapter discusses selected validation results of the different components used in the brownout simulation methodology. In the second part, representative results of the aerodynamic effects of the fuselage and the tail rotor on the main rotor wake are shown, along with their effects on the velocities induced on the ground. The simulations are then used to predict brownout dust clouds for different rotor/rotor and rotor/fuselage combinations

during a simulated landing flight maneuver. Analyses were conducted to trace the development of the flow field and the dust clouds for the different configurations. Finally, metrics were developed and used to help quantify the severity of the different brownout clouds to understand the role of the fuselage and rotor combinations, and also to explore aspects of brownout mitigation.

3.1 Comparison with Measurements

This section presents results from studies conducted to validate the brownout methodology. However, a prerequisite is the validation of the rotor flow in ground effect operations. Although performance results from the FVM model for ground effect conditions have been previously validated [89,108], the present work focuses on the prediction of the wake structure and flow velocities closer to the ground. To this end, several studies were conducted for laboratory-scale and full-scale rotors. Furthermore, studies were conducted to establish the efficacy of the panel method used to model the fuselage, and the influence of the fuselage shape on rotor performance and wake structure.

3.1.1 Validation of Free Vortex Method

The flow field produced beneath a helicopter is a largely complex, three-dimensional, aperiodic, and unsteady flow. If the helicopter is operating close to the ground, this flow field is further complicated by the presence of the ground, which causes the pronounced stretching and straining of the vortical elements and can result in increased turbulence of the flow near the ground; see Fig. 1.6 in Chapter 1. Accurate predictions of the flow environment around a helicopter requires

validation with experimental data that accurately captures all of the varying flow physics. Because of the challenges involved in making such measurements, there are currently no measurements for full-scale rotorcraft that provides a comprehensive data set against with numerical predictions can be validated. However, there exist experimental measurements of rotor performance and flow fields for different laboratory-scale rotors, and these data have been used in the present study to validate the FVM.

3.1.1.1 Laboratory-Scale Rotor

Flow field measurements were conducted by Lee et al. (Ref. 19) using a small rotor hovering in ground effect at various heights above the ground using particle imaging velocimetry (PIV). The details of this rotor are given in Table F.1 in Appendix F. The airfoil for these blades was a circular-arc of thickness of 3.7% and a camber of 3.3% of the blade chord. Kalra et al [56] also compared these measurements using a RANS based CFD solver, and overall good agreement with measurements were obtained. In the present work, the measurements from Lee et al. [30] and the CFD calculations from Kalra et al. [56] were both used to validate the results obtained from the FVM.

Figure 3.1 shows the vertical and radial displacements of the tip vortices in hovering flight at $z/R = 1$ as a function of wake age predicted by the FVM and by the CFD. The tip vortex trajectories predicted by the FVM show a somewhat larger radial contraction when compared to the CFD, however, overall the agreement is still acceptable. As the tip vortices approach the ground, notice the significant radial expansion and stretching of the filaments, as shown in Fig. 3.1(c).

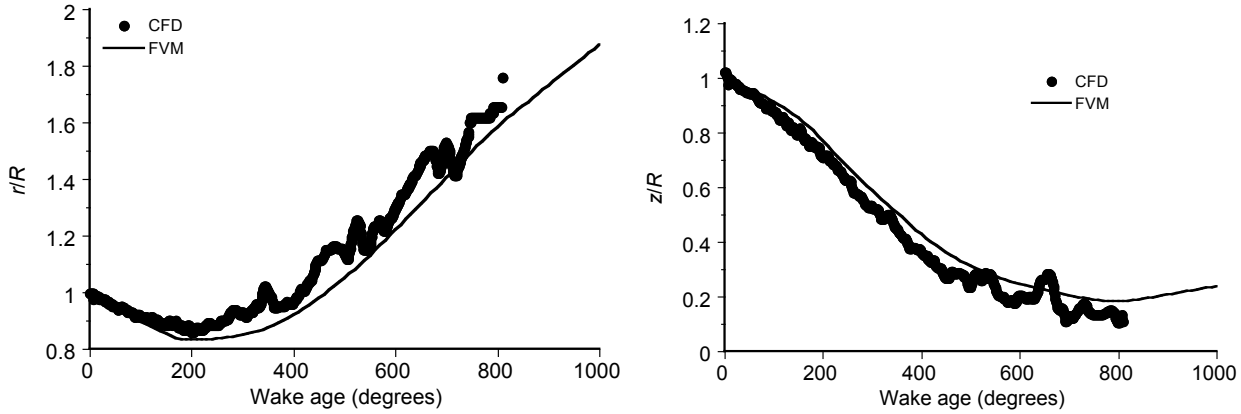

(a) Radial displacements versus wake age

(b) Vertical displacements versus wake age

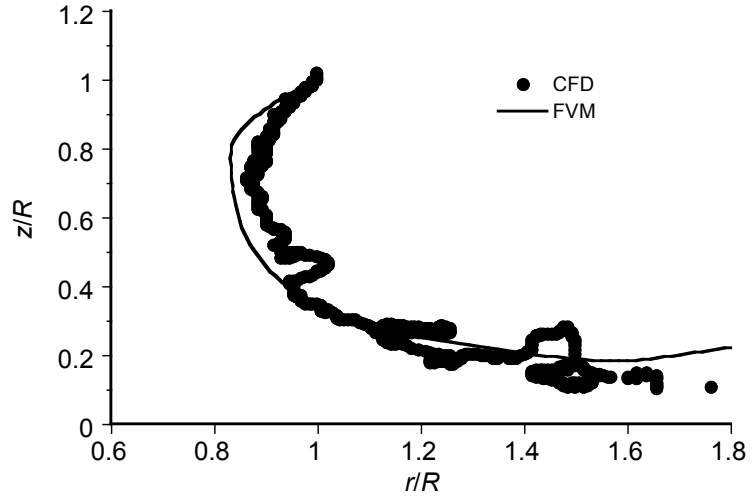

(c) Wake boundary

Figure 3.1: FVM and CFD predictions for the: (a) radial displacement, (b) vertical displacement, and (c) wake boundary, of the tip vortices with wake age for the laboratory-scale rotor hovering in ground effect at $z/R = 1$.

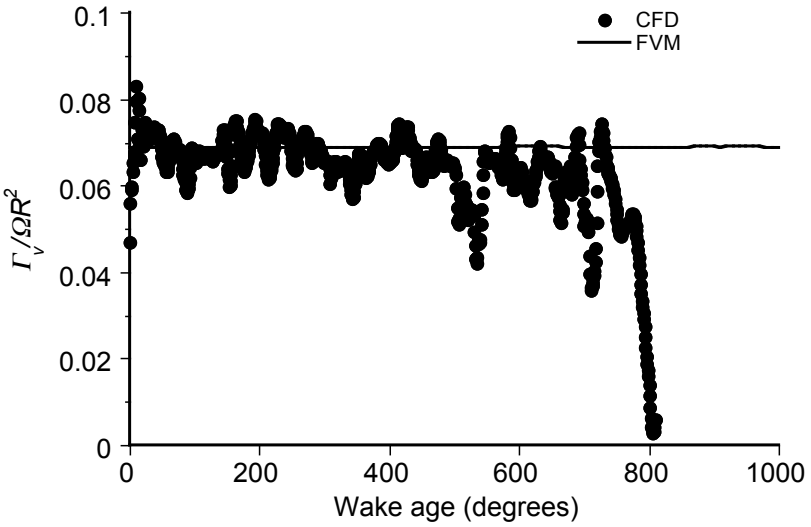

(a) Tip vortex strength versus wake age

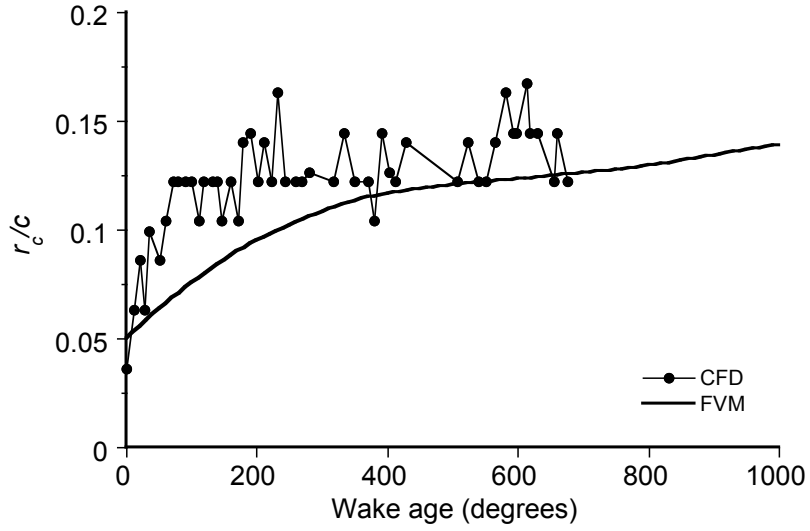

(b) Core radius versus wake age

Figure 3.2: FVM and CFD predictions for the normalized: (a) tip vortex strength, and (b) core radius, versus wake age for a rotor hovering in ground effect at $z/R = 1$.

A further comparison of the corresponding tip vortex strength and core radius versus wake age is shown in Fig. 3.2. Extracting the tip vortex strengths and core radii from the PIV measurements is challenging and, therefore, in the present study the predictions from FVM and CFD were compared against each other. The predictions of the vortex strength were found to agree well with each other, as shown in Fig. 3.2(a). Notice that the CFD predicts somewhat a larger core radius at earlier wake ages than that of the semi-empirical model of the FVM, as shown in Fig. 3.2(b). The effects of turbulence from the merging of wake sheets, eddies, relaminarization of vortex core, etc., are modeled in the FVM by using the semi-empirical core growth model (described previously in Section 2.5.2), which has been derived from both full-scale as well as model-scale rotary-wing measurements. The larger value of r_c predicted by the CFD results can be attributed to the effects of grid size, i.e., the use of coarser grids in CFD can result in artificial dissipation of vorticity that can result in a somewhat larger core radius. In fact, the sensitivity of the CFD results on grid size, especially as it affects the core radius, were shown in the work by Kalra et al. [56], and refining the grid size reduced the value of the predicted core radius.

Figure 3.3 shows predictions of the time-averaged radial velocity profiles from the FVM and CFD against the measurements of Lee et al. [30] for r/R = 0.8, 1.0, 1.25, 1.5, 1.75, and 2.0, where r is the radial distance from the rotational axis. The velocities were normalized by the rotor hover induced velocity, i.e., $v_h = \sqrt{T/2\rho A}$ where T/A is the rotor disk loading (measured), and the wall-normal distance, z, was non-dimensionalized by the rotor radius, R. The resultsin Fig. 3.3 shows the formation of a wall-jet, which decreases in height with increasing distance from the rotational axis. The magnitude of the wall-jet increases to a maximum of $2v_h$ at $r/R = 1.5$ (Fig. 3.3(d)) and then

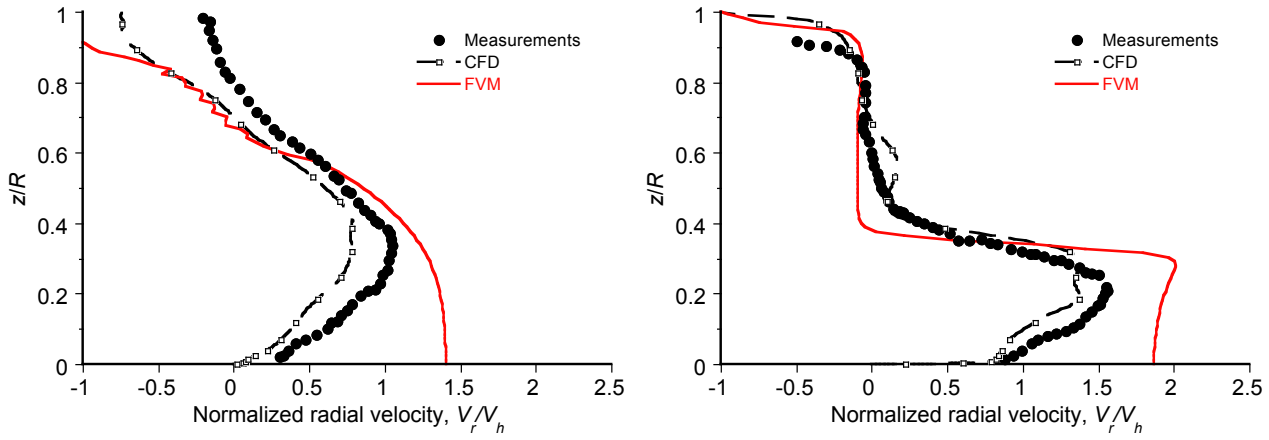

(a) $r/R = 0.80$

(b) $r/R = 1.00$

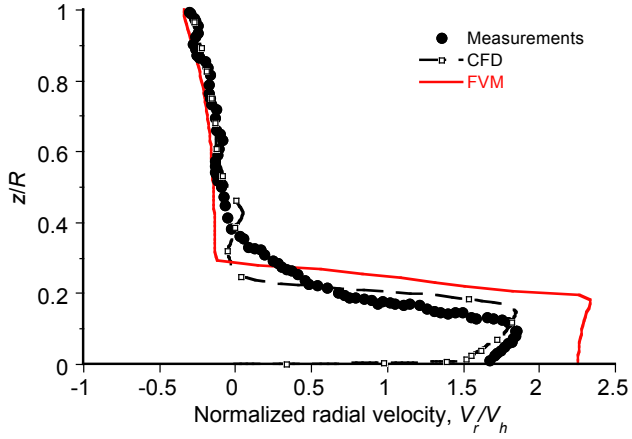

(c) $r/R = 1.25$

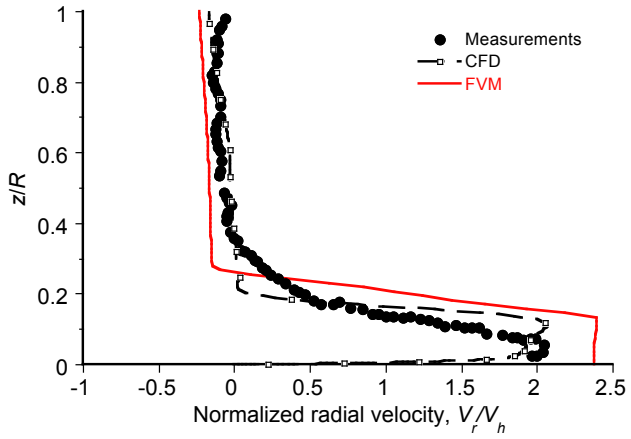

(d) $r/R = 1.50$

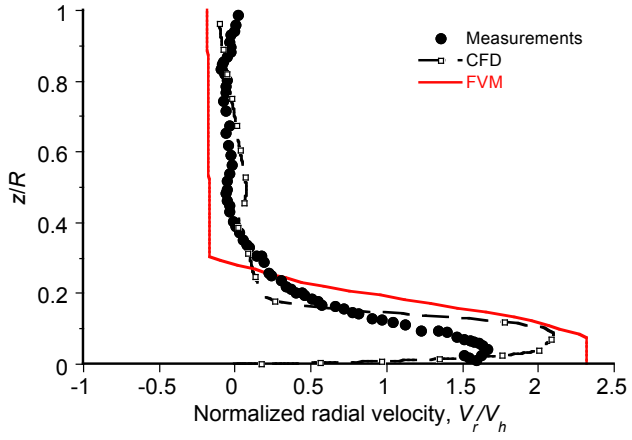

(e) $r/R = 1.75$

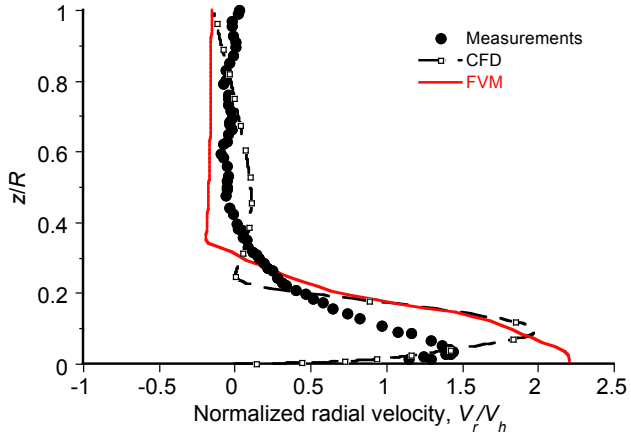

(f) $r/R = 2.00$

Figure 3.3: Variation of the time-averaged radial velocity profiles at: (a) $r/R = 0.8$, (b) $r/R = 1.0$, (c) $r/R = 1.25$, (d) $r/R = 1.5$, (e) $r/R = 1.75$, and (f) $r/R = 2.0$, versus normalized height above the ground, as obtained from experiments, CFD, and the FVM.

decreases at greater radial distances. Away from the ground, there is reasonable agreement between the predictions from the FVM and the measurements. At greater radial downstream distances, both the CFD and the FVM overpredict the radial velocities of the wall-jet. In particular, notice that the radial velocity predicted by the FVM does not satisfy the no-slip condition, which is because the FVM is an inviscid model. Therefore, a representation of the flow field closer to the ground was made by assuming a logarithmic boundary layer profile, as explained previously in Section 2.8. In this approximation, the magnitude of the maximum wall-jet velocity and the height at which it occurs, are correlated to the flow velocity at the edge of the boundary layer and the height of the boundary layer, respectively. The boundary layer height is highly dependent on the induced flow velocities on the ground and varies at different locations over the ground [8, 33]. Because of the difficulty in extracting the variation of boundary layer height from experiments, an assumed boundary layer profile was used in the present work, as was discussed in Section 2.8.

The accurate modeling of the viscous region can only be achieved by either using a full viscous solution (e.g., Kalra et al. [56]), or by a coupling the FVM with a viscous CFD solution in the immediate region of the ground (e.g., Thomas et al. [72, 125]). However, these techniques significantly increase the computational cost of the aerodynamic solutions and the use of these methodologies is currently limited to simulations in hover.

The present work also involves simulating the brownout environment for multi-rotor helicopter platforms. However, experimental measurements of rotor performance and wake geometries are very limited for multiple rotors, but with more studies focusing on the performance of coaxial rotor systems; see Coleman [126] for a review. Harrington [127] performed measurements

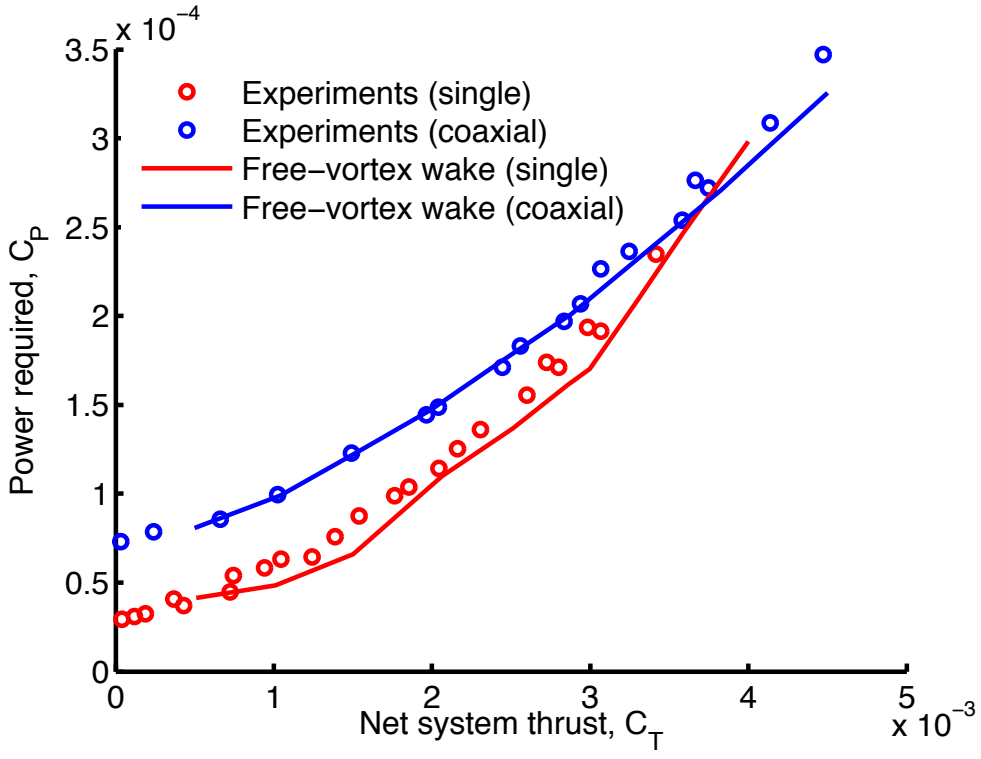

Figure 3.4: Predictions of the power requirements of for a coaxial rotor configuration as a function of the system thrust.

of the rotor thrust and power of a coaxial rotor system; the rotor specifications of this coaxial system is given in Table F.6 of Appendix F. Figure 3.4 shows the predictions of the required power as a function of the net system thrust for the Harrington rotor along with the measured values. The results from the FVM show good agreement with the measurements; any differences between the experiments and the FVM can be attributed to the more complex aerodynamic interactions between the upper and lower rotors of the coaxial, beyond those shown in Fig. 3.5.

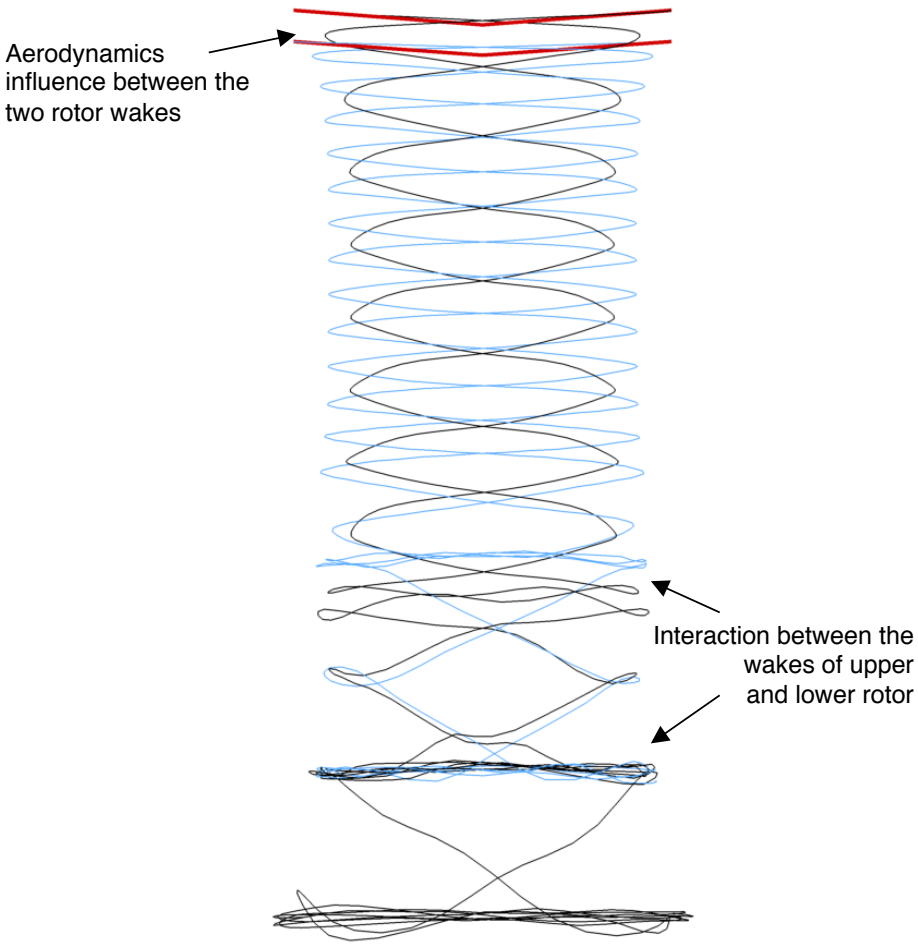

Figure 3.5: Wake geometry of the coaxial rotor.

3.1.1.2 Full-Scale Rotor in Ground Effect

Measurements of groundwash velocities were made by Leese et al. [128] for several full-scale helicopters, which were used to compare to the FVM predictions. Out of the seven helicopters, the two examined in the present work were the CH-54 and the UH-1M. The rotor specifications for the CH-54 and UH-1M are given in Tables F.4 and F.5 of Appendix F, respectively. Only the isolated rotors were modeled in this comparison study. The velocity measurements were made using a number of horizontal wind-velocity sensors (turbine anemometers), that were mounted vertically along a stand, and were capable of sensing the groundwash velocities up to 6 ft above the ground surface [128]. These sensors were fitted with small induction generators whose electrical output was proportional to the rotational frequency of the anemometer propellers and were calibrated in a wind tunnel.

Figure 3.6 shows the time-averaged groundwash velocities at 0.3 ft above the ground as produced by the CH54 rotor when it was hovering at 40 ft and 80 ft off the ground. Similarly, Fig. 3.7 shows the time-averaged velocities at 0.3 ft above the ground produced by the UH-1M rotor when it was hovering at 44 ft above the ground. The results show that velocity field predictions from the FVM (which modeled only the main rotor wake in this case) are in good agreement with the measurements, especially in terms of the peak values and the radial locations at which they were attained. Notice from Figs. 3.6 and 3.7 that the peak flow velocities at the ground occurred just outside of the diameter of the rotor disk, and then decreased quickly as the rotor wake expanded radially over the ground. Away from the rotor, the flow velocities along the ground are under-predicted by the FVM compared to the measurements.

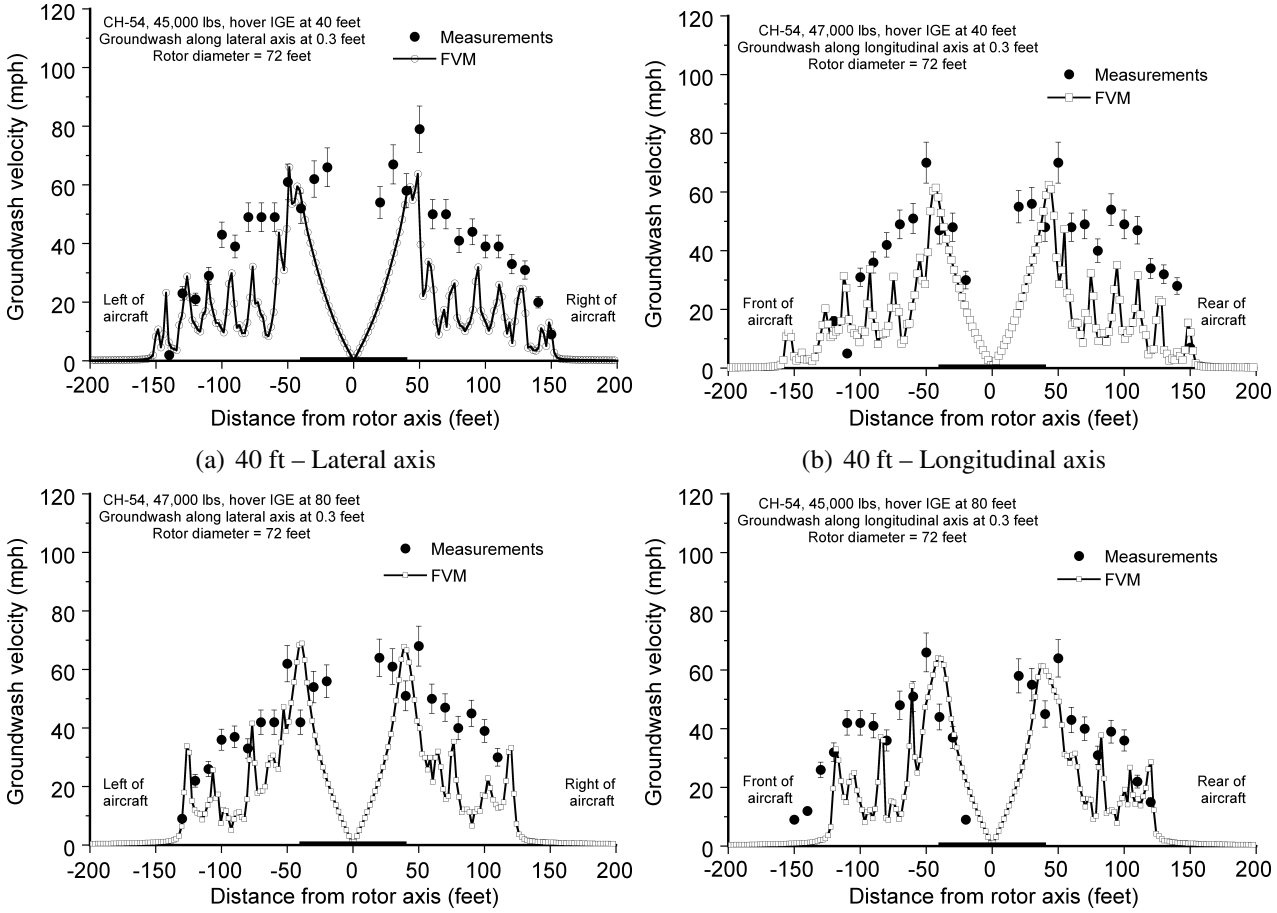

(a) 40 ft – Lateral axis

(b) 40 ft – Longitudinal axis

(c) 80 ft – Lateral axis

(d) 80 ft – Longitudinal axis

Figure 3.6: Variation of time-averaged groundwash velocity at 0.3 ft above the ground for a CH-54 helicopter hovering at: (a) 40 ft along the lateral axis, (b) 40 ft along longitudinal axis, (c) 80 ft along the lateral axis, and (d) 80 ft along longitudinal axis.

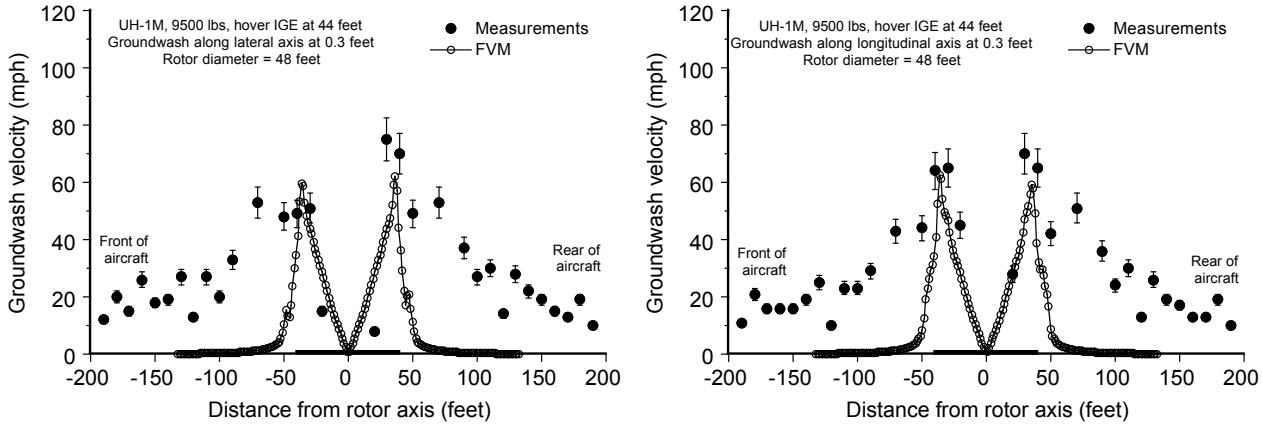

(a) Lateral axis

(b) Longitudinal axis

Figure 3.7: Variation of time-averaged groundwash velocity at 0.3 ft above the ground for a CH-54 helicopter hovering at 44 ft along the: (a) 40 ft along the lateral axis, and (b) 40 ft along longitudinal axis.

While some differences will inevitably arise because of the limitations inherent to the aerodynamic modeling, it should be recognized that the nature of the sensors used in this case means that the measurements themselves were only approximate. The measurements were affect, in part, because of the inertia of the propeller and the generator used in the wind-velocity sensors, which requires a finite amount of time to re-adjust to the unsteady local flow velocities. The aperiodic and unsteady nature of the flow field beneath a helicopter coupled with the inherent inertial lag in the sensors may also result in errors in the velocity measurements. Furthermore, the vertical placement of the sensors can cause interference effects in the flow field that were not accounted for in the measurements, which could further help explain the differences in the flow velocities between the FVM and the measurement data.

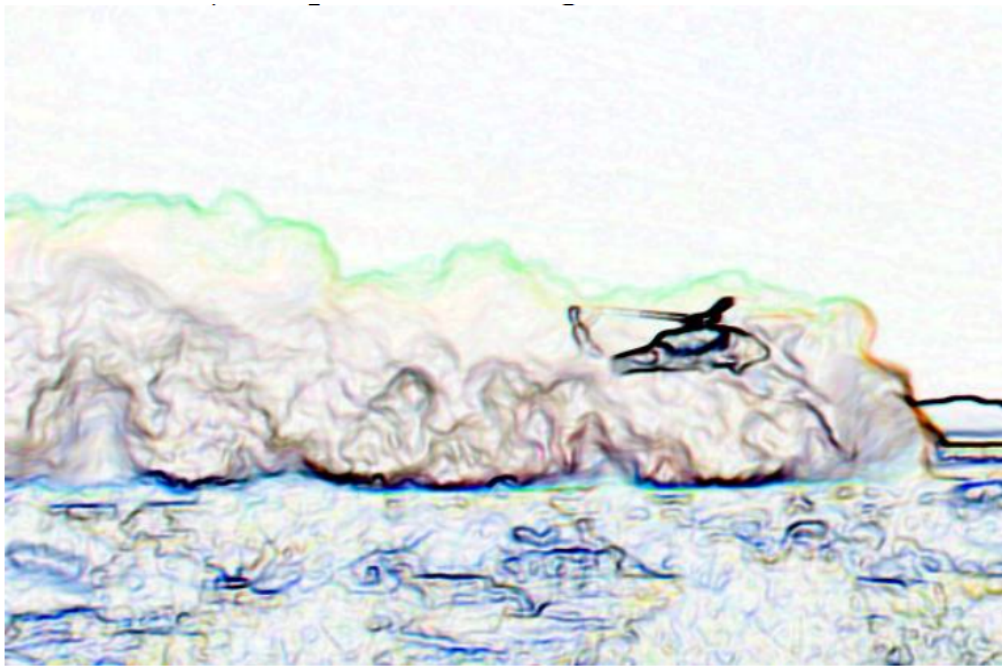

Figure 3.8: Processed image of the brownout cloud obtained through photogrammetry technique highlighting the structures and the envelope of the cloud (Source: Tanner [10]).

3.1.1.3 Comparison of Predicted Dust Clouds to Measurements

Validation of the predicted brownout dust clouds with measurements is very difficult because of the dearth of actual measurements of any type. However, Wong & Tanner [38] have conducted photogrammetry studies to obtain measurements of the sizes and shapes of the brownout dust clouds that were generated by a full-scale utility helicopter during taxi-pass and approach-to-touchdown maneuvers. Although not all of the data required to validate the numerical simulations were measured or were otherwise available, these measurements were used in the present work to help establish confidence in the predictive capabilities of the current model. In this photogrammetry method, accurate measurements of the external dimensions of a developing brownout cloud were extracted through synchronized images from different locations on the ground. Tanner [10]

used image processing techniques to isolate key external geometric features of the brownout cloud, particularly the presence of columnar features; see Fig. 3.8. The essential characteristics of the helicopter are given in Table F.7 of Appendix F.

Figure 3.9 shows the particle positions predicted by the FVM (Section 2.5) combined with the sediment tracking algorithm (Section 2.9) compared to the photogrammetric measurements of the outside envelopes of the dust clouds. These results were measured at t = 0, 4, 10, and 22 s during a taxi-pass maneuver where the helicopter flew at a relatively constant airspeed and altitude above the ground. While the exact weight of the helicopter was not available, it was estimated based on initial fuel load and flight time to the test to be between 14,500 and 16,300 lb. The simulated dust clouds at different times during a taxi-pass maneuver are shown in Fig. 3.9. Although there is relatively good agreement with measurements in the top (plan) view, it can be seen that in the side view that the vertical extent of the cloud is somewhat underpredicted by the simulation. Nevertheless, bearing in mind the complexity of the brownout problem the results from this type of modeling are to the level that parametric studies can be attempted.

3.1.2 Validation of the Unsteady Panel Method

Validation of the panel method was undertaken by comparison of flow over a sphere, an isolated fuselage in freestream, and with a fuselage beneath an operating rotor. Surface pressure measurements, rotor performance metrics and wake trajectories were used to compare the capabilities of the panel method with the measurements.

The flow over a sphere is a convenient test case because the exact solution is available for

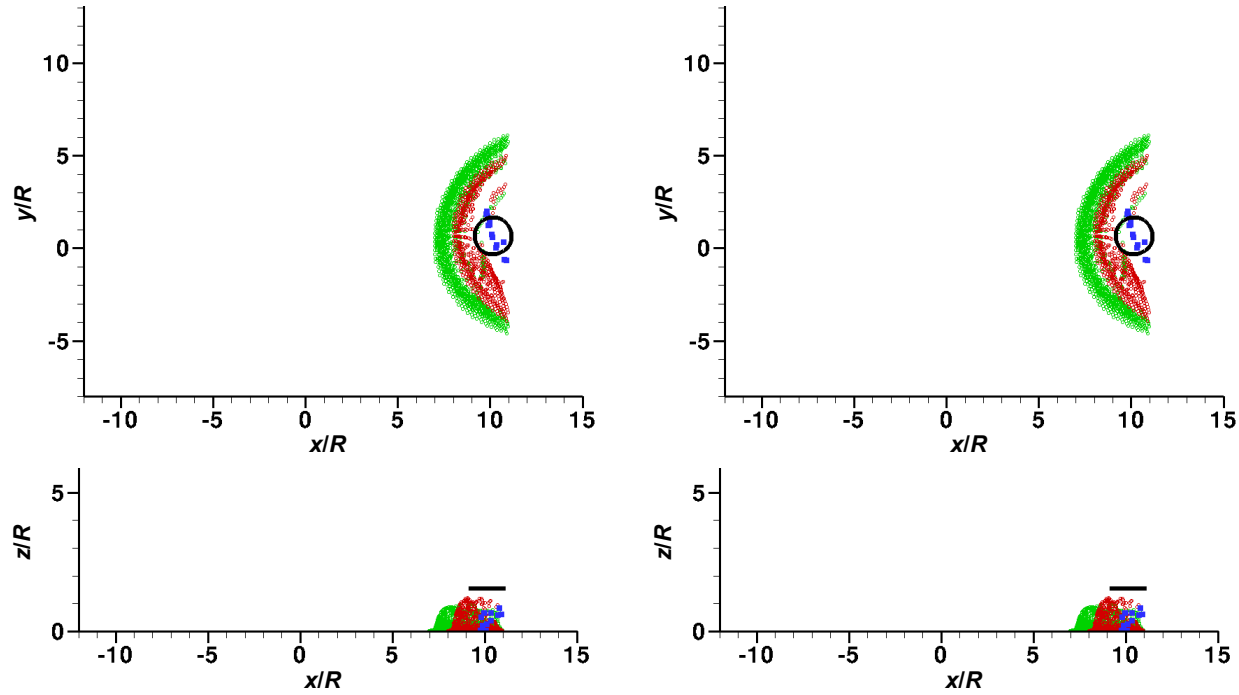

(a) Top and side view at $t = 0$ s

(b) Top and side view at $t = 4$ s

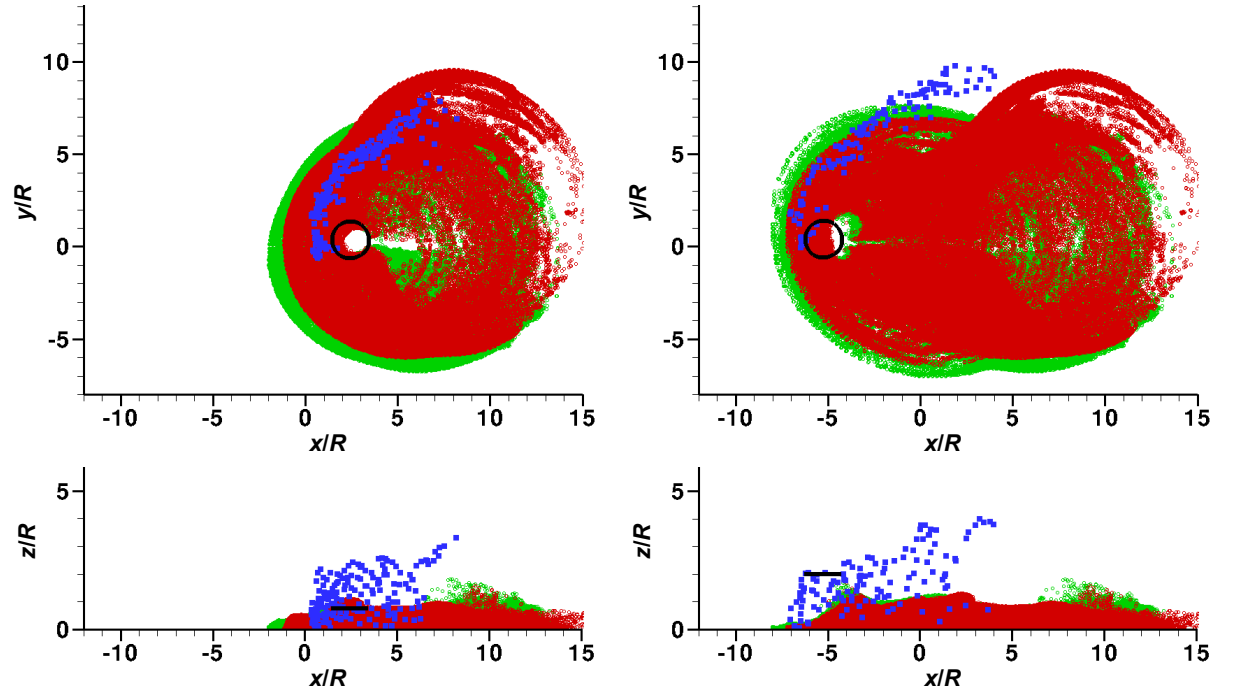

(c) Top and side view at $t = 10$ s

(d) Top and side view at $t = 22$ s

Figure 3.9: Comparison of the predicted dust clouds for weights of 14,500 lbs (shown in red) and 16,300 lbs (shown in green) with photogrammetric measurements (shown in blue) for the taxi-pass maneuver at t = 0, 4, 10, and 22 s.

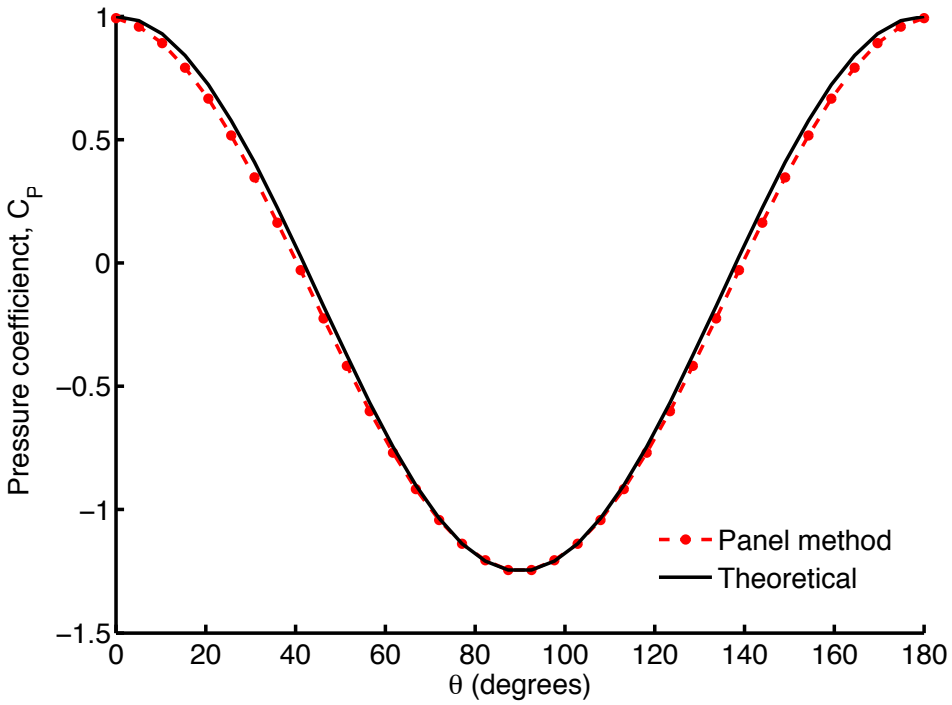

Figure 3.10: Pressure distribution on the surface of a sphere.

potential flow using a three-dimensional doublet singularity in a steady and uniform freestream. The pressure distribution on a sphere in uniform flow is well known (see Krishnamurthy [92]) and is given by

$$C_p(\theta) = 1 - \frac{9}{4}\sin^2\theta \tag{3.1}$$

where θ is the angle measured from the axis aligned to the freestream and C_p is the non-dimensional pressure.

Figure 3.10 shows the pressure distribution over the surface of a sphere obtained using the exact theoretical result and the predictions of the panel method. A total of 882 panels were used with 50 panels in the streamwise direction and 36 panels distributed around the circumference. The calculated pressure distribution show excellent agreement with the exact solution. Another impor-

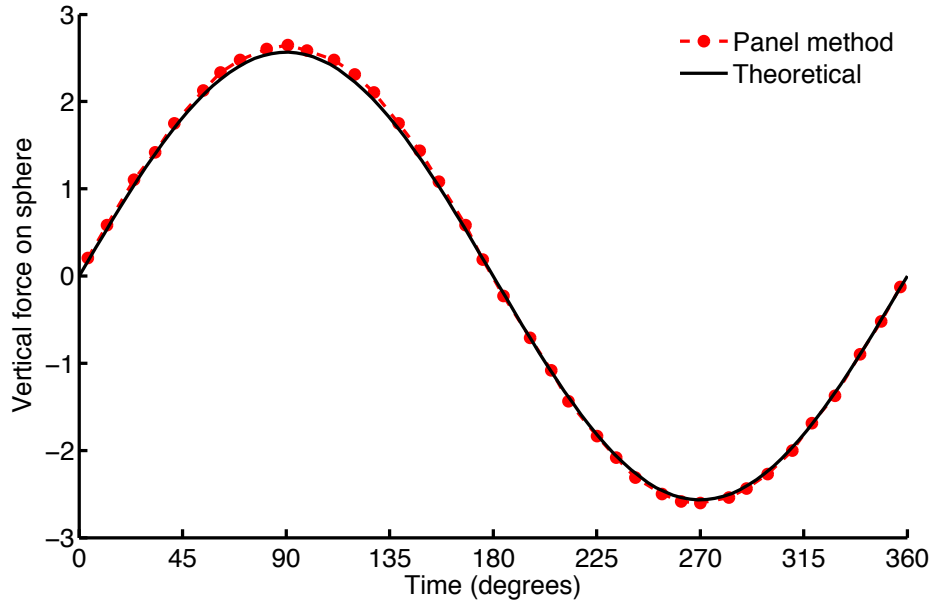

Figure 3.11: Time history of unsteady force on an osciallating sphere.

tant aspect of the panel model is the calculation of unsteady forces. The exact solution to a sphere undergoing a plunge motion can be derived from potential theory [92], i.e., the noncirculatory (apparent mass) force on a sphere in an oscillating flow is

$$F = -\frac{2}{3}\pi\rho R^3 \left(\frac{\partial V}{\partial t}\right) \tag{3.2}$$

where R is the radius of the sphere and $\partial V/\partial t$ is the time-rate of change of the fluid velocity. For the onset velocity specified as $V = V_\infty + \bar{h}\omega\cos\omega t$, where V_∞ is the freestream velocity, this oscillating apparent mass force is

$$F = 2\pi\rho R^3 \bar{h}\omega^2 \sin\omega t \tag{3.3}$$

which for incompressible flows is in-phase with the velocity fluctuations.

Figure 3.11 shows the time-history of the noncirculatory force (from Eq. 3.3), and the results

are compared with the computed results from the panel method for one period of oscillation. For this test case, the values, $R = 1$ m, $\overline{h} = 1$ m, $\omega = 1$ rad s^{-1} and a time step $\Delta t = 0.05$ s were used.Similar to the previous test case, the total number of panels used to represent the sphere were 882. As with the pressure distribution shown previously in Fig. 3.10, the comparison with the exact result is excellent.

Figures 3.12(a) and 3.12(b) show the variation in the amplitude and phase, respectively, of the vertical force (apparent mass force) computed using the panel method and the theoretical solution for an sphere oscillating at different frequencies. Figure 3.12(a) shows that the predictions in the maximum vertical force using the panel method agreed well with the theoretical results (Eq. 3.3), with the error in the maximum vertical force using the panel method being only 2.7% of the theoretical result at $\omega = 5$ rad s^{-1}. However, there was an increase in the phase lag in the computed solution compared to the theoretical results, as shown in Fig. 3.12(b), with the phase lag being 7° at an $\omega = 5$rad s^{-1}.

Validation of the surface singularity method was also undertaken using the slender AGARD body (i.e., a simplified helicopter fuselage) standard test case [129]. Pressure measurement on the fuselage surface was obtained in a isolation, i.e., in the absence of a rotor. The incoming flow was of uniform velocity at a zero angle-of-attack to the fuselage centerline. A panel representation of the AGARD fuselage, consisting of 1,400 panels, is shown in Fig. 3.13. Figure 3.14 shows the variation of pressure coefficient against longitudinal distance along body when the rotor was operating in hover. Each color represents the data from the pressure taps installed on the three sides of the AGARD body. The results were found to be in good agreement with the measured data, but

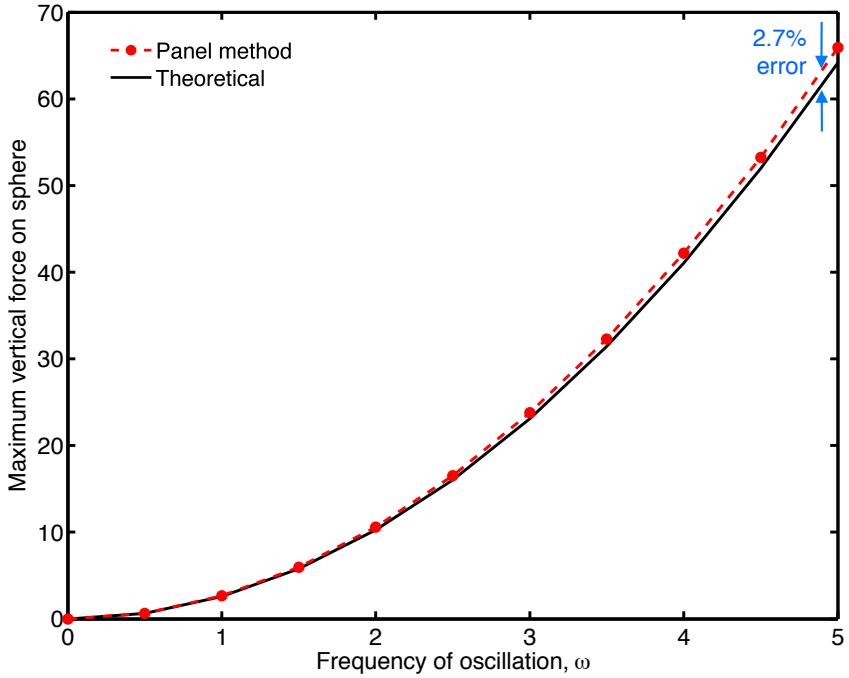

(a) Amplitude

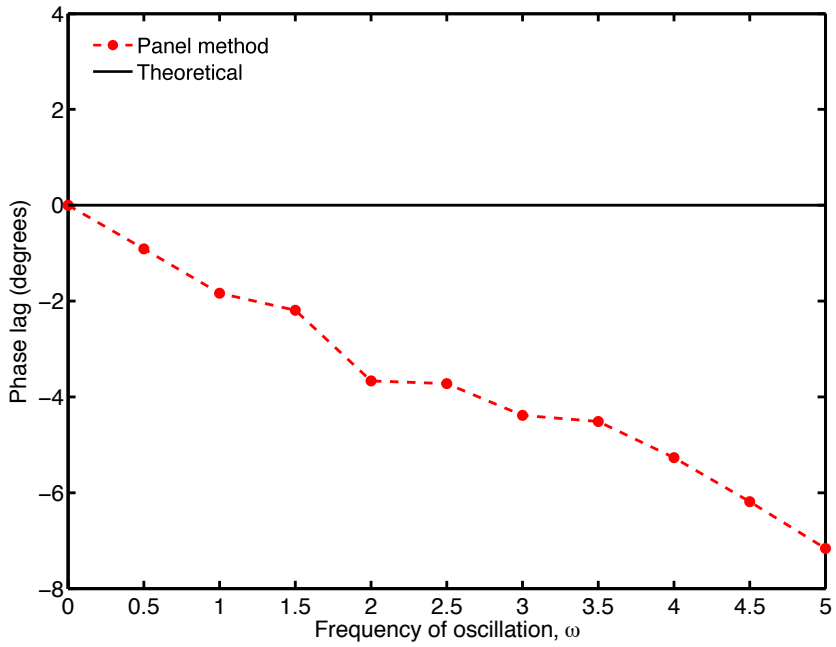

(b) Phase

Figure 3.12: Deviation of the: (a) amplitude, and (b) phase, of the apparent force over a sphere at different oscillating frequencies.

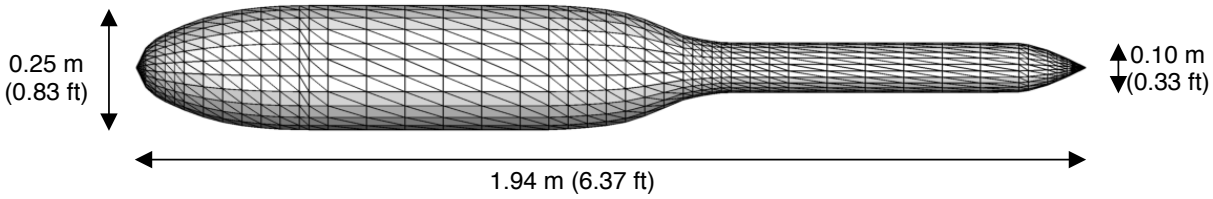

Figure 3.13: Panel representation of the slender body AGARD fuselage.

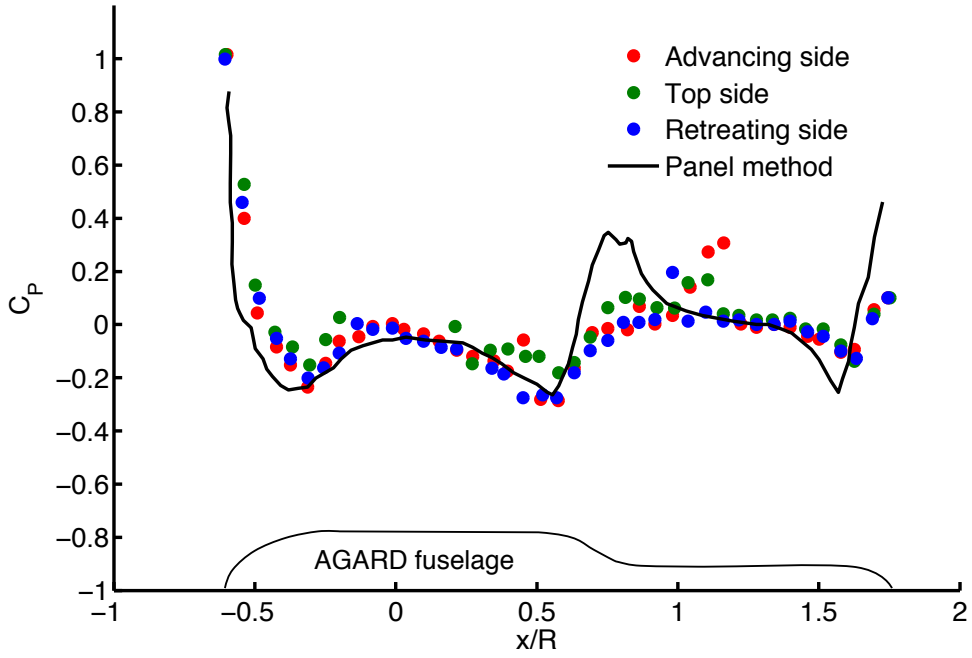

Figure 3.14: Comparison of surface pressure measurements of the time-averaged pressure distribution on the AGARD fuselage.

there are clear differences.

Comparison of the FVM predictions were also conducted for a fuselage beneath an operating rotor. Figure 3.15 shows time-averaged pressure comparison between the experimental data and numerical prediction on the top and retreating side of the AGARD fuselage in forward flight (at an advance ratio, μ, of 0.05). The rotor specifications are given in Table F.3 of Appendix F. The azimuthal discretization of the wake was 10° and was truncated after 6 turns. In this case, the differences on the top surface arise because of the bluff body nature of the rotor hub and its wake that was not modeled in this study. The model also overpredicts the velocity at the front end of the fuselage leading to decreased pressure values on the retreating side.

A study was also conducted to quantify the influence of the fuselage on the performance of the rotor. Figure 3.16 shows the variation of the rotor figure of merit against the blade loading coefficient, C_T/σ, with and without the AGARD fuselage (see Fig. 3.13) operating in hover out of ground effect. The solid circles indicate experimental measurements, while the dashed lines represent FVM predictions. As the rotor thrust increases, the presence of the fuselage produces an increase in the rotor figure of merit; an increase of about 5% at $C_T/\sigma = 0.1$ is clearly significant.

A key reason for the change in rotor performance is the effect of the fuselage on the sectional airloads on the main rotor. The presence of the fuselage beneath the rotor behaves aerodynamically similar to a ground and, therefore, a reduction in inflow is produced along the span of the rotor, especially in the inboard sections of the rotor as shown in Fig. 3.17(a). This reduced inflow results in a lower induced power requirement, which manifests as an increase in the effective figure of merit (Fig. 3.16). Furthermore, the lower inflow results in the local blade sections operating at

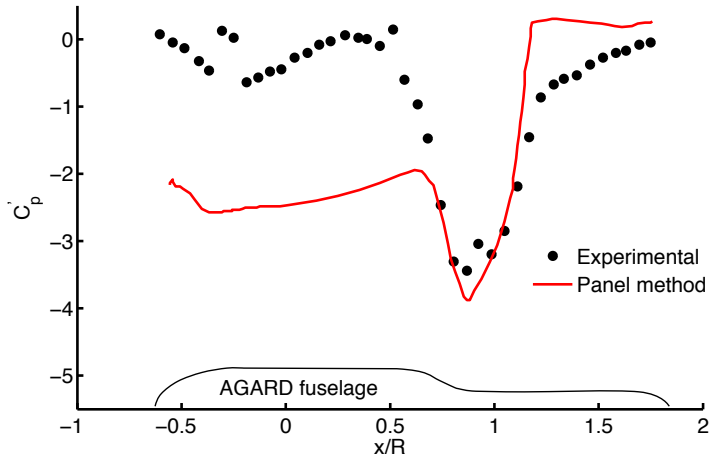

(a) Retreating side

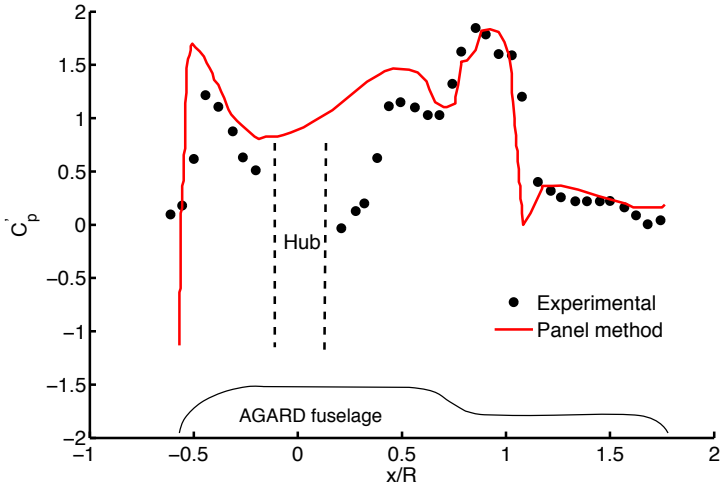

(b) Top surface

Figure 3.15: Validation of the surface singularity method for the AGARD fuselage. Steady pressure distribution on the: (a) Retreating side; (b) Top surface.

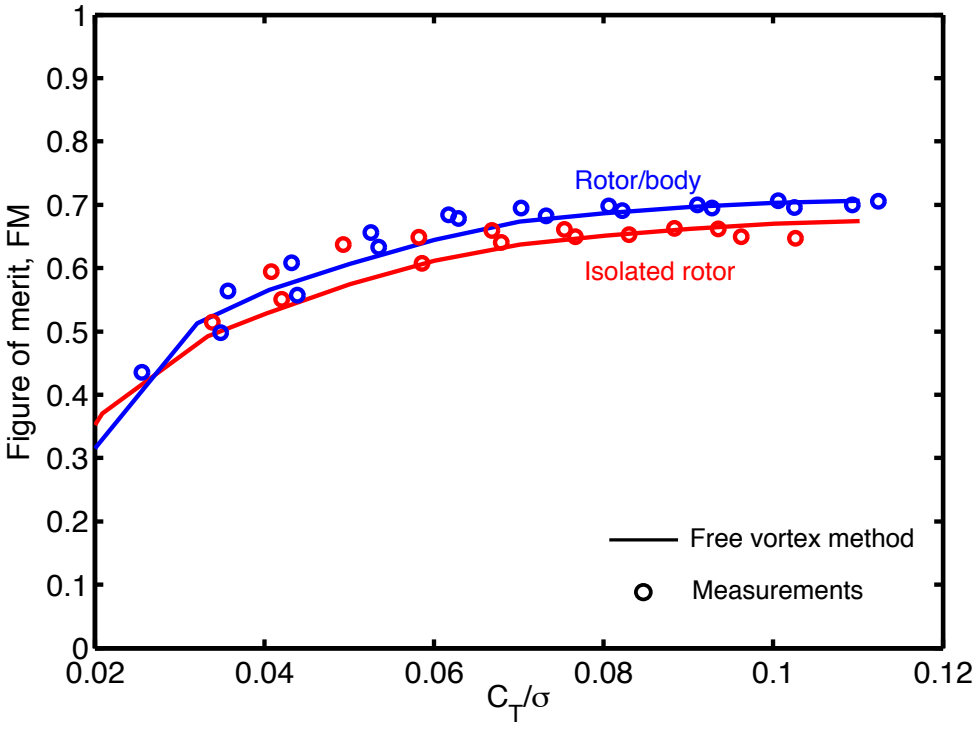

Figure 3.16: Variation of the figure of merit of the rotor with and without the presence of a fuselage. Source of experiments: Bagai & Leishman [11].

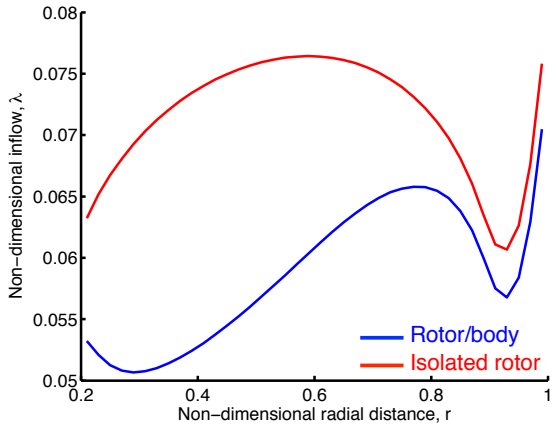

(a) Inflow

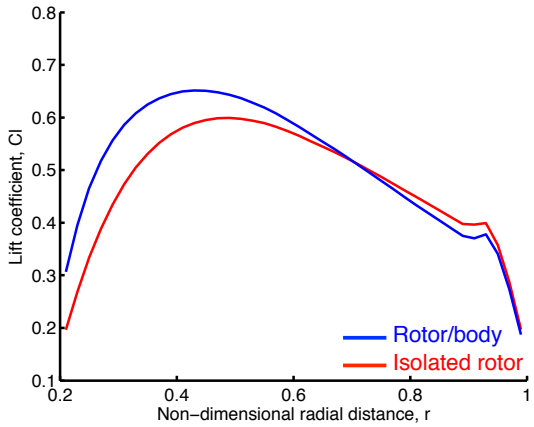

(b) Lift coefficient

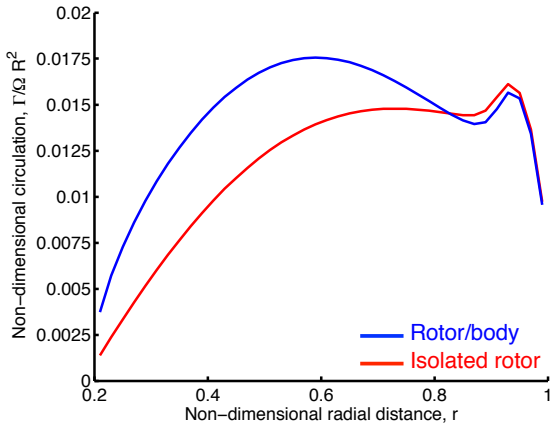

(c) Blade bound circulation

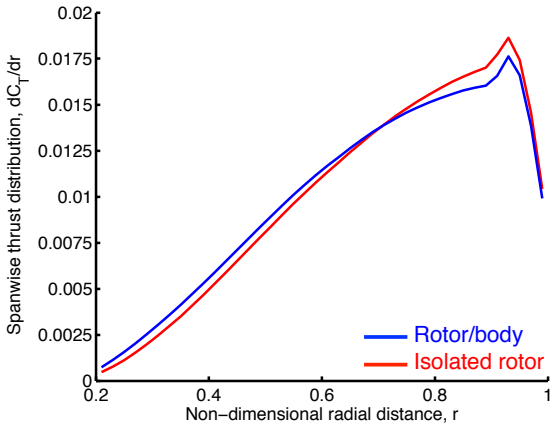

(d) Thrust

Figure 3.17: Spanwise variation of: (a) Inflow, (b) Lift coefficient, (c) Blade bound circulation, and (d) Thrust, with and without the presence of fuselage.

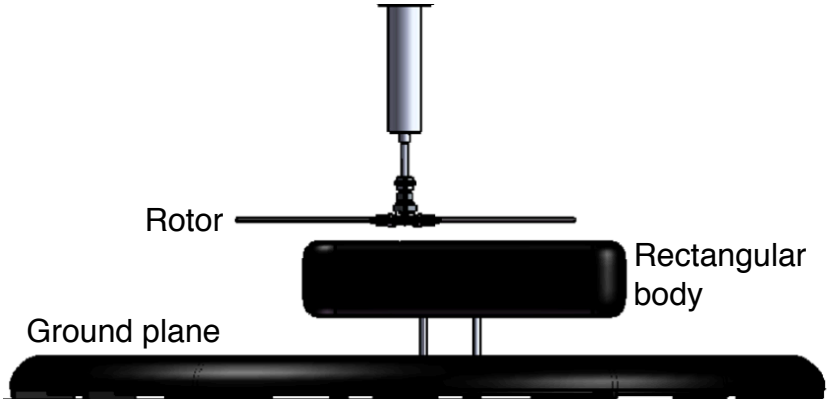

Figure 3.18: A schematic of the position of the rotor, the body and the ground plane used in the experimental setup of Hance [12].

a higher angle of attack, which causes an increase in the local lift coefficient in the presence of the fuselage, as shown in Fig. 3.16(b). As a consequence of the reduced inflow and increase lift coefficient in the inboard sections of the rotor blade, an increase in the blade bound circulation and spanwise thrust was observed in Figs. 3.17(c) and 3.17(d), respectively.

Measurements of the tip vortex in the presence of a fuselage were performed by Hance [12] for a 2-bladed laboratory scale rotor hovering in ground effect, a schematic of the setup shown in Fig. 3.18, with the cross-section of the rectangular body shown in Fig. 3.19. Figure 3.20 shows the comparison of tip vortex trajectories for an isolated rotor and ahead of the rectangular fuselage. The wake trajectories ahead of the rotor disk are very similar between the isolated rotor and in the presence of the fuselage. The vertical (z/R) value prediction with wake age agrees well with the measurements, while the radial (r/R) value is underpredicted. This outcome most likely arises because of the inviscid nature of the methodology, which does not account for the momentum loss in the vertical direction from viscosity and turbulence, and so leading to some decrease in the radial contraction of the wake compared to what is seen in the experiments.

(a) Top view

(b) Side view

Figure 3.19: Top and side cross-section views of the rectangular body.

3.2 Effects of the Tail Rotor on Main Rotor

In general, a tail rotor has to operate in a relatively demanding aerodynamic environment, and its performance will be affected by the presence of the the main rotor wake and also to some extent by the aerodynamics of the airframe. While the tail rotor can also distort the main rotor wake, its actual effects are difficult to isolate. As noted previously, there have only been only a handful of studies to document the interaction of the main and tail rotor, primarily from a performance aspect [52, 53, 70, 130].

FVM predictions have been performed for a representative single main rotor (SMR) and tail rotor (TR) combination operating in hover and forward flight, both in ground effect and out of ground effect. The geometries of the rotors are given in Tables F.7 and F.8 of Appendix F. The azimuthal discretization of the vortex wakes (both rotors) was 10°, and the filaments were

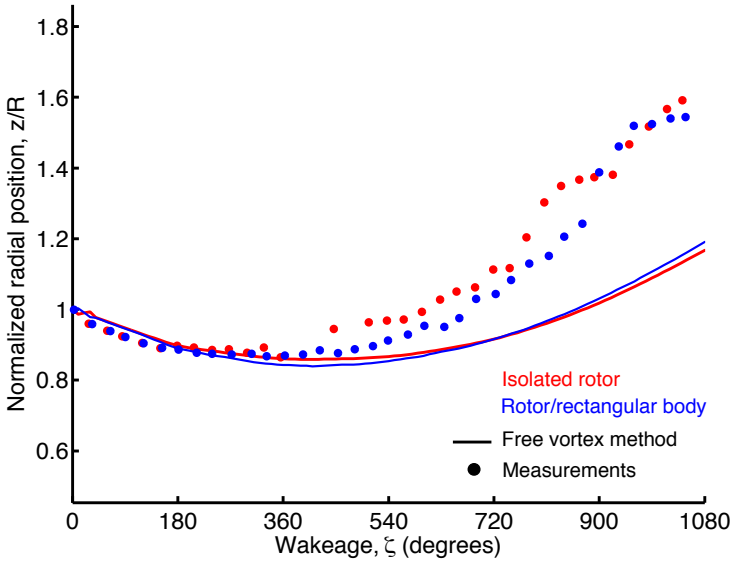

(a) Radial displacements versus wake age

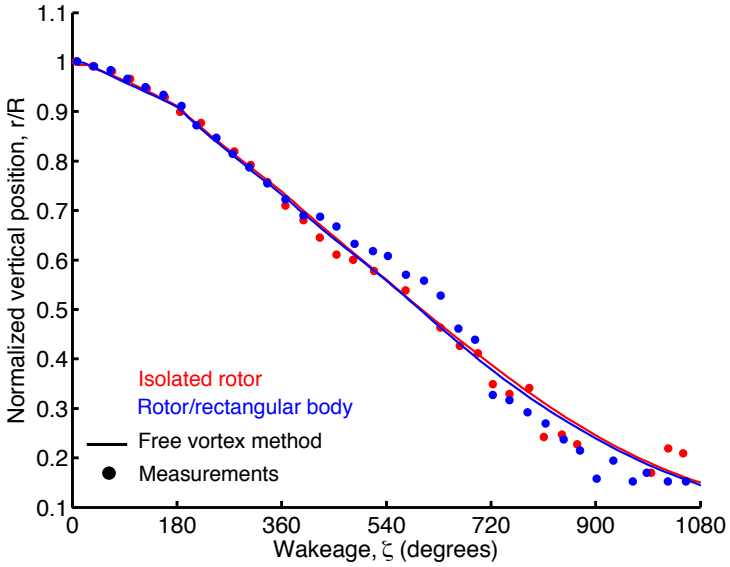

(b) Vertical displacements versus wake age

Figure 3.20: Experimental measurements and FVM predictions for the: (a) radial displacement, and (b) vertical displacement of the tip vortices with wake age ahead of the fuselage for the laboratory-scale rotor hovering in ground effect at $z/R = 1$ with and without the presence of a rectangular body.

truncated after 10 rotor revolutions at which point their vorticity had mostly diffused and their induced velocities were much weaker.

Figures 3.21(a) and 3.21(b) show the longitudinal and lateral views of the predicted wake geometry with and without the presence of a tail rotor, respectively, for the hovering rotor operating out of ground effect. The isolated rotor wake was noted to be periodic and axisymmetric for nearly four rotor revolutions, as shown in Fig. 3.21(a). At later wake ages, bundling of the tip vortices produced aperiodic wake developments. It was found that the presence of the tail rotor distorted the main rotor wake and also led to increased levels of aperiodicity in the wake at earlier wake ages, as shown in Fig. 3.21(b).

The tail rotor vortex filaments (highlighted in blue) were entrained through the downwash of the main rotor where it interacted with the tip vortex filaments of the main rotor at very early wake ages. As compared to the tip vortex structure of the isolated rotor, the presence of the tail rotor introduced mild disturbances in the early ages of the main rotor wake developments, which resulted in the bundling of main rotor tip vortices as early as the first rotor revolution. The induced velocity of the tail rotor on the main rotor wake also resulted in a lateral wake skew tilt exhibited by the wake of the main rotor, as shown in Fig. 3.21(b).

Figures 3.22 and 3.23 shows instantaneous and time-averages total velocity contours along the longitudinal and lateral plane, respectively, for a main rotor/tail rotor combination hovering out of ground effect. While the time-averaged flow measurements showed the general nature of the flow as the rotor wakes interacted with each other, the instantaneous realization revealed the detailed flow interactions. The trajectories of the tip vortices can be clearly identified as they

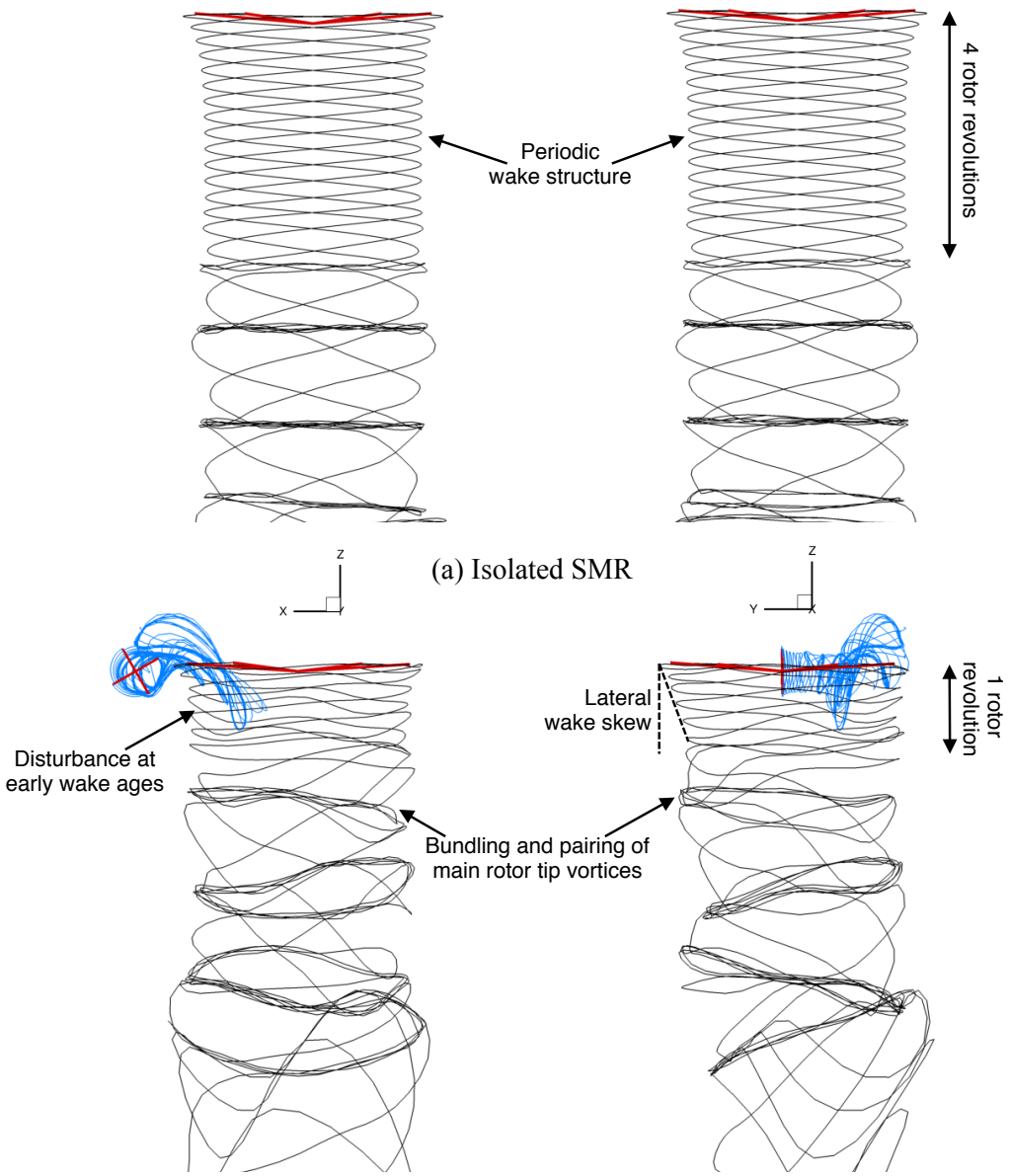

(a) Isolated SMR

(b) SMR with TR

Figure 3.21: Longitudinal and lateral wake geometries for (a) an isolated SMR and (b) SMR with a TR operating in hover out of ground effect.

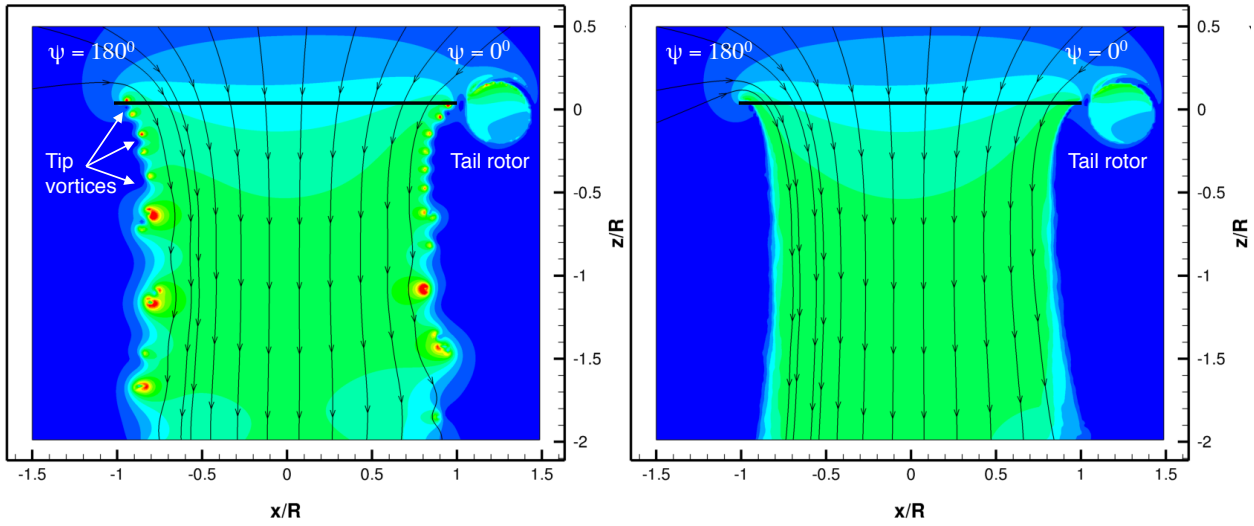

(a) Instantaneous

(b) Time averaged

Figure 3.22: Total velocity contours showing the: (a) instantanoues, and (b) time-averaged velocity profile along the longitudinal plane for a SMR with TR operating out of ground effect.

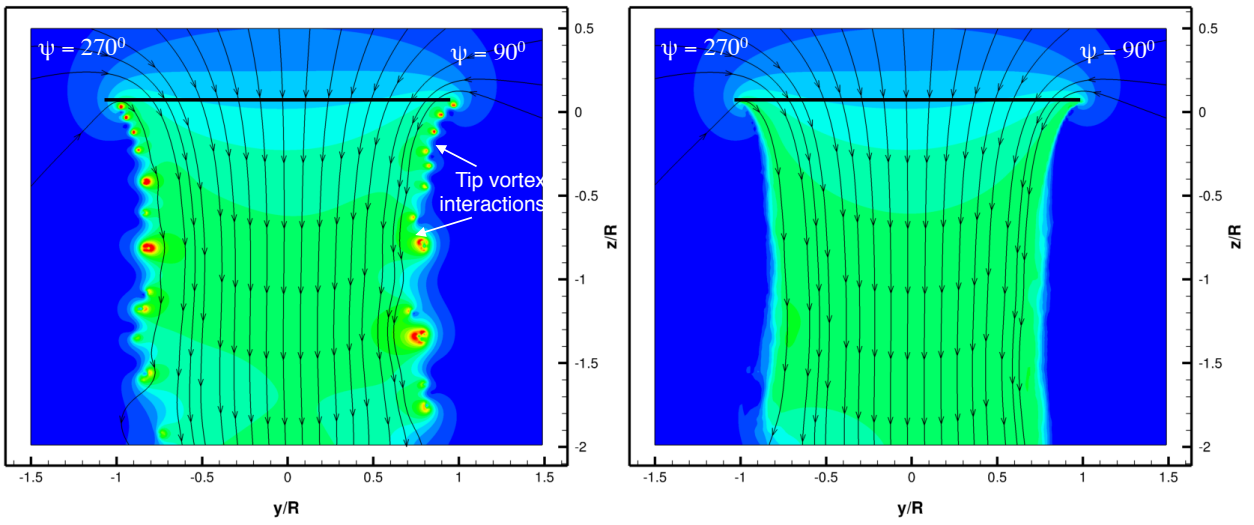

(a) Instantaneous

(b) Time averaged

Figure 3.23: Total velocity contours showing the: (a) instantanoues, and (b) time-averaged velocity profile along the lateral plane for a SMR with TR operating out of ground effect.

convect towards the ground. Significant pairing and merging of the tip vortices can be seen along the lateral plane in Fig. 3.23(a), and these increased vortex/vortex interactions can be attributed to the influence of the tail rotor.

Bhagwat and Leishman [131] have shown that the helicoidal form of rotor wakes is such that they naturally exhibit certain modes of instability, which are pronounced at half-integer multiples of the number of rotor blades. For example, a four bladed rotor would experience these modes at frequencies of 2/rev, 6/rev, 10/rev, etc. In particular, the main rotor wake experiences distortions in the form of waves, which propagate through the wake to older wake ages. Therefore, the tail rotor wake interacts with the main rotor wake and could be responsible in exciting some of these modes.

Figure 3.24 shows the radial and axial displacements of the main rotor wake filaments as a function of wake age for the instantaneous realization presented in Fig. 3.21. The results reflect the aperiodic behavior of the tip vortices in the presence of a tail rotor when compared to an isolated rotor. Large variations were observed in the radial position of the tip vortex filaments in the presence of the tail rotor as compared to the wake produced by the isolated main rotor, as shown in Fig. 3.24(a). Notice however, that these oscillations are bounded and are not actually instabilities that could potentially cause the numerical solution to diverge.

Contour plots of the time averaged velocity distribution normal to the plane of the rotor are shown in Fig. 3.25. The velocities are representative of the inflow through the rotor disk, and according to the convention used, negative values are velocities downward through the rotor disk and positive values are velocities upward through the disk. The average velocity distribution for the isolated rotor was axisymmetric and consistent with the periodic wake solution. The presence

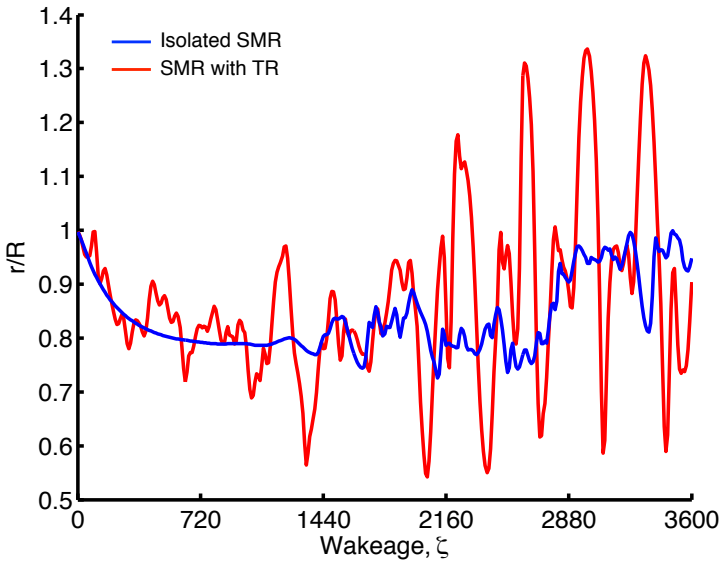

(a) Radial wake displacement

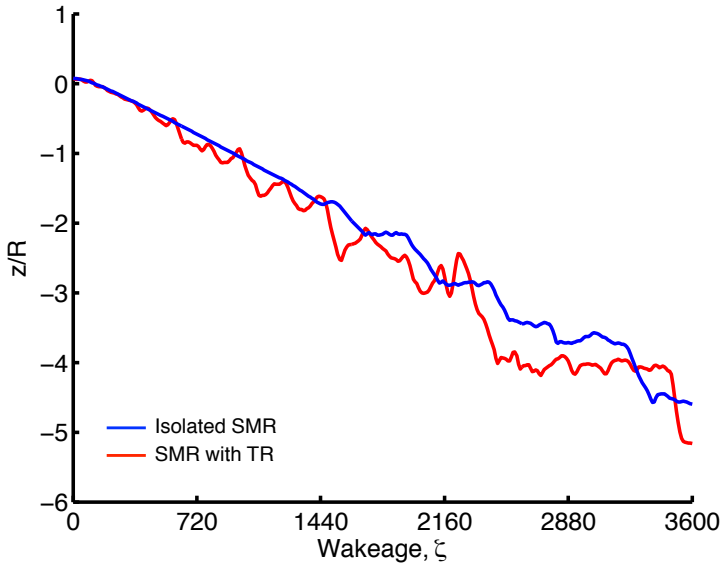

(b) Axial wake displacement

Figure 3.24: Comparison of the radial and axial displacements of the tip vortex filaments versus wake age for a single main rotor with and without the presence of a tail rotor operating in hover out of ground effect. Results from a single blade are shown for clarity.

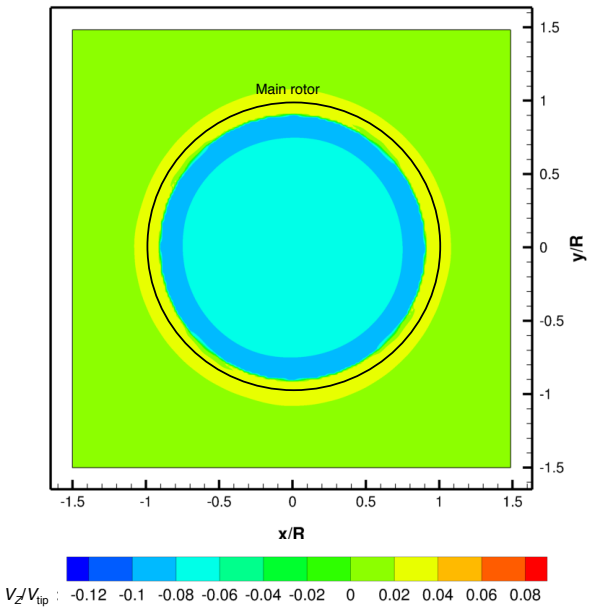

(a) Isolated SMR

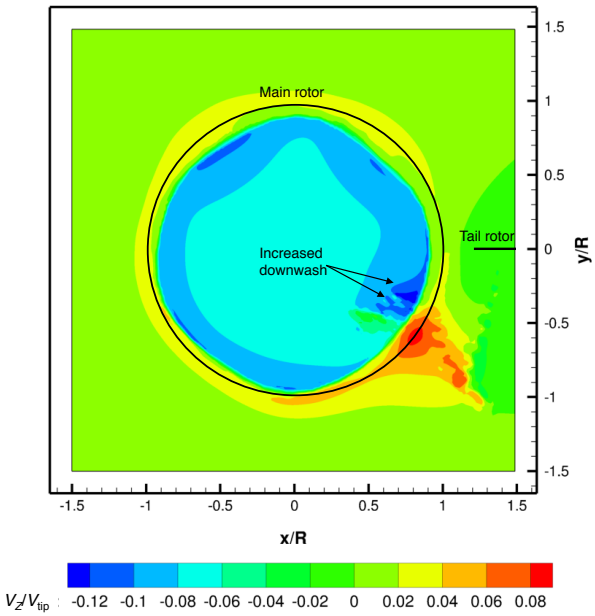

(b) SMR with TR

Figure 3.25: Time averaged out of plane velocity at the rotor plane ($z/R = 0$) for (a) isolated SMR, and (b) SMR with TR, operating in hover out of ground effect.

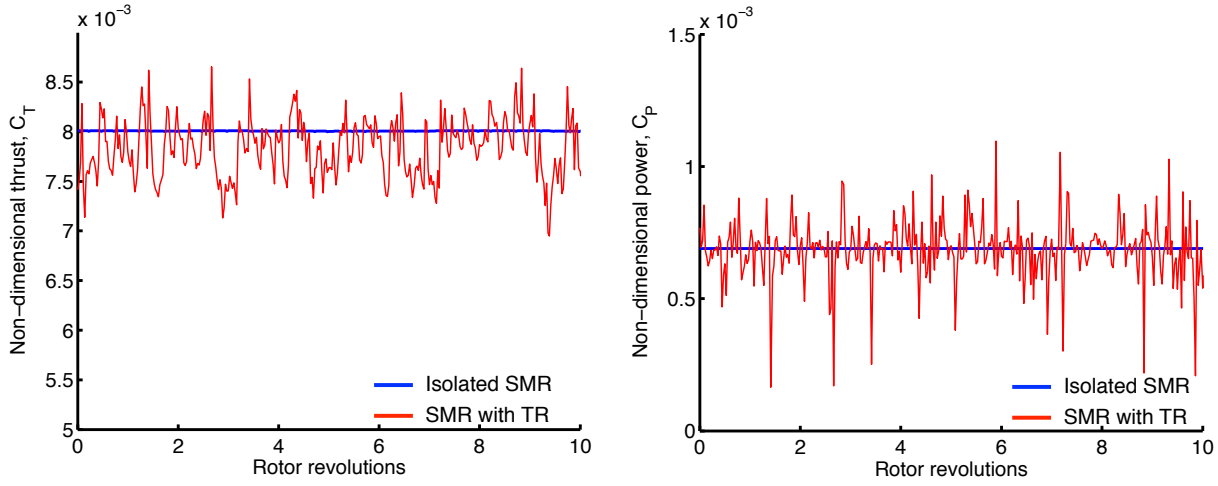

(a) Thrust variation

(b) Power variation

Figure 3.26: Variation of non-dimensional thrust and power for a single main rotor in hover with and without the presence of a tail rotor operating in hover out of ground effect.

of the tail rotor, however, was observed to influence the inflow distribution through the main rotor, with regions of increased downwash through the rotor disk where the tail rotor interacted with the main rotor.

The effects of the tail rotor on the rotor thrust and power were also examined. Figure 3.26 shows the variations in the values of non-dimensional thrust and power as a function of rotor time after the initial transients in the solution had dissipated. The rotor was trimmed, using the methodology described in Section 2.7.3, to a target thrust of $C_T = 0.008$. For the case of the isolated rotor (blue), both the thrust and power were constant, with the thrust produced by the rotor being equal to the required target thrust of $C_T = 0.008$. Although the average net vehicle thrust produced by the main rotor/tail rotor combination is approximately equal to the target thrust, relatively large fluctuations were seen in the instantaneous values of thrust. Similar trends were also observed in the non-dimensional values of rotor power; see Fig. 3.26(b). These fluctuations about

the mean were mainly a consequence of the time-varying airloads produced by the aerodynamic interactions between the two rotors. Notice that these deviations in the thrust and power are fairly random and not at any one particular frequency, which further confirms the aperiodic nature of the resulting flow.

Figure 3.27 shows the wake geometry of the isolated rotor in hover and well as the main rotor wake geometry in the presence of the tail rotor. The isolated rotor wake was noted to be mostly periodic and axisymmetric, except near the ground where the rollup and bundling of the tip vortices produced some aperiodic wake developments. However, the presence of the tail rotor clearly distorted the main rotor wake, and also led to increased aperiodicity in the wake at earlier wake ages, as shown in Fig. 3.27(b), similar to operation out of ground effect (Fig. 3.21). The aerodynamic environment of the main rotor wake caused the wake of the tail rotor to be entrained into the downwash of the main rotor wake, as shown in Fig. 3.27(b).

Figure 3.28 shows total velocity contours along the longitudinal and lateral plane passing through the center of the rotor disk for a main rotor/tail rotor combination hovering in ground effect at a rotor height of $z/R = 1$ above the ground. An instantaneous realization of the velocity field and the time-averaged flow is shown along with the streamline patterns. The time-averaged flow measurements (Fig. 3.28(a)) showed the general nature of the flow as the rotor wakes interacted with each other and with the ground, which was basically similar to an isolated rotor operating in ground effect. However, the instantaneous realization (Fig. 3.28(b)) revealed the detailed flow interactions that took place. The trajectories of the tip vortices can be identified as they convected towards the ground. Significant pairing and merging of the tip vortices can be seen along the lateral

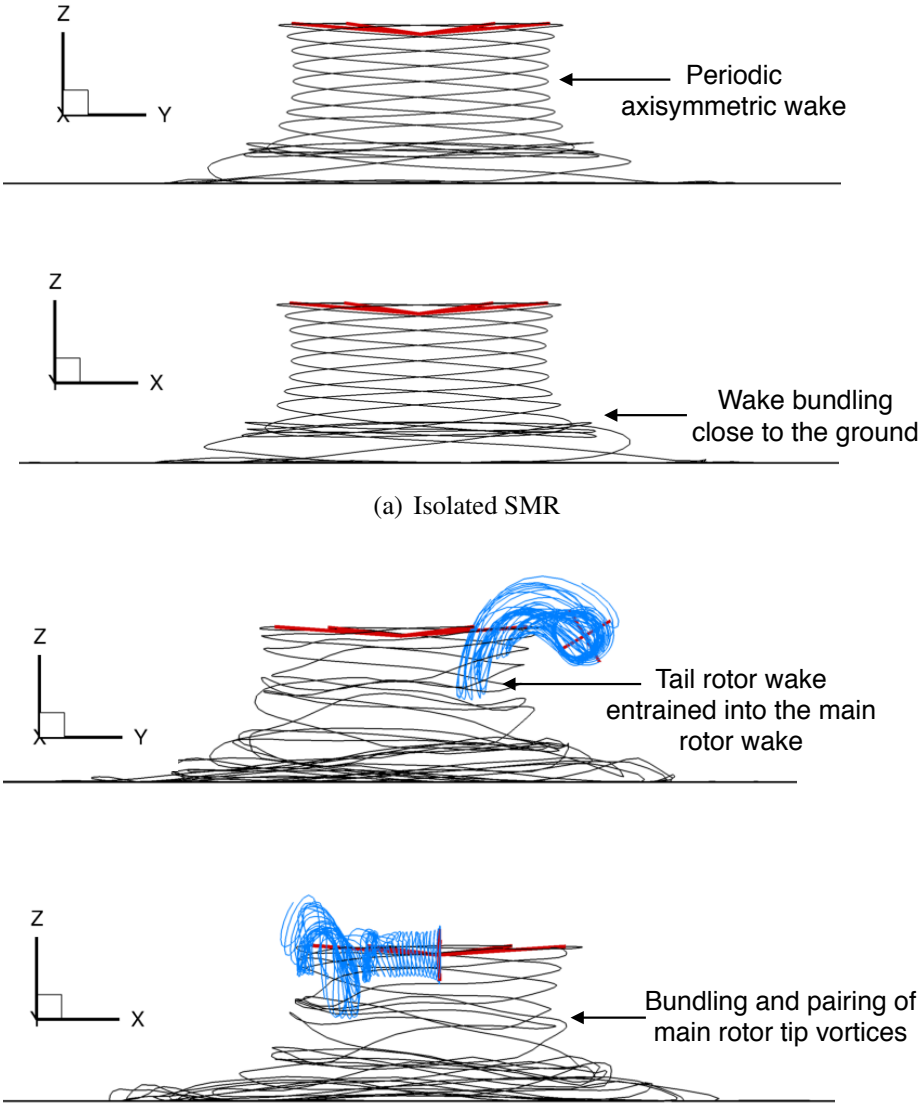

(a) Isolated SMR

(b) SMR with TR

Figure 3.27: Longitudinal and lateral wake geometries for (a) an isolated SMR and (b) SMR with a TR hovering above the ground at $z/R = 1$.

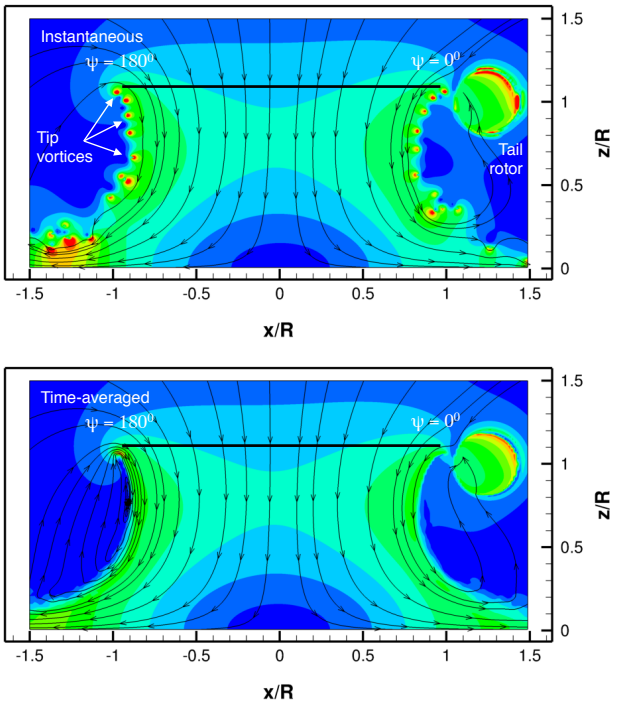

(a) Longitudinal plane

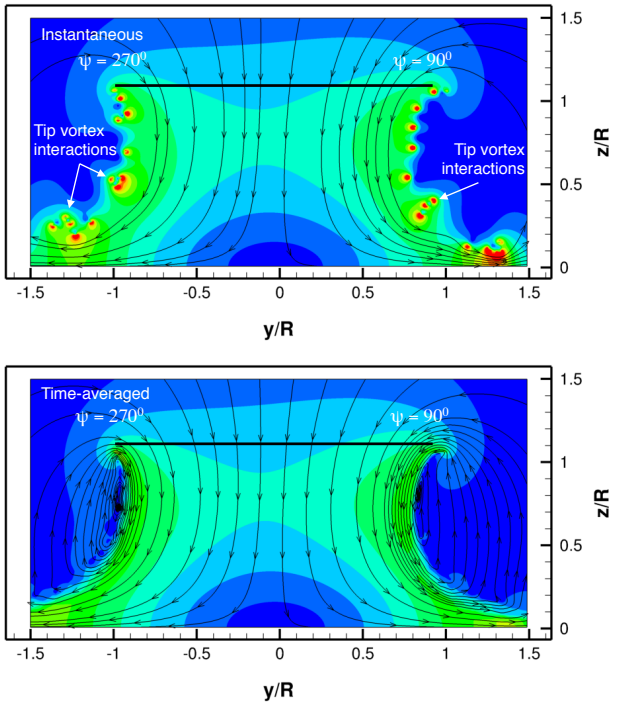

(b) Lateral plane

Figure 3.28: Total velocity contours showing the instantanoues and time-averaged velocity profile along the: (a) longitudinal, and (b) lateral plane for a SMR with TR hovering above the ground at $z/R = 1$.

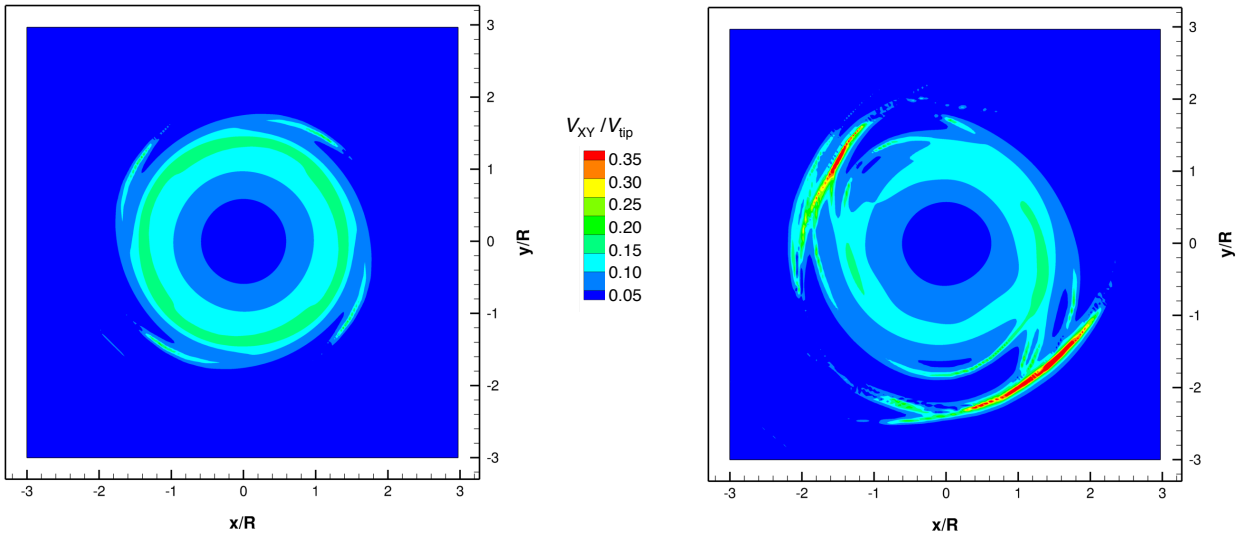

(a) Isolated SMR

(b) SMR with TR

Figure 3.29: Total inplane velocity on the ground for (a) isolated SMR, and (b) SMR with TR hovering above the ground at $z/R = 1$.

plane in Fig. 3.28(b), and this increased levels of vortex/vortex interactions can be attributed to the influence of the tail rotor.

Within the context of rotorcraft brownout, particles are mobilized and entrained from the sediment bed primarily by exceeding the threshold friction velocity, which is dependent on the induced velocity on the sediment bed. Although the tail rotor wake did not convect all the way to the ground, it significantly altered the main rotor wake structure and produced a different groundwash velocity field compared to that of the isolated main rotor, as shown in Fig. 3.29. The regions of higher flow velocities shown in Fig. 3.29(b) were found to coincide with the impingement of the tip vortices onto the ground plane.

Figure 3.30 shows the wake geometry produced by the single main rotor with and without the presence of the tail rotor when it is operating in forward flight conditions at an advance ratio $\mu = 0.1$. Unlike operation in hover (see Fig. 3.21) where the tail rotor significantly interacted with

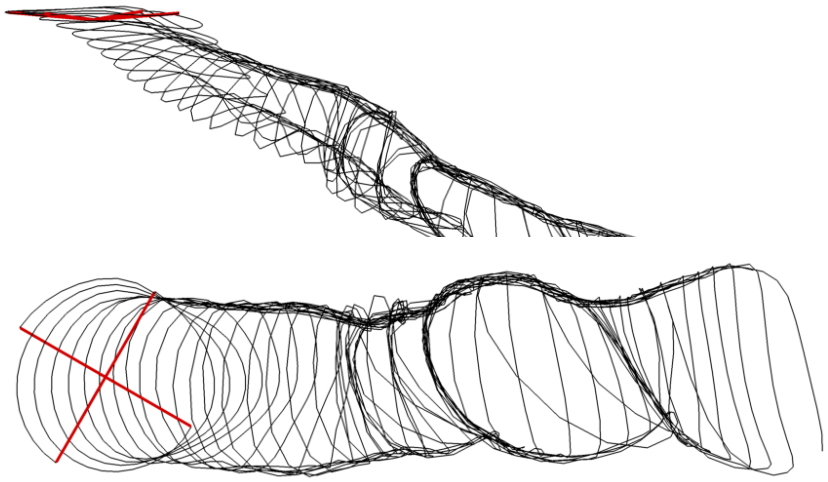

(a) Isolated SMR

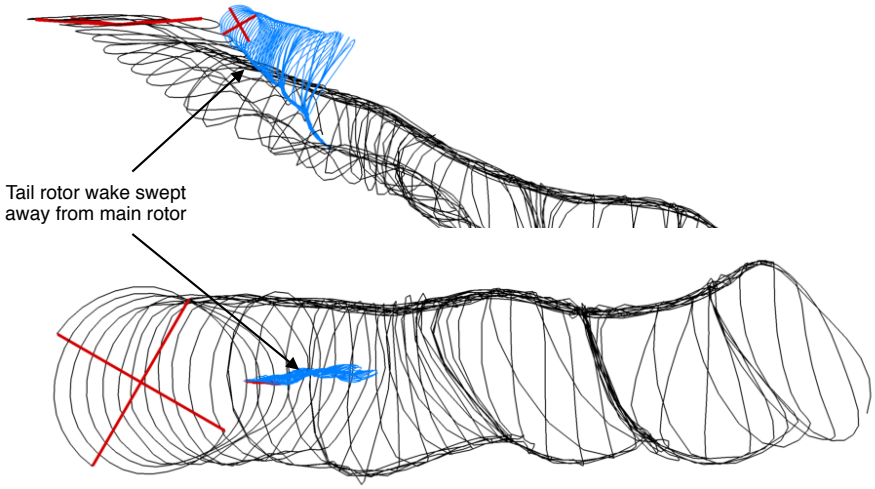

(b) SMR with TR

Figure 3.30: Longitudinal and lateral wake geometries for (a) an isolated SMR and (b) SMR with a TR operating at an advance ratio of $\mu = 0.1$ out of ground effect.

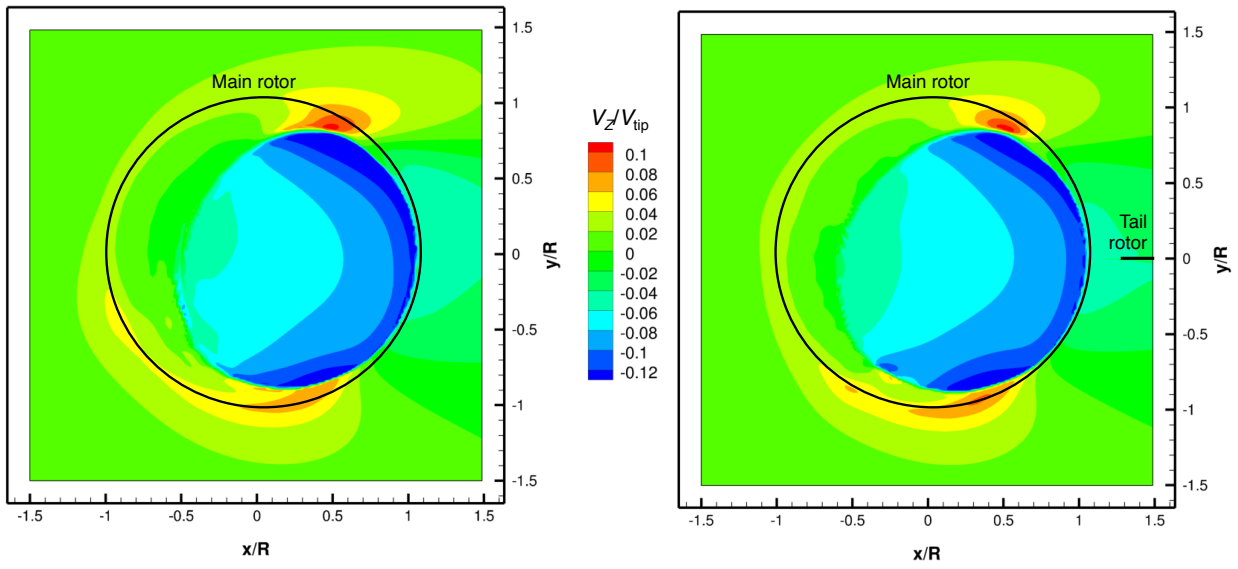

(a) Isolated SMR

(b) SMR with TR

Figure 3.31: Time averaged inplane velocity at the rotor plane ($z/R = 0$) for (a) isolated SMR, and (b) SMR with TR operating at an advance ratio of $\mu = 0.1$ out of ground effect.

the main rotor, the tail rotor wake was swept downstream from the main rotor under the action of the freestream velocity. Although there were minor interactions between the two rotor wakes, Fig. 3.31 shows the resulting velocities induced at the plane of the rotor were similar with and without the presence of the tail rotor.

In summary, the foregoing results has given further insight and understanding of the role of the tail rotor in affecting the aerodynamic environment of the main rotor. In particular, the influence of the tail rotor on the main rotor wake is significant in hover (Figs. 3.21 and 3.27), because of the effect of the mutually induced velocities of the wakes of the two rotors. When compared to the isolated SMR, the presence of the tail rotor results in a local increase in downwash velocities at the plane of the rotor towards the rear of the main rotor disk. This increased inflow through the rotor disk may require small adjustments in the pilot control inputs (especially the lateral cyclic

θ_{1c}) in the trim solution. The presence of the tail rotor affects the development of the wake of the main rotor, particularly increasing the frequency of vortex pairing and bundling, and produced an aperiodic wake flow. The increased aperiodicity in the flow was also shown to affect the induced velocities on the ground, i.e., at the sediment bed.

3.3 Effects of the Fuselage

The problem of aerodynamic interactions between the rotor and airframe have been studied for several decades, both experiments and simulations having helped in the understanding of this very difficult problem; see Chapter 11 of Leishman [4] for a review. Most studies have focused on the modified performance of the rotor in the presence of the fuselage and the aerodynamic characteristics of the body in the presence of the rotor wake. However, studies to quantify the role of the rotor/airframe interactions as they might affect the flow at the ground have been more limited [5,12]. Therefore, this section addresses the influence of the fuselage on the rotor environment and the effects of fuselage shape on the development of the wake structure and its interactions with the ground.

As discussed previously, the introduction of the fuselage into the flow field beneath a rotor can give a beneficial reduction in rotor power requirements for a given thrust, as shown previously in Fig. 3.16. One of the reasons for this reduction in power is the effect of the fuselage on the induced inflow through the rotor disk. Figure 3.32 shows a contour plot of the inflow through the rotor disk in the presence of the fuselage. Notice the reduced inflow through the rotor disk in regions directly above the fuselage as compared to the values produced by the isolated rotor. This

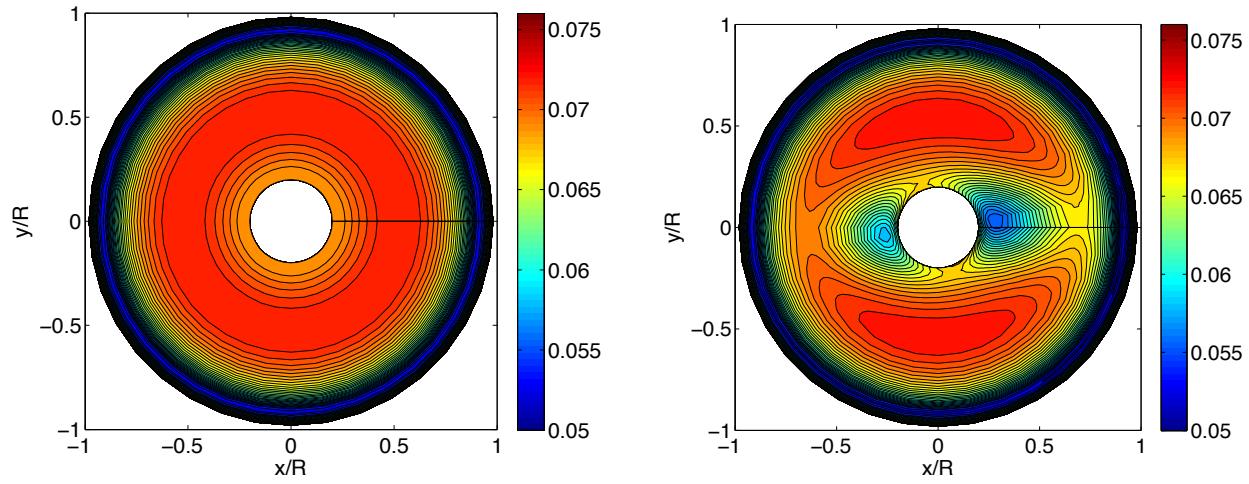

(a) Isolated rotor (b) Rotor/fuselage

Figure 3.32: Comparison of the rotor inflow in hover in the presence of a fuselage.

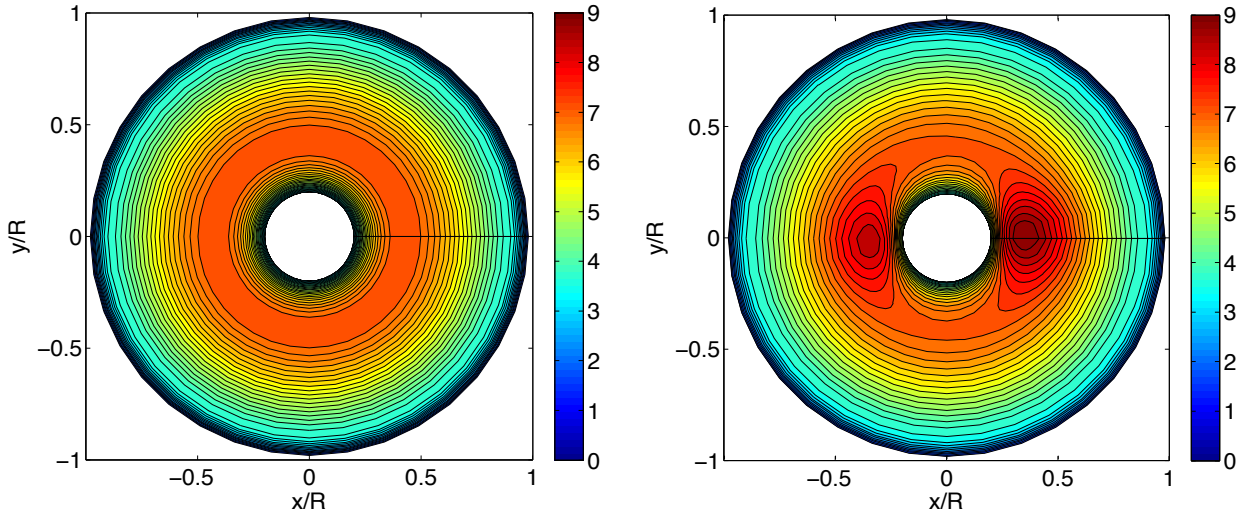

(a) Isolated rotor (b) Rotor/fuselage

Figure 3.33: Comparison of the angle of attack across the rotor in hover in the presence of a fuselage.

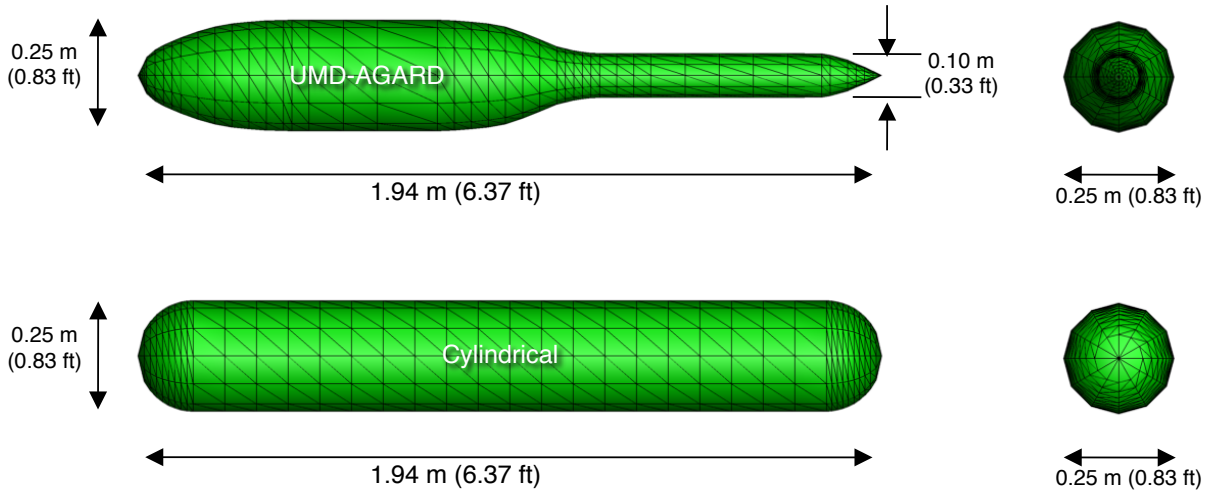

Figure 3.34: Panel representation of the UMD-AGARD and cylindrical fuselage shapes.

reduction in inflow is similar to those observed with rotors operating in ground effect, where the presence of the fuselage beneath the rotor behaves aerodynamically similar to a particular ground plane [9,23,24]. The reduced inflow, in turn, causes an increase in the local angles of attack, which become biased towards stations inboard on the rotor blade for a given thrust, as shown in Fig. 3.33.

Aside from requiring lesser power at a given rotor thrust, the presence of a fuselage beneath a rotor also increases the fuselage drag (usually 5% of the total vehicle weight in hover) as a consequence of flow separation from its sides. The rotor, therefore, will have to provide additional thrust to overcome this fuselage drag and maintain the same net total vertical force. However, the current implementation of the fuselage model using a panel method does not include the effects of flow separation, which implies that the requirements of a higher rotor thrust to offset the drag are not imposed on the trim solution. As a consequence, the rotor collective and the power requirements are slightly underpredicted in the current simulations in the presence of a fuselage.

In the present work, two representative fuselage shapes were considered to approximately

quantify the effect of the fuselage shape on the development of the main rotor wake and the effects produced at the ground: 1. A geometrically simplified helicopter fuselage [129], referred to as the UMD-AGARD fuselage, and 2. A fuselage with a cylindrical cross-section and hemispherical caps, as shown in Fig. 3.34. A representative full-scale four-bladed rotor was used in the present study; the rotor specifications are given in Table F.7 of Appendix F. The fuselages were scaled to be 55.4 ft (2.05R) in length with their longitudinal centerline located 0.3R below the rotor plane. Both shapes had a maximum radius of 4.1 ft (0.15R). While the cylindrical body was of uniform cross-section, the UMD-AGARD fuselage had a cylindrical main body that tapered at the nose and a cylindrical tail boom body of radius 1.6 ft (0. 06R) that tapered at the tail; see Fig. 3.34. These fuselages were modeled using a surface panel grid consisting of 50 lengthwise sections and 36 azimuthal sections, i.e., 1,800 panels.

Figure 3.35 shows the wake geometries of the isolated SMR, as well as the SMR in the presence of the two fuselage shapes. The results are shown in terms of the filament locations as they intersect the longitudinal plane. For the UMD-AGARD fuselage, the trailed tip vortices interacted primarily with the slender tail boom where the filaments were only minimally distorted as they slowed and stretched around the tail; see Fig. 3.35(b). In comparison, the tip vortex filaments were disturbed to a greater extent by the cylindrical fuselage, as shown in Fig. 3.35(c). This interaction also initiated sinuous wake disturbances which were seen to propagate to the front of the rotor wake and then to the ground. This result means that even local wake/fuselage interactions may have some effects on the overall flow environment at the ground.

Figure 3.36 shows contours of the resulting total velocity at the ground place produced by

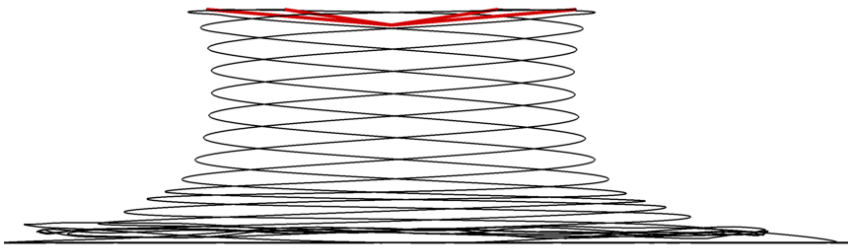

(a) Isolated SMR

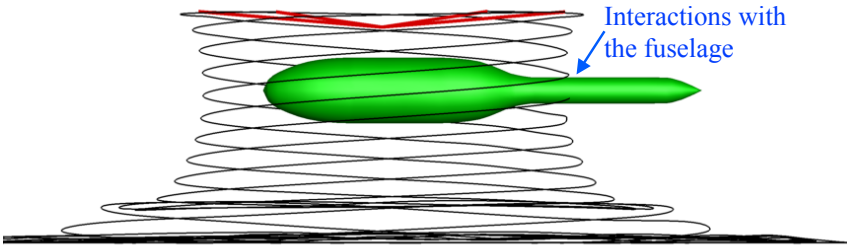

(b) UMD-AGARD fuselage

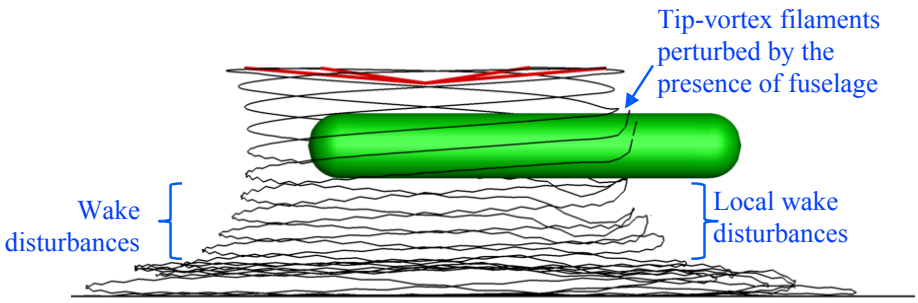

(c) Cylindrical fuselage

Figure 3.35: Comparison of the rotor wake geometries in ground effect operation for the: (a) isolated SMR, (b) SMR with the UMD-AGARD body, and (c) SMR with the cylindrical body.

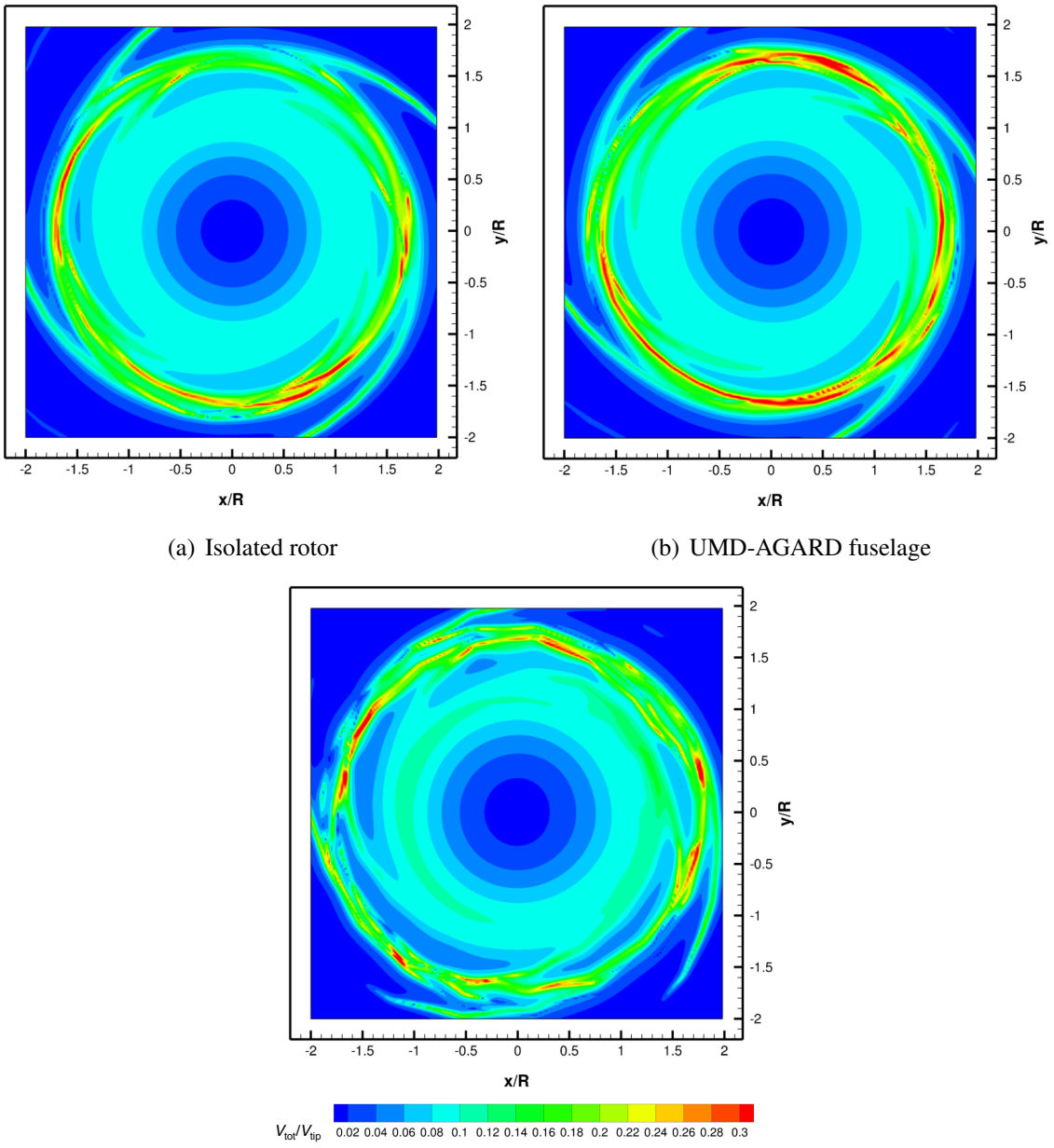

(a) Isolated rotor

(b) UMD-AGARD fuselage

(c) Cylindrical fuselage

Figure 3.36: Comparison of the total velocity contours at $z/R = 0.02$ for the: (a) isolated SMR, (b) SMR with the UMD-AGARD body, and (c) SMR with the cylindrical body.

the isolated rotor and the fuselages. It was found that while the contours are similar to each other, there were differences in the induced velocity field that can be attributed to the trajectories of the tip vortices as they interacted with the ground. Therefore, any upstream differences caused by the bodies manifest as differences in the flows at the ground, which can also potentially affect the problem of sediment mobilization.

Figure 3.37 shows representative instantaneous realizations of the total velocity contours around the UMD-AGARD fuselage and rotor combination. In these images, the vortices in the flow can be identified by the regions of higher concentrations in velocity. As shown in Fig. 3.37(b), the induced flow field along the longitudinal plane is significantly different at the nose and tail ends of the fuselage. Ahead of the rotor disk, the trajectories of the tip vortices appeared to be undisturbed by the presence of the fuselage, and were similar in form to that of the isolated rotor (Fig. 3.37(a)). At the tail end of the fuselage, however, bundling of the tip vortices were seen, which is a manifestation of the disturbances produced by the interactions of the rotor wake with the fuselage. Figure 3.37(c) shows an instantaneous realization of the flow field along the lateral plane. Notice that because the flow about the fuselage was based on potential flow assumptions, flow separation was not predicted over the lower surface of the cylinder, and the flow remained completely attached there.

3.4 Grid Convergence Studies

The convergence of the wake positions and induced velocities predicted by the FVM were performed for a rotor in hover, forward flight, and while performing a prescribed landing maneuver.

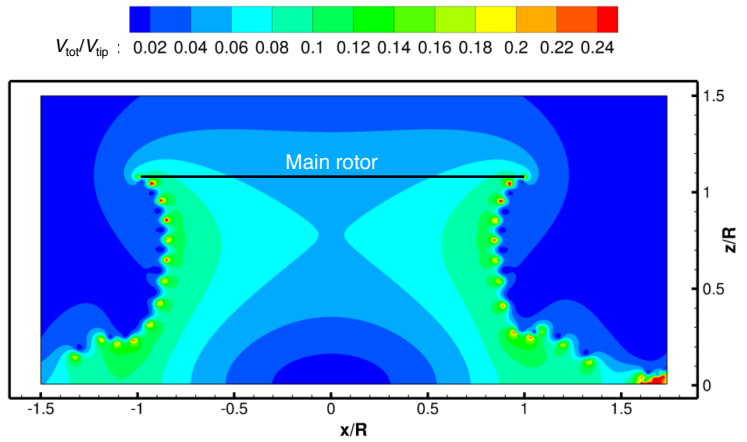

(a) Isolated rotor

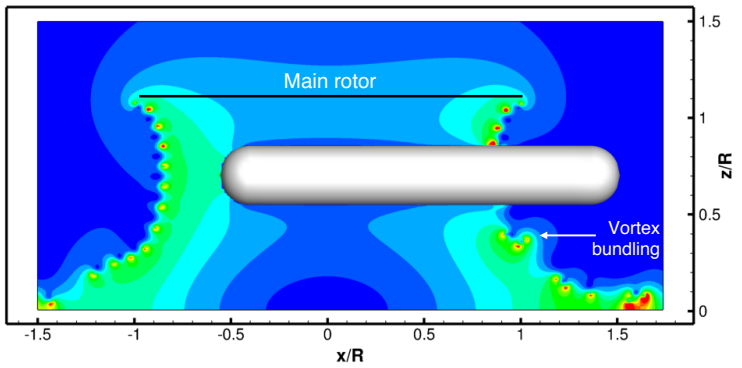

(b) Rotor/fuselage - Longitudinal plane

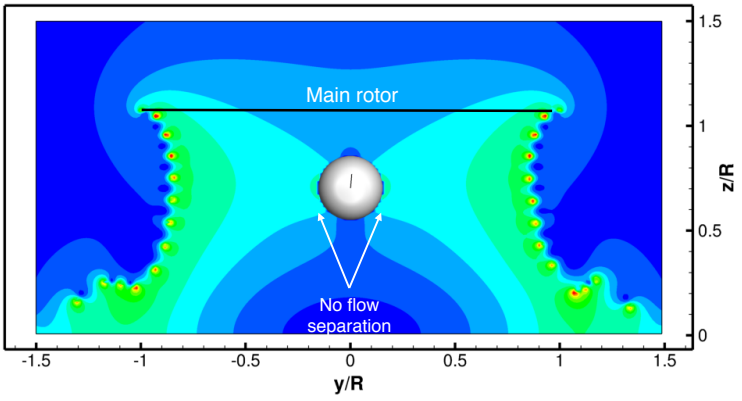

(c) Rotor/fuselage - Lateral plane

Figure 3.37: Comparison of the rotor wake geometries in ground effect operation for the: (a) isolated SMR, (b) SMR with the UMD-AGARD body, and (c) SMR with the cylindrical body.

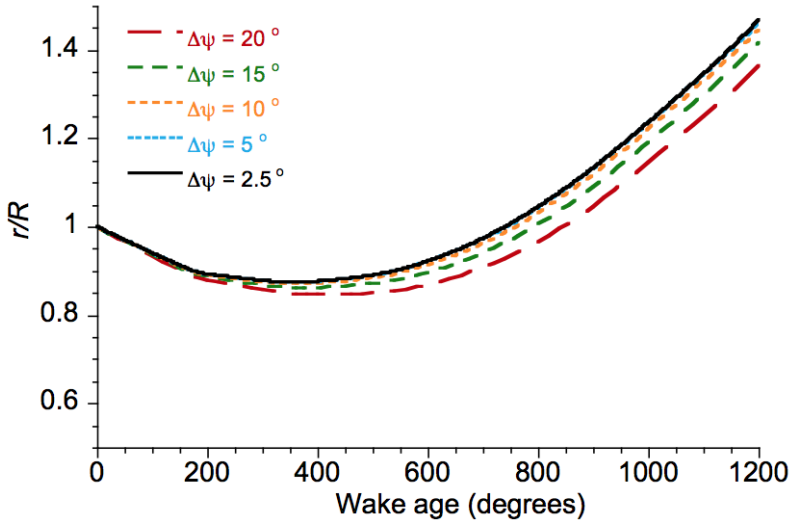

(a) r/R versus wake age

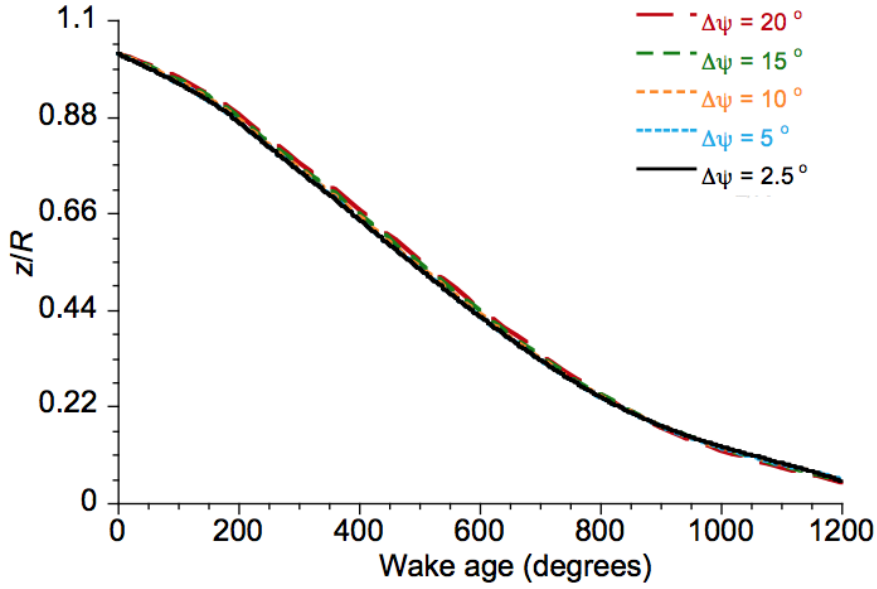

(b) z/R versus wake age

Figure 3.38: Numerical solution from the FVM for different discretization showing grid independence for finer resolution: (a) Radial displacements, r/R, and (b) Vertical displacements, z/R, as a function of wake age.

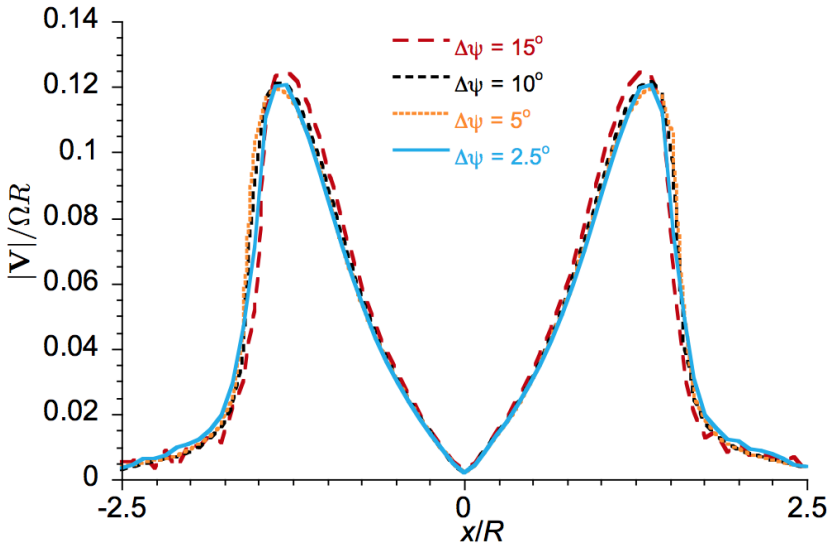

Figure 3.39: Variation of the total induced velocity along a longitudinal axis at $z/R = 0.02$ for a rotor hovering at $z/R = 1$.

Figure 3.38 shows the radial and axial displacements of the wake filaments as a function of wake age for different grid discretization. The solution confirms the converging trend with increasing grid resolution. The solutions with grid resolutions of 15° and 20° show considerable differences compared to the solution with the 2.5° grid resolution. For values of $\Delta\psi = \Delta\zeta$ less than 10°, the radial and axial wake displacements are close to the solution for $\Delta\psi = \Delta\zeta = 2.5°$. This convergent nature of the problem also shows that all of the numerical schemes are convergent.

The flow velocities induced at $z/R = 0.02$ above the ground along the longitudinal axis with different grid resolutions are shown in Fig. 3.39. It can be seen that there is a converging trend with increasing grid resolution. The velocities induced with $\Delta\psi = \Delta\zeta \leq 10°$ also show good agreement for smaller values of $\Delta\psi$ and $\Delta\zeta$.

Figures 3.40(a) and 3.40(b) show the top and side views of the wake geometry produced by a rotor operating in forward flight ($\mu = 0.1$), respectively. The FVM solutions were truncated

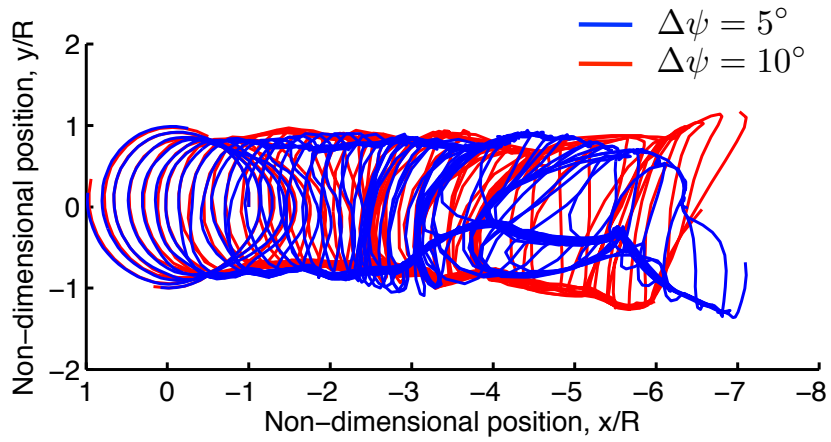

(a) Top view

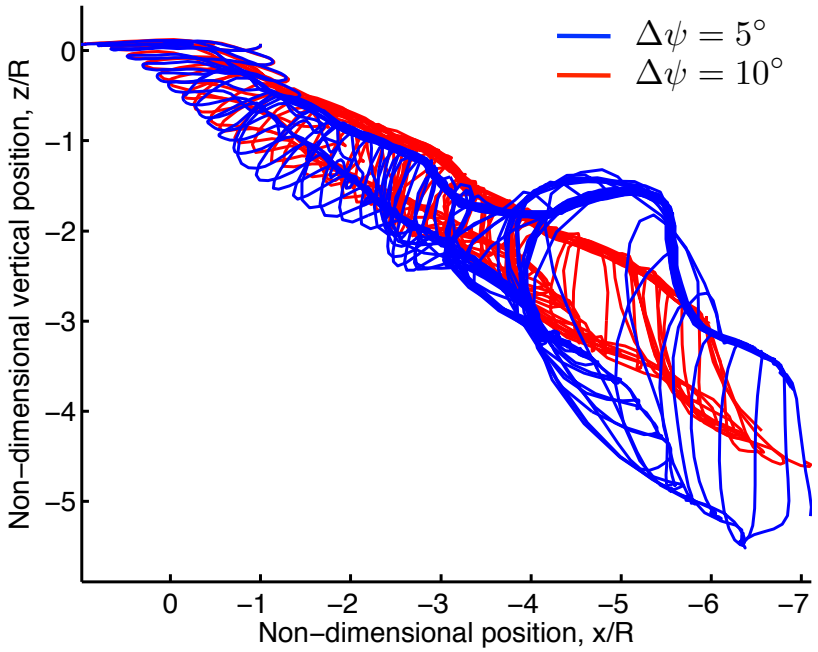

(b) Side view

Figure 3.40: Forward flight wake geometries in: (a) Top view, and (b) Side view, for 5° and 10° azimuthal discretization.

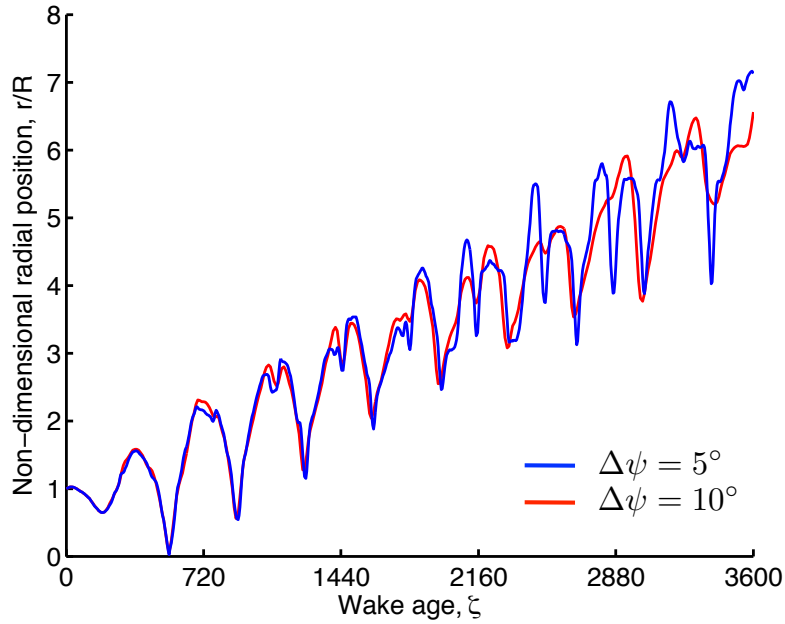

(a) r/R versus wake age

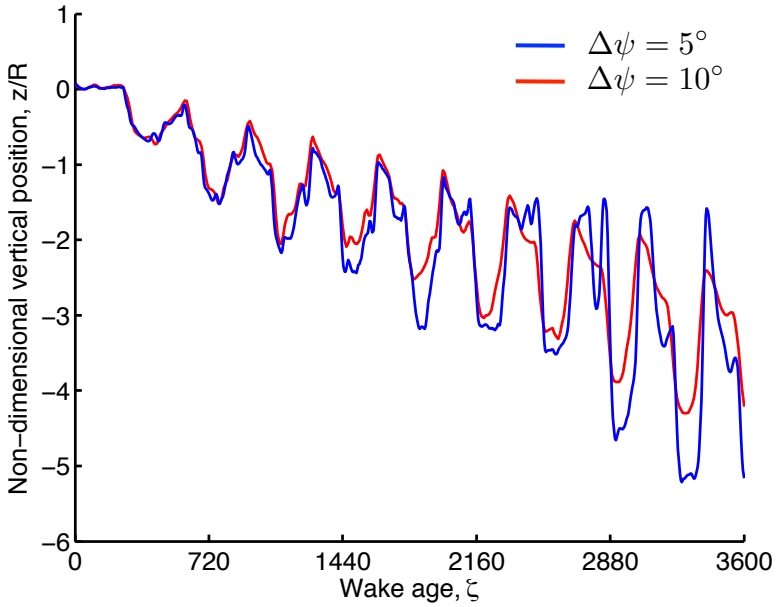

(b) z/R versus wake age

Figure 3.41: Predicted wake positions from the FVM for a rotor operating in forward flight for different discretization: (a) Radial displacements, r/R, and (b) Vertical displacements, z/R, as a function of wake age.

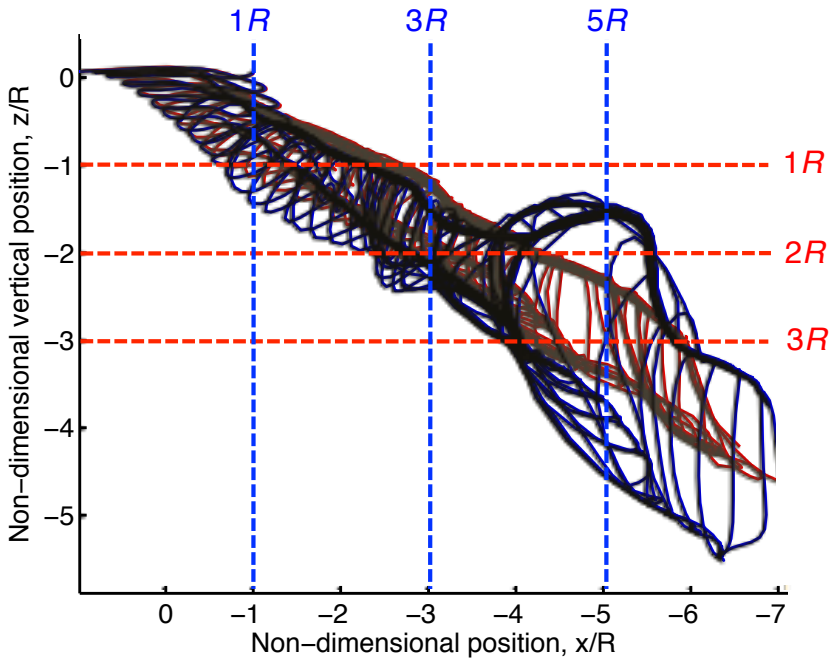

Figure 3.42: Schematic showing the planes of interest where induced velocities were extracted.

after 10 wake turns. While the wake geometries in hover showed a converged trend (Fig. 3.38), the solution with a 5° grid resolution showed considerable differences in forward flight when compared to the 10° resolution, especially at later wake ages. These differences in the filament positions are better illustrated in Figs. 3.41(a) and 3.41(b), which show the radial and axial displacements of the wake filaments at different discretizations. Good agreement is seen between the 5° and 10° wake geometries at early wake ages, i.e., $\zeta < 1,440°$, but the difference increase between the two discretizations at later wake ages.

Because for the problem of brownout the induced velocities in the flow field are of interest, vertical and horizontal planes of the total velocity contours were extracted at the planes shown in Fig. 3.42. The planes were chosen to identify the changes in the induced velocity field both closer and farther away from the rotor. Figure 3.43 shows the time-averaged total induced velocity

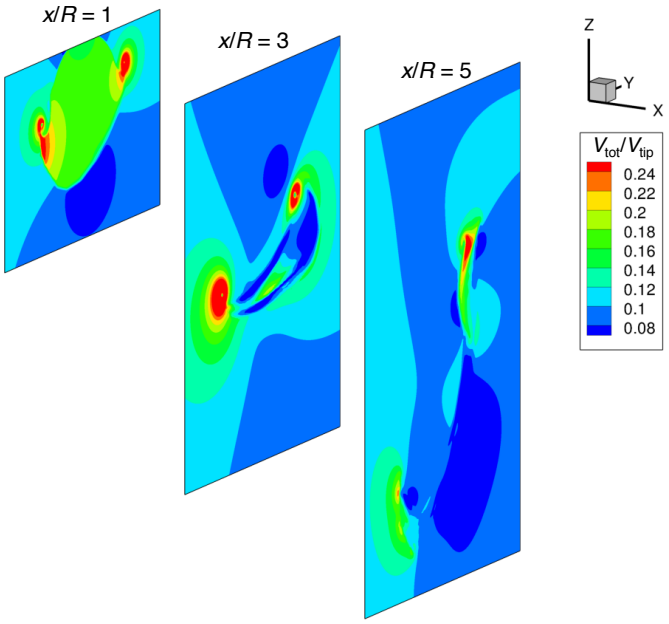

(a) 5° azimuthal discretization

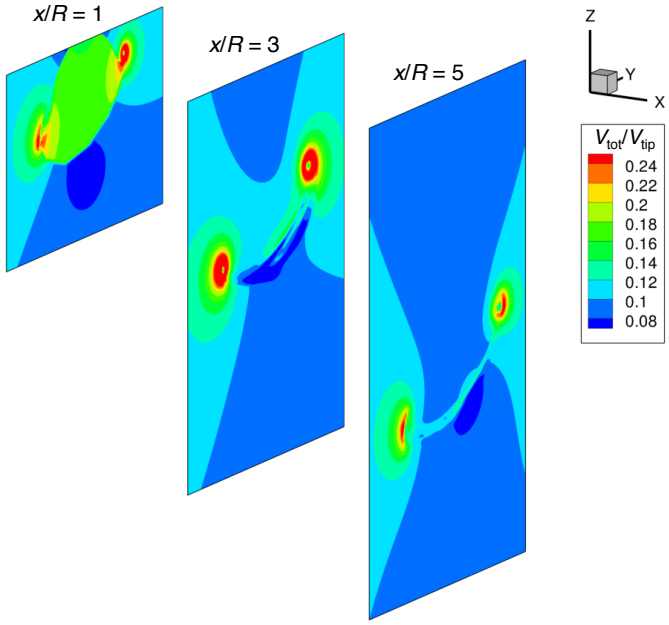

(b) 10° azimuthal discretization

Figure 3.43: Time-averaged total induced velocity contours induced at the planes $x/R = 1$, $x/R = 3$, and $x/R = 5$ for: (a) $\Delta\psi = 5^\circ$, and (b) $\Delta\psi = 10^\circ$

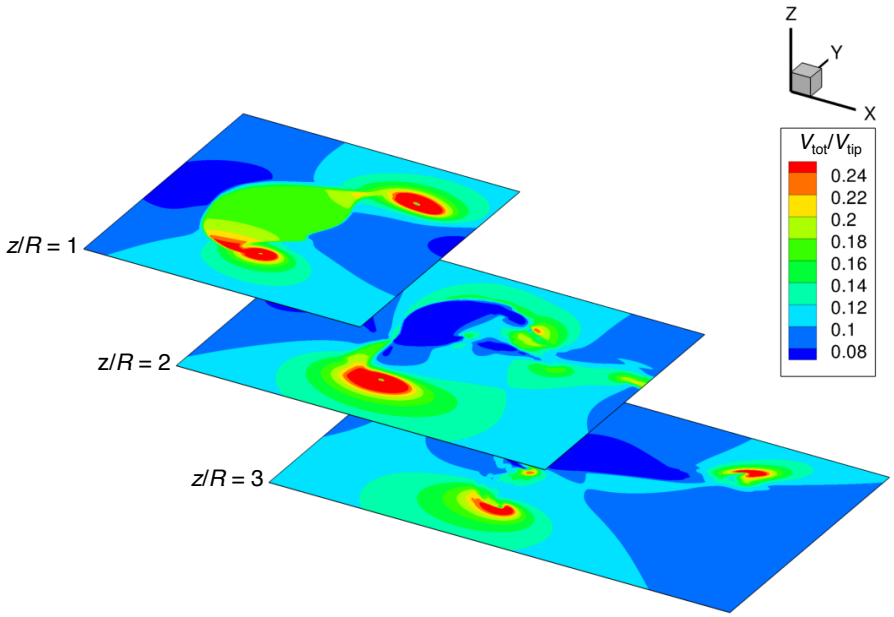

(a) 5° azimuthal discretization

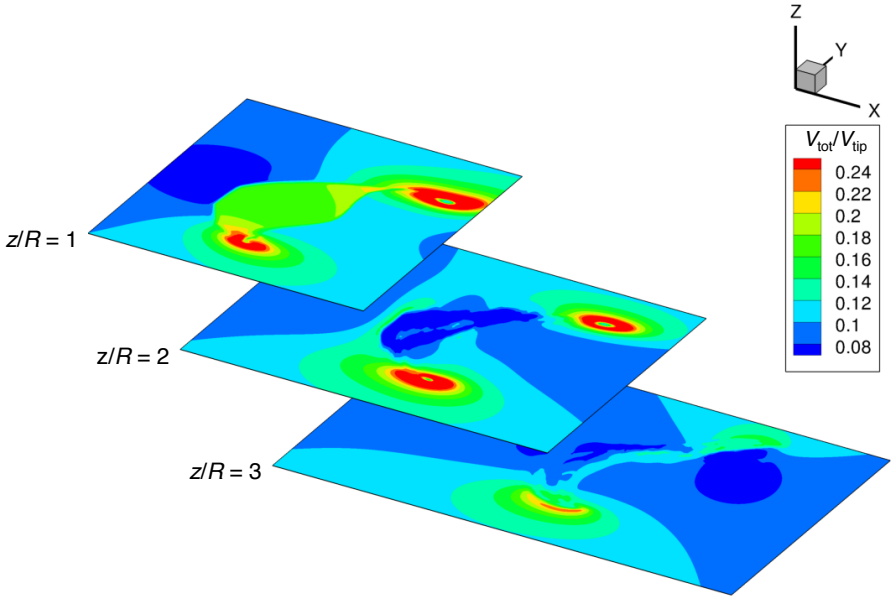

(b) 10° azimuthal discretization

Figure 3.44: Time-averaged total induced velocity contours induced at the planes $z/R = 1$, $z/R = 2$, and $z/R = 3$ for: (a) $\Delta\psi = 5°$, and (b) $\Delta\psi = 10°$

at the vertical planes at $x/R = 1$, $x/R = 3$, and $x/R = 5$ from the rotor shaft axis for azimuthal discretizations of 5° and 10°. While the general trend of the velocity contours are similar for the solutions obtained using the two discretizations, the velocity contours increasingly differ farther away from the rotor. This outcome is expected as the wake filament geometries are different at later wake ages; see Fig. 3.41. Similar trends were observed at the chosen horizontal planes of interest, as shown in Fig. 3.44, where the differences in the induce velocity contours were the highest for the plane farthest from the rotor, i.e., for $z/R = 3$.

The foregoing convergence studies show that while grid convergent wake geometries can be obtained for $\Delta\zeta = 10^\circ$ for a rotor in hover, a convergent solution for the wake positions (especially at later wake ages) is considerably more challenging to obtain for a rotor operating in forward flight. This difficulty in grid convergence may be attributed in part to the effects of curvature correction associated with the discretization of the continuous tip vortex filaments into straight-line segments; a detailed study of which is presented in Appendix A. The computed self-induced velocity using the traditional Biot–Savart law is dependent on the azimuthal discretization and the vortex core radius, and does not accurately recover the self-induced velocity in regions of high filament radius of curvature (e.g., for a rolled up tip vortex in forward flight), or for a fat-core vortex (e.g., increased core sizes at later wake ages because of vortex diffusion); see Fig. A.3 in Appendix A. The subsequent differences in the self-induced velocities computed using different azimuthal discretizations may account for the different wake geometries shown in Fig. 3.41.

Figure 3.45 shows six instantaneous realizations of the wake geometries during a representative maneuver for 5° and 10° azimuthal discretizations. At time step t_1, the wake geometry in

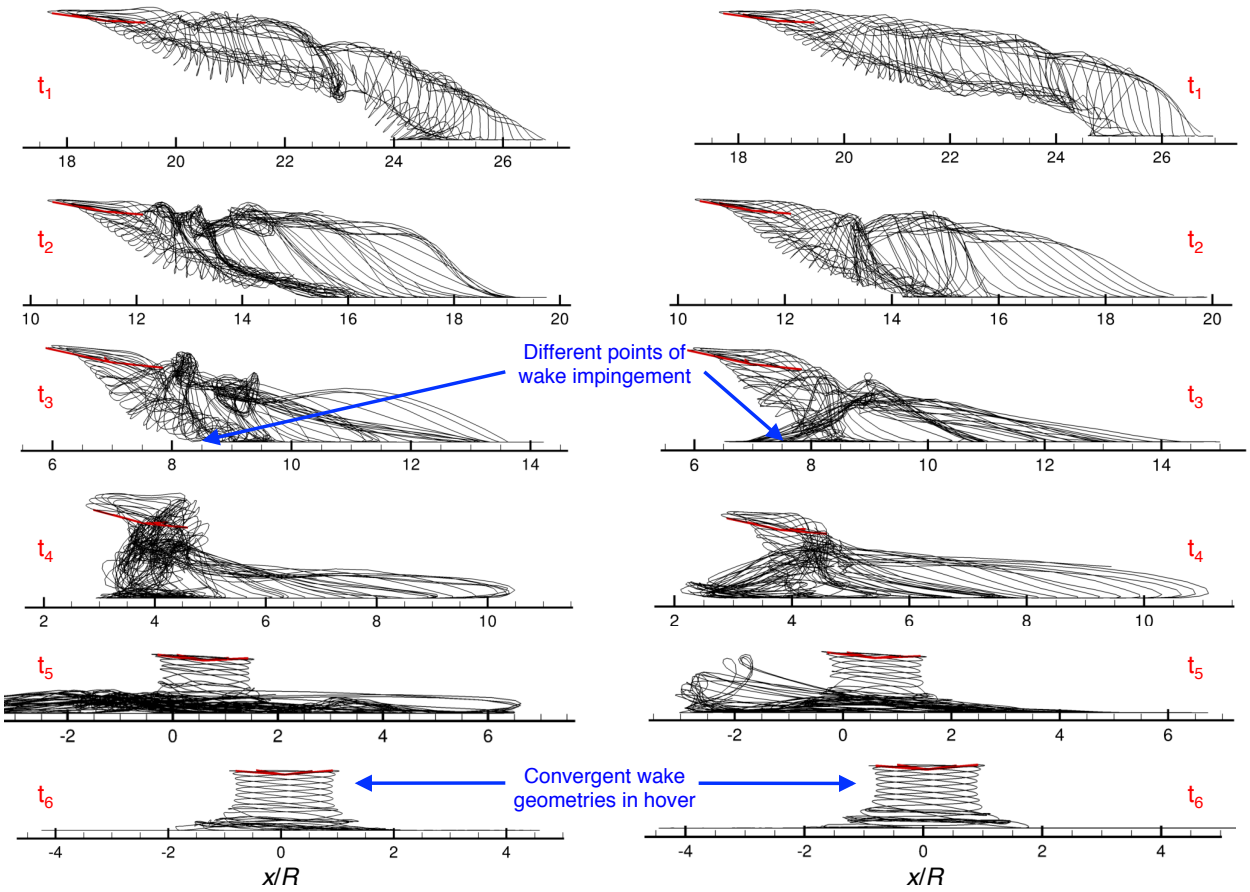

(a) 5º azimuthal discretization

(b) 10º azimuthal discretization

Figure 3.45: Instantaneous wake geometries at six instances during a representative landing maneuver with: (a) 5° and (b) 10°, azimuthal discretization.

forward flight differs between the two discretizations, as shown previously in Fig. 3.40. Consequently, as the rotorcraft approaches closer to the ground the point of impingement of the vortex with the ground occurs at different locations (as shown in time step t_3). The complex interactions of the rotor wakes are compounded by the presence of the ground and, therefore, any initial differences between the wake geometries can grow as the maneuver develops. However, as the rotorcraft settled into hover (at time step t_6), a convergent wake geometry was observed that was independent of the azimuthal discretization.

While further work is required to better understand the behavior of the wake geometry in forward flight, it is recommended that the maximum azimuthal discretization of the tip vortex filament be 10° to reasonably capture the effects of a time varying wake close to the ground. It is further recognized that the inability of the FVM to accurately represent viscous phenomena such as vortex merging and bundling may also limit the far-wake convergence characteristics.

3.5 Brownout Dust Cloud Simulations

Brownout dust cloud simulations are shown for different rotor/rotor and rotor/airframe configurations during a representative landing maneuver. Different instances in the histories of the developing dust clouds were analyzed to gain further insight into the differences caused by the various configurations. Dust clouds produced by the rotors with the UMD-AGARD and cylindrical fuselages were compared against the isolated single main rotor (SMR) to quantify the effect of the fuselage in the development of these clouds. The dust clouds produced by the SMR with the tail rotor (TR), tandem rotor, coaxial system, and side-by-side rotor configurations were analyzed to

identify the relative effects that were produced.

The composition and mineralogy of the sediment particles were obtained from studies of soil samples used in full-scale brownout field tests [38]. The surface of the test range was prepared by tilling the sand prior to the tests to loosen the compacted top layer. A soil sample taken from the range was obtained and analyzed by an independent laboratory to determine the mineralogy and particle size distribution. The particles were found to be mostly quartz, plagioclase, mica and various feldspars, with trace amounts of other minerals and some organic materials; see Fig. 3.46(a). The density of the particles subsequently used in the modeling was a weighted-average of the components in the measured sediment sample, i.e., $\rho_p = 2{,}850$ kg m^3. The corresponding particles size distribution is shown in Fig. 3.46(b), indicating that a large fraction of particles were in the medium (approximately 100 μm) to small (less than 10 μm) diameter range. Obviously, the larger particles are heavier and more difficult to mobilize, and are also not so easily suspended when (or if) they are mobilized. Unless otherwise stated, the current simulations used monodisperse particles that were 20 μm diameter and $\rho_p = 2{,}850$ kg m^3.

The nominal landing profile for the simulations as shown in Fig. 3.47 was developed from Moen et al. [132]. The maneuver begins with the rotorcraft in steady forward flight at an airspeed of 50 kts and at a descent rate of 100 ft min^{-1}. The helicopter then executes a flare maneuver and decelerates into a steady hover with the rotor plane stabilizing at a height of one rotor radius above the ground. The duration of the entire approach is about 35 s, and time is referenced to the start of the brownout simulation, as shown in Fig. 3.47. This simulation was initiated sufficiently far upstream such that initial transients in the free-vortex solution had propagated out, and that the

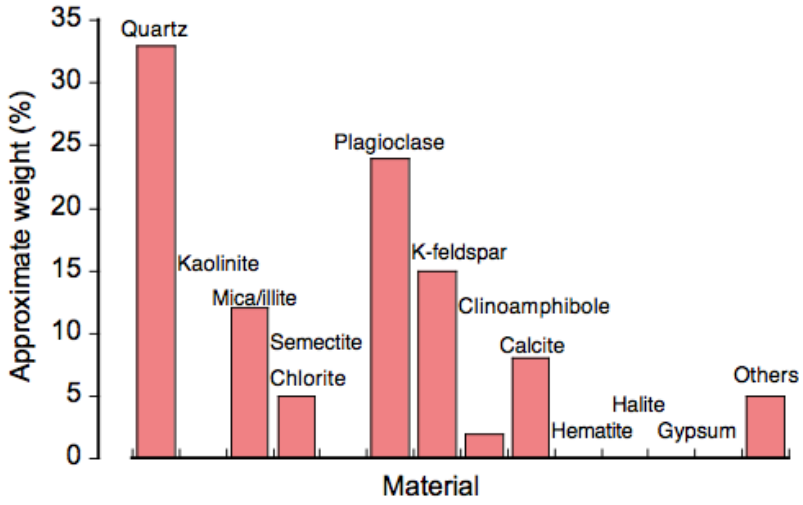

(a) Minerology study of the sample

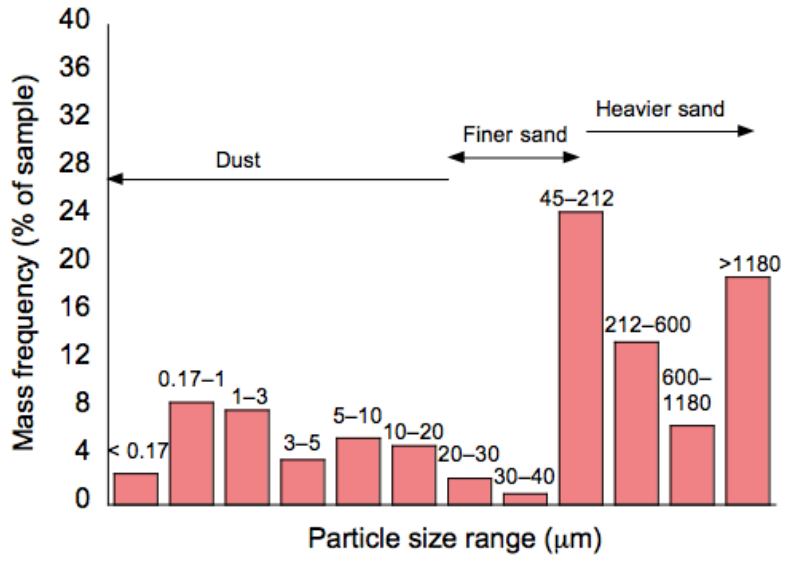

(b) Particle size distribution of the sample

Figure 3.46: Minerology study and particle distribution of a sample from the test range used for full-scale brownout field tests.

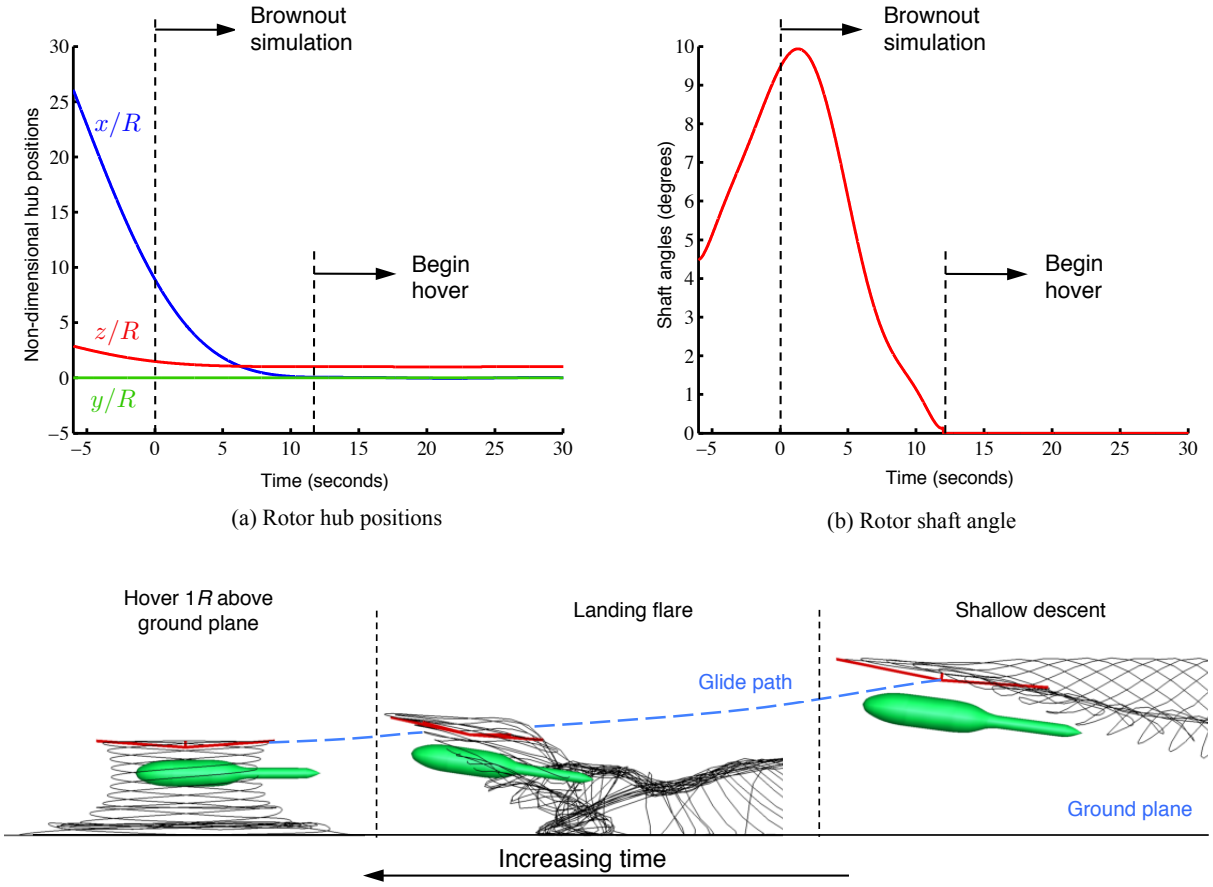

(a) Rotor hub positions

(b) Rotor shaft angle

(c) Representative approach-to-touchdown maneuver

Figure 3.47: Assumed approach profile for landing: (a) Rotor hub center positions; (b) Shaft tilt angles; (c) Overall maneuver.

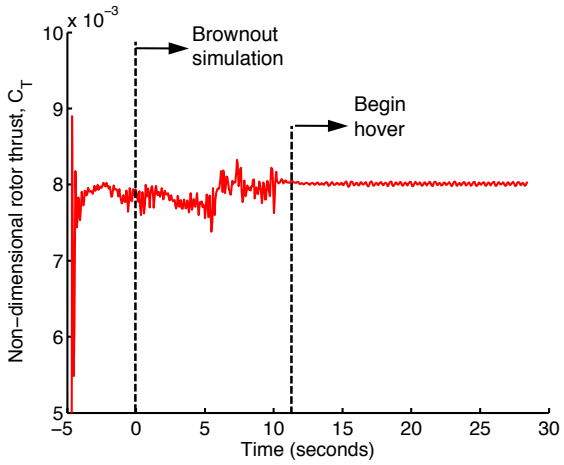

(a) Non-dimensional thrust

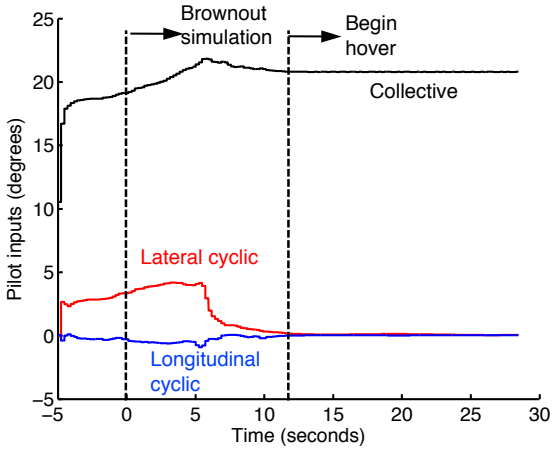

(b) Pilot inputs

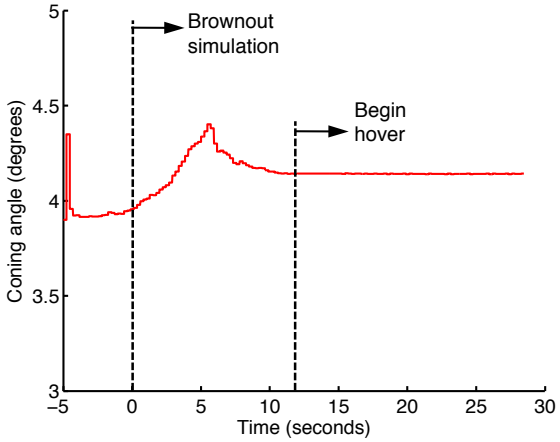

(c) Rotor coning response

Figure 3.48: Representative variation of: (a) Rotor thrust; (b) Pilot control inputs; (c) Rotor flap response, during the prescribed trajectory.

tip vortex filaments were also far enough away from the sediment bed so as not to mobilize any particles.

As previously described in Section 2.7, the rotor is trimmed to a target thrust and zero cyclic flapping response. The rotor thrust, which is assumed perpendicular to the rotor tip path plane, is set to balance the vertical weight of the rotorcraft. Figure 3.48(a) shows the representative variation of the non-dimensional rotor thrust throughout the prescribed trajectory. The large variations in the thrust at the start of the maneuver was attributed to the initial transients in the aerodynamic solution and the fluctuations before the hover phase was a result of the complex interactions of the wake with the rotor and the ground. Figures 3.48(b) and 3.48(c) shows the pilot inputs and the rotor coning response, respectively. The longitudinal and lateral flapping responses were zero because they were the chosen trim targets.

As modeled, the sediment bed consisted of 40 layers of particle clusters that were evenly distributed from $-6R$ to $6R$ longitudinally and from $-6R$ to $6R$ laterally. Notice that the size of the sediment bed is an order of magnitude greater than the size of the rotor, which is required to properly capture the development of the dust cloud. In each layer, 2.25×10^4 particle clusters were eligible for pickup, giving a total of 9×10^5 potentially uplift-eligible clusters. The clusters were assumed to be associated with 10^2 particles each, giving up to 1.9×10^7 initial particles in the dust cloud simulation. Additional particles could be entrained into the simulation from bombardment processes, which typically added about 10^7 particles to the dust cloud at later times.

3.5.1 Effects of the Fuselage

The effects of the UMD-AGARD fuselage as well as the cylindrical fuselage on the development of the dust clouds during the landing maneuver are presented in this section. The development of the wake geometry, the induced velocity field near the ground, and the dust cloud were tracked at four instances during the landing maneuver corresponding to an approach to landing ($t = 4$ s), flare ($t = 6$ s), settle into hover ($t = 10$ s), and hover ($t = 22$ s). Towards the end of the landing maneuver, the rotorcraft hovers above the sediment bed for $t = 12$ s, which allows for the understanding of the effects of the rotor wake on the development of the dust cloud as a steady state hover is realized. A further comparative study of the dust clouds between the two different fuselages is presented later in Section 3.5.1.2.

3.5.1.1 UMD-AGARD Fuselage

Figure 3.49(a) shows the dust cloud and induced velocity at t = 4 s after the beginning of the simulation, when the helicopter is decelerating and transitioning toward the hover state. Notice how the main rotor wake interacts with the fuselage, specifically as it wraps around the tail. At this earlier time, the interactions between the rotor wake and the sediment bed were rather weak, so very few particles were mobilized from the surface of the bed.

Figure 3.49(b) shows an instantaneous realization of the dust cloud during the flare phase of the landing maneuver. The nose-high attitude of the helicopter was accompanied by rapid changes in the wake geometry. At this stage, the vortex filaments interacted with the fuselage at both the nose and tail. The velocity contour plots in Fig. 3.49(b) show relatively large regions

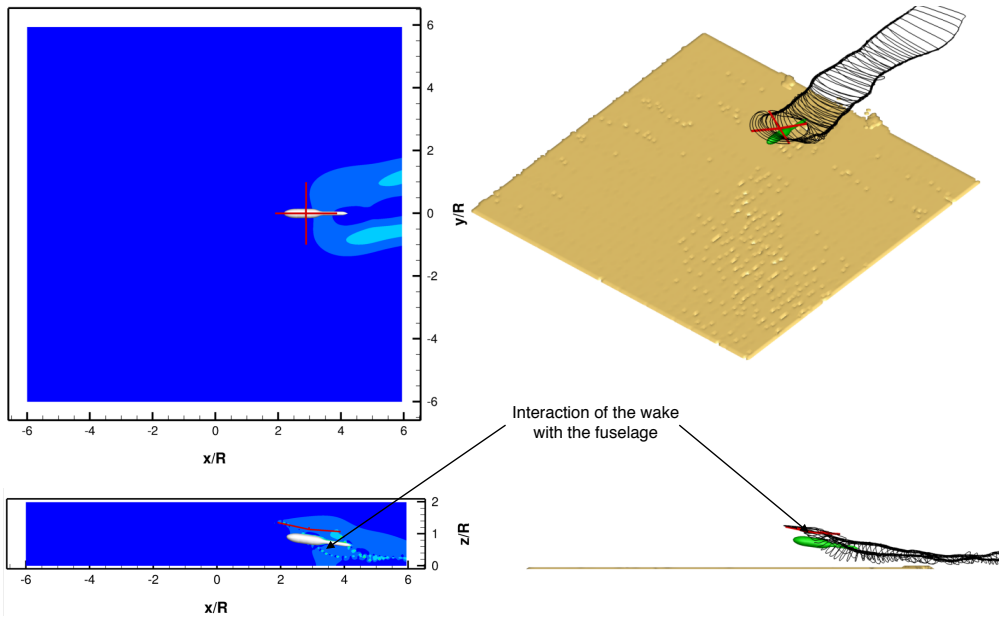

(a) $t = 4$ s

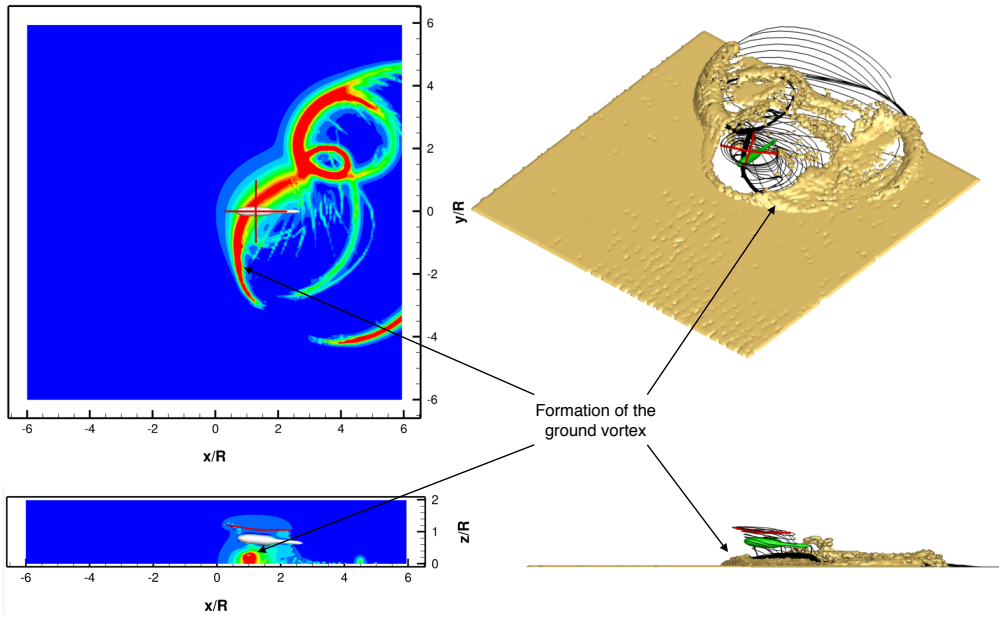

(b) $t = 6$ s

Figure 3.49: Development of the dust cloud when using the UMD-AGARD fuselage configuration at time $t = 4$ and 6 s of the landing maneuver.

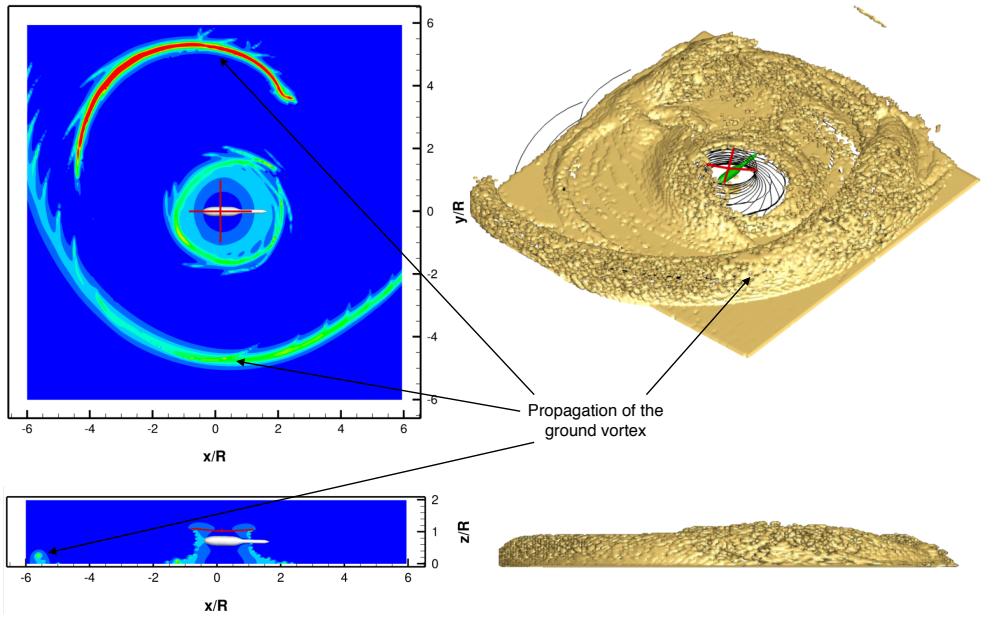

(a) $t = 10$ s

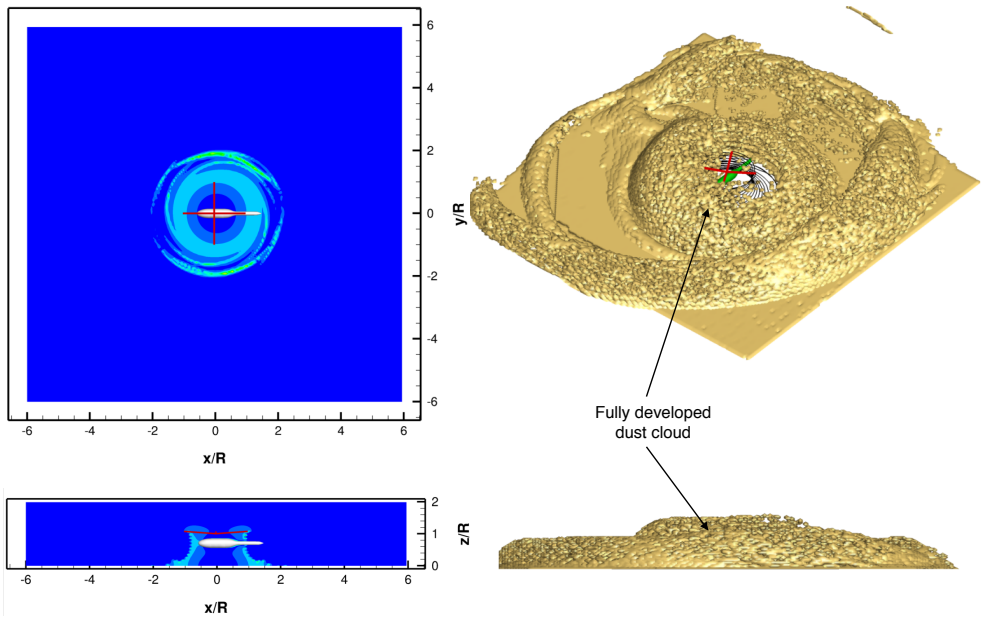

(b) $t = 22$ s

Figure 3.50: Development of the dust cloud when using the UMD-AGARD fuselage configuration at time $t = 10$ and 22 s of the landing maneuver.

of higher induced velocities that were caused by the formation of a ground vortex ahead of the rotor disk [64, 66]. In these regions, the particle threshold velocities on the bed were exceeded, and significant quantities of sediment were mobilized and uplifted there, a result also seen experimentally [8]. Notice that uplifted particles that were trapped within this ground vortex were recirculated and bombarded back onto the particle bed, thereby ejecting many more new particles into the simulation.

At time $t = 10$ s, as shown in Fig. 3.50(a), the wake starts to expand forward of the rotor disk as the rotorcraft decelerates and enters into hovering flight. Because of the expansion of the wake boundaries along the ground relative to the rotor, the regions of higher flow velocity shift radially away from the rotor, as does the development of the dust cloud, which then starts to form into a toroidal shape. The radial expansion of the wake is evident in the induced velocity field, which shows the forward propagation of the ground vortex over the bed. The side-view of the dust cloud in Fig. 3.50(a) shows that the dust reaches both the rotor and the fuselage, and this stage would probably be accompanied by some loss of some visual cues for the pilot. At time $t = 22$ s, as shown in Fig. 3.50(b), the dust cloud has become fully developed into a characteristic dome-shaped cloud with significant amounts of dust being continuously reingested through the rotor disk.

3.5.1.2 Cylindrical Fuselage

Figures 3.51 and 3.52 show the development in wake geometry, induced velocity field near the ground, and the dust cloud at four time steps during landing maneuver for the rotor with the fuselage with the cylindrical cross-section. Qualitatively, the results shown for the cylindrical

fuselage were found to be similar to those for the UMD-AGARD fuselage, as shown previously in Figs. 3.49 and 3.50.

Figure 3.51(a) shows the solution at t = 4 s after the beginning of the simulation, when the helicopter is decelerating and transitioning toward the hover state. Similar to the results shown in Fig. 3.49(a), the interactions between the rotor wake and the sediment bed at this time were weak, resulting in the uplift of just a few particles.

Figure 3.51(b) shows an instantaneous realization of the dust cloud in the flare phase of the landing maneuver. The vortex filaments interacted with the fuselage at both the nose and tail, and the regions of higher induced velocities in the contour plots in Fig. 3.51(b) again shows the formation of a ground vortex. Notice the differences in the induced velocity profile between the UMD-AGARD and the cylindrical fuselage, as shown in Figs. 3.49(b) and 3.51(b), respectively. These differences can be attributed to the changes in the wake geometry because of the unique rotor/fuselage interactions associated with each fuselage shape.

The structure of the propagating ground vortex also appears to depend on the shape of the fuselage, as shown in induced velocity contours in Figs. 3.50(a) and 3.52(a). The radial shift in the higher flow velocity region away from the rotor also affects the development of the outer structures of the dust cloud. Notice that there are also features in the dust cloud that are not associated with the ground vortex, which in this case are a result of the vortices that impinge on the ground during the transition phase of the maneuver (Fig. 3.52(a)). The side-view of the dust cloud in Fig. 3.52(a) shows that the dust is vertically uplifted to the height of the rotor and fuselage. At time t = 22 s, as shown in Fig. 3.52(b), the induced velocity field indicated the formation of disturbances that are

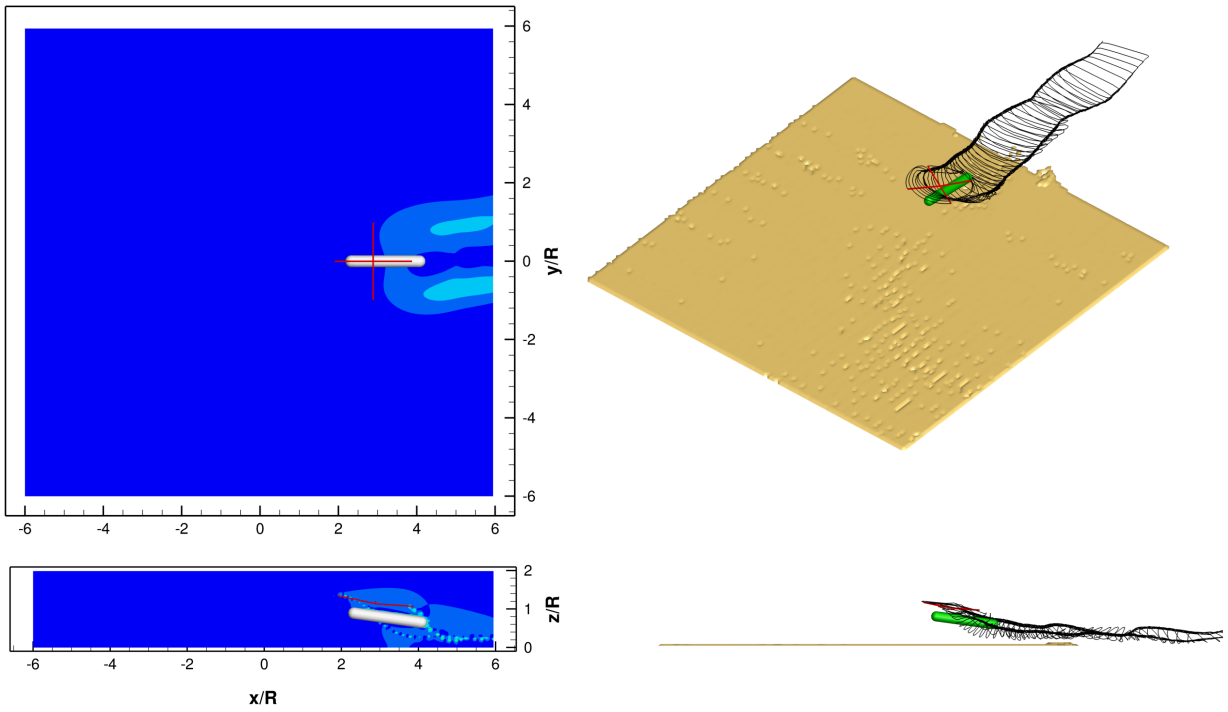

(a) $t = 4$ s

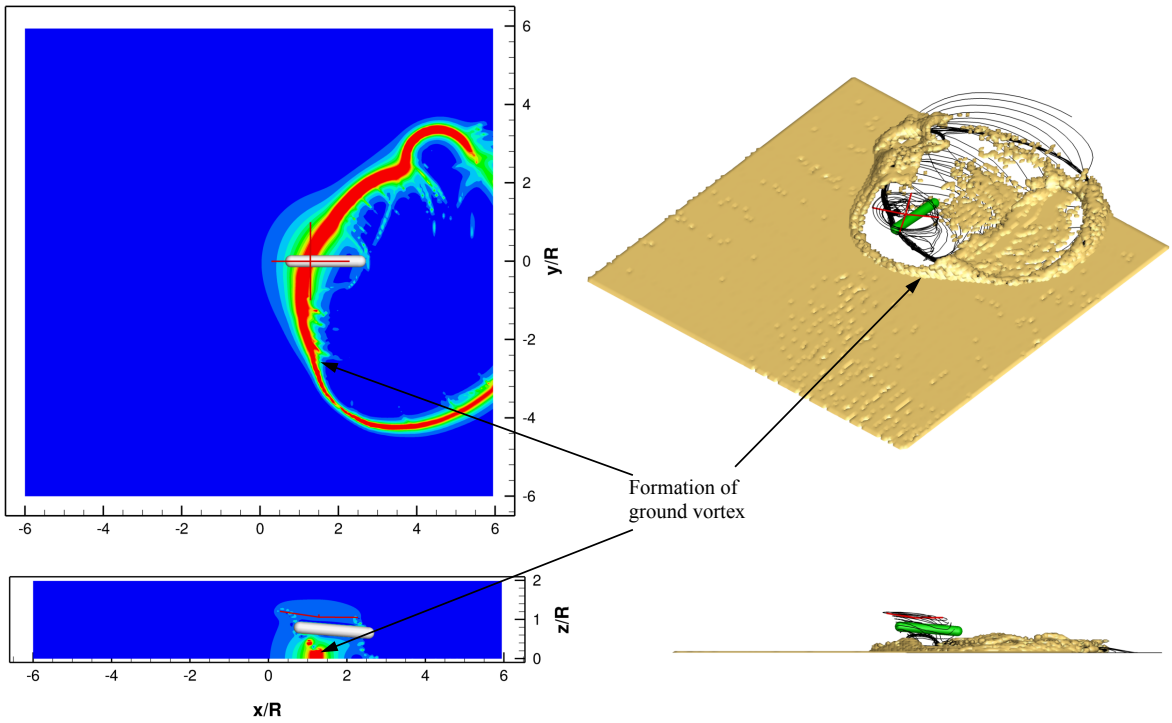

(b) $t = 6$ s

Figure 3.51: Development of the dust cloud when using the cylindrical fuselage configuration at time $t = 4$ and 6 s of the landing maneuver.

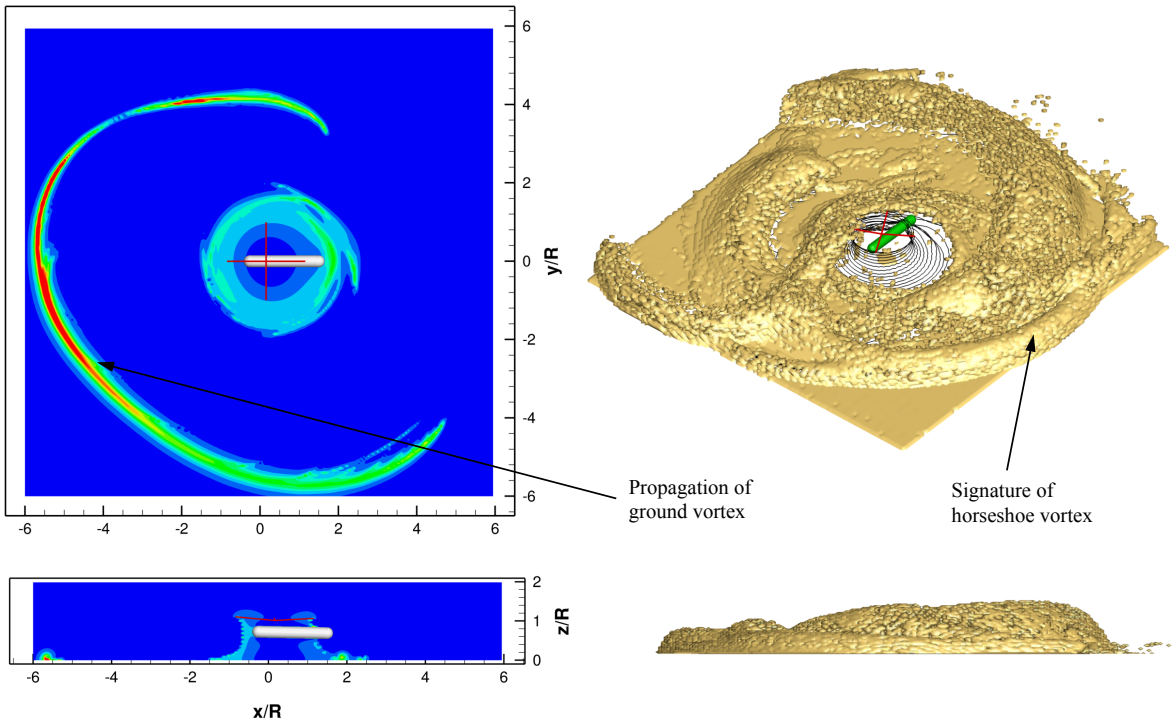

(a) t = 10 s

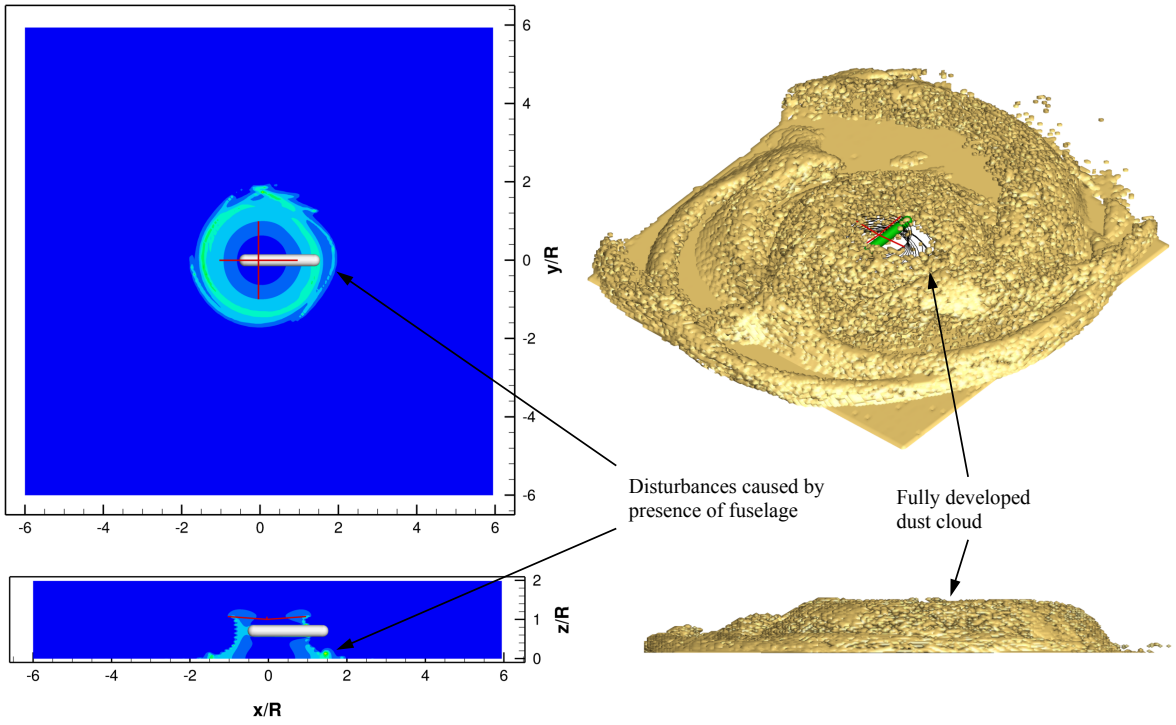

(b) t = 22 s

Figure 3.52: Development of the dust cloud when using the cylindrical fuselage configuration at time t = 10 and 22 s of the landing maneuver.

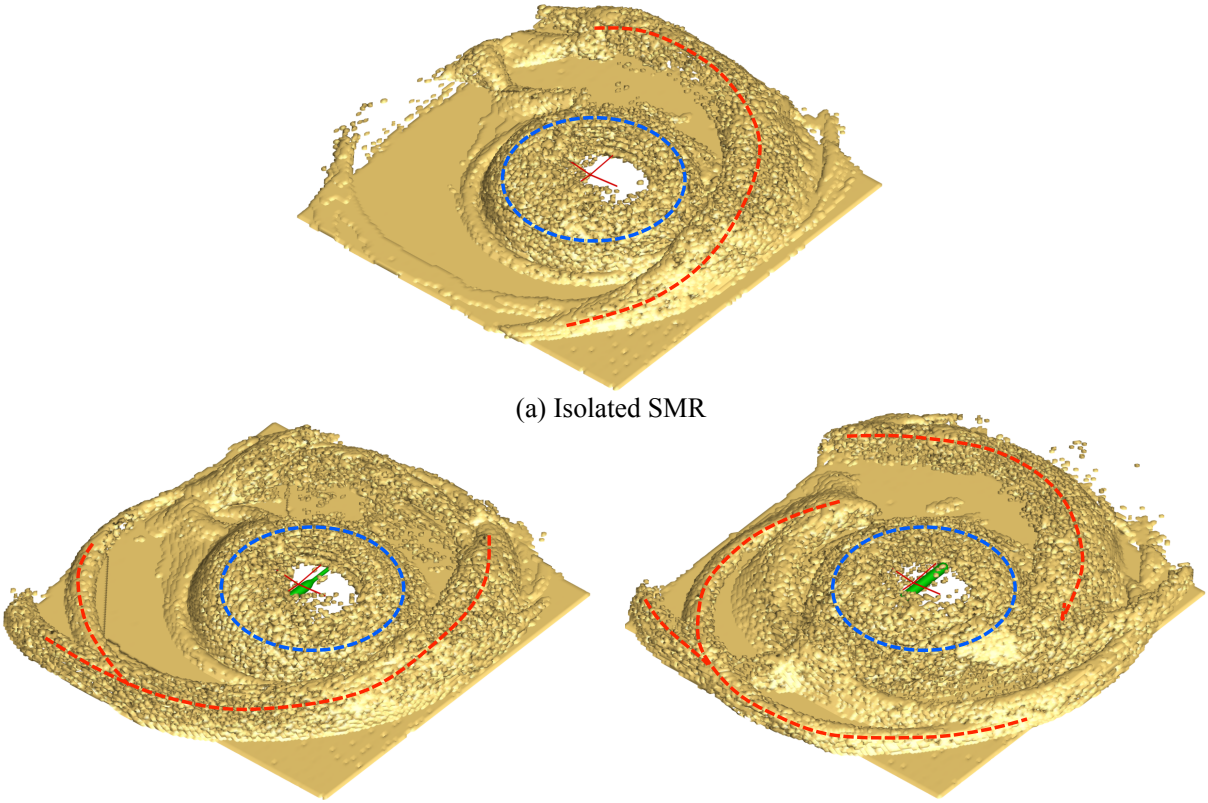

(a) Isolated SMR

(b) UMD-AGARD fuselage

(c) Cylindrical fuselage

Figure 3.53: Simulated dust cloud profiles for the (a) Isolated rotor; (b) Rotor and UMD-AGARD fuselage; and (c) Rotor and cylindrical fuselage.

developed because of the interaction of the rotor wake with the fuselage (Fig. 3.35), and the dust cloud has become fully developed with significant amounts of dust being continuously reingested through the rotor disk.

Figure 3.53 shows predictions of the dust clouds as produced by the isolated SMR at the end of the simulation, as well as for the SMR with the UMD-AGARD fuselage, and for the SMR with the cylindrical fuselage, respectively. As shown in Fig. 3.53, the dust cloud can be decomposed into two distinct regions, namely an outer structure and an inner structure. The outer structure, highlighted in red, develops during the formation and propagation of the ground vortex, similar

to that shown previously in Figs. 3.51(b) and 3.52(a). These structures contain particles that were uplifted by the induced velocity field produced by the propagating vortex (i.e., by exceeding the threshold friction criteria) and also by those particles that were trapped within the ground vortex and so ejecting more particles by bombardment mechanisms. The outer structure of the cloud appears to be sensitive to what happens during the transitional phase from forward flight to hover, in which wake distortions caused by the presence of the fuselage translate into more global flow distortions and further intricacies in the evolving structure of the dust cloud.

The inner structure of the cloud, highlighted in blue in Fig. 3.53, is characteristic of the dome-shaped dust cloud that based on field tests in brownout conditions [6, 7] is often seen to engulf the rotor. Because the presence of fuselage only slightly modifies the rotor wake in hover (see Fig. 3.35), the inner structure of the cloud was seen to be fairly similar in all cases. However, it is recognized that these solutions may change when flow separation effects produced by the fuselage are included into the modeling, which cannot be predicted in this case because of the limitations of the potential flow model being used.

Figure 3.54 shows the time-histories of the total number of particle clusters that were uplifted during the landing maneuver in each case, for the isolated rotor, UMD-AGARD, and cylindrical fuselage configurations, respectively. The step nature of the plot is an artifact of the numerical implementation of mobilization from the sediment bed, where subsequent layers of the bed were activated at pre-determined time intervals. The particle growth quantity trend was similar in all cases, with particles being entrained primarily through the shear mechanism ($t < 5$ s), followed by a rapid increase in the number of particles ($5 < t < 12$ s) from the bombardment ejections that

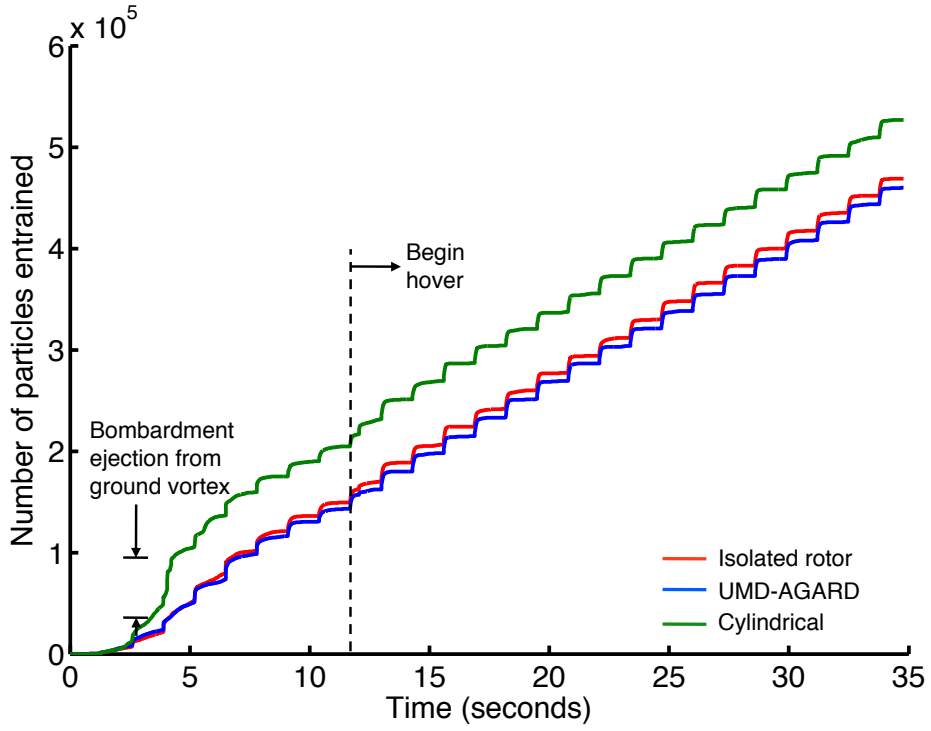

Figure 3.54: Time-history of the total number of particle clusters entrained during the maneuver for different fuselage configurations.

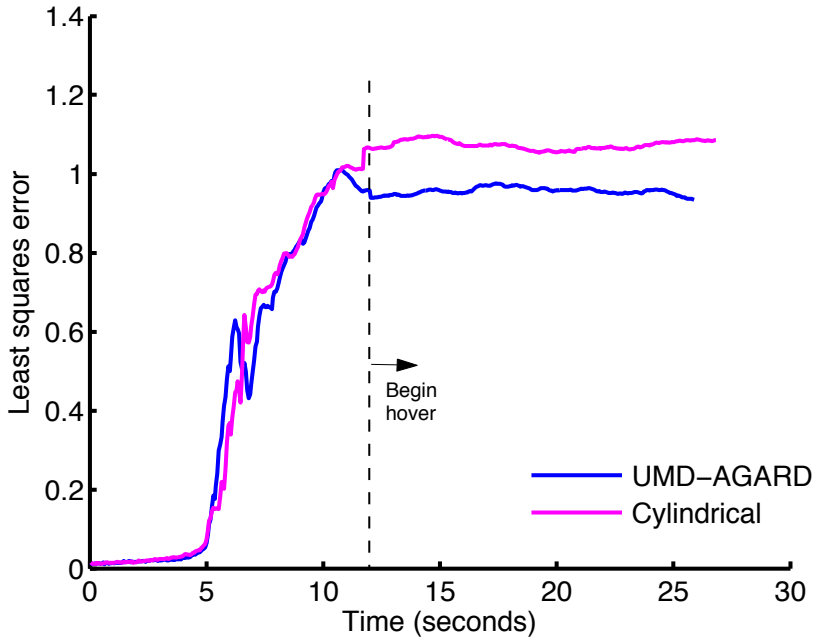

Figure 3.55: Time-history of the least squares error of the particle density in the visual field of between different fuselage configurations and the isolated rotor.

are associated with the formation and propagation of the ground vortex, and finally an increase in particle entrainment in hover ($t > 12$ s). The inclusion of the fuselage resulted in a increase in the total number of particles being uplifted, with the cylindrical fuselage entraining more sediment particles compared to the UMD-AGARD fuselage.

One of the ways of quantifying the differences in the dust cloud is through the use of the spherical map representation, as shown later in Figs. 3.58(a) and 3.58(b), which allows the dust clouds to be compared between a control and baseline configuration, in this case at the end of landing maneuver. Another way of quantifying the differences between two clouds is shown in Fig. 3.55, which shows the time-history of the least square error of the differences in the spherical map between the control (UMD-AGARD or cylindrical fuselage) and the baseline (isolated rotor).

A zero value indicates no differences in the two dust clouds and higher the value, the higher the differences in the clouds.

The initial increase in the value of the error is because of the differences in the cloud structure brought on by the presence of the fuselage, and are consistent with the interpretations of the dust clouds that were shown previously, where local differences in the aerodynamic solution manifest as differences in the clouds as might be seen by the pilot. Once the rotor starts to hover, the error is nearly constant for both the UMD-AGARD and cylindrical fuselage configurations, indicating that the dust solution in hover is nearly identical to that produced by the isolated rotor. Overall, the slender body of the UMD-AGARD fuselage produces minimal rotor-body interactions, while the larger cylindrical fuselage results in larger changes compared to the isolated rotor.

3.5.1.3 Pilot's Field of View

While it is useful to obtain an understanding of the process involved in the formation of a dust cloud from an external observer's point-of-view, brownout is fundamentally a problem of visual obscurations for the pilot, i.e., the pilot is deprived of normal visual cues used to fly the helicopter. To this end, the predicted particle positions in Cartesian space were transformed to a spherical coordinate system centered around the pilot's eyes, as given by

$$r = \sqrt{x^2+y^2+z^2} \tag{3.4}$$

$$\theta_P = \tan^{-1}\left(\frac{y}{x}\right) \tag{3.5}$$

$$\phi_P = \cos^{-1}\left(\frac{z}{r}\right) \tag{3.6}$$

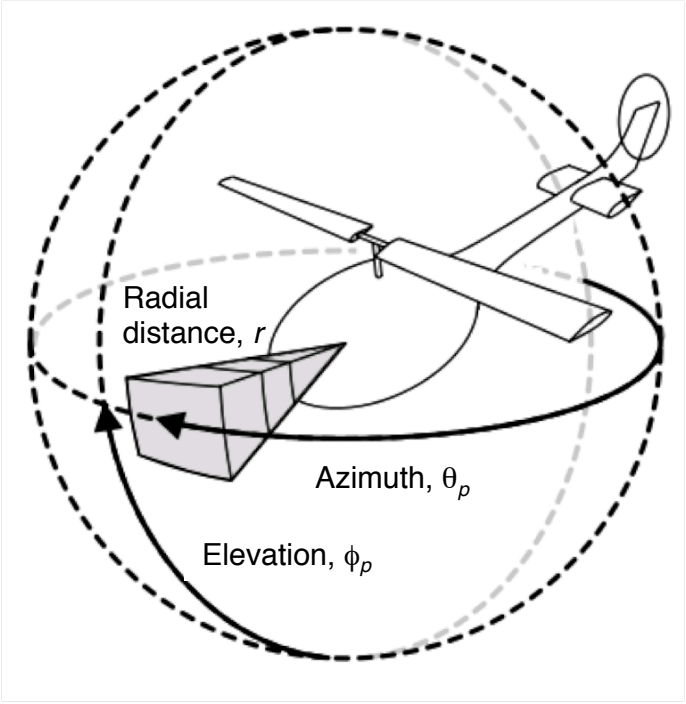

Figure 3.56: Schematic of the coordinate system for projecting the cloud in the pilots FOV. Adpated from Tritschler [13].

where r is the distance of the particle from the pilot, θ_P is the azimuthal location of the particle, and ϕ_P is the elevation of the particle, as shown in Fig. 3.56. The number of particles along a given line of sight (along any radial direction) was assumed to be a surrogate for the degree of expected visual obscuration, i.e., the higher the number of particles along a particular direction, the higher the expected optical obscuration.

These results are plotted on a spherical map, which is shown in Fig. 3.57, with the pilot's position being at $(\theta_P, \phi_P) = (0^\circ, 0^\circ)$. The horizontal axis indicates the azimuthal direction such that either end of the axis $(\phi_P = \pm 180^\circ)$ refers to a point behind the pilot, while the vertical axis indicates the elevation. Also annotated in these plots is a box ranging from -90° to $+90^\circ$ along the azimuth, and -50° to $+5^\circ$ along the elevation axis, which represents the pilot's immediate field of

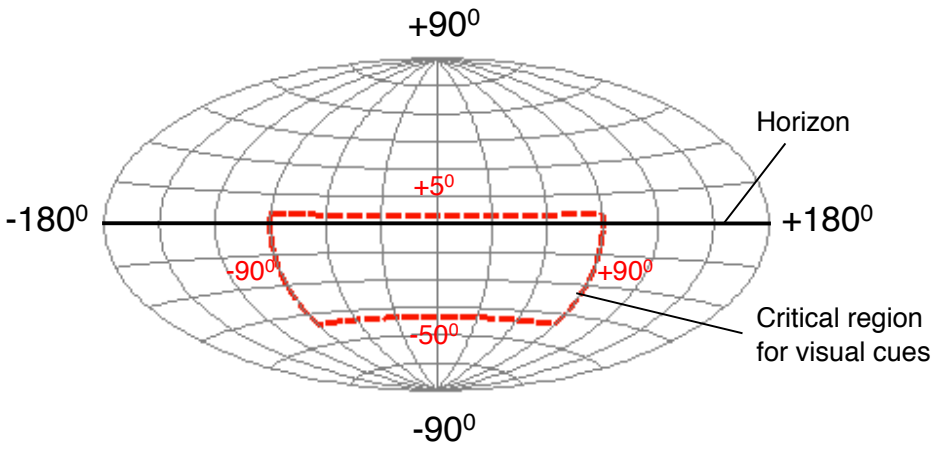

Figure 3.57: Representation of the spherical map centered around the pilot.

view (FOV) from the cockpit [84], although in practice there are portions of this FOV that could be limited, such as the window frames or other parts of the aircraft structure.

Spherical maps of the dust cloud were created for the isolated rotor and for the rotor with a fuselage. These two maps were then subtracted to quantify any differences. Figure 3.58 shows the comparative result for the UMD-AGARD and cylindrical fuselages at the end of the landing maneuver, i.e., t = 22 s. The green color indicates a lower particle count compared to the baseline case (i.e., the isolated rotor), and red indicates a higher particle count. Clearly, differences in the dust cloud are caused by the presence of the fuselage, which suggests that different visual obscurations would also occur compared to those produced by the isolated rotor. These differences arise because of the aerodynamic distortions to the main rotor wake by the fuselage, which does not just manifest just as a local effect, and hence changes occur in the flow environment at many points over the ground.

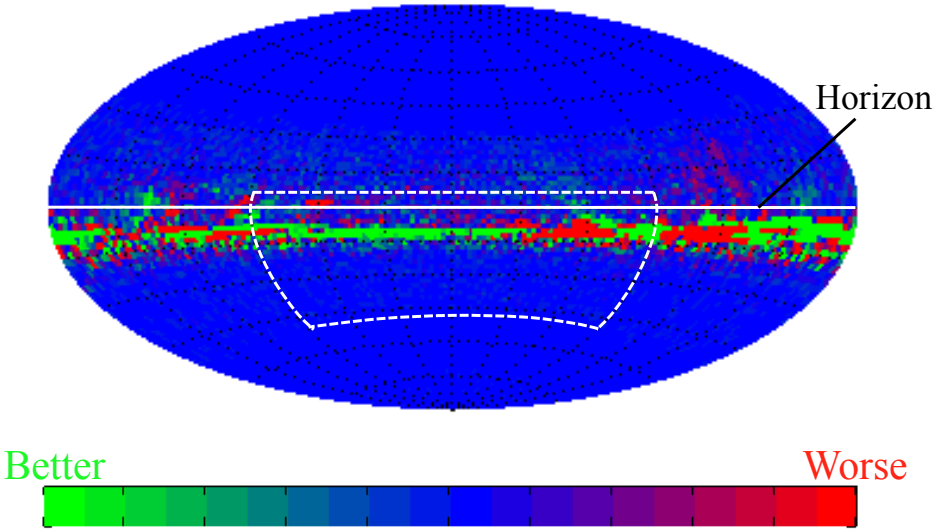

(a) UMD-AGARD fuselage

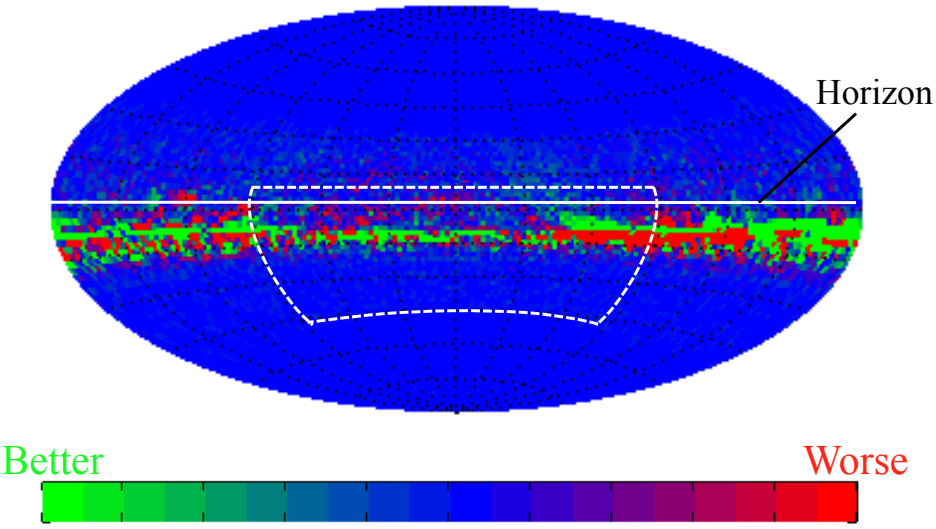

(b) Cylindrical fuselage

Figure 3.58: Differences in particle count in the pilot's FOV for the rotor with the cylindrical fuselage versus the isolated rotor configuration.

3.5.2 Effects of Rotor Configurations

Field observations suggest that different rotorcraft produce different brownout signatures, these being influenced by variations of rotor disk loading, blade loading coefficient, blade geometry, etc [2]. Because of the large number of problem parameters that may influence the formation and evolution of a dust cloud, it becomes increasingly challenging to select one or more suitable metrics that can be held constant and so used to compare two or more different rotor systems or rotorcraft platforms. However, it is still useful to understand why different rotorcraft configurations produce different dust clouds and varying levels of brownout severity, and also to know if there exists a preferred rotor, airframe, and/or other configuration that gives a more benign dust cloud and so may lead to better visibility for the pilot if brownout conditions were to develop.

For example, one way of comparing different configurations is simply by means of a direct comparison of the results produced using geometric and operational parameters of representative rotorcraft. Although this comparison does not necessarily hold constant any particular problem parameter such as disk loading or blade loading, such an approach has the advantage of predicting (e.g., from an operational standpoint) which rotorcraft configuration is most likely to produce a less severe brownout signature under a given set of circumstances, and also to understand why. Such results can be useful for mission planning, and for assessing operational risks that may be associated with the development of brownout conditions during landings and/or takeoffs over certain terrain.

Clearly, the landing weight of the rotorcraft can result in different brownout signatures (see Fig. 3.9), but the signatures will also be dependent on the flight path followed, the actual piloting

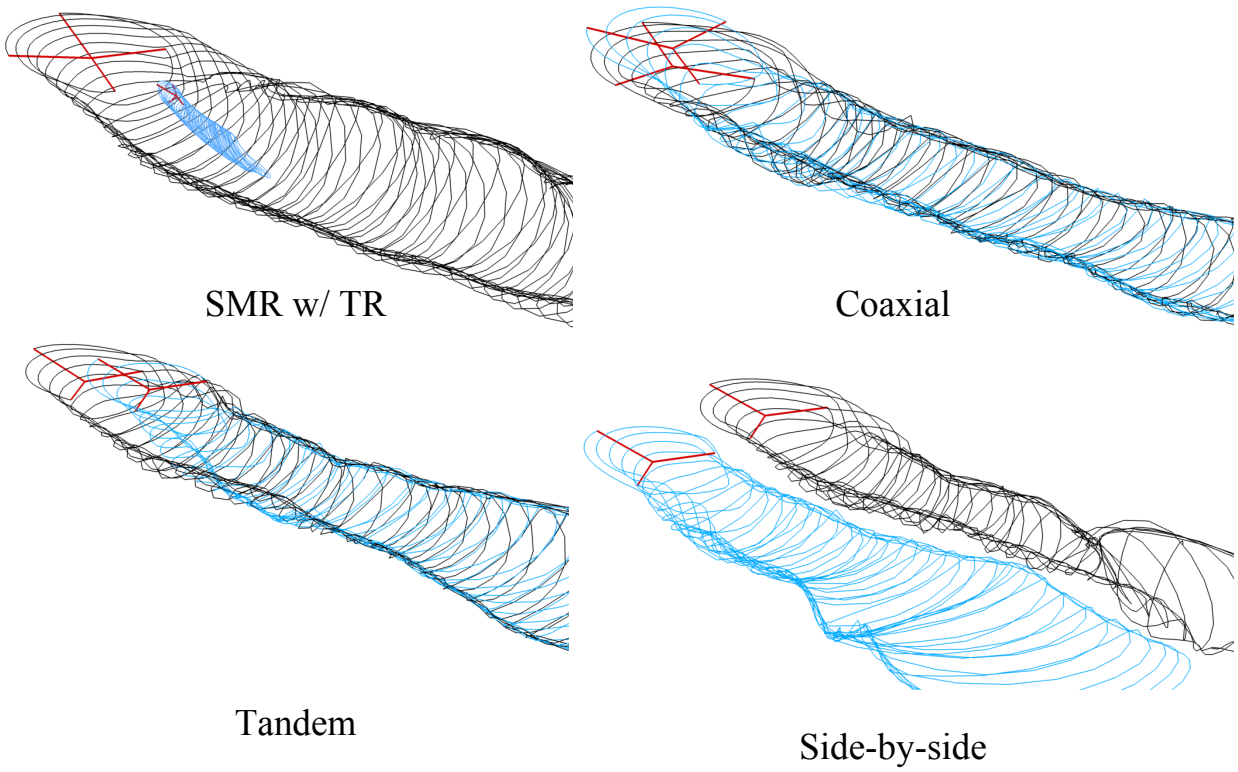

Figure 3.59: Representative wake geometries of the SMR (with TR), coaxial, tandem, and side-by-side rotor configurations.

strategies, and other aspects unique to a given rotorcraft at a particular flight condition. Because a detailed calculation of the landing weight taking into account the various factors affecting it is beyond the scope of the present work (i.e., fuel burn depends on the exact mission followed), the weight of the rotorcraft during landing was assumed to be equal to its published gross weight. The single main rotor (with a tail rotor), coaxial, tandem, and the side-by-side configuration were chosen in the present study with the relevant geometric and operational parameters given in Tables F.7 – F.11 in Appendix F. Only isolated rotor configurations in the absence of an airframe were considered. Examples the of instantaneous realizations of the vortex wakes produced by these configurations is shown in Fig. 3.59.

As in the manner presented previously for the fuselage configurations (see Figs. 3.51 and 3.52), a decomposition of the dust cloud developments for the different rotor configurations are presented in this section. The vortex filaments from each rotor were color coded individually to better understand how the respective wakes evolve. The results are compared to the other rotor configurations in Fig. 3.70.

3.5.2.1 Single Main Rotor with Tail Rotor

Figure 3.60(a) shows the rotorcraft at $t = 4$ s as it approaches the sediment bed. At this instant, the main rotor wake interacted with the ground and a precursor to the formation of the ground vortex can be seen in induced velocity contour maps. The wake from the tail rotor convected all the way to the ground and interacted with the sediment bed.

As the rotorcraft enters the flare phase of the maneuver, at $t = 6$ s, the propagation and the radial expansion of the ground vortex can be seen in the induced velocity contours, as shown in Fig. 3.60(b). This ground vortex is formed by the radial propagation of previously formed vortex (see Fig. 3.60(a)) and results in a band of higher velocity region ahead of the rotor disk, which uplifts vast quantities of dust from the sediment bed. The mobilization and entrainment of sediment is dominated by the induced velocities of the main rotor wake as the tail rotor wake does not convect very close to the ground, as shown in Fig. 3.60(b).

Figure 3.61(a) shows an instantaneous realization of the dust cloud development as the rotorcraft begins to settle into hover. The uplifted dust produced by the earlier propagation of the ground vortex was seen to be reingested through the rotor disk and then bombarding the ground.

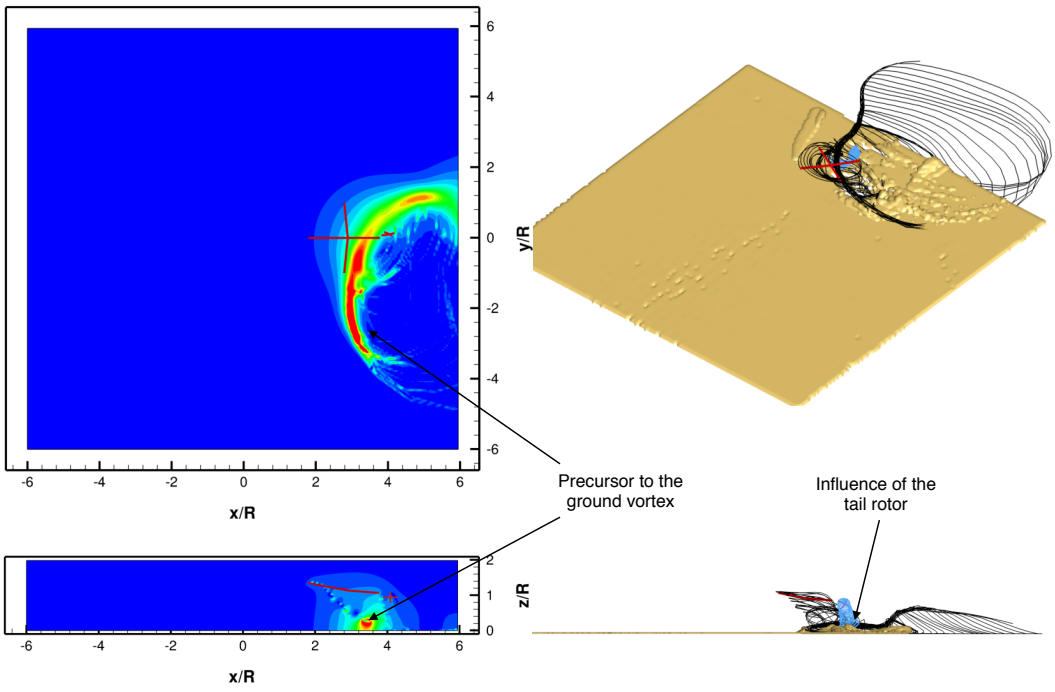

(a) $t = 4$ s

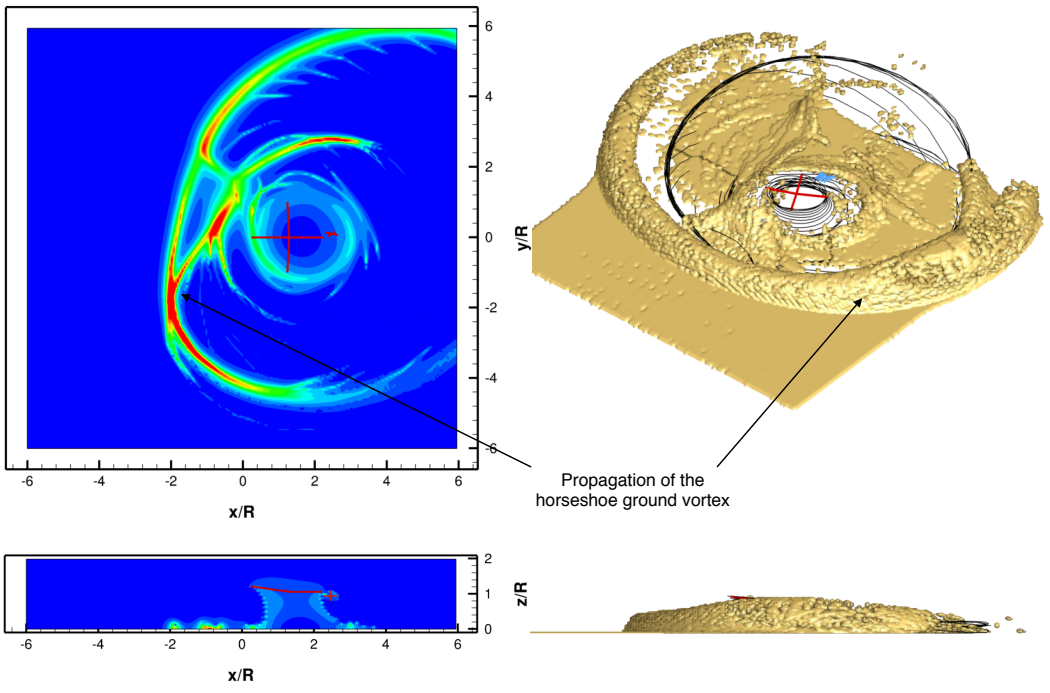

(b) $t = 6$ s

Figure 3.60: Development of the dust cloud for the SMR with TR configuration at time $t = 4$ and 6 s of the landing maneuver.

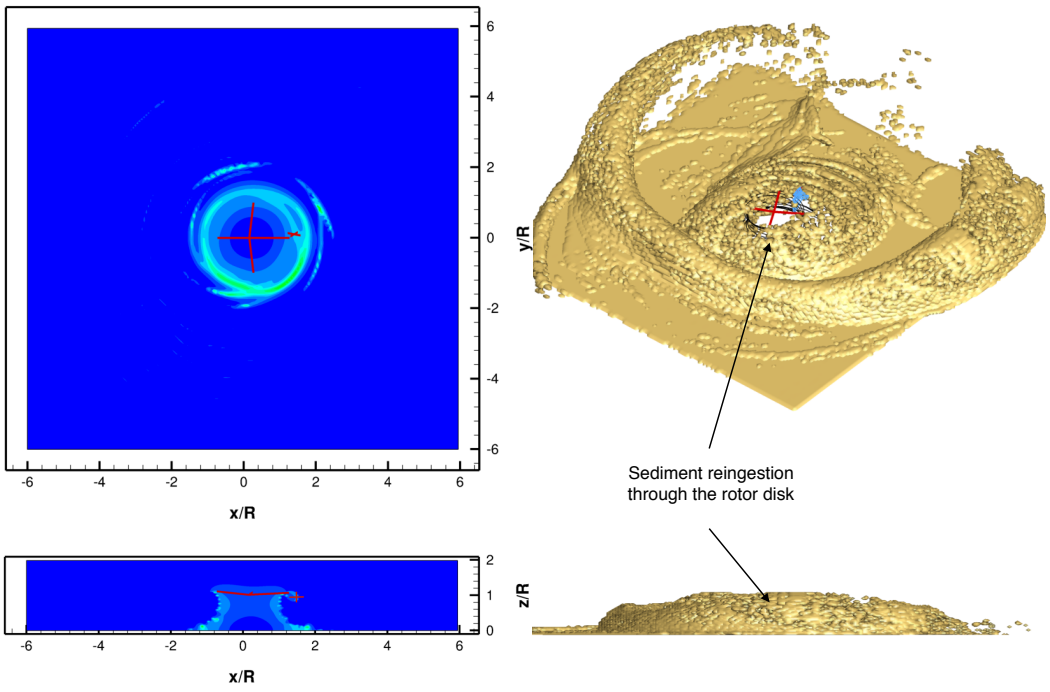

(a) t = 10 s

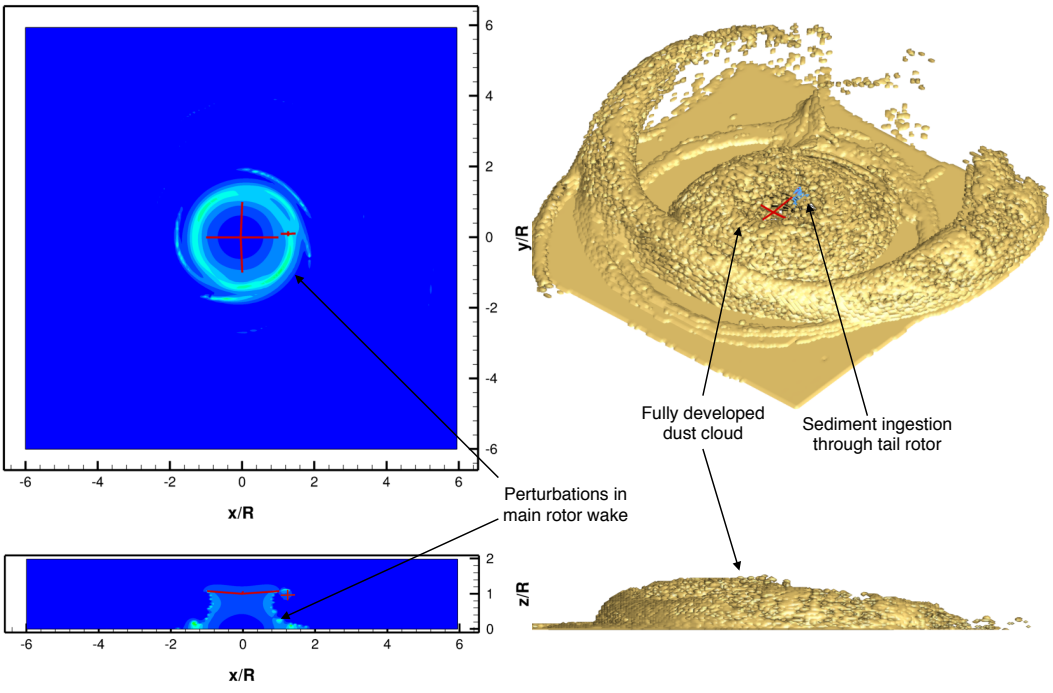

(b) t = 22 s

Figure 3.61: Development of the dust cloud for the SMR with TR configuration at time t = 10 and 22 s of the landing maneuver.

Figure 3.61(b) shows the uplift of sediment particles around the rotor system at $t = 22$ s, with the dust cloud evolving in a familiar dome-shaped structure. Uplifted sediment particles were now ingested both the rotor disks of the main and tail rotor. Because of the downwash of the tail rotor convecting particles away from it, a region of better local visibility was observed in the vicinity of the tail rotor. Notice that the aerodynamic influence of the tail rotor also caused disturbances in the rotor wake of the main rotor, which were observed in the induced velocity profile shown in Fig. 3.61(b).

3.5.2.2 Coaxial Rotor Configuration

Figure 3.62(a) shows the rotorcraft at $t = 4$ s as it approaches the sediment bed. At this instant, the interactions between the upper and lower rotors of the coaxial system caused an increased downwash velocity, which resulted in the tip vortices impinging on the ground closer to the rotor disk as compared to the isolated SMR (see Fig. 3.66(a)). A precursor to the formation of the ground vortex can be identified in the induced velocity contours shown in Fig. 3.62(a).

As the rotorcraft enters the flare phase of the maneuver, at $t = 6$ s, the propagation and the radial expansion of the ground vortex can be seen in the induced velocity contours, as shown in Fig. 3.62(b). As previously discussed, this ground vortex is formed by the bundling of the vortices from the upper and lower rotor and is the source of much of the uplift of dust from the sediment bed, with an increased concentration of dust being formed ahead of the rotor disk, as shown in Fig. 3.62(b).

Figure 3.63(a) shows an instantaneous realization of the dust cloud development as the ro-

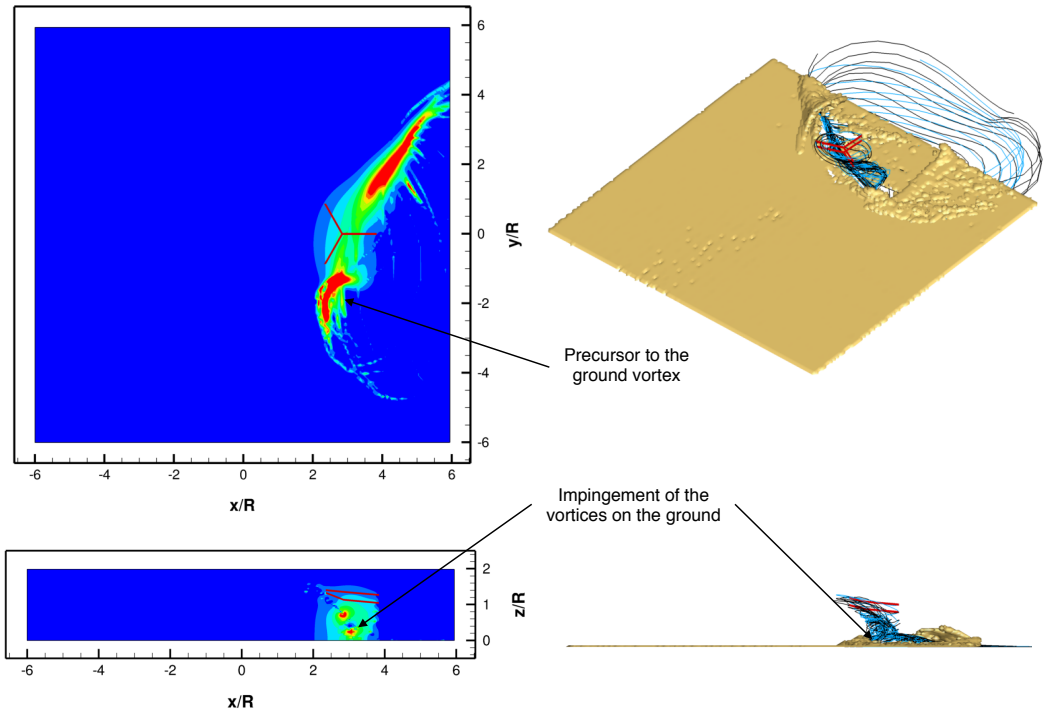

(a) $t = 4$ s

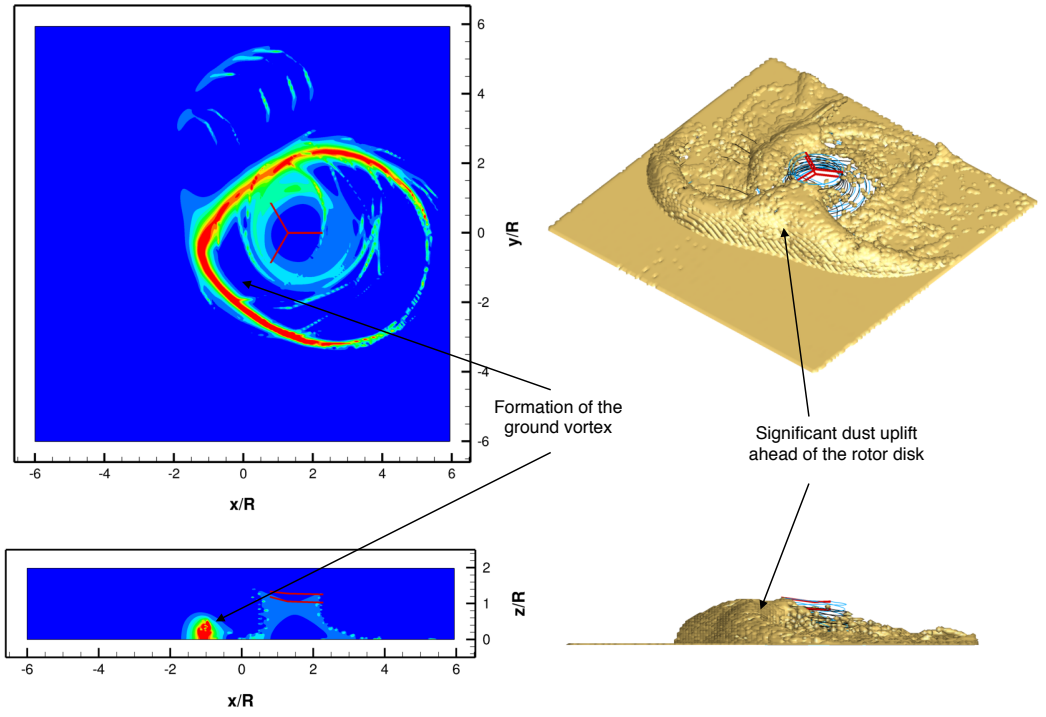

(b) $t = 6$ s

Figure 3.62: Development of the dust cloud for the coaxial rotor configuration at time $t = 4$ and 6 s of the landing maneuver.

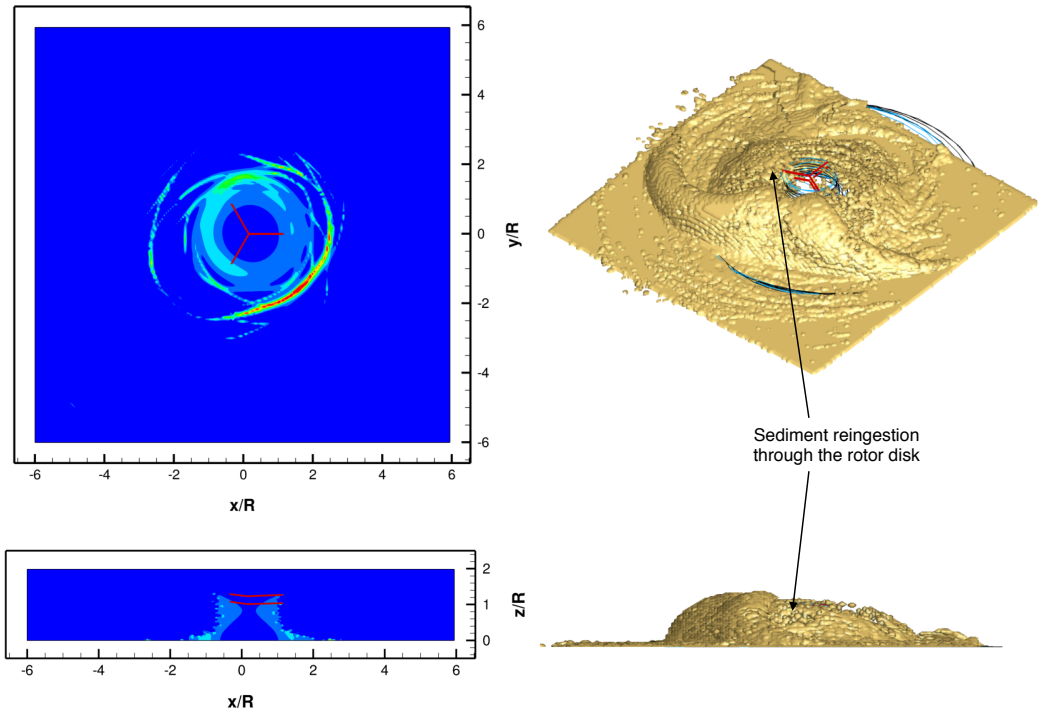

(a) t = 10 s

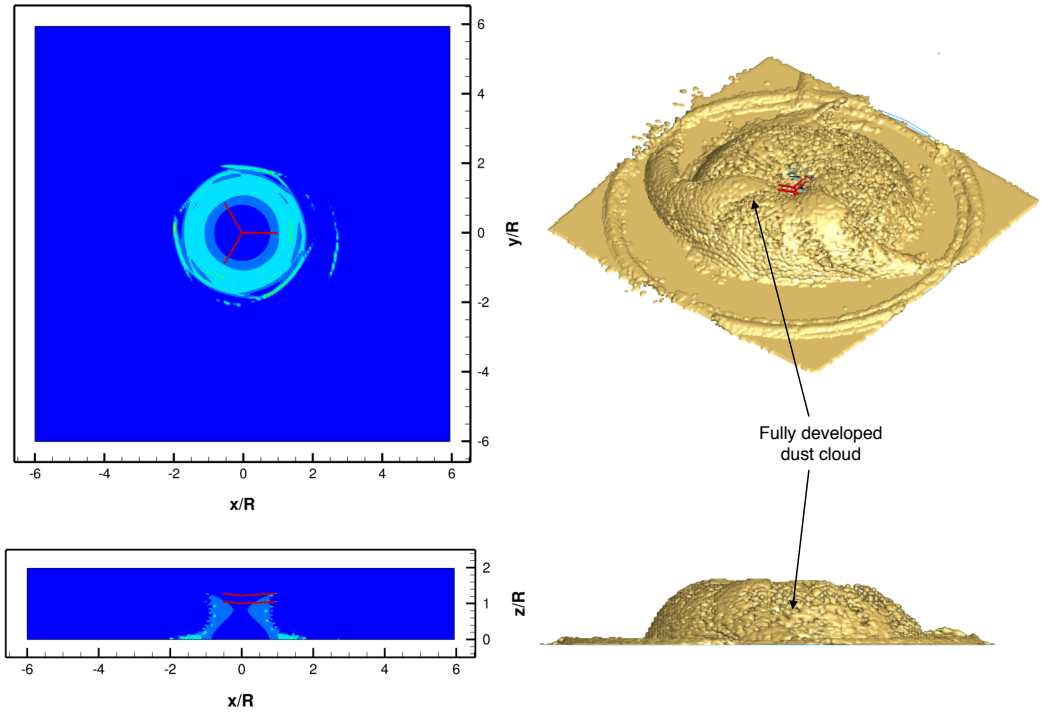

(b) t = 22 s

Figure 3.63: Development of the dust cloud for the coaxial rotor configuration at time t = 10 and 22 s of the landing maneuver.

torcraft begins to settle into hover. The uplifted dust produced by the earlier propagation of the ground vortex was seen to be reingested through the front of the rotor disk and then bombarding the ground. This process uplifted more particles from the sediment bed, which could be expected to increase the levels of visual obscurity for the pilot. The iso view of the dust cloud (Fig. 3.63(b)) shows the uplift of sediment particles around the rotor system and by $t = 22$ s, with the rotor system in hover, the evolution of the dust cloud into a fully developed dome-shaped structure can be seen in Fig. 3.63(b). At this stage, significant reingestion of dust through the rotor system was also observed.

3.5.2.3 Tandem Rotor Configuration

Figure 3.64(a) shows an instantaneous realization of the dust cloud and induced velocity at t = 4 s when the rotorcraft is in descending forward flight. When compared to the SMR results shown previously in Fig. 3.51(a), the induced downwash of the interacting rotor wakes convects the combined wake towards the ground and forms a ground vortex, which can be seen in the velocity profile in Fig. 3.64(a).

At t = 6 s, the ground vortex formed ahead of the rotor quickly propagates forward as the rotorcraft executes the flare portion of the maneuver, as shown in Fig. 3.64(b). The shape of the ground vortex, which can be identified by the region of high velocities in the contour map, is not of the more classic horseshoe shape as was seen with the SMR, but in this case is a more complex system that evolves from the interacting wakes from both rotors. There was also a second, but weaker, ground vortex in this case that was seen to form ahead of the rear rotor that can be seen in

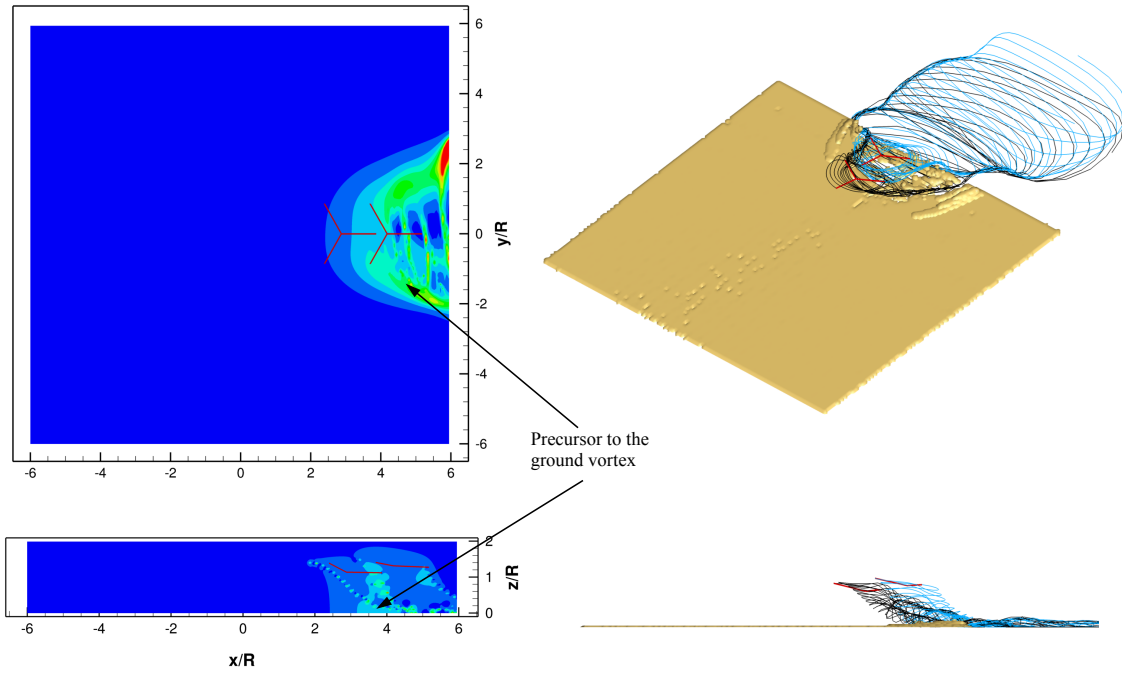

(a) $t = 4$ s

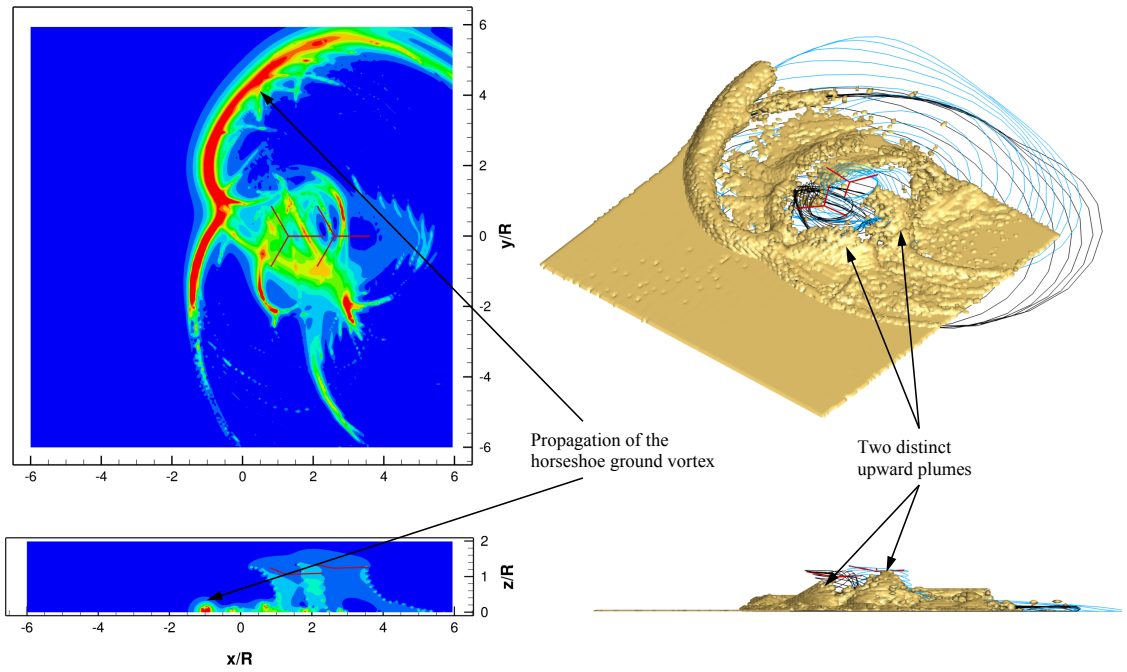

(b) $t = 6$ s

Figure 3.64: Development of the dust cloud for the tandem rotor configuration at time $t = 4$ and 6 s of the landing maneuver.

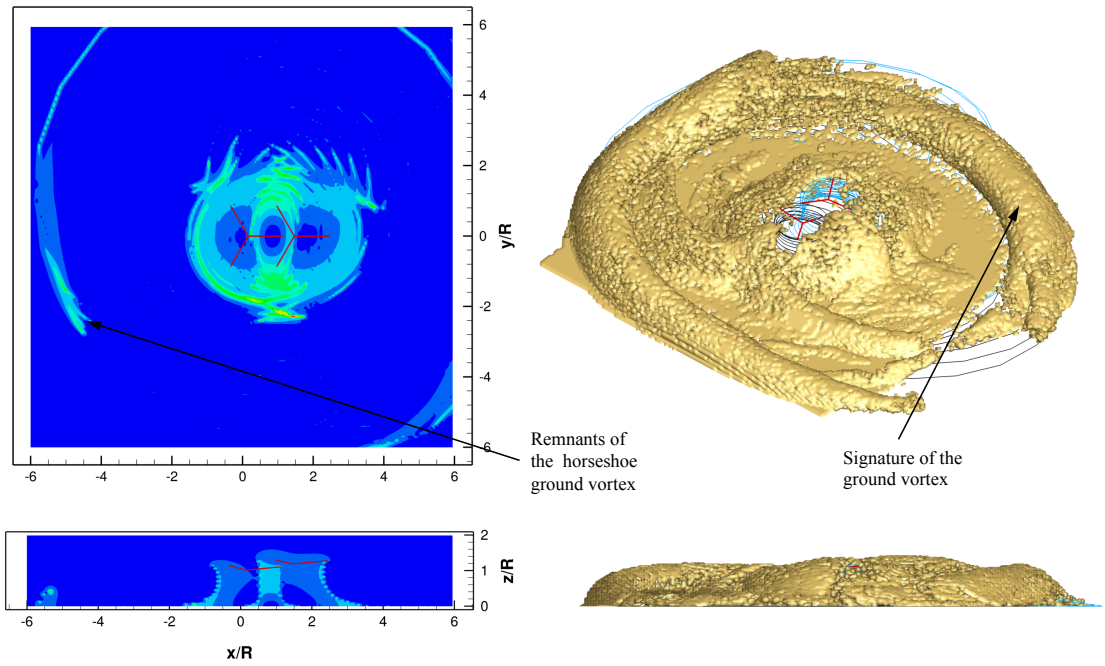

(a) $t = 10$ s

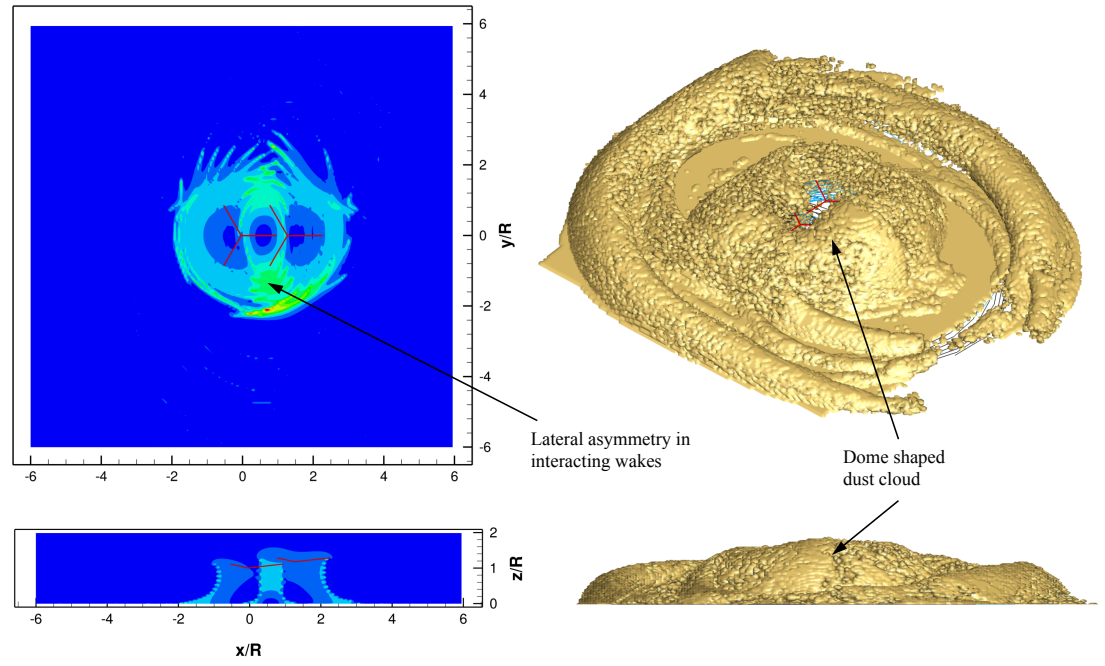

(b) $t = 22$ s

Figure 3.65: Development of the dust cloud for the tandem rotor configuration at time $t = 10$ and 22 s of the landing maneuver.

the groundwash profile (Fig. 3.64(b)), which is responsible for the two distinctive upward plumes of dust.

By t = 10 s, with the rotor about to settle into a steady hover, the radially outward propagating ground vortex mobilizes and uplifts significant quantities of particles that then nearly encircle both of the rotors in a large toroidal cloud, as shown in Fig. 3.65(a). Particles ejected by means of bombardment mechanisms reach a maximum quantity during this phase of the landing. The vertical extent of the dust cloud also exceeds a rotor radius at this stage of cloud development. Notice that the overlapping counterrotating rotors create a strong lateral asymmetry in the wake, which results in significantly higher flow and dust particle velocities in the region between the two overlapping rotors.

Figure 3.65(b) shows the development of the dust cloud at time t = 22 s. By this point, the dust cloud has almost fully developed into a dome shape, with significant reingestion of the suspended particles through both of the rotor disks. The increased downwash in the rotor overlap region and the two lateral outflows of higher velocity is obviously a major source of particle mobilization and uplift, but this effect does not occur in front of the pilot and would not be expected to contribute to further visual obscuration, at least in the shorter term.

3.5.2.4 Side-by-Side Rotor Configuration

Figure 3.66(a) shows the induced velocity field and dust cloud at $t = 4$ s for a side-by-side configuration. Notice that at such an early stage in the landing maneuver, far more sediment particles have been uplifted from the bed compared the SMR, coaxial, and tandem configurations.

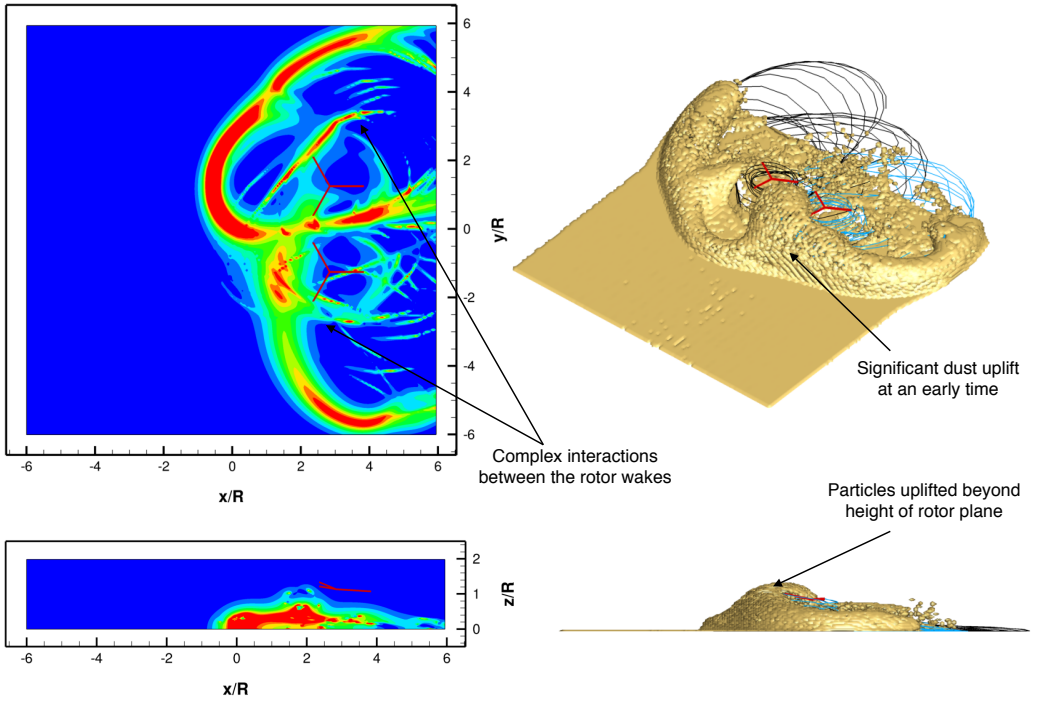

(a) $t = 4$ s

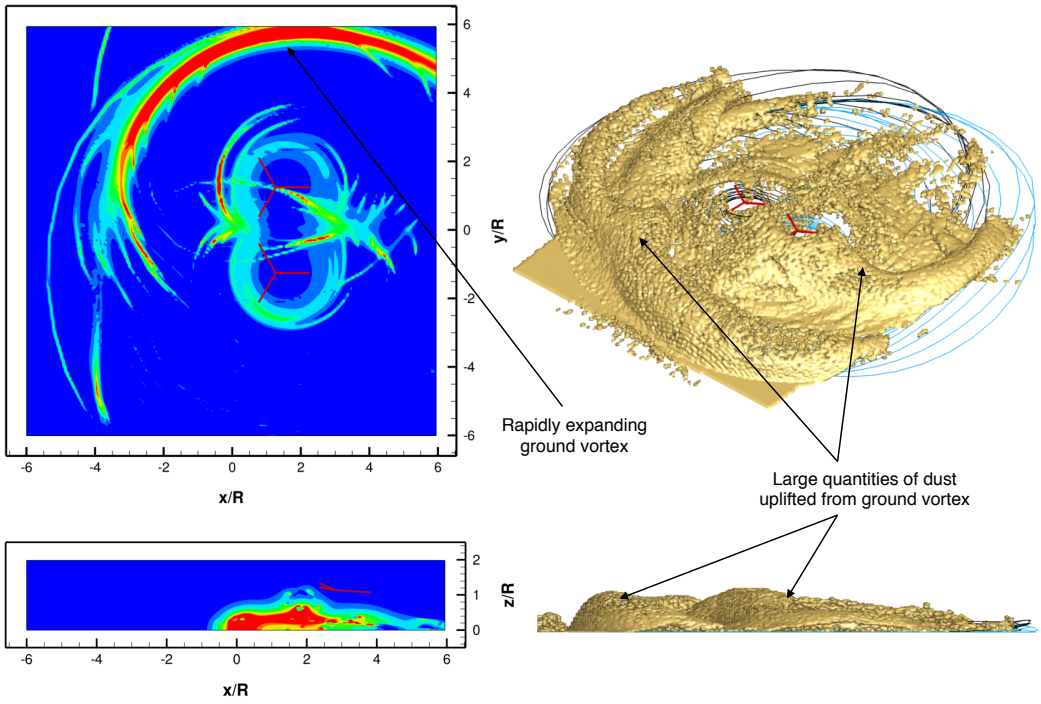

(b) $t = 6$ s

Figure 3.66: Development of the dust cloud for the side-by-side rotor configuration at time $t = 4$ and 6 s of the landing maneuver.

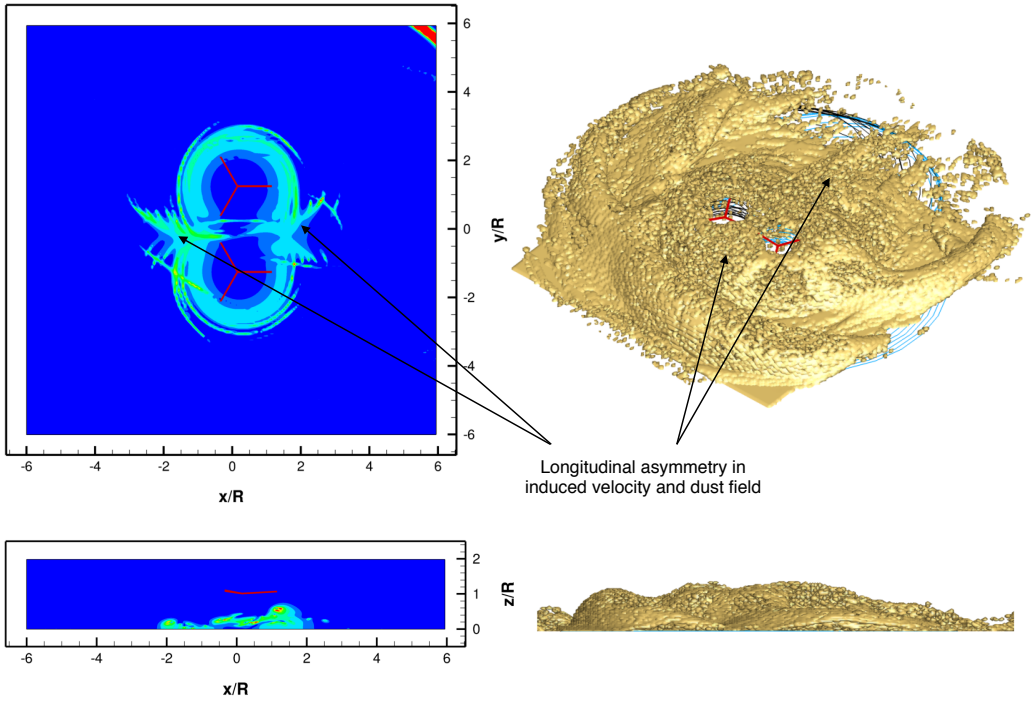

(a) $t = 10$ s

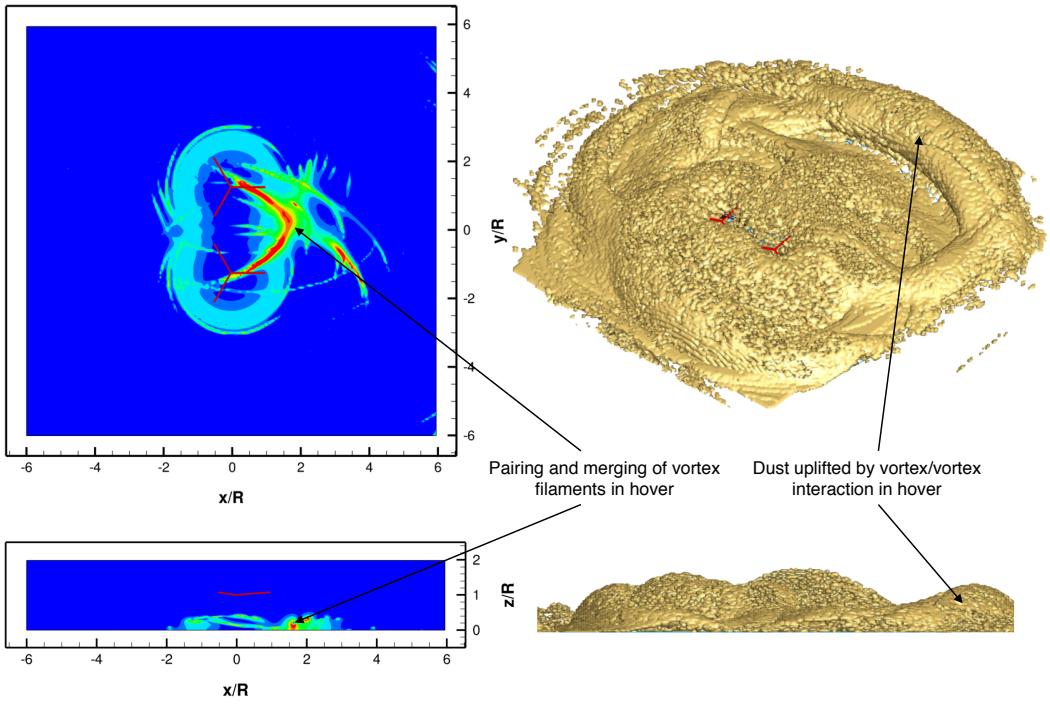

(b) $t = 22$ s

Figure 3.67: Development of the dust cloud for the side-by-side rotor configuration at time $t = 10$ and 22 s of the landing maneuver.

The side view of the dust cloud also shows that sediment particles have been uplifted to heights above the plane of the rotor. This rapid development of the dust cloud is because of the many regions of higher induced velocity (shown in red) on the sediment bed, as shown in Fig. 3.66(a).

At $t = 6$ s, as the rotorcraft enters the flare phase of the lading maneuver, the outward propagation of the ground vortex can be seen in the induced velocity contours, as shown in Fig. 3.66(b). The rapid development of the dust cloud under the influence of the ground vortex was seen in the isometric view of the dust cloud, which extended across both the length ($12R$) and width ($12R$) of the sediment bed. The vertical extent of the dust cloud was higher than the plane of the rotor disks.

By $t = 10$ s, with the rotorcraft about to settle into a steady hover, and the radially outward propagating ground vortex begins to mobilize and uplift significant quantities of particles, as shown in Fig. 3.67(a). Notice that the side-by-side rotor configuration created a strong longitudinal asymmetry in the wake, which resulted in significantly higher flow velocities and also particle velocities in the region between the two rotors, i.e., a type of longitudinal jet.

Figure 3.67(b) shows the dust cloud at $t = 22$ s in hover. By this point, there was significant amount of dust reingestion seen through the rotors, which ejected more particles from the bed by means of bombardment ejections. The induced velocity field produced by the side-by-side rotor configuration was also seen to uplift sediment particles at larger distances away from the rotors, as shown in Fig. 3.67(b). The side view of the dust cloud also showed that sediment particles were uplifted to nearly twice the rotor radius above the ground. Notice that the induced velocity contours showed regions of higher velocities that were directed toward the rear of the rotorcraft. This latter effect is a consequence of the wake behavior of the side-by-side rotor configuration, and

is further explained in detail below.

Figure 3.68 shows six instantanoues realizations of the wake geometries of the side-by-side rotor configuration in hover tracing the development of a ground vortex. Figures 3.68(a) and 3.68(a) show the interaction between the tip vortices from the two counter-rotating rotors and the initial pairing of the vortex filaments. The induced velocity of the filaments on each other result in the bundling of the tip vortices and these vortices then propagate along the ground toward the rear of the rotorcraft, as shown in Figs. 3.68(c)–3.68(e), similar to a ground vortex. The process of pairing and bundling of tip vortices was seen to repeat again starting with the initial interaction between the tip vortices, as shown in Fig. 3.68(f).

Figure 3.69 shows three non-contiguous instantaneous realizations of the dust cloud produced by the side-by-side rotor configuration. Figure 3.69(a) shows the dust cloud when the rotorcraft had settled into hover and the transient associated with the flare phase of the maneuver had propagated through the solution. The outer structures of the cloud associated with the initial propagation of the ground vortex can be seen along, with the dust being ingested through the rotor disks to produce a dome-shaped cloud. Figure 3.69(b) shows an instantaneous realization during which the bundling of the tip vortices from the two rotors can be seen. These vortices then propagate along the ground towards the rear of the rotorcraft, uplifting large quantities of sediment in the process. This vortex, in effect, behaves similarly to an initially formed ground vortex.

Figure 3.69(c) shows the dust cloud after 12 s, which shows the large amount of sediment being uplifted towards the rear of the rotorcraft. From an operational standpoint, this side-by-side rotor configuration would require large clearances on all sides to safely operate in brownout

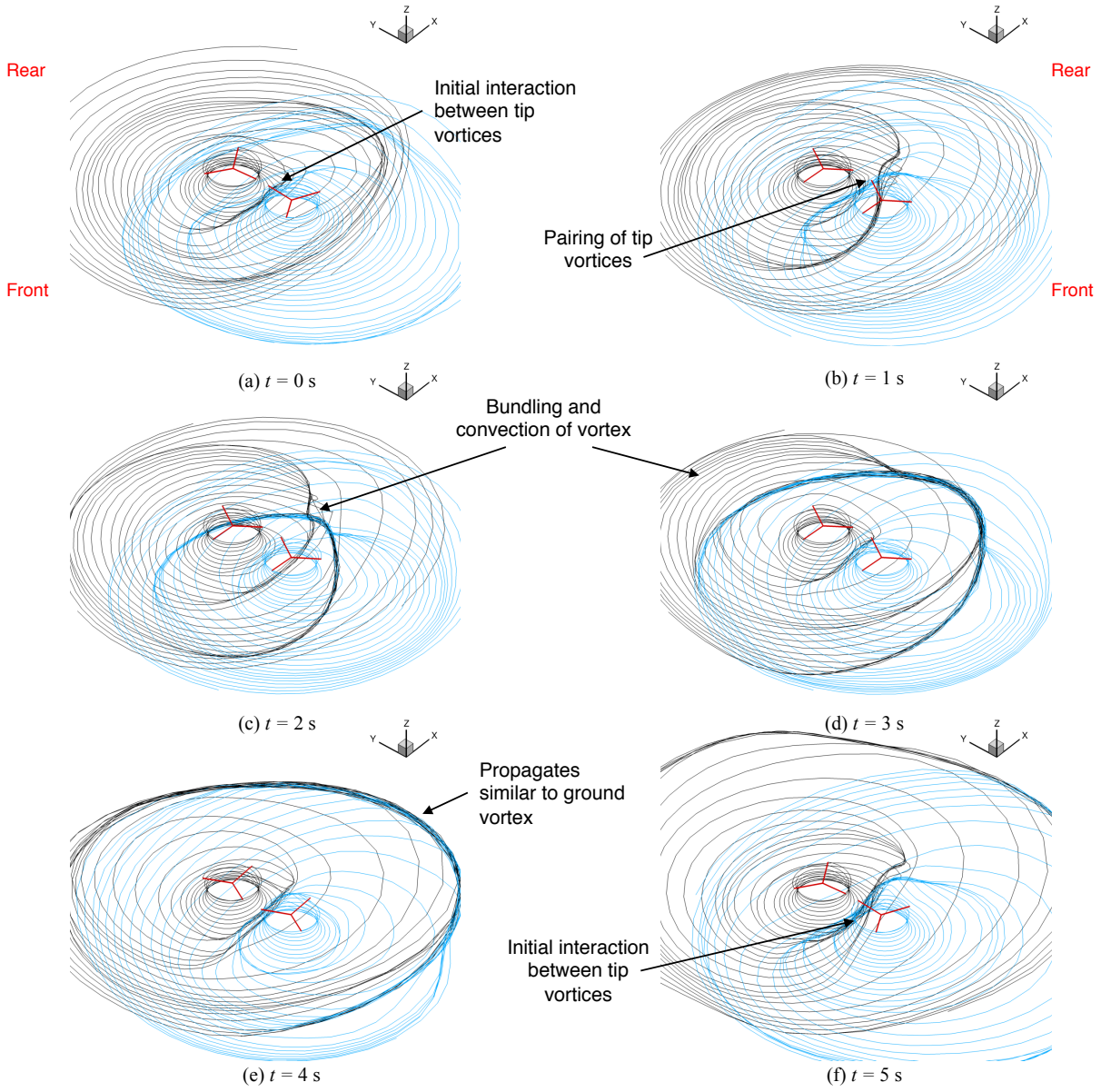

Figure 3.68: Development of the ground vortex dust cloud in hover for a side-by-side rotor configuration.

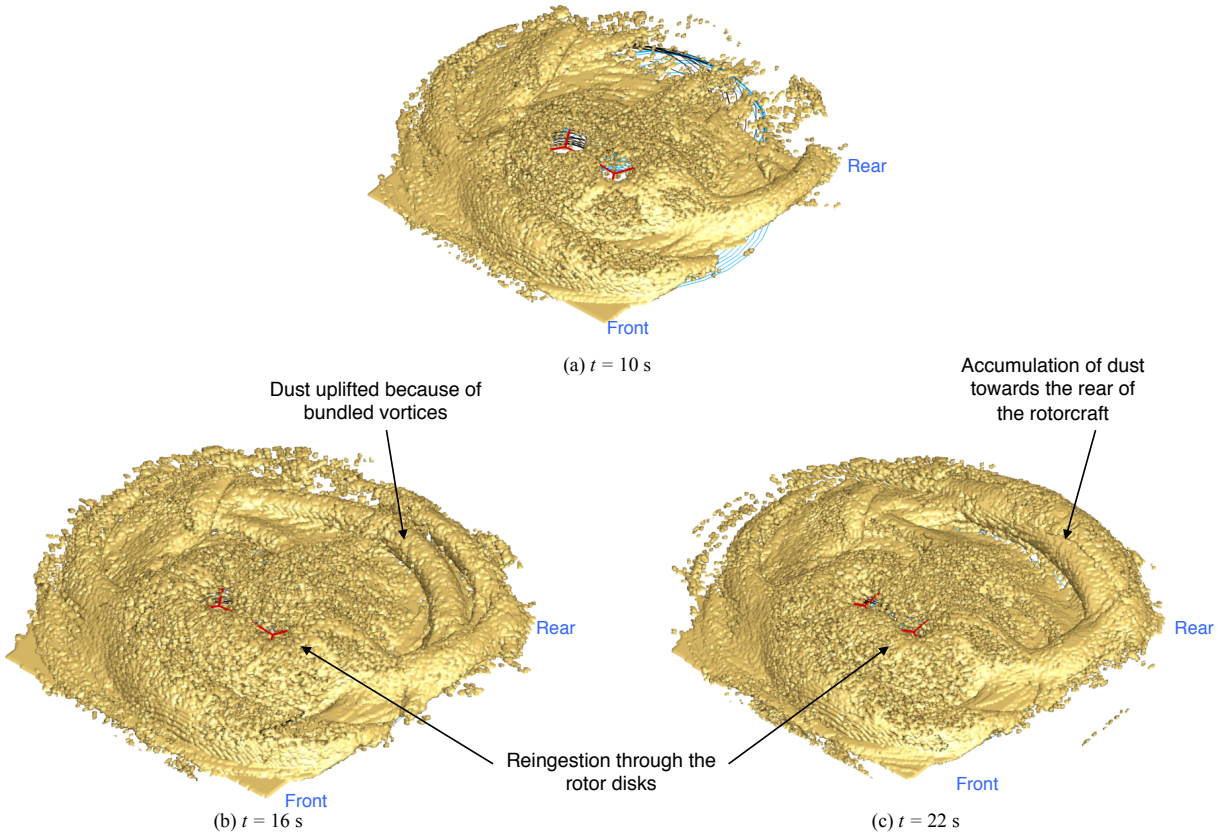

Figure 3.69: Development of the dust cloud in hover for a side-by-side rotor configuration.

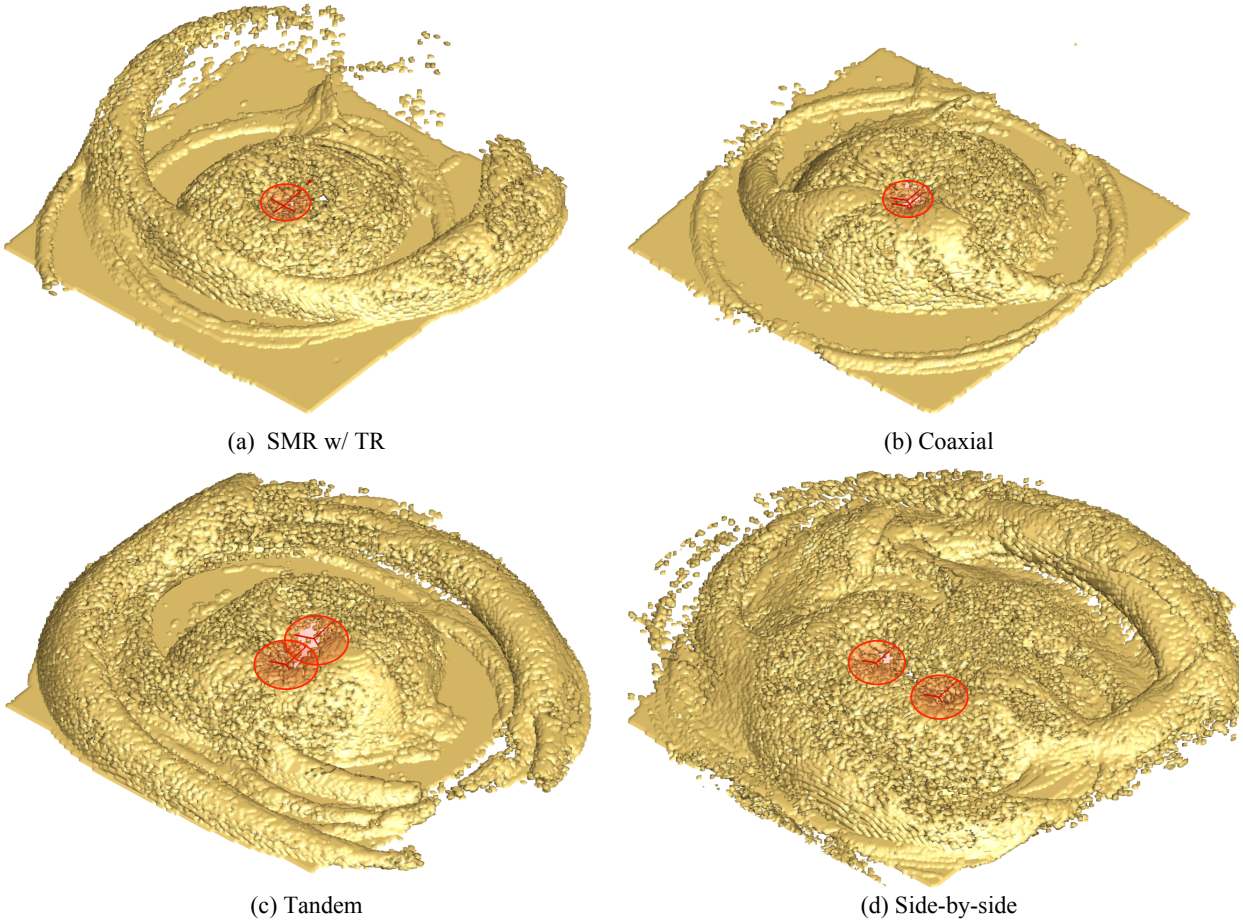

(a) SMR w/ TR (b) Coaxial

(c) Tandem (d) Side-by-side

Figure 3.70: Dust clouds formed by a SMR (with TR), coaxial, tandem, and side-by-side rotors at the end of the simulated landing maneuvers.

environments. Also notice, that during the hover phase sediment particles are constantly reingested through the rotor disk, further exacerbating the problem of brownout. In the current side-by-side configuration, the starboard rotor rotates counter clockwise when viewed from above. If the direction of rotation were to be reversed, i.e., starboard rotor rotates clockwise, the waves of dust uplifted would now convect ahead of the rotor disk, potentially causing significant visual obscurations for the pilot.

Figure 3.70 shows the dust cloud structures formed by the SMR (with TR), coaxial, tandem,

and side-by-side rotor configurations at the end of the simulated landing maneuver. The dust cloud produced by the SMR, as shown in Fig. 3.70(a), is similar in structure to that produced by the isolated SMR, with minor differences. The aerodynamic influence of the tail rotor (shown in Fig. 3.21) causes bundling of the tip vortices and makes the resulting dust cloud considerably less axisymmetric. The inclusion of the tail rotor also modifies the dust cloud by causing airborne particles to be entrained into its own inflow and downwash field.

Figure 3.70(b) shows the dust cloud produced by the coaxial rotor system. Unlike other rotor configurations, the lower rotor of the coaxial significantly increases the overall slipstream velocities in the wake, which causes the tip vortices to impinge on the ground earlier during the maneuver than for the other rotor configurations. The vortex filaments from the upper and lower rotor also bundle together and convect along the ground, uplifting large quantities of dust through bombardment mechanisms. The coaxial rotor configuration produces a dome shaped dust cloud that is more axisymmetric relative to the rotor compared to the other configurations.

Figure 3.70(c) shows the dust cloud produced by the tandem rotor configuration. In this case, the resulting cloud consisted of a large toroidal outer cloud structure formed by the propagation of the ground vortex. The inner structure of the dust cloud was formed by the reingestion of sediment particles through the rotor disks. Notice that there is a strong lateral asymmetry in the dust cloud because of the fore/aft placement of the two rotors.

The dust cloud produced by the side-by-side rotor configuration is shown in Fig. 3.70(d). It is evident that this configuration uplifts large quantities of dust that is distributed on all sides, potentially causing severe visual obscuration all around the rotorcraft. As was seen with the tandem

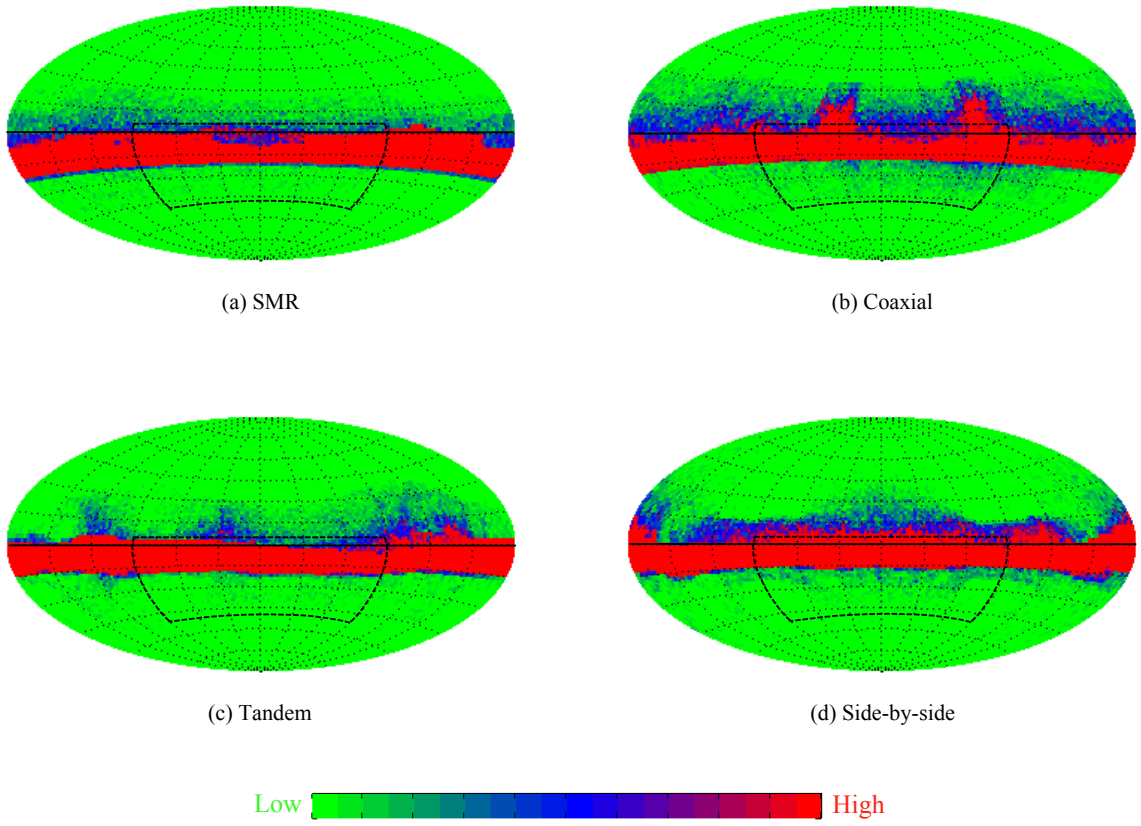

Figure 3.71: Relative particle count in the pilot's field of view for the tandem configuration versus the SMR configuration.

rotor configuration, a strong asymmetry in the development of the dust cloud is formed because of the positioning of the rotors. However, in this case, the tip vortex filaments from each rotor bundle more readily and more frequently, and they also form a much stronger ground vortex, which in this case convects towards the rear of the rotorcraft, uplifting large quantities of dust in the process. The side-by-side configuration was the only configuration where large quantities of dust were continuously mobilized, which is because of the relatively higher flow velocities near formed the ground and the continuous bundling of the tip vortex filaments in the outer regions of the wake.

Figures 3.71(a)–3.71(d) show the particle count from the pilot's perspective for the SMR,

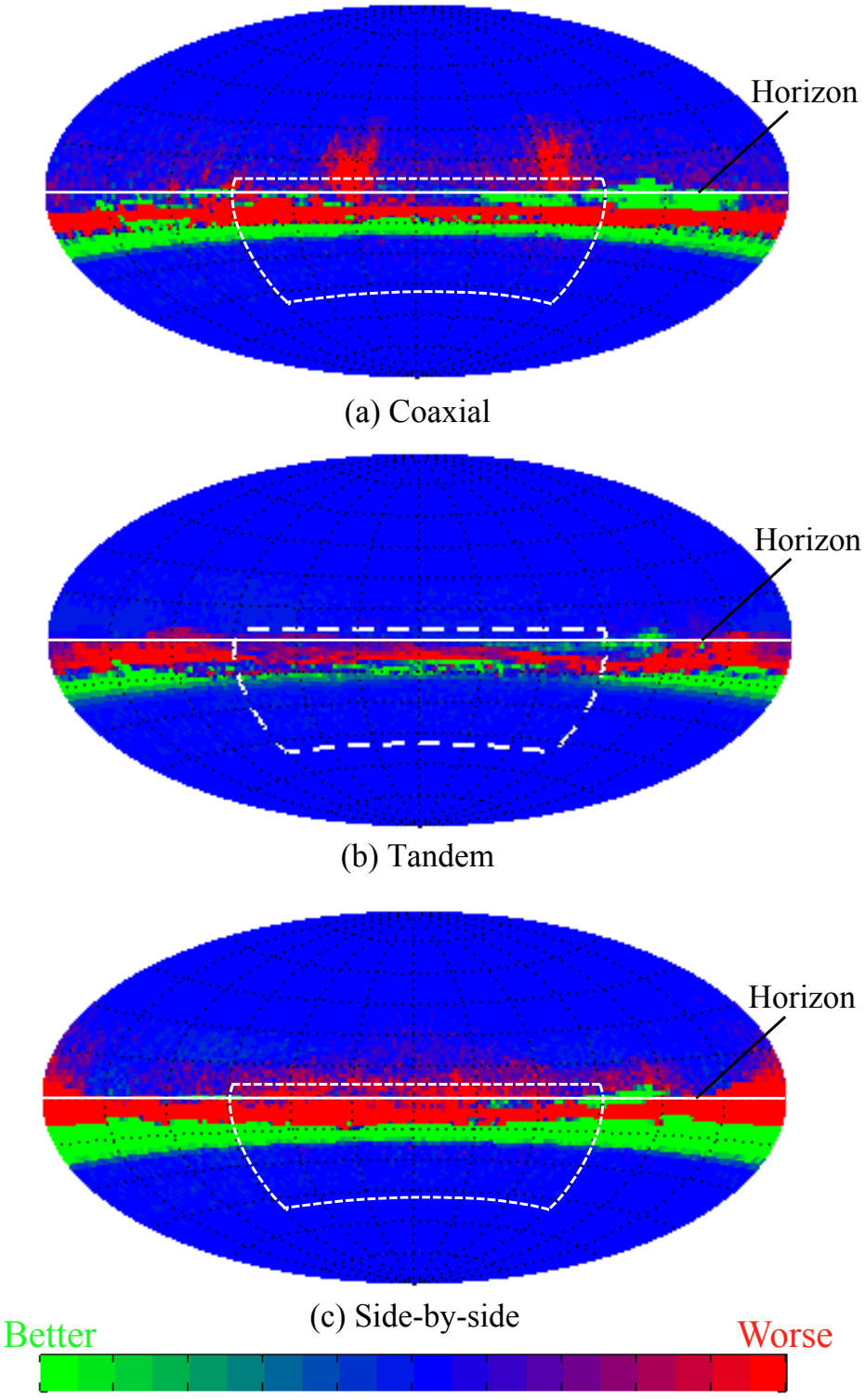

Figure 3.72: Relative particle count in the pilot's field of view for the tandem configuration versus the SMR configuration.

coaxial, tandem, and side-by-side rotor configurations, respectively, on a spherical map centered at the pilot. The red colour denoted a higher particle count along any direction and green indicates low particle count, i.e., no visual obscuration. It is clear that the spatial distributions of the particles in the pilot's FOV is dependent on the rotor configuration. Figures 3.72(a)–3.72(c) shows the differences in the particle count (from the pilot's perspective) between the coaxial, tandem, and side-by-side rotor configurations with the SMR as the baseline configuration at t = 22 s, respectively. The green color indicates a lower particle count compared to the baseline; red indicates higher particle count (the latter implying higher visual obscuration); and blue indicated regions where there were no appreciable differences in cloud densities. Although the multirotor configurations generated much more dust overall compared to the SMR (see Fig 3.73), there was actually a lower particle count closer to the pilot, indicated by the regions of green.

From the foregoing results, it is clear that different rotor configurations produce brownout dust clouds that differ vastly in both their structure and quantity of dust uplifted. The structure of the dust clouds depend primarily on the relative positioning of the rotors and the interaction of the tip vortices from these rotors, which then uplift sediment particles from the bed. Lateral and longitudinal asymmetry was shown to occur in the induced velocity fields and dust cloud because of the fore/aft (tandem) and side-by-side positioning of the rotors; see Figs. 3.65(b) and 3.67(b). Notice in the side-by-side confguration that although the positioning of the rotors is symmetric about the longitudinal plane, the dust cloud is asymmetric in structure (Fig. 3.67(b)). As the overlap between the rotors was increased, i.e., from a tandem or side-by-side to a coaxial configuration, the structure of the dust cloud was observed to resemble that of a SMR configurations; see Fig. 3.70.

It is recognized that in the present work, no particular rotor parameter was held constant, and that different rotor configurations were compared based on their operational gross weight. The objective of the present study was not to design a rotorcraft that produced the most benign dust cloud, but to evaluate the severity of brownout of representative rotorcraft that frequently encounter brownout conditions in the field. Comparing dust cloud based on holding certain rotor parameters constant such as disk loading or blade loading may be valuable in a formal optimization study, where the objective is to design a rotorcraft with the least severe brownout conditions.

3.5.3 Brownout Severity

The severity of a brownout cloud depends not only on the quantity of dust particles uplifted, but also on the spatial and temporal distribution of particles in the cloud and the rapidity at which the particles are uplifted. Milluzzo and Leishman [2] hypothesized that certain rotor geometric and operating parameters are likely to play a key role in determining brownout severity, such as the total wake strength, disk loading, and reduced frequency of the convection of the vortex wake toward the ground. Tritschler et al. [84] used the number of particles convected up into the pilot's FOV as a surrogate to quantify the visual obscuration. In the present study, the following metrics were applied to quantify the relative severity of brownout, with no distinction being made to differentiate between single or multi-rotor configurations in their definitions.

1. Visual obscuration: The loss of visual cues experienced by a pilot during brownout can be quantified by using the total number of particles present in the pilot's FOV (as a surrogate metric for optical attenuation), which is usually computed at the end of the brownout simu-

lation, i.e.,

$$N_{\text{FOV}} = \sum_{\phi=-90^\circ}^{+90^\circ} \sum_{\theta=-5^\circ}^{+50^\circ} n_P(\phi,\theta) \tag{3.7}$$

where $n_P(\phi,\theta)$ is the number of particles in a one-degree solid angle centered at ϕ and θ. The double summation in Eq. 3.7 is the total number of particles in a region of the pilot's FOV (N_{FOV}) that extends in azimuth from ϕ = -90° to +90° and in elevation from θ = -5° to θ = +50°.

2. Total quantity of particles: The intensity of a brownout cloud depends in part, on the total number of particles uplifted and entrained into the flow. The fewer the number of particles, the lower the expected severity of brownout. The total number of particles entrained at the end of the simulation (N_{Total}) was computed by using

$$N_{\text{Total}} = \sum_{\phi=-180^\circ}^{+180^\circ} \sum_{\theta=-90^\circ}^{+90^\circ} n_P(\phi,\theta) \tag{3.8}$$

3. Rapidity of cloud development: The frequency at which the individual blade tip vortices convect toward the ground below the rotor can be correlated to the average rate at which particles are mobilized and uplifted into the flow and, hence, to the rapidity at which the brownout dust cloud is likely to develop. This quantity is defined as a vortex wake frequency, $\Omega_s = N_r N_b \Omega$, where N_r is the number of rotors, N_b the number of blades per rotor, and Ω is the rotational frequency of the rotor.

4. Total wake strength: A major contributor to the development of brownout is the entrainment of dust by the mechanism of sediment particle trapping, which happens when the induced

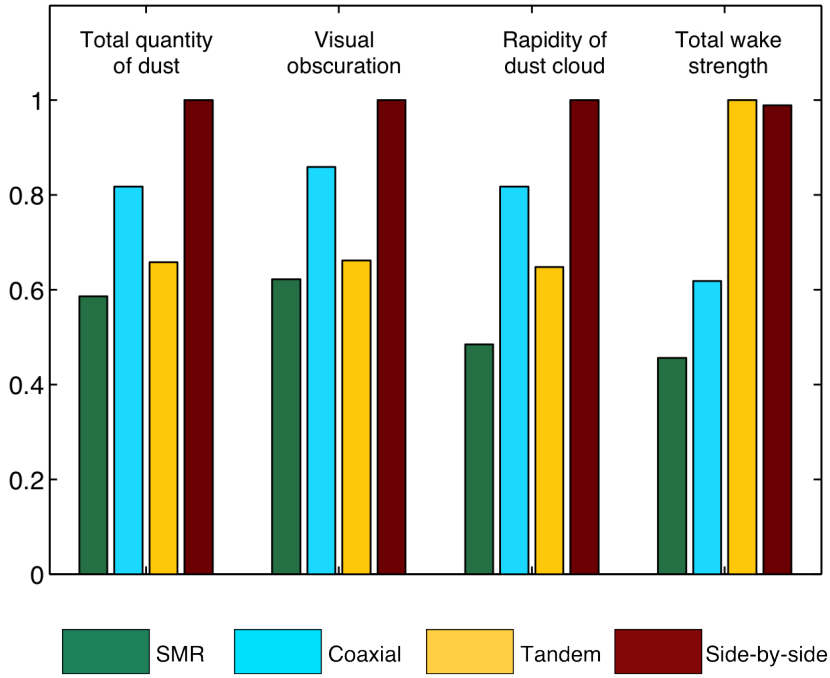

Figure 3.73: Comparative levels of brownout severity for different rotor configurations.

flows from the individual blade tip vortices mobilize and uplift particles. The total wake strength represents the combined tip vortex strength (circulation) of vortices from all the blades, as defined by $\Gamma_w = N_r N_b \Gamma_v \approx N_r N_b (C_T/\sigma)\Omega R c$.

Figure 3.73 shows the relative severity of brownout dust cloud produced by the different rotor configurations in a bar chart format. Each of the severity metrics were normalized based on the maximum value of the metric in each category such that the value of the metrics lie between 0 and 1, with 0 being least severe and 1 being most severe. The side-by-side rotor configuration was clearly the most severe in terms of these defined metrics. The relatively high total wake strength combined with the higher rapidity of the vortices impinging on the ground resulted in the large quantity of particles being mobilized. The side-by-side configuration uplifted large quantities of particles even in hover (see Fig. 3.70) and, therefore, it can be expected that this configuration will

produce the most severe visual obscurations for the pilot.

Although the tandem rotor configuration had the highest total wake strength among all configurations (which represents the potential to uplift particles from the sediment bed), the lower rapidity of the impingement of the vortices (attributed to the lower disk loading) reduced the severity of brownout. Compared to the side-by-side configuration, the tandem configuration produced approximately 60% of (a) the total quantity of dust being uplifted, (b) amount of visual obscuration relative to the pilot, and (c) the rapidity of the development of the particle cloud; see Fig. 3.73.

As shown in Fig. 3.73, the fully overlapping rotor configuration of the coaxial system results in a large quantity of dust being uplifted and present in the pilot's FOV when compared to the SMR or the tandem rotor, which is reflected in the greater levels of visual obscurations. The increased quantity of dust entrained by the coaxial rotor system can be attributed to the bundling interactions of vortices from the upper and lower rotors, which results in a stronger combined net vortex flow that has a higher potential to mobilize particles from the sediment bed. Because these particles remain in the pilot's FOV, they will potentially lead to more severe visual obscurations compared to those produced by either the SMR or the tandem rotor configurations.

3.5.4 Vection Illusions

While visual obscurations can give spurious sensory cues to the pilot, the rapid convection of sediment particles relative to pilot may also contribute to sensory illusions. This perceived motion (i.e., a vection illusion) in the spatial environment (which can be a sensation of linear or angular motion) may cause the pilot to apply a corrective or cyclic control input where one is

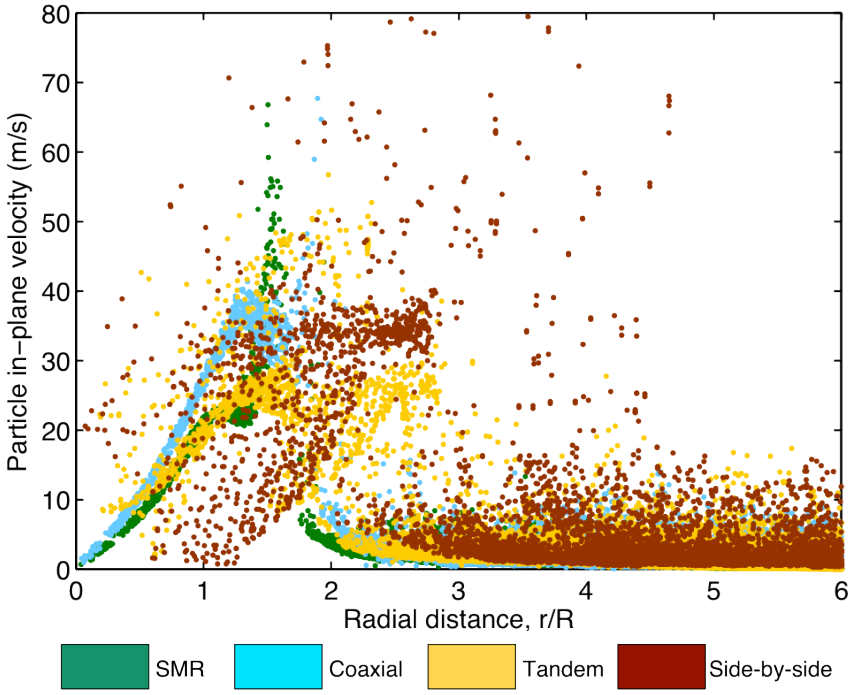

Figure 3.74: Particle convection velocities along the ground for the different rotor configurations.

not needed, which if done near the ground may quickly result in a mishap. While there has been anecdotal evidence of pilots experiencing vection illusions when encountering severe brownout conditions, a quantifiable metric to predict the severity of the expected effects has not yet been established. Although vection and other illusions that may be experienced by pilots in brownout conditions is a field of study in itself, the root cause of these potential issues lie in the complex spatial and temporal developments of the evolving dust clouds, information that is available from the present simulations. In the first instance, the particle velocities relative to the pilot's eyes is a good candidate as a metric to help quantify relative motion effects and hence, for assessing the likelihood of a vection illusion affecting the pilot's decision-making when in brownout conditions.

Figure 3.74 shows a plot of the in-plane particle velocities produced along the sediment bed

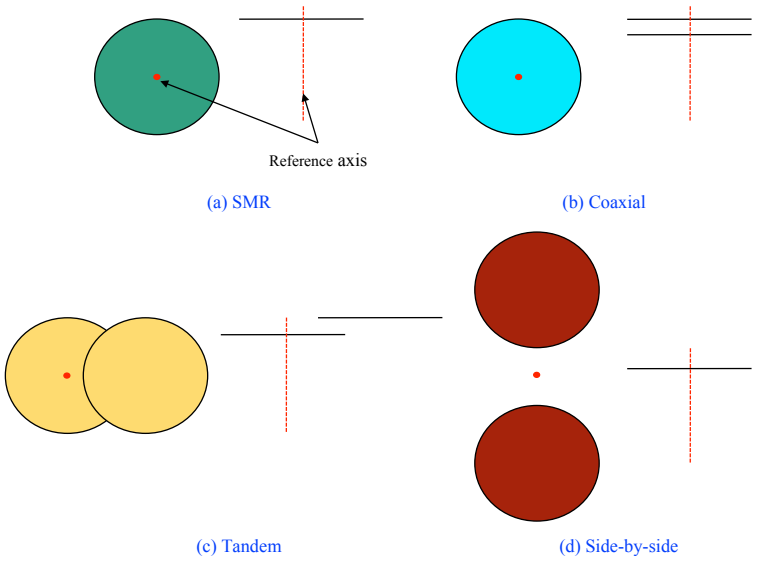

Figure 3.75: Top-view and side-view of the different rotor configurations with the reference axes (highlighted in red).

for each of the different configurations against the radial position from a reference axis, with each dot representing a different particle. Because vections illusions could be experienced by the pilot, the reference axis was chosen to reflect the position of the pilot's seat; the in-plane velocity of the particle reflects the convective velocity of the particle away from the reference axis (i.e., away from the pilot). Top-views and side-views of the reference axes for the different rotor configurations are shown in Fig. 3.75, with the axes being highlighted in red.

Figure 3.74 shows a plot of the in-plane particle velocities produced along the sediment bed for each of the different configurations against the radial position from a reference axis, with each dot representing a different particle. Because vections illusions could be experienced by the pilot, the reference axis was chosen to reflect the position of the pilot's seat; the in-plane velocity of the particle reflects the convective velocity of the particle away from the reference axis (i.e., away from the pilot). Top-views and side-views of the reference axes for the different rotor configurations are

shown in Fig. 3.75, with the axes being highlighted in red.

Figure 3.74 shows a plot of the in-plane particle velocities produced along the sediment bed for each of the different configurations against the radial position from a reference axis, with each dot representing a different particle. Because vections illusions could be experienced by the pilot, the reference axis was chosen to reflect the position of the pilot's seat; the in-plane velocity of the particle reflects the convective velocity of the particle away from the reference axis (i.e., away from the pilot). Top-views and side-views of the reference axes for the different rotor configurations are shown in Fig. 3.75, with the axes being highlighted in red.

These results show that the particle velocities increases from the reference axis to peak values at a radial distance of approximately $1.5R$, and then decrease with increasing distance from the reference axis. At the peak, the particles move along the ground at relatively high velocities of about 50 ms^{-1} ($\sim$110 mph) away from the rotor(s). The tandem and side-by-side rotor configurations both showed a much broader peak compared to the SMR or coaxial rotor, indicating that particles are convecting nearer to the ground and with higher velocities and over larger distances, i.e., from $3R$–$4R$. The peak particle velocities produced by by the side-by-side rotor configuration were predicted to exceed 70 ms^{-1} ($\sim$157 mph); see Fig. 3.74. Such particle velocities may lead to powerful vection illusions if the pilot is deprived of other confirmatory orientation cues from focal vision.

Figure 3.76: “Donut” dust cloud brownout signature of Rotorcraft A.

3.5.5 Dust Cloud Comparison with Field Observations

Different rotorcraft are known to produce different dust cloud signatures with varying levels of brownout severity; see Fig. 1.4 in Chapter 1. Amongst the different rotorcraft, some are known to produce unique dust cloud signatures, such as the so-called “donut” dust cloud shown Fig. 3.76. The spatial distribution of dust from this configuration (referred to as Rotorcraft A) allows for a clear region of ground visibility around the rotorcraft and aids in giving the pilots better visibility during landing operations, thereby mitigating the dangers of landing in brownout conditions.

The methodology developed in the present work was used to model the rotorcraft in an attempt to better understand the physics of the donut dust cloud. The details of this rotor are given in Table F.12 in Appendix F and a panel representation of the fuselage used is shown in Fig. 3.77. Figure 3.78 shows the dust cloud development for Rotorcraft A at four instances during the prescribed landing maneuver. Being a single main rotor configuration, the overall features of

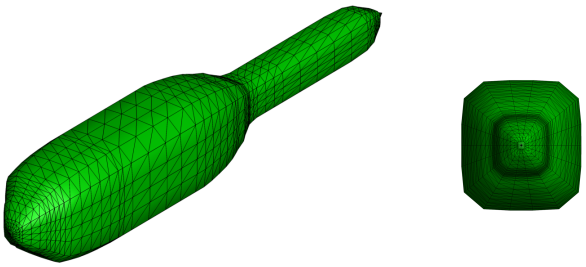

(a) Iso-view (b) Rear-view

Figure 3.77: Representative fuselage shape of Rotorcraft A.

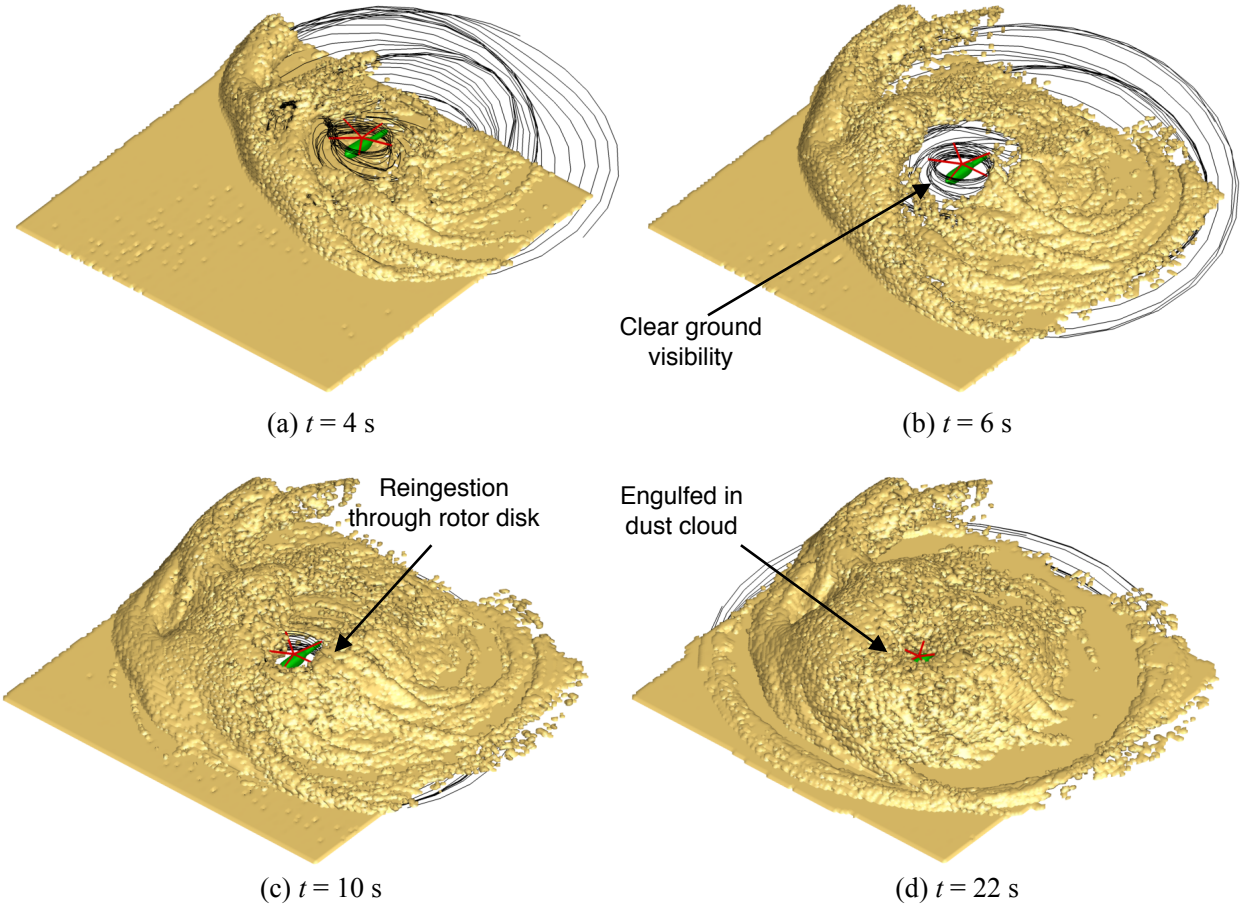

(a) $t = 4$ s (b) $t = 6$ s

(c) $t = 10$ s (d) $t = 22$ s

Figure 3.78: Dust cloud development at: (a) $t = 4$ s, (a) $t = 6$ s, (a) $t = 10$ s, and (a) $t = 22$ s, of the prescribed landing maneuver for Rotorcraft A.

the dust cloud are similar to those previously observed (see Figs. 3.60 and 3.61). During the flare phase of the maneuver, shown in Fig. 3.78(b), a region of clear ground visibility around the rotor can be seen. This region of lower dust accumulation is similar to the field observation shown in Fig. 3.76. However, as the rotorcraft settles into hover, reingestion of dust through the rotor disk was observed with the dust cloud completely engulfing the rotorcraft; see Figs. 3.78(c) and 3.78(d).

While the current methodology contain certain assumptions and simplifications in the modeling of the carrier phase and the dust phase, the inability to accurately replicate the donut dust cloud signature can be attributed to many other contributing factors. For instance, the mineralogy of the bed and soil properties beneath the rotor, such as the packing of the sediment particles, temperature, and moisture content play key roles in the mobilization of the sediment particles and the extent of the sediment uplift above the ground. These factors can alter the cohesive and electrostatic forces between the particles on the bed and influence their subsequent mobilization.

In summary, the foregoing results have given some further insight and understanding of the roles of the different (and often interdependent) factors that may affect the fluid dynamics of brownout. In particular, the present study has shown that localized changes to the wake (such as from vortex/surface interactions on the fuselage) can have more global effects on the formation of the dust clouds, which may help to explain why some rotorcraft experience more severe brownout conditions than others. However, the present results have been computed for an idealized landing maneuver, and while this introduces the inherent time-dependencies of the real brownout problem into the simulations, they are not necessarily the actual flight profiles that would be used operationally. Assessments of brownout severity also pose many challenges that go beyond particle

uplift simulations, and future work will require a broader and more coordinated effort between experiments, field tests, simulations, optical characterization, and aeromedical factors.

3.6 Blade Erosion

Blade erosion occurs because of the interaction of the rotor blades with the suspended particulates causing wear and tear of the leading edge of the blades. In a brownout environment, this erosion process is greatly accelerated [1]. To prevent damage from dust/sand erosion, metallic abrasion strips, typically composed of stainless steel or titanium, are bonded to the blade leading edge to serve as a hard surface that absorbs the kinetic energy of the sand particle. These impacting sand particles, however, slowly erode away the metallic material. This is a bigger issue near the outboard blade tip, where the high blade velocity means that the dust particles impact with greater kinetic energy. Constant replacement of these damaged abrasion strips and caps on the rotor blades leads to increased maintenance cost and reduced operational readiness. A secondary concern with the erosion of metal abrasion strips pertains to the visible signature that occurs when microscopic metallic pieces are eroded away.

Current efforts include preventive measures such as coatings and abrasion strips to delay the erosive effects of blade erosion [133]. To better understand the problem, representative simulations were performed to better understand the process of particle/blade collisions. In the first instance, two-dimensional results were calculated for particles colliding with an airfoil, which was then extended to study particle collisions in a three-dimensional brownout cloud for a helicopter in hover.

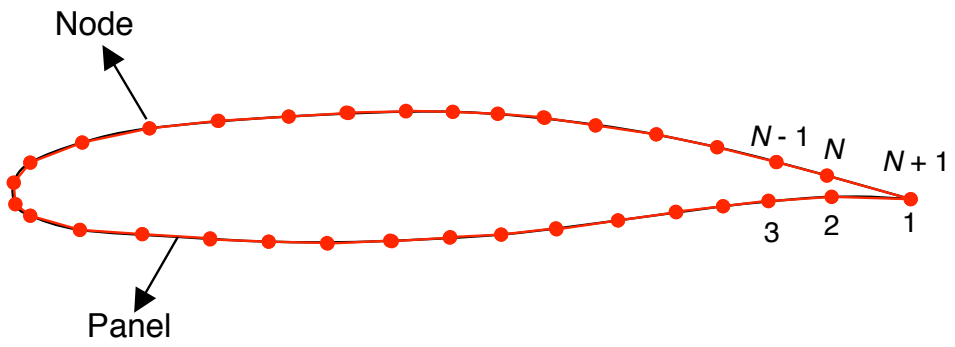

Figure 3.79: Schematic representation of the source-vortex panel of an airfoil.

Two-dimensional flow around an airfoil was modeled using a surface singularity technique and the interaction of the particle with the surface of the airfoil was solved using conservation of momentum. Simulations were performed using particles of different diameters to study their effect on the process of blade/particle collisions. The results were analyzed in terms of the particle trajectories and the loss of kinetic energy of the impacting particles. Erosion is a complex process that involves multi disciplines of science, the accurate prediction of which is beyond the scope of the current work. Therefore, in the current work, the loss in kinetic energy of the particles as they collide with the blade was used as a surrogate to quantify the energy transferred to the blade, which inturn may lead to erosive effects. Three-dimensional simulations were performed in hover using the FVM and the sediment tracking methodology. The different dust clouds were analyzed to determine the diameters of particles that are uplifted to the plane of the rotor, and to quantify the energy transferred to the rotor disk.

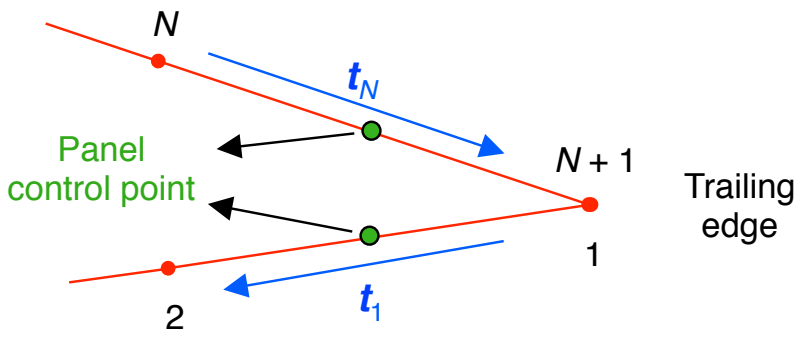

Figure 3.80: Kutta condition at the trailing edge of the airfoil.

3.6.1 Two-Dimensional Flow Around an Airfoil

Figure 3.79 shows a panel representation of the surface of an airfoil. The assumptions and equations used in predicting the flow around the airfoil is equivalent to those described in Section 2.6, which was for the case of a three-dimensional fuselage. While a constant source strength was assumed for each the panels of the fuselage, the panels of the airfoil are of constant source and vortex strength. The source strength can vary for each panel, but the vortex strength is constant and equal over all the panels of the airfoil.

If N_P panels are used to represent the surface of the airfoil, there are $N_P + 1$ total unknowns, i.e., N_P source strengths and one vortex strength, requiring $N_P + 1$ equations. Similar to Eq. 2.43 in Chapter 2, flow tangency condition at the panel control points, i.e.,

$$\mathbf{V} \cdot \mathbf{n}_i = 0 \quad i = 1, 2, \cdots, N_P \tag{3.9}$$

where $\mathbf{V}$ is the total induced velocity at a panel control point and is given by

$$\mathbf{V} = \mathbf{V}_\infty + \sum_{j=1}^{N} \left(\frac{q_j}{2\pi r_{\mathrm{ij}}} \mathbf{e}_r + \frac{\gamma}{2\pi r_{\mathrm{ij}}} \mathbf{e}_\theta \right) \quad i = 1, 2, \cdots, N_P \tag{3.10}$$

where $\mathbf{V}_\infty$ is the freestream velocity, q if the source strength of the panel, γ is the vortex strength, $\mathbf{r}_{\mathrm{ij}}$ is the distance between the i^{th} and j^{th} panel, $\mathbf{e}_r$ and $\mathbf{e}_\theta$ are the unit vectors in polar coordinate system, respectively. The coordinate transformation between the polar and Cartesian systems is given by

$$\mathbf{e}_x = \mathbf{e}_r \cos\theta - \mathbf{e}_\theta \sin\theta \tag{3.11}$$

$$\mathbf{e}_y = \mathbf{e}_r \sin\theta + \mathbf{e}_\theta \cos\theta \tag{3.12}$$

where $\mathbf{e}_x$ and $\mathbf{e}_y$ are the unit vectors in Cartesian coordinate system.

The Kutta condition is enforced to predict the lift and drag on the airfoil. This condition states that the flow must leave the trailing edge smoothly, which implies that at the trailing edge the pressures on the upper and lower surface are equal. The Kutta condition is satisfied by equating velocity components tangential to the panels adjacent to the trailing edge on the upper and lower surface

$$(\mathbf{V} \cdot \mathbf{t})_{\mathrm{Panel_1}} = -(\mathbf{V} \cdot \mathbf{t})_{\mathrm{Panel_N}} \tag{3.13}$$

where V is the velocity at the panel control point and t is the tangential vector along the panel. Because of the importance of the Kutta condition in determining the flow, the solution is extremely sensitive to the flow details at the trailing edge.

Equations 3.9 and 3.13 are solved simultaneously for the panel source strengths, q, and vortex strength, γ, which are then used to compute the velocity on the panel control points. The surface pressure on the airfoil can then be computed using the Bernoulli's equation

$$p_\infty + \frac{1}{2}\rho \mathbf{V}_\infty^2 = p + \frac{1}{2}\rho \mathbf{V}^2 \tag{3.14}$$

where p and $\mathbf{V}$ are the pressure and velocity, respectively, and subscript $()_\infty$ indicates freestream flow conditions.

3.6.2 Particle Collision

At every time step of the simulation, the position of the particles are compared against those of the airfoil surface to determine if a collision has occurred. Solving for the intersection of the particle trajectory with the surface of the panels is computational costly as is $O(N_\mathrm{P} N_\mathrm{Part})$, where N_P and N_Part are the number of panels and particles, respectively. Therefore, in the present study, the particle positions were compared against the analytical equation of the airfoil surface. NACA airfoils were used and the mathematical expressions for the upper and lower surface of these airfoils are given in Abbott & von Doenhoff [134].

Figure 3.81 shows a schematic of a particle colliding with the surface on an airfoil. If a collision is detected, conservation of momentum equations for the particle are solved about the

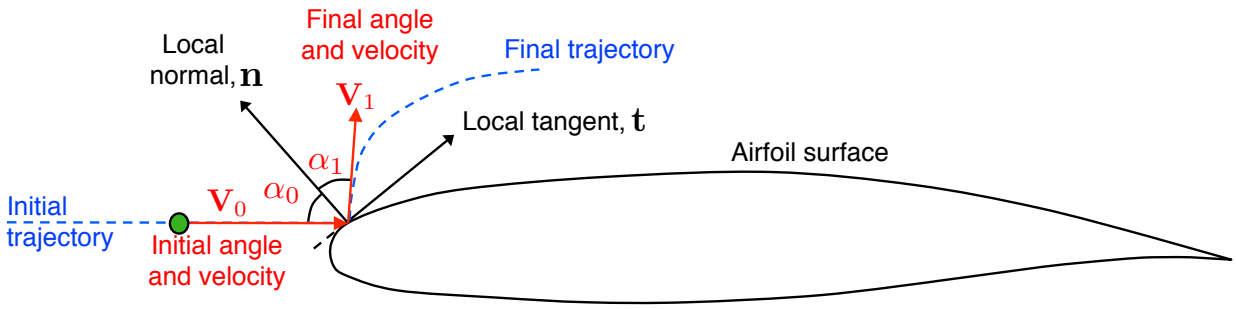

Figure 3.81: Schematic representation of a particle colliding with the surface of an airfoil.

local normal and tangent vectors on the airfoil at the point of impact, as shown in Fig. 3.81, i.e.,

$$m\mathbf{V}_0 \sin\alpha_0 = m\mathbf{V}_1 \sin\alpha_1 \tag{3.15}$$

$$e\,(m\mathbf{V}_0 \cos\alpha_0) = -m\mathbf{V}_1 \cos\alpha_1 \tag{3.16}$$

where m is the mass of the particle and e is the coefficient of restitution of the airfoil surface. It is assumed that upon collision, the particle does not disintegrate. The initial particle velocity is computed based on the aerodynamic solution of the airfoil, discussed previously in Section 3.6.1. Equations 3.15 and 3.16 can be used to solve for the particle angle, α_1, and velocity, $\mathbf{V}_1$, after impact, i.e.,

$$\alpha_1 = \tan^{-1}\left(\frac{\tan\alpha_0}{e}\right) \tag{3.17}$$

$$\mathbf{V}_1 = \mathbf{V}_0\left\{1-\cos^2\alpha_0(1-e^2)\right\}^{1/2} \tag{3.18}$$

Therefore, through repeated application of the equations of motion, particle trajectories are tracked as they collide with the surface of the airfoil.

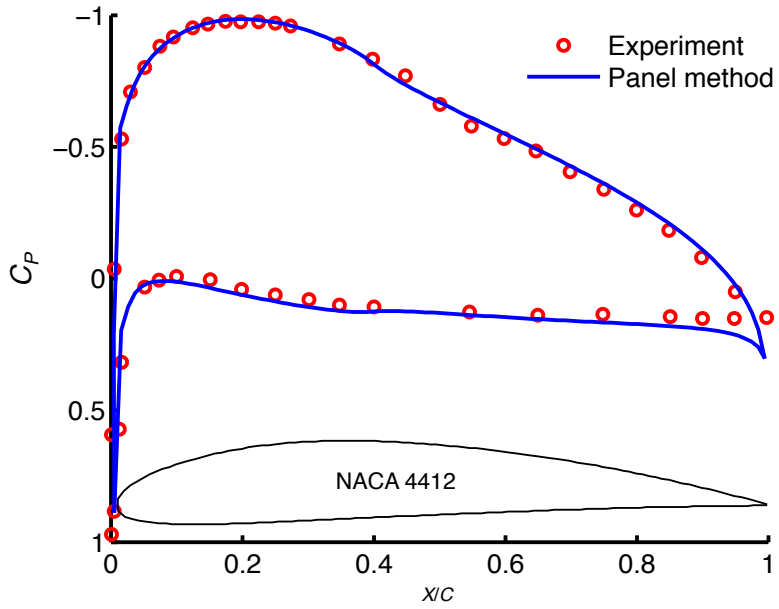

Figure 3.82: Comparison of the variation of non-dimensional pressure on the upper and lower surfaces of a NACA 4412 airfoil between the two-dimensional panel method and experiments (Source: Stack et al. [14]).

3.6.3 Two-Dimensional Simulation

Figure 3.82 shows the comparison of the pressure measurements over the surface of a NACA 4412 airfoil against the predictions of the panel method. The non-dimensional pressure, C_P is defined as

$$C_P = \frac{p - p_\infty}{\frac{1}{2}\rho V_\infty^2} \tag{3.19}$$

where V_∞ is the freestream velocity, p and p_∞ are the local and freestream static pressure, respectively. For this study, 198 panels were used to represent the surface of the airfoil, shown as an inset in Fig. 3.82. In general, excellent correlation is seen between the experimental measurements and the predictions of the panel method. The primary area of disagreement is seen at the trailing edge where the viscous effects act to prevent the recovery of the experimental pressure to the levels

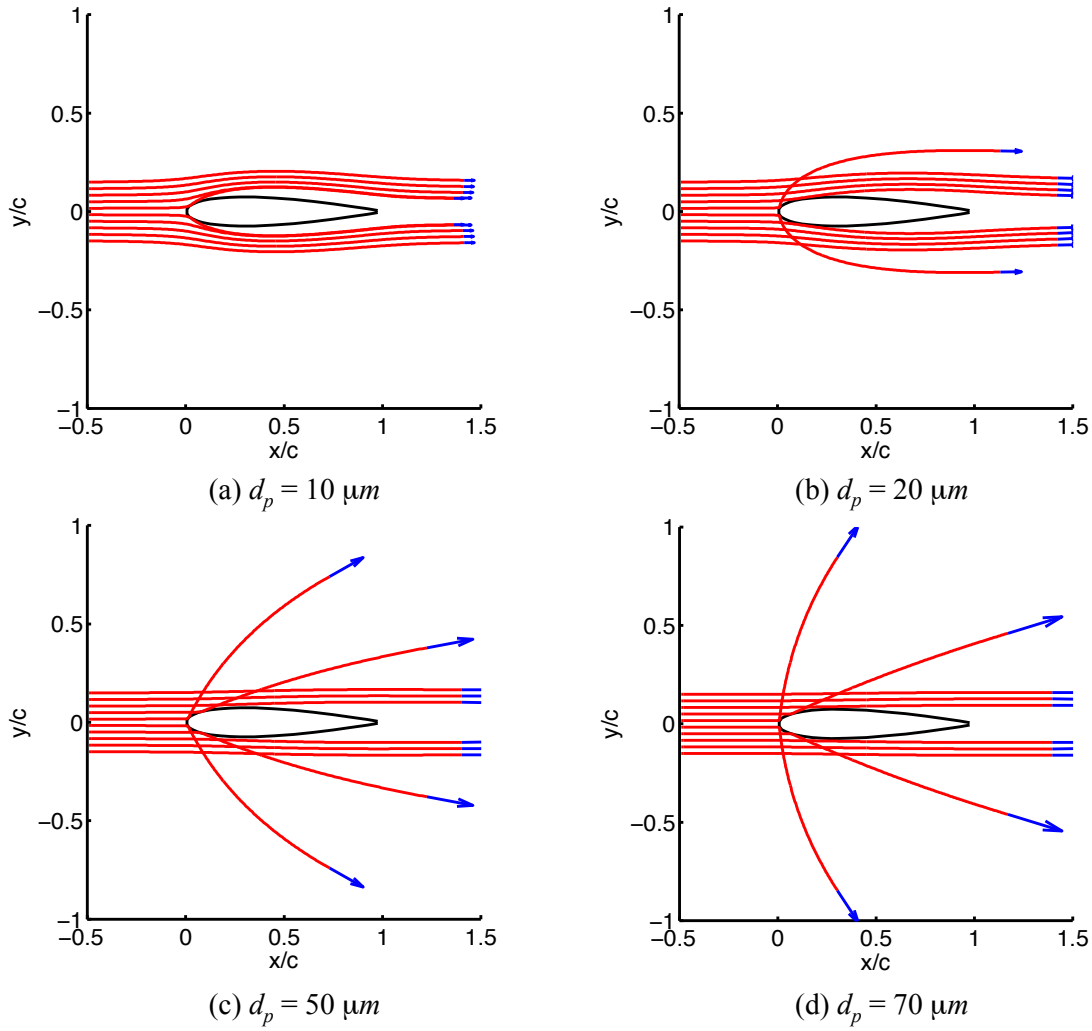

(a) $d_p = 10\ \mu m$ (b) $d_p = 20\ \mu m$

(c) $d_p = 50\ \mu m$ (d) $d_p = 70\ \mu m$

Figure 3.83: Trajectories of particles colliding with a NACA 0015 airfoil at 0° for particles sizes of (a) 10 μm, (b) 20 μm, (c) 50 μm, and (d) 70 μm.

predicted by the inviscid solution.

Figure 3.83(a)–3.83(d) shows the trajectory of particles of sizes 10 μm, 20 μm, 50 μm, and 70 μm, respectively, as they convect around a NACA 0015 airfoil. The airfoil was operating at 0° angle of attack. The time taken by a spherical particle to respond to changes in the flow, i.e., particle time constant, is proportional to the square of particle diameter d_p^2; see Eq. 2.85. As shown in Fig. 3.83(a), particles with smaller diameter have adapted quickly to changes in the flow around

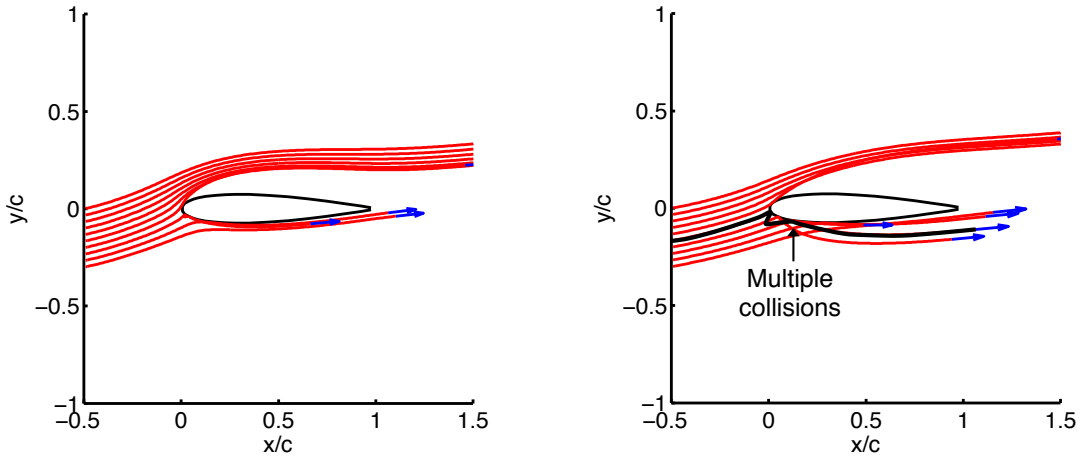

(a) $d_p = 10\ \mu m$ (b) $d_p = 20\ \mu m$

(c) $d_p = 50\ \mu m$ (d) $d_p = 70\ \mu m$

Figure 3.84: Trajectories of particles colliding with a NACA 0015 airfoil at 10° for particles sizes of (a) 10 μm, (b) 20 μm, (c) 50 μm, and (d) 70 μm.

the airfoil and, therefore, the chances of colliding with the airfoil are small. However, as the particle diameter was increased, the particles begin to collide with the airfoil. Fig. 3.83(d) shows that, under the conditions chosen for this simulation, particle trajectories can be altered close to 90° upon colliding with the nose of the airfoil.

Figure 3.84(a)–3.84(d) shows the trajectory of particles under similar flow conditions to Fig. 3.83, except that the airfoil was now operating at a 10° angle of attack to the freestream

flow. As the particle diameter increases, the chances of colliding with the airfoil surface increased, similar to the results shown in Fig. 3.83. The larger the particle time constant (Eq. 2.85), the longer it takes to alter its trajectory, and, hence, it has a higher probability of colliding with the airfoil. Figure 3.84(b) shows that under certain flow conditions, multiple collisions of the same particle with the airfoil surface can occur (trajectory highlighted in black).

Simulations of particles of different sizes interaction with a NACA 0015 airfoil at 0° angle of attack were performed and the changes in the net kinetic energy of the particles before and after colliding with the airfoil were computed. Figure 3.85 shows the loss in kinetic energy as particles of different sizes collide with an airfoil is shown for two different freestream velocities of 50 ms^{-1} and 200 ms^{-1} on a log-log plot. As previously mentioned, the loss in particle kinetic energy can be used as a surrogate metric to quantify blade erosion.

The trend observed in Fig. 3.85 can be explained based on an representative collision model of a single particle impacting a surface, a schematic of which is shown in Fig. 3.86. The kinetic energy lost by a particle of mass m_p, density ρ_p, diameter d_p, impacting a surface with initial velocity V_0 at an angle α_0 to the surface can be expressed as

$$\begin{aligned} \Delta\text{KE} &= \text{KE}_1 - \text{KE}_0 && (3.20)\\ &= \frac{1}{2} m_p (\mathbf{V}_1^2 - \mathbf{V}_0^2) && (3.21)\\ &= \frac{1}{2}\left(\frac{4}{3}\rho_p \frac{d_p^3}{8}\right)(\mathbf{V}_1^2 - \mathbf{V}_0^2) && (3.22) \end{aligned}$$

The ejection velocity $\mathbf{V}_1$ can be related to the impact velocity $\mathbf{V}_0$ through conservation of momen-

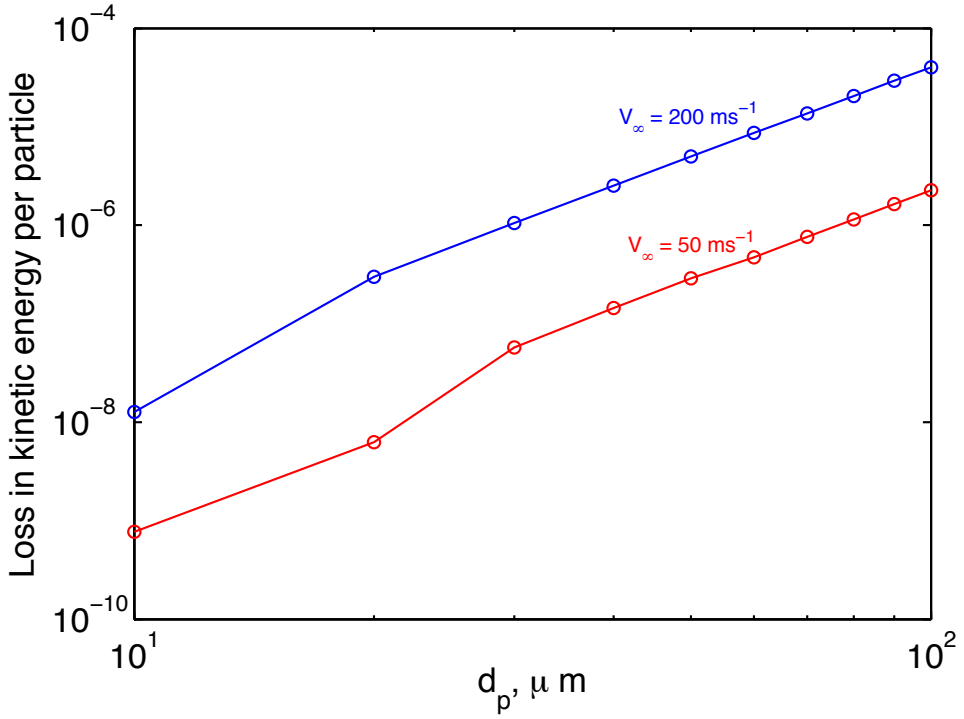

Figure 3.85: Variation of loss of kinetic energy per particle versus particle diameter upon colliding with a NACA 0015 for different freestream velocities.

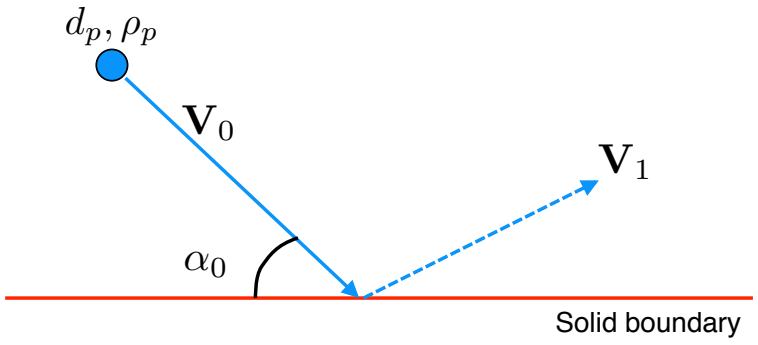

Figure 3.86: Schematic representation of a particle colliding with a solid boundary.

tum along the wall parallel and wall normal axis, i.e.,

$$\mathbf{V}_1^2 = \mathbf{V}_0(1-e^2) \tag{3.23}$$

where e is the coefficient of restitution. Combining Eqs. 3.22 and 3.23, an expression for the loss in kinetic energy of the particle can be obtained, i.e.,

$$\Delta\mathrm{KE} = \frac{\pi\rho_p d_p^3}{12} V_0^2 (1-e^2)\sin^2\alpha_0 \tag{3.24}$$

Taking the logarithm of the above equation

$$\log(\Delta\mathrm{KE}) = \log\left(\frac{\pi\rho_p}{12}\right) + 3\log d_p + 2\log(V_0) + \log(1-e^2) + 2\log(\sin\alpha_0) \tag{3.25}$$

which shows a linear variation between $\log(\Delta\mathrm{KE})$ and $\log(d_p)$, as shown in Fig. 3.85.

3.6.4 Three-Dimensional Simulation

Three-dimensional brownout simulations were performed on a full-scale representative single main rotor helicopter, with the helicopter operating in hover at a height of one rotor radius above the sediment bed. In the present study the detailed interaction between the particles and the airfoil was not modeled for the three-dimensional simulations because of the significant increase in the computational cost. This high cost is associated with checking the position of the millions of particles against the coordinates of the surface of the airfoil for potential collisions and solving

for the subsequent particle position and velocity in the event of a collision.

Figure 3.87 shows the side-view of the dust cloud for sediment particle diameters of 10 μm, 20 μm, 50 μm, and 70 μm. It is important to predict the range of particle sizes that are uplifted to the plane of the rotor, as these particle sizes could potentially contribute to blade erosion. Notice that as the particle size increased, fewer number of particles were uplifted to the plane of the rotor. On one hand, the sediment in the dust cloud predicted by the 10 μm particles size were uplifted to heights beyond the plane of the rotor and were found to be entrained into the recirculation flow through the rotor disk, while on the other hand, very few particles in the dust cloud produced by the 70 μm particle size reached the plane of the rotor.

Because particle/blade collisions were not modeled for the three-dimensional simulations, the number of particles entrained through the rotor disk was used as a surrogate metric to quantify the potential for collisions. The probability of particle/blade collisions is directly dependent on the number of particles entrained through the rotor disk, i.e., higher the number of particles entrained, higher are the changes of collisions. Figure 3.88 shows the distribution of the total number of particles of different particle diameter that were entrained through the rotor disk at the end of the brownout simulation. Comparison of the different dust clouds showed a prepondarence of smaller diameter particles, i.e., 2–3 orders of magnitude greater than the amount larger diameter particles. This trend shown in Fig. 3.88 can be related to the forces acting on the particle, primarily the gravitational force, which varies as d_p^3, where d_p is the particle diameter. Therefore, the smaller particles tend to remain suspended in the flow field to long times because of their low settling velocities.

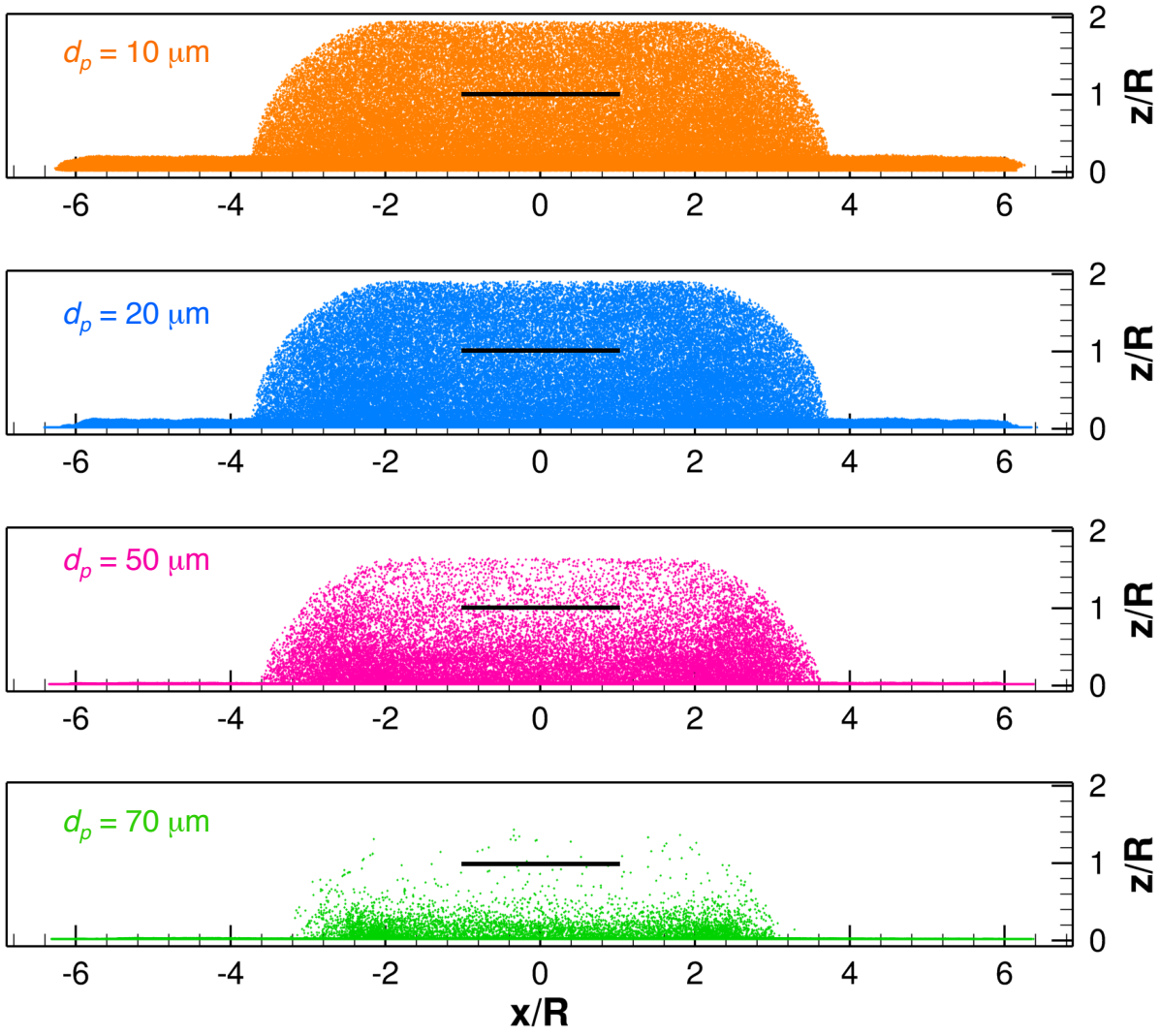

Figure 3.87: Comparison of the predicted brownout dust clouds in hover for different particle sizes.

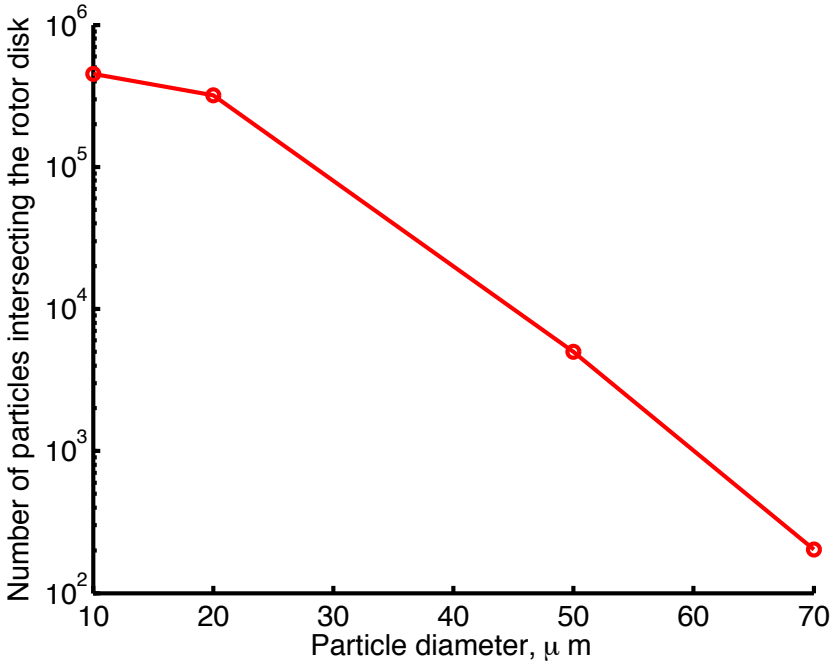

Figure 3.88: Total number of particles versus particle diameter entrained through the rotor disk for brownout clouds in hover.

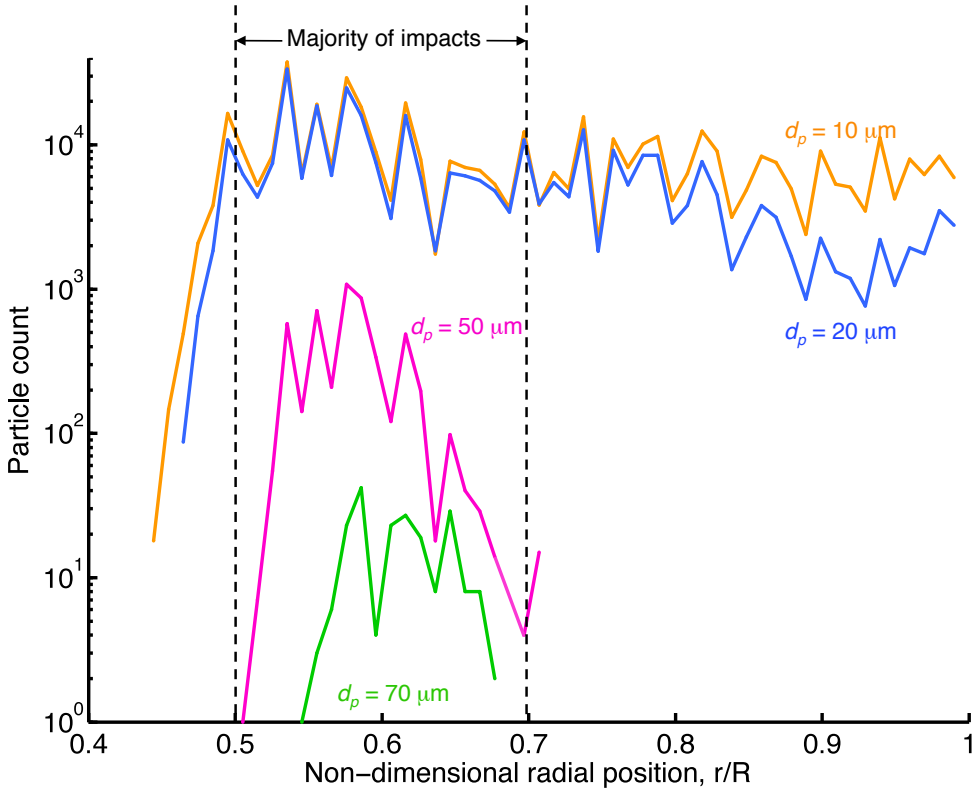

Figure 3.89: Total number of particles versus particle diameter entrained through the rotor disk for brownout clouds in hover.

An analysis was performed to quantify the number of potential blade/particle collisions along the span of the rotor disk. Figure 3.89 shows the total number of particle impacts along the span of the rotor for varying particle diameters. Majority of the impacts were found to occur between $r/R = 0.5$ and $r/R = 0.7$ for all particle diameters. This spanwise region coincided with the particle trajectories as they were entrained through the rotor disk. However, for smaller particle diameters (i.e., $d_p \leq 20\mu$m), particle impacts were also seen to occur in the outer spanwise locations. While the results shown in Fig. 3.89 indicate that most of the collisions occur somewhat in the middle spanwise locations of the rotor, studies of eroded rotor blades in brownout conditions [1] have shown that the tip regions of the rotor blades are most eroded; see Fig. 1.2 in Chapter 1. Results similar to those observed in flight tests may be obtained by performing similar erosion studies on rotors operating in forward flight or while performing landing/takeoff maneuvers, but this is beyond the scope of this preliminary study.

While the underlying physics of rotor blade erosion seen in rotors operating in dusty environments are not fully understood, the present study provides insights into some of the mechanisms involved in the process of erosion. In particular, representative two-dimensional and three-dimensional studies were performed and key parameters responsible in blade/particle collisions were identified, such as the particle diameter, impact velocity, and impact angle. To facilitate the= further understanding of the problem of blade erosion, simulations of higher fidelity are required that are capable of representing and solving in practical computational times, the detailed interactions between the blade and particles in three-dimensions.

Chapter 4

Conclusions

4.1 Summary

Rotorcraft brownout is a complex multiphase three-dimensional aerodynamic problem that has contributed to numerous human-factor related mishaps, particularly with military helicopters, and has resulted in much loss of life and property. The significance of the brownout problem is that its onset can markedly reduce the pilot's visibility of the ground during landing or takeoffs, which can pose a safety of flight risk. The structure of brownout dust clouds are highly sensitive to rotor parameters, operating conditions, and soil properties, amongst others. Further complicating the brownout phenomenon is the presence of the fuselage and different rotor configurations.

The overall goal of the present work was to develop and implement a comprehensive numerical methodology to analyze the processes involved in the formation of brownout dust clouds produced by different rotor and rotor/airframe configurations in ground effect operations. The methodology also needed to be computationally efficient enough to be practically used to study brownout clouds produced by different rotorcraft configurations, eventually helping to explore the possibilities of brownout mitigation in the process of design. The work also contributed to an initial understanding of the process of blade erosion, by studying aspects of blade/particle interactions. This final chapter discusses the key conclusions that have been drawn from the present work, and also suggests directions for future research.

4.2 Detailed Conclusions and Specific Contributions

The key observations and conclusions drawn from the present work are summarized in this section. These conclusions are divided into five subsections: 1. The overall brownout simulation methodology, 2. Analysis of the development of dust clouds produced by different fuselage configurations, 3. Dust cloud development produced by different rotor configurations, 4. Analysis of blade/particle collisions, and 5. Curved filament approximation to straight-line vortex segments.

4.2.1 Methodology

1. A time-accurate three-dimensional free-vortex method was used to model the rotor wake. The free-vortex wake model was shown to give good predictions of the flow environment, except at regions close to the ground. The approach was also validated against results from CFD RANS based solution, with good agreement being shown. The flow close to the ground was represented using a self-similar logarithmic boundary layer assumption. The confidence obtained with the free-vortex method lent confidence in the prediction of the resulting action of the rotor wake flow on the development of the dust clouds.

2. The free-vortex method was extended to include multiple rotors operating at different rotational frequencies, such as a main and tail rotor. Because the governing equations of the free-vortex method were expressed in rotor time rather than physical time, a numerical coupling strategy was developed to exchange flow solutions between the computational domains of the two rotors to ensure the numerical solution from the respective rotors are synchronized in physical time. The results showed that the aerodynamic influence of the tail rotor

on the main rotor resulted in increased susceptibility of vortex/vortex interactions and vortex bundling in the main rotor wake.

3. The aerodynamic effect of a fuselage was modeled using an unsteady surface singularity method (panel method) and coupled to the rotor wake model. Surface pressure measurements and tip vortex positions from experimental measurements for an isolated fuselage and a fuselage beneath a rotor were compared against those predicted by the panel method, with good agreement being shown. While the current manifestation of the panel method cannot model flow features typical of bluff body interactions such as flow separation or vortex bursting, it retained the key features of rotor/airframe interactions and gave reasonable predictions of the perturbations produced by the fuselage on wake developments.

4. The dust phase was represented using a Lagrangian based sediment mobilization and tracking methodology. The sediment mobility model included effects that are prevalent in vortex dominated flows, such as the unsteady pressure generated on the sediment particles by vortices passing over the mobile bed. A bombardment ejection model was also included to predict the quantity of the dust uplifted and the velocity of ejected particles after an impact from a previously suspended particle.

5. Once mobilized, these particles were convected based on the resulting forces acting on them using an efficient, multi-step, second-order accurate time-marching scheme. The predictions of the dust from the current model were compared against those obtained with full scale field tests during a touchdown-to-landing approach, with good correlation observed in the envelop of the dust clouds along the longitudinal and lateral directions. However, the simulated dust

clouds were underpredicted in terms of their vertical developments.

6. The aerodynamic modeling of multiple rotors in ground effect for long time durations along with the large number of suspended particles typical of brownout conditions means that the accumulating costs are a serious concern in any form of calculation of this problem. The computational time required for the simulations was reduced by an order of magnitude by implementing the self-induced and velocity field computations on graphics processing units (GPUs) in double precision. While some errors are incurred in the use of this approach, especially in the wake structure, they were not significant enough to alter the key features of the evolving dust clouds.

4.2.2 Effects of Fuselage

1. The interaction of the rotor wake with the fuselage resulted in large local changes to the wake geometry, and subsequently created flow disturbances that propagated throughout the wake, particularly in the form of sinuous waves on the tip vortices that also increased the susceptibility for vortex pairing. Such changes in the wake developments affected the flow at the ground plane as well as the mobilization and uplift of dust particles. The larger cylindrical fuselage was shown to produce larger distortions to the rotor wake compared to the slender tailboom of the UMD-AGARD fuselage, and greater differences seen in the development of the dust clouds were also predicted.

2. Dust clouds analyzed at the end of the landing maneuver with the different fuselage shapes showed that the clouds could be decomposed into two regions, i.e., the outer and inner struc-

ture. The outer structure of the cloud was found to be sensitive to the transitional phase of the landing maneuver, when there were more significant aerodynamic interactions between the rotor wake and the fuselage. The structure of the initially formed ground vortex was shown to be dependent on the resulting propagation of the rotor wake in close proximity to the ground. The predominantly dome-shaped inner structure of the dust cloud was found to be a result of the induced velocities from the rotor wake in hover, which is only modified slightly in the presence of fuselage. However, it is recognized that these solutions may change when flow separation effects produced by the fuselage are included.

3. An analysis of the number of particles entrained into the flow showed that while there were minor differences between the fuselage shapes, the larger cylindrical fuselage uplifted more particles a result of the greater perturbations to the developing rotor wake. Furthermore, the dust clouds were projected onto a spherical map centered around the pilot to quantify the potential visual obscuration. It was found that while the quantity of particles entrained into the flow from the different configurations are similar, their spatial distribution was highly varied and is sensitive to the fuselage shapes with certain regions in the field of view being more favorable to the pilot in terms of visual obscuration.

4.2.3 Effects of Multiple Rotors and Rotor Configurations

1. The presence of the tail rotor was found to have significant effects on the development of the wake and the resulting dust cloud. Although the vorticity in the tail rotor wake diffused substantially before reaching the ground, the aerodynamic influence of the tail rotor on the

main rotor wake led to an increased susceptibility of vortex/vortex interactions and vortex bundling in the main rotor wake. These interactions also altered the inflow distribution and the performance characteristics of the main rotor. Such effects were found to change the uplift and convection of the dust particles. The tail rotor also modified the development of the dust cloud by causing previously suspended particles to be entrained into its own wake.

2. Different rotor configurations were shown to produce different brownout dust clouds that depended strongly on the relative positioning of the rotors, i.e., tandem, coaxial or side-by-side. The interaction of the vortex wakes between the rotors and the resulting asymmetries in the wake structures associated with each configuration, were seen to play an important role in the formation and development of the predicted brownout clouds, potentially leading to various degrees of visual obscuration for the pilot. Specifically, the side-by-side configurations was shown to uplift vast quantities of dust as a result of the repeated pairing and bundling of the tip vortices from the different rotors as they convect along the ground.

3. Brownout severity metrics were developed based on the quantity of dust in the cloud, the rapidity of formation of the cloud, and the non-uniform spatial variations of sediment in the cloud. Metrics based on particle velocity were developed to help quantify what could be interpreted by pilots as vection illusions. Amongst the rotor configurations chosen, the single main rotor produced the most benign brownout cloud signature while the side-by-side rotor produced the most severe. However, amongst the multirotor configurations, the tandem rotor configurations produced the most benign type of brownout cloud.

4.2.4 Blade Particle Collisions

1. Two-dimensional studies of blade/particles collisions showed that the trajectory of these particles were dependent on their diameter. Smaller diameter particles can adapt quickly to changes in the flow environment and convect around the airfoil, whereas larger diameter particles, which have an increased particle time constant collide with the surface of the airfoil. Upon collision, the trajectories of these particles can be drastically modified and in some cases, impact again onto the airfoil resulting in multiple collision events. Therefore, to accurately capture collisions between the particles and the rotor blades, the local flow environment around the airfoil section has to be well resolved.

2. An analysis of the evolving dust clouds at older times showed that they were comprised primarily of smaller-sized particles, a result also seen in field experiments with helicopters encountering brownout conditions. This outcome is because the smaller particles tend to remain suspended in the flow field to long times because of their low settling velocities. Simulations of dust clouds in hover showed that most of the particle/blade interaction occurred at radial stations $05.5 < r/R < 0.7$, which coincided with the particle reingestion through the rotor disk. However, these results may vary when similar studies are performed in forward flight or landing maneuevers.

3. The kinetic energy loss as particles collided with the airfoil was used as a surrogate metric to quantify erosive effects, i.e., higher the loss the higher the potential blade erosion. This loss in kinetic energy was found to be higher for larger diameter particles, and varied as a cube of the particle diameter. However, the number of larger diameter particles that reached

the plane of the rotor were significantly lower than smaller diameter particles. Therefore, there may exist a particular range of particle diameters that have the largest impact on blade erosion, the identification of which requires further studies.

4.2.5 Curved Filament Correction

1. Numerical calculations of the self-induced velocity of a thin-cored vortex ring showed that for smaller discretizations, i.e., for $\Delta\theta^2 < r_c/R$, discrete calculations using straight-line vortex segments produced only half of the actual value of induced velocity. The use of local curved elements for the self-induced velocity calculations recovered the correct analytical logarithmic singularity in the core radius, given that the thin-core assumption is valid in the context of the discretization of the curved vortex elements, i.e., for $r_c/R < \Delta\theta_c^2$.

2. For the problem of a vortex ring, different values of global and local discretizations can be used to evaluate the total self-induced velocity. However, when extended to the problem of actual rotor wakes, which have a varying radius of curvature, an additional constraint is required, i.e., $(\Delta\theta_c)_{\min} \leq \Delta\theta$, which ensures that the local curved filaments do not deviate from the actual vortex trajectories.

3. The thin-core assumption is not universally valid and there may be only some segments of the vortex filament where its applicability can be justified. However, the regions of applicability of the correction term are determined by the local core radius, radius of curvature, and the subtended angle, which is problematic in application because rotor wake geometries evolve in time, especially for non-steady and maneuvering flight conditions.

4. The application of the correction term to a hovering rotor resulted in increased axial convection of the wake, which reduced the inflow distribution on the rotor blades. The validity of the correction term was shown to dependent on the azimuthal discretization of the wake which influenced the local subtended angle, $\Delta\theta$. In hovering flight, reducing the azimuthal discretization from 10° to 5° caused the thin-core condition to be violated at early wake ages.

5. In forward flight, the thin-core assumption became mostly invalid in regions of tight radius of curvature, such as the rolling up of the vortices on the advancing side, which results in large values of r_c/R and so violating the thin-core condition. A small radius of curvature also results in high local self-induced velocity, as V_Z is inversely proportional to R, which resulted in a non-physical behavior of the rotor wake.

4.3 Recommendation for Future Work

The research presented in this dissertation has demonstrated the use of a time-accurate multi-rotor FVM to study rotorcraft encountering brownout conditions in practical computational times. While the predictions show reasonable agreement with existing measurements, there are several issues that need to be addressed to improve its capabilities and its applicability to a wide range of rotorcraft problems. This section will suggest potential ways in which these research findings may be leveraged in future work.

1. The comprehensive modeling of brownout dust clouds is clearly a significant computational challenge. The high computational cost involved in the calculation of the induced velocity field from the rotor and fuselage not only limits the time step size that can be used, but also

limits the total number of particles that can be convected in the flow. Both of these issues compromise the overall fidelity of dust cloud simulations. To this end, implementation of Fast Multipole Methods (FMM) could be considered to achieve significant reductions in computational time. Ultimately, the best reductions in time can be obtained by implementing the entire methodology on one or many GPUs, i.e., the needed computational accelerations must be achieved by using both the FMM and GPU techniques.

2. The modeling of a secondary rotor in the current formulation of the FVM is limited by the governing equation being expressed in rotor time. This formulation along with the PC2B time marching scheme used, limits the ratios of rotational speeds of the two rotors that can be simulated. However, many free-vortex wake methods using time-marching schemes that are readily accommodative of rotors operating at different frequencies (such as a Runge–Kutta scheme) show non-physical wake behavior, especially in the presence of the ground. Therefore, numerical schemes can be explored that express the governing equations in physical time while maintaining the stability and accuracy of the solution.

3. The modeling of the flow near the ground and over the surface of the fuselage can be improved by using CFD techniques that can more accurately represent the viscous nature of the flow. Although a CFD simulation of the entire flow field can be computationally prohibitive, innovative hybrid techniques could be adopted in which the flow field from the FVM can be coupled to a localized CFD solution near the surfaces of the fuselage and at the ground. Such a methodology must allow for the calculations of friction velocities without any prior assumptions of the boundary later profile, which will necessitate an improvement

in the turbulence models used to predict dual-phase vortex dominated flows.

4. The dust cloud simulation methodology should be advanced further by modeling multidisperse dust clouds, i.e., dust particle simulations should be undertaken with nonuniform particle sizes. To this end, modeling the particle/particle interactions during bombardment ejections and particle collisions may be needed. In regard to bombardment ejections that occur in multidisperse dust clouds, a particle impacting the underlying bed could eject various particles of different sizes. In regard to modeling particle collisions, overcoming high computational costs will remain the main challenge because of the large number of particles present in the dust clouds and the potentially large number of collisions.

5. Free-vortex methods that represent the continuous vortex filaments using straight-line segments are frequently employed to study rotor wakes and rotor performance. However, the self-induced velocities obtained using the straight-line segments were not accurately recovered when compared against analytical results. While steps were taken to formulate and adopt a curvature correction term to eliminate the error in the self-induced velocity computations, its application to three-dimensional wakes was not shown to be universal and was limited to thin-cored filaments. To this end, further studies should be performed to better resolve the curved filaments to resolve the limitations associated with computation of self-induced velocity error or new techniques should be proposed to more accurately model the continuous vortex filaments.

6. The current state of the art relies heavily on experimental evidence to predict component life span (such as those of a rotor blade) when subjected to erosive effects that occur during

brownout conditions. A better understanding of the physical processes of blade erosion is required to design rotor components that are more resistive to erosion and can have potentially longer life span. The simulations performed in the current study are preliminary and future studies could explore a multidisciplinary approach involving material sciences that could enable a more thorough understanding of the problem of erosion.

7. The present study showed that fuselage shape and rotor positioning have a profound impact on the resulting brownout dust clouds. Previous optimizations studies have been performed to determine an optimal blade geometry in terms of the rotor radius, blade chord, twist, and flight path. However, the inclusion of fuselage shapes and rotor geometries as optimization parameters greatly increases the chances of arriving at a vehicle design that produces a benign dust cloud. Such a vast parametric study would require a highly efficient and accurate overall brownout methodology that can minimizes the computational time.

8. The aerodynamic models and the brownout simulation could be coupled with a full pilot-in-the-loop flight dynamic simulation methodology to better simulate the various flight maneuvers, i.e., moving away from the a priori prescription of the flight profile. The landing maneuvers simulated in the present work were only approximate because of the assumptions made about the rotor trim state. A careful coupling of the rotor solution to a flight dynamics analysis that incorporates a full free-flight aircraft model should allow for better simulations of the landing and takeoff maneuvers.

9. Further laboratory-scale experiments and flight tests must also be conducted to measure the overall characteristics of the brownout dust clouds if more thorough validation of the

predicted clouds is to be obtained. The measurement of as many parameters as possible must be the objective. While it is understood that not everything that might be desired can be measured, the present results give better insight as to what parameters are more important and those that might be less so. The characteristics of the dust bed and the various properties of the sediment bed should also be measured if the more complete validation of modeling approaches is to be obtained.

Appendix A: Curvature Correction

A.1 Introduction

FFree-vortex methods are one of the most common approaches in the modeling of helicopter rotor wakes, which often use vortex lines to represent the trailed vorticity for the blades. The force-free motion of such vortex lines is governed by the vorticity transport theorem, Helmholtz's third law [93], which states that vortex lines are convected as material lines. The numerical solution of this free-vortex problem requires, in part, some form of discretization of the continuously trailed vortices into discrete vortex elements or segments. These vortex elements can be of different forms, such as straight-line segments [135–137], curved segments [138] or blobs [139]. Straight-line segmentation of the vortex filaments is by far the most common and intuitive discretization strategy [68, 136, 137, 140], an advantage being that the induced velocity of each filament can be evaluated exactly using the Biot–Savart law [97]. Such an approach generally gives good accuracy when sufficiently fine levels of discretization are used for the particular problem in hand, the degree to which, in part, depends on the radius of curvature of the vortex filaments.

For the potential (inviscid) vortex ring problem, it has been shown previously [15, 141] that for straight-line segmentation the discrete induced velocity calculations are second-order accurate with respect to the discretization for all points in the flow that do not lie on the vortex ring itself. However, the solution for the self-induced velocity is singular and can only be evaluated by using an azimuthal "cutoff" inside the Biot–Savart integral [15]. One way of eliminating this singularity is by using a desingularized or regularized core, such as a semi-empirical viscous core model, for which there are many [4]. Analytical approximations to the self-induced velocity of a thin-

cored vortex ring show that the self-induced velocity has a logarithmic singularity with respect to the core radius [15]. However, calculations using non-zero core sizes show that for a given core size, the differences appear between the analytical and numerical solutions when smaller levels of discretization are used [16], thereby demonstrating an interdependence between spatial discretization and core size.

The use of curved vortex elements to eliminate this cutoff issue was proposed by Scully [135], where curved elements were used to replace the two straight-line elements that were adjacent to the evaluation point; this approach used the result of Kelvin [142]. Recently, Bhagwat & Leishman [16] showed that the use of locally curved elements can recover the analytical solution of the self-induced velocity for a thin-cored vortex-ring problem. They further demonstrated the second-order accuracy of the self-induced velocity calculated for the vortex ring problem when using straight-line segmentation augmented with the use of local curved elements. However, the correction term was based in a "thin-core" model, which requires the core radius to be at least an order of magnitude smaller than the segment length. Consequently, the validity of the correction term could be violated either in the presence of a "fatter" core (i.e., a more diffused vortex) or in regions where the vortex filaments have a higher radius of curvature, such as when individual vortices roll up with other vortices.

The present study builds on the work reported in Bhagwat & Leishman [16], and extends the analysis from a somewhat idealized vortex ring to more realistic three-dimensional simulations of rotor wakes using a free-vortex method. The fundamental assumptions involved in the development of the correction term are examined, and the relevance of the correction to rotor wake modeling

is discussed. Details of the numerical implementation of the correction term are described, with emphasis on improving accuracy and reducing computational costs for wake modeling different flight conditions, including hover, forward flight, ground effect and maneuvers.

A.1.1 Straight-Line Segmentation

The velocity induced by a curvilinear vortex filament at any point can be computed approximately by discretizing the filament into small straight-line vortex elements. The velocity induced by a straight vortex element of length l at an evaluation point located at $\mathbf{r}$ from the vortex elements can be determined by using the Biot–Savart law, i.e.,

$$\mathbf{V} = \frac{\Gamma}{4\pi}\int_l \frac{d\mathbf{l}\times\mathbf{r}}{|\mathbf{r}|^3} = \frac{\Gamma}{4\pi h}(\cos\theta_1 - \cos\theta_2)\mathbf{e} \tag{A.1}$$

where h is the perpendicular distance between the evaluation point and the vortex element, θ_1 and θ_2 are the angles subtended between the vortex elements and the position vector of the evaluation point relative to the two end points of the vortex element, respectively.

A.1.2 Core Regularization

For a infinite line vortex, the induced velocity (as given by Eq. A.1) is $\mathbf{V} = \Gamma/4\pi h$, which is obviously singular when h is zero. This singularity can be removed by using a real viscous core model to desingularize (or regularize) the vortex core. In the present work, the generalized core

model of Vatistas et al. [102] was used, which modifies the induced velocity in Eq. A.1 to read

$$\mathbf{V} = \frac{\Gamma}{4\pi}\int_l \frac{h^2}{(h^{2n}+r_c^{2n})^{1/n}}\frac{\mathrm{d}\mathbf{l}\times\mathbf{r}}{|\mathbf{r}|^3} = \frac{\Gamma}{4\pi}\frac{h}{(h^{2n}+r_c^{2n})^{1/n}}(\cos\theta_1-\cos\theta_2)\mathbf{e} \tag{A.2}$$

where r_c is the core radius, which is defined as the value of r at which the tangential velocity (i.e., swirl velocity) attains its maximum value (see Saffman, Ref. 143, Section 2.1, p. 23). Equation A.2 describes a family of vortex profiles based on the choice of parameter n. The choice of $n = 1$, corresponds to the well known "Scully" core model [135], the $n = 2$ case is an algebraic approximation to the Lamb–Oseen exponential vortex profile [142, 144], and as $n \to \infty$ the model approaches the Rankine vortex [145] with a core that rotates as a solid body.

A.1.3 Curved Filament Correction

The relationship between core radius and self-induced velocity is shown in Fig. A.1 (from Bhagwat & Leishman [15]), which exposes the limitations of accounting for only the effects of filament discretization. Figure A.1 shows the comparison between the analytical and discretized calculations of the self-induced velocity field for different core sizes when used on a vortex ring. Notice that the self-induced velocity has a logarithmic singularity and increases as $-\log\Delta\theta$, in this case where $\Delta\theta$ is the azimuthal discretization. The self-induced velocities for $r_c/R < \Delta\theta^2$ follow the analytical results for the inviscid vortex ring, suggesting that the core regularization has no effect on the solution. However, for $r_c/R \geq \Delta\theta^2$, the self-induced velocity remains almost independent of the discretization, which means that core regularization effects dominate over the resolution determined by the discretization.

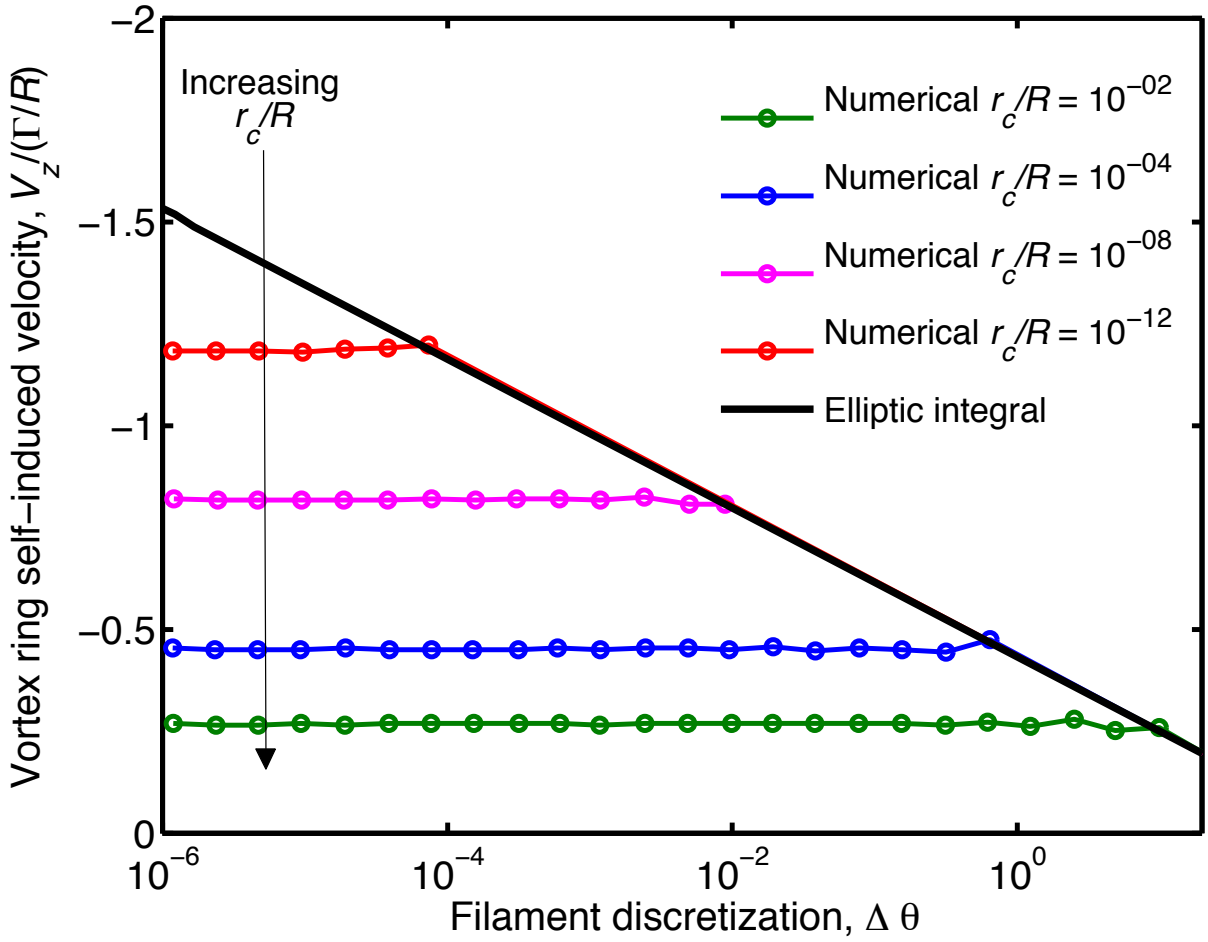

Figure A.1: Comparison of the self-induced velocity produced by a vortex ring calculated analytically and numerically by using a discretization $\Delta\theta$ with a traditional core regularization with $n \to \infty$ [15].

Recently, Bhagwat & Leishman [16] showed that the correct values of the self-induced velocities for smaller values of the azimuthal discretization (i.e., $\Delta\theta^2 < r_c/R$ in Fig. A.1) can be recovered by using a curved filament correction term. This correction was based on the approach that the two straight-line elements adjacent to the evaluation point are replaced by curved vortex elements. The self-induced velocity of the curved vortex elements was based on the analytical approach given by Kelvin [109] and Scully & Sullivan [146], where the induced velocity at the end of a curved vortex segment of extent $\Delta\theta_c$ and the radius of curvature, R, is given by

$$\Delta\mathbf{V} = \frac{\Gamma}{8\pi R}\left[\log\left(\frac{8R}{r_c}\tan\left(\frac{\Delta\theta_c}{4}\right)\right) - \frac{1}{4}\right] \tag{A.3}$$

Kelvin's solution assumes a thin-cored vortex ring with $r_c \ll R$ to allow mathematical simplifications based on leading-order approximations, which in this case ensures that the core effects are restricted to a very small region close to the vortex ring. The underlying thin-core assumption in Kelvin's formulation requires that the core radius be at least an order of magnitude smaller than the segment length, i.e.,

$$\frac{r_c/R}{\Delta\theta_c} \leq O(\varepsilon) \tag{A.4}$$

For small levels of discretization, then $\Delta\theta$ and $\Delta\theta_c$ are both small and the above conditions may be written as

$$\frac{r_c/R}{\Delta\theta_c} \leq \Delta\theta \quad \text{or} \quad \frac{r_c/R}{\Delta\theta} \leq \Delta\theta_c \tag{A.5}$$

Therefore, for the vortex ring problem, the extent of the curved segments should be at least $\Delta\theta_c^2 \geq r_c/R$ to be consistent with the thin-core assumption in Eq. A.3.

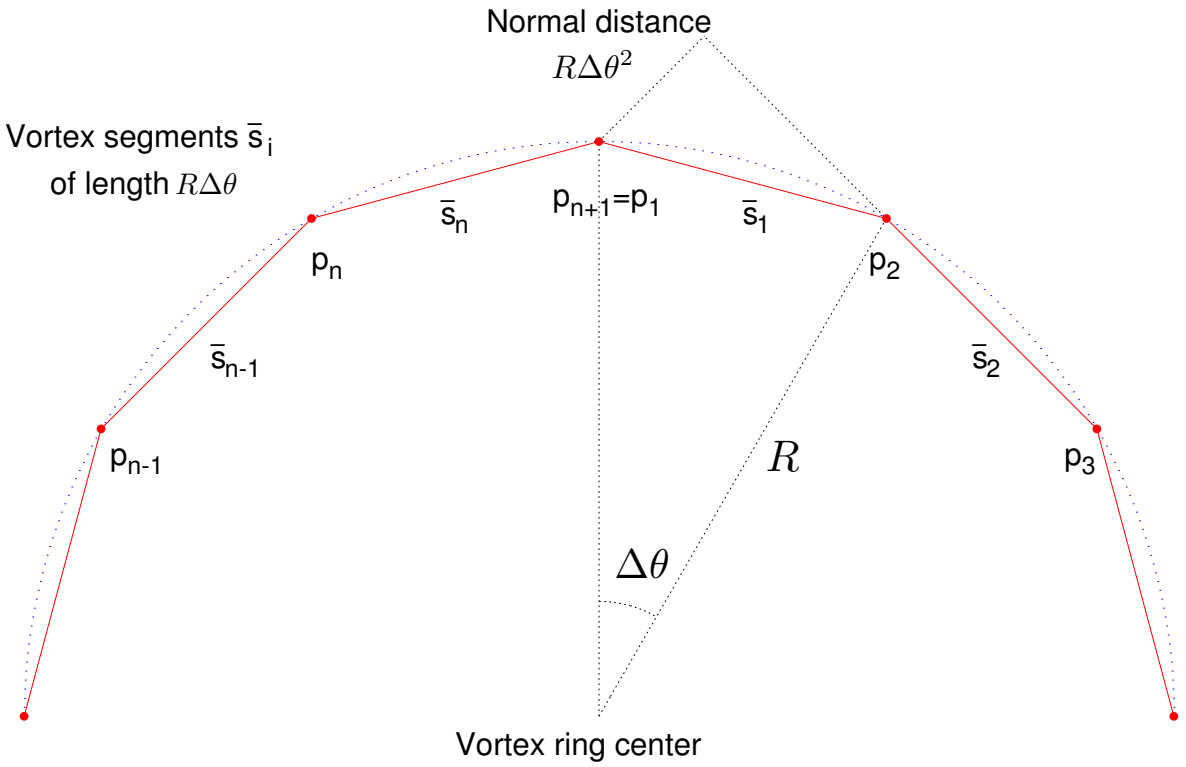

Figure A.2: Schematic of a discretized vortex ring [16].

To better understand the effect of core regularization and the curvature correction term, consider a vortex ring discretized using straight-line segments as shown in Fig. A.2. The vortex ring is discretized into n straight vortex elements of length approximately $R\Delta\theta$. Consider the self-induced velocity calculated at the evaluation point p_1 on the vortex ring. The elements s_1 and s_n do not contribute to the induced velocity at point p_1 because of the cutoff produced by the discretization in the numerical implementation. The next elements, s_2 and s_{n1}, have the shortest normal distance to the evaluation point, p_1 , which is approximately $R\Delta\theta^2$.

Assuming for convenience a Rankine vortex with a solid body core (i.e., $n \rightarrow \infty$ in Eq. A.2),

the evaluation point, p_1 , will always be outside the vortex core if $r_c < R\Delta\theta^2$, and the discretized calculations will not include any effects of the core, i.e., in a discretized sense the vortex ring behaves just like a potential vortex ring. This latter result suggests that when $r_c/R < \Delta\theta^2$, then the core radius is so small that its effects are negligible and the self-induced velocity is governed by the level of discretization. The core regularization effect is observed only in the discrete calculations when the core radius is large enough, i.e., when $r_c/R > \Delta\theta^2$, or when the discretization is small enough, i.e., when the segments are short.

Figure A.3 shows the self-induced velocity of a vortex ring as a function of the core radius as calculated numerically by using both the local curved vortex elements (Eq. A.3) and the traditional core regularization approach (Eq. A.2). Notice that the use of the latter produces only half of the analytical value of the actual self-induced velocity, whereas using the curvature correction correctly recovers the analytical result.

It should be noted that there are two aspects of the vortex segment discretizations: the global straight-line segmentation with discretization $\Delta\theta$, and the local curved vortex elements with extent $\Delta\theta_c$, as shown in Fig. A.4. The thin-core assumption gives a lower limit on the extent of the local curved vortex elements for a given core radius and radius of curvature, i.e., $\Delta\theta_c \geq r_c/R$, but the global discretization $\Delta\theta$ is not otherwise restricted and can be smaller.

A.1.4 Numerical Implementation

Bhagwat & Leishman [16] implemented and tested the validity and accuracy of the curvature correction term on an idealized two-dimensional vortex ring. However, the implementation of

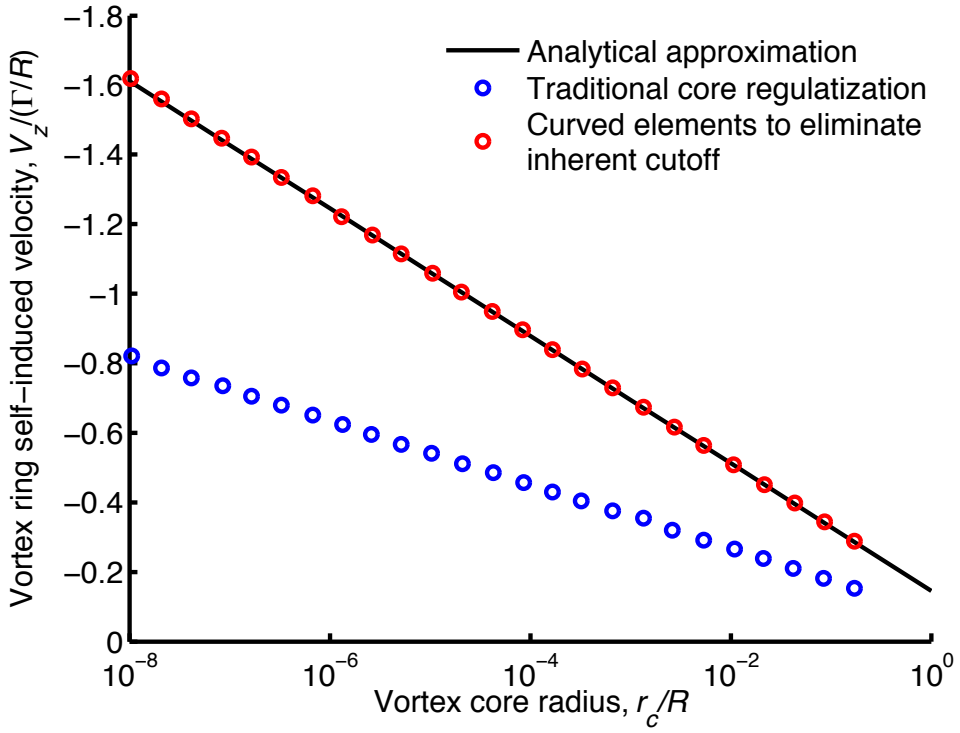

Figure A.3: Self-induced velocity of a thin-cored vortex ring as calculated numerically using the traditional core regularization (Eq. A.2) with $n \to \infty$, and the curvature correction by using Eq. A.3 with $\Delta\theta_c = 2r_c/R$ [16].

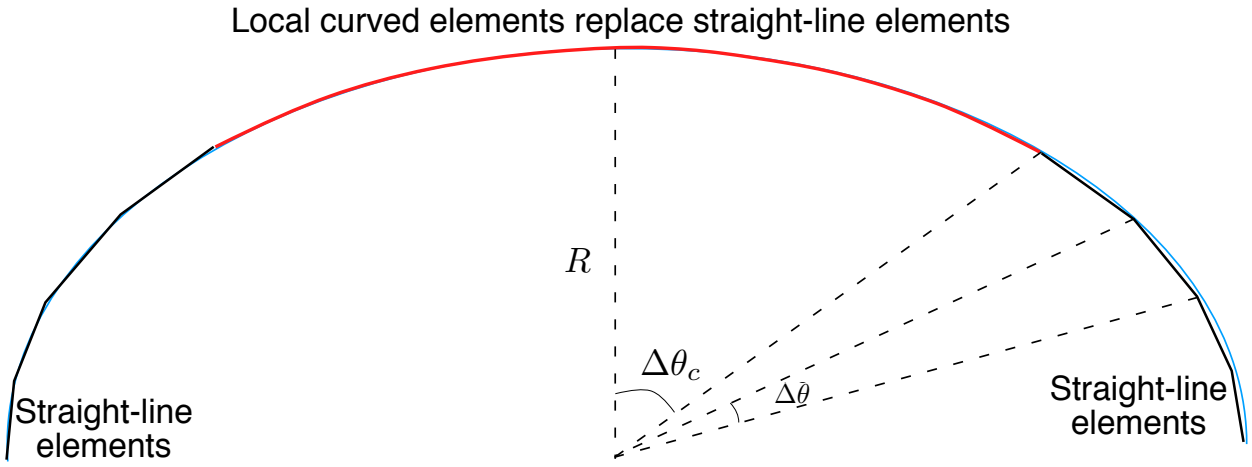

Figure A.4: Schematic illustrating the use of different global ($\Delta\theta_c$) and local discretizations ($\Delta\theta$).

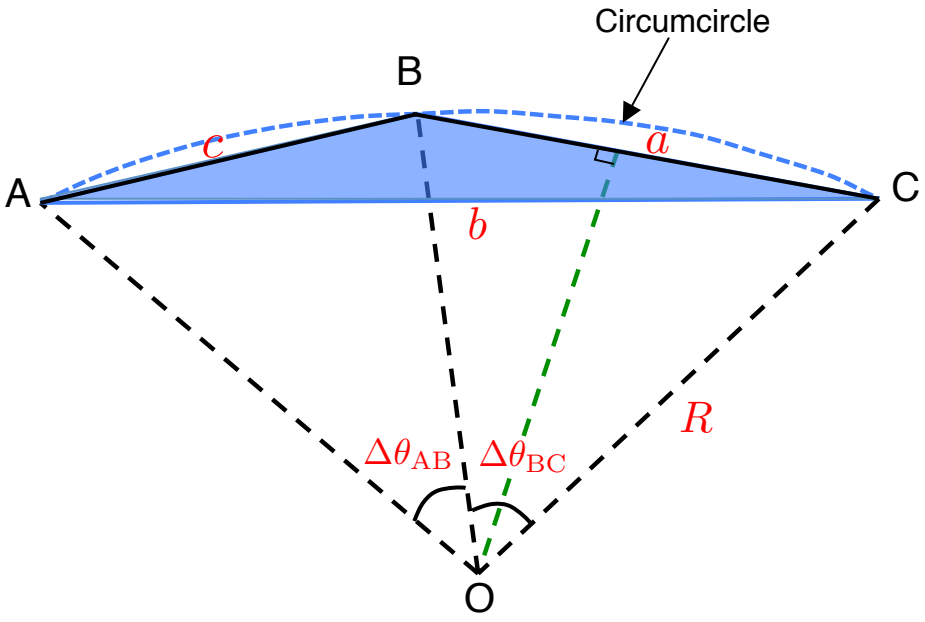

Figure A.5: Evaluation of the subtended angles of the straight-line segments at the circumcenter.

the correction term within the framework of a more general free-vortex method requires careful consideration and evaluation of the parameters in Eq. A.3.

Figure A.5 shows a schematic of a section of a vortex filament representing three collocation points (A, B, C) as they would be normally modeled using straight-line segments, such as in a free-vortex method. The self-induced velocity at B from the curved vortex filaments **AB** and **BC** is given by Eq. A.3. The angles subtended by the filaments **AB** and **BC** at the circumcircle (O) is denoted by $\Delta\theta_{AB}$ and $\Delta\theta_{BC}$, respectively, and R is the radius of curvature. Unlike the case of a vortex ring, however, evaluation of R and $\Delta\theta$ is not trivial. The quantity R in Eq. A.3 is the radius of curvature of the vortex filament at point B in Fig. A.5. From geometric considerations, any three non-collinear points in space (A, B, C) lie on a plane, and the radius of the circumcircle of the triangle formed by these three points is the radius of curvature R. The radius of the circumcircle is

given by

$$R = \frac{abc}{4K} \tag{A.6}$$

where K is the area of the triangle and $a, b,$ and c form the sides of the triangle, as shown in Fig. A.5. The area of the triangle can be represented in term of the lengths of its sides, i.e.,

$$K = [s(s-a)(s-b)(s-c)]^{1/2} \tag{A.7}$$

where s is the semiperimeter of the triangle, i.e., $s = (a+b+c)/2$. Notice that for a highly skewed triangle (e.g., one of the internal angles of the triangle is close to π), one of the terms in Eq. A.7 will approach zero and lead to a numerically small value of K. This small value will result in a large value of R in Eq. A.6, which may be non-physical and can lead to numerical issues. However, a numerically stable version (because of the algebraic organization of its constituent terms) of Eq. A.7 can be employed, where

$$K = \frac{1}{4}\Big[(a+(b+c))(c-(a-b))(c+(a-b))(a+(b-c))\Big]^{1/2} \tag{A.8}$$

with the sides of the triangle being sorted in descending order of lengths, i.e., $a \geq b \geq c$ [147].

The angle subtended by line segments **AB** ($\overline{AOB}$) and **BC** ($\overline{BOC}$) at the center of the circum-circle (O) (i.e., $\Delta\theta_{AB}$ and $\Delta\theta_{BC}$) must also be determined. Using the bisector theorem in geometry, it is known that a perpendicular line from the center of a circle to a chord on the circle bisects the

chord, which can be used to compute the subtended angle at the center of the circle, i.e.,

$$\begin{aligned} \overline{AOB} &= \Delta\theta_{AB} = 2\sin^{-1}\left(\frac{c}{2R}\right) \\ \overline{BOC} &= \Delta\theta_{BC} = 2\sin^{-1}\left(\frac{a}{2R}\right) \end{aligned} \tag{A.9}$$

The velocity induced by the curved filaments at the evaluation point is normal to both segments **AB** and **BC**, and the unit normal vector ($\mathbf{e}_V$) can be expressed as

$$\mathbf{e}_V = \frac{(\mathbf{AB} \times \mathbf{BC})}{|\mathbf{AB} \times \mathbf{BC}|} \tag{A.10}$$

Therefore, the self-induced velocity correction term at point B from the curved filaments AB and BC (in Fig. A.5) based on Eq. A.3 is

$$\Delta\mathbf{V} = \frac{\Gamma_{AB}}{8\pi R}\left[\log\left(\frac{8R}{r_{c_{AB}}}\tan\left(\frac{\Delta\theta_{AB}}{4}\right)\right) - \frac{1}{4}\right]\mathbf{e}_V + \frac{\Gamma_{BC}}{8\pi R}\left[\log\left(\frac{8R}{r_{c_{BC}}}\tan\left(\frac{\Delta\theta_{BC}}{4}\right)\right) - \frac{1}{4}\right]\mathbf{e}_V \tag{A.11}$$

where R is the radius of curvature (Eq. A.6), $\Delta\theta_{()}$ is the angle subtended at the circumcenter (Eq. A.9), $\mathbf{e}_V$ is the unit normal vector of the self-induced velocity (Eq. A.10), $\Gamma_{()}$ and $r_{c_{()}}$ are the vortex filament strength and core radius, respectively. Each term in Eq. A.11 corresponds to the self-induced velocity of a curved filament at its end points, i.e., the induced velocity of segment AB at point B and segment BC at point B.

However, this curved filament correction is valid only under the assumption of a thin-core,

which enforces a lower limit on the extent of the curved filament ($\Delta\theta_c$), i.e.,

$$\Delta\theta_c \geq \sqrt{\frac{r_c}{R}} \tag{A.12}$$

Therefore, for the curved segments **AB** and **BC** to satisfy Eq. A.12,

$$\Delta\theta_{AB} \geq \sqrt{\frac{r_{c_{AB}}}{R}} \quad \text{and} \quad \Delta\theta_{BC} \geq \sqrt{\frac{r_{c_{BC}}}{R}} \tag{A.13}$$

A.1.5 Free-Vortex Method

The aerodynamic flow field was modeled using a time-accurate free-vortex method (FVM) and is presented in detail in Section 2.2 of Chapter 2. In the FVM, the blades are represented using a Weissinger-L type lifting-line model with a full span, but truncated, near-wake. The near wake from each blade is coupled to a far wake consisting of a rolled-up tip vortex using a circulation preserving boundary condition. The far-wake consists of individual vortex trailers, usually between 10 and 12 rotor revolutions in length, which are discretized into short, continuous straight-line elements connected by discrete wake markers. Under the assumptions of irrotational and incompressible flow, the convection of these markers can be reduced to a set of linear convection equations of the form

$$\frac{\mathrm{d}\mathbf{r}}{\mathrm{d}t} = \mathbf{V}(\mathbf{r}), \quad \mathbf{r}(0) = \mathbf{r}_0 \tag{A.14}$$

where $\mathbf{r}$ is the position vector of a point on the vortex, $\mathbf{r}_0$ is the initial position vector and $\mathbf{V}(\mathbf{r})$ is local fluid velocity at the point $\mathbf{r}$.

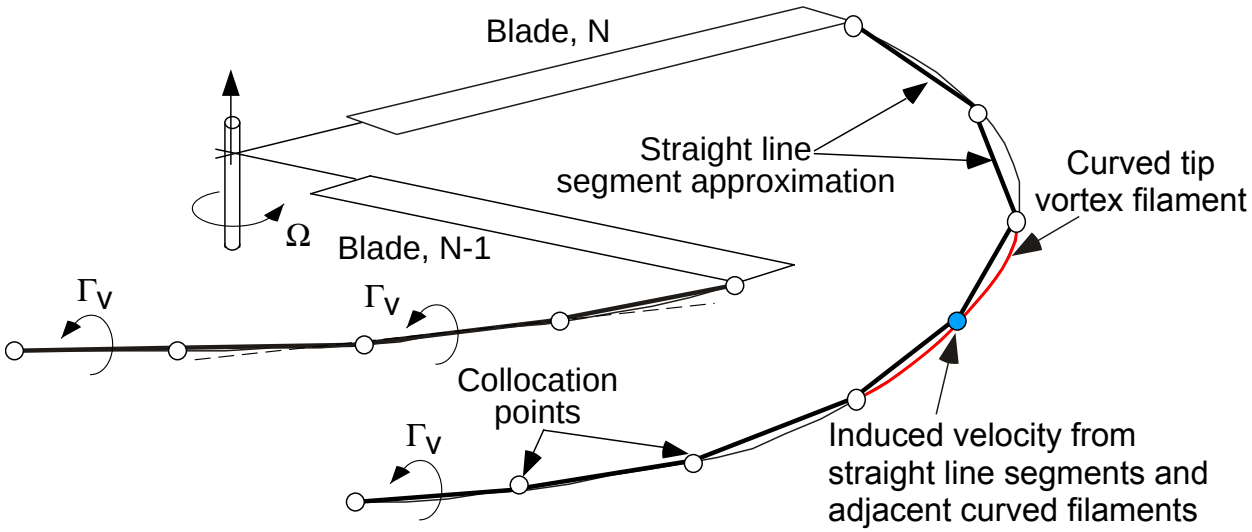

Figure A.6: Total self-induced velocity at a vortex collocation point (blue) arises from Biot–Savart computations (line-segments) and adjacent curved filaments (red).

The total induced velocity at a particular collocation point on the vortex filament is a summation of the self-induced and mutually-induced velocities of all the straight-line vortex filaments present in the solution and the self-induced velocity of the curved filaments on either side of the collocation point, as shown in Fig. A.6. This total self-induced velocity can be expressed as

$$\mathbf{V}(\mathbf{r}) = \underbrace{\sum_{j=1}^{N} \mathbf{V}_{\text{Biot}}(\mathbf{r})}_{\text{Biot–Savart computations}} + \underbrace{\Delta\mathbf{V}(\mathbf{r})}_{\text{Curved filament correction}} \tag{A.15}$$

where N is the total number of vortex filaments in the solution. The first term in Eq. A.15 is a repeated evaluation of the induced velocity using the Biot–Savart law (Eq. A.2), whereas the second term is the curved filament correction term (Eq. A.11). Notice that the induced velocity from the straight-line filaments adjacent to the evaluation point are zero when evaluated using the Biot–Savart law because the perpendicular distance to the vortex filament, h, is zero.

From the wake solutions, the resulting distribution of airloads on each blade are then computed by resolving the three-component velocity field at each blade element. The hub moments, rotor thrust, and torque are obtained by integrating the airloads over the blade span and around the rotor azimuth. A tight coupling of blade motion to the rotor wake solution is performed, with rotor being continuously trimmed using collective and cyclic blade pitch inputs to obtain a converged solution at the specified flight condition(s) with the needed rotor thrust.

For the problem of a vortex ring, where the radius of curvature is a constant at all collocation points, the curved elements can be used to replace straight-line elements with possibly different values of global and local discretization; see Fig. A.4. However, for the case of a rotor wake,the radius of curvature of the vortices will generally be different at each of the collocation points and are not known apriori. The minimum extent of the curved filament is dependent on the local core radius and radius of curvature, i.e., $(\Delta\theta_c)_{\min} = \sqrt{r_c/R}$; Eq. A.12. However caution must be exercised when applying the curved filament correction. As shown in Fig. A.7, the curved filament may not follow the trajectory of the actual vortex filament and therefore, may result in a spurious value for the induced velocity at the collocation point. Consequently, an additional condition has to be satisfied when applying the curved filament correction, especially to rotor wakes, i.e.,

$$(\Delta\theta_c)_{\min} \leq \Delta\theta \tag{A.16}$$

where $\Delta\theta$ is the local subtended angle.

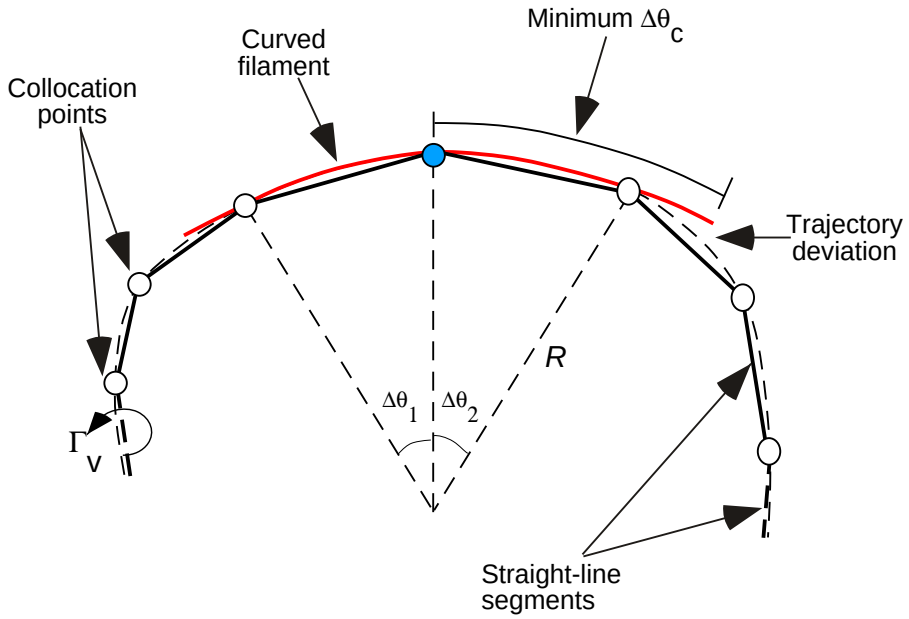

Figure A.7: Schematic illustrating the deviation of the curved filament (red) from the original tip vortex trajectory (dashed-black).

A.1.6 Curvature Correction Term

The variation of the curvature correction term with respect to the independent parameters $\Delta\theta_c$, r_c/R, and R has been examined, along with the validity of the thin-core assumption. The correction term (Eq. A.3) is repeated for convenience in its non-dimensional form, i.e.,

$$\frac{\Delta \mathbf{V}}{\Gamma/R} = \frac{1}{8\pi}\left[\log\left(\frac{8R}{r_c}\tan\left(\frac{\Delta\theta_c}{4}\right)\right) - \frac{1}{4}\right] \tag{A.17}$$

Figure A.8(a) shows the variation of $\Delta\mathbf{V}/(\Gamma/R)$ in Eq. A.17 against the subtended angle, $\Delta\theta_c$, for a constant value of radius of curvature, R, and varying values of core radius, r_c/R. The dashed line indicates the limit of the validity of the thin-core assumption, which is violated when $\Delta\theta < \sqrt{r_c/R}$. As the value of r_c/R increases, the limiting value of $\Delta\theta_c$ (Eq. A.12) also increases

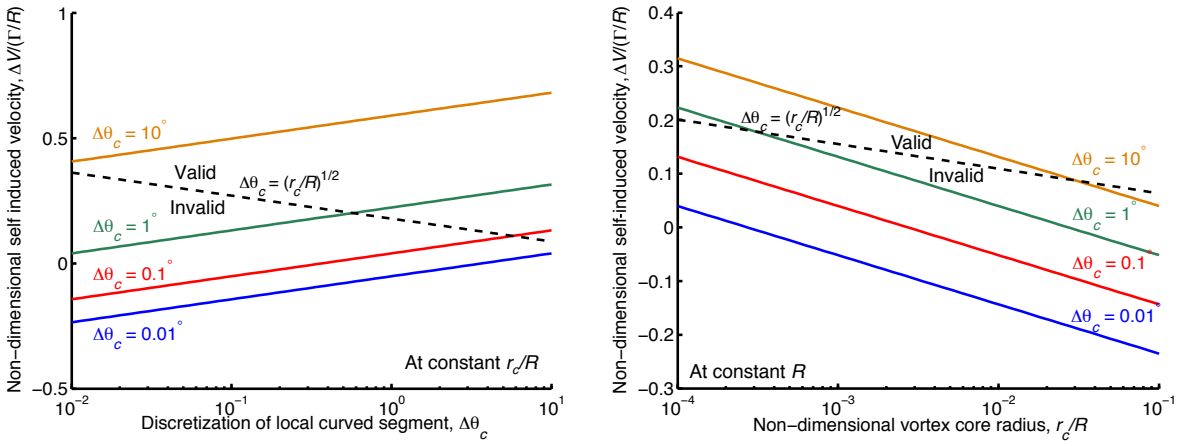

(a) Variation with $\Delta\theta_c$

(b) Variation with r_c

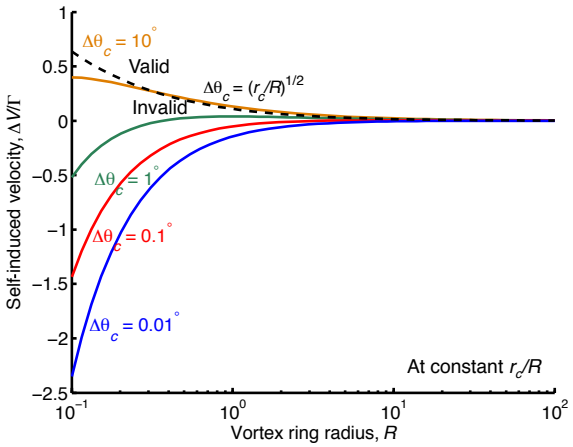

(c) Variation with R

Figure A.8: Variation of the self-induced velocity correction term with: (a) $\Delta\theta_c$, (b) r_c, and (c) R.

for the curvature correction term to be applicable. Notice that the correction term can be positive or negative based on the values of the dependent parameters.

Figure A.8(b) shows the variation of Eq. A.17 against the core radius, r_c/R, for a constant radius of curvature, R, and varying values of $\Delta\theta_c$. Greater values of r_c/R for a constant value of R indicates a "fatter" core, and so a correspondingly higher value of $\Delta\theta_c$ is needed to ensure that the evaluation point lies outside the core region necessary to satisfy the thin-core assumption; see Fig. A.2.

The curvature correction term in Eq. A.17 contains the parameter R. To evaluate the variation of the correction term as a function of R, Eq. A.17 can be re-written as

$$\frac{\Delta \mathbf{V}}{\Gamma} = \frac{1}{8\pi R}\left[\log\left(\frac{8R}{r_c}\tan\left(\frac{\Delta\theta_c}{4}\right)\right) - \frac{1}{4}\right] \tag{A.18}$$

Figure A.8(c) shows the variation of $\Delta\mathbf{V}\Gamma$ versus the radius of curvature, R, for varying values of $\Delta\theta_c$, and a constant value of the core radius, r_c. As the radius of curvature decreases (i.e., the vortex filaments form "tighter" loops) the thin-core assumption becomes increasing invalid for ranges of the subtended angles ($\Delta\theta_c$). The magnitude of the correction term approaches zero for higher value of R, as is evident from the $1/R$ behavior in Eq. A.18, which confirms that filaments with high radius of curvature geometrically approach a straight line, obviating the need for a curvature correction to the self-induced velocity.

A.1.7 Applicability to the Free-Vortex Method

Based on the foregoing, the thin-core assumption involved in the development of the curved filament correction require the following conditions to be satisfied: (a) the global and local discretizations, $\Delta\theta_c$ and $\Delta\theta$, respectively to be small angles, (b) a minimum extent of the curved filament, $\Delta\theta_c \geq r_c/R$, (c) the core radius be much smaller in magnitude compared to the local radius of curvature, i.e., $r_c \ll R$, and (d) $(\Delta\theta_c)_{\min} \leq \Delta\theta$, which is an additional condition required for filaments with varying radius of curvature, typical of rotor wakes (Eq. A.16).

Representative simulations were performed for a 4-bladed rotor of diameter 54 ft, chord of 1.7 ft, and 16° of linear nose-down blade twist. The thrust coefficient, C_T was 0.008 in both hovering and forward flight conditions.

A.1.7.1 Hovering Flight

Figure A.9 shows the wake geometry of a rotor operating in hover with discretizations, $\Delta\psi$, of 10° and 5°, respectively. The solutions for the wake geometry included the use of the curvature correction term for the self-induced velocity, with the black circles on the wake indicating the locations of the filaments where the thin-core condition (Eq. A.13) were violated. Figure A.9(a) shows that with an azimuthal discretization of 10° the thin-core condition was violated at later wake ages where bundling and grouping of the vortex filaments occurs. However, Fig. A.9(b) shows that at an azimuthal discretization of 5°, the thin-core condition was violated nearly for all of the collocation points along the filament, including those at early wake ages.

Figure A.10 shows the variation of $\Delta\theta - (\Delta\theta_c)_{\min}$ at different wake ages for azimuthal dis-

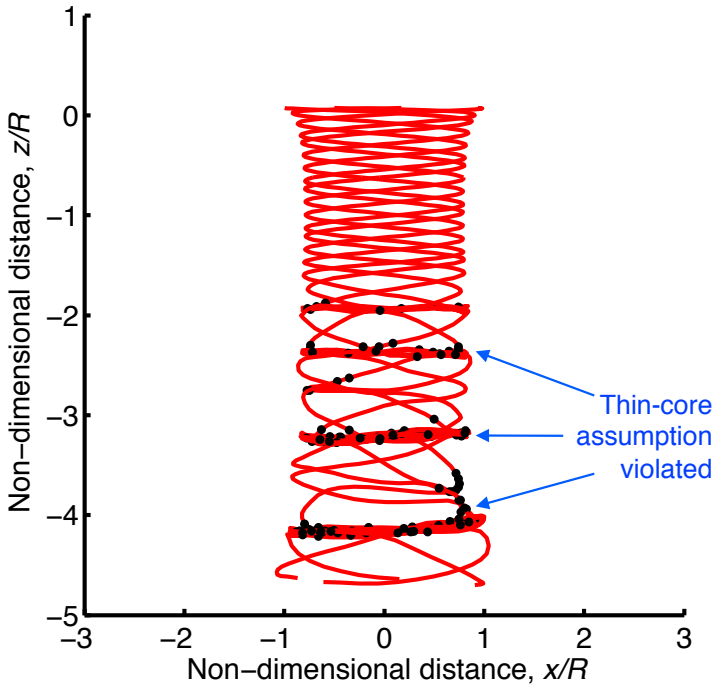

(a) $\Delta\psi = 10°$

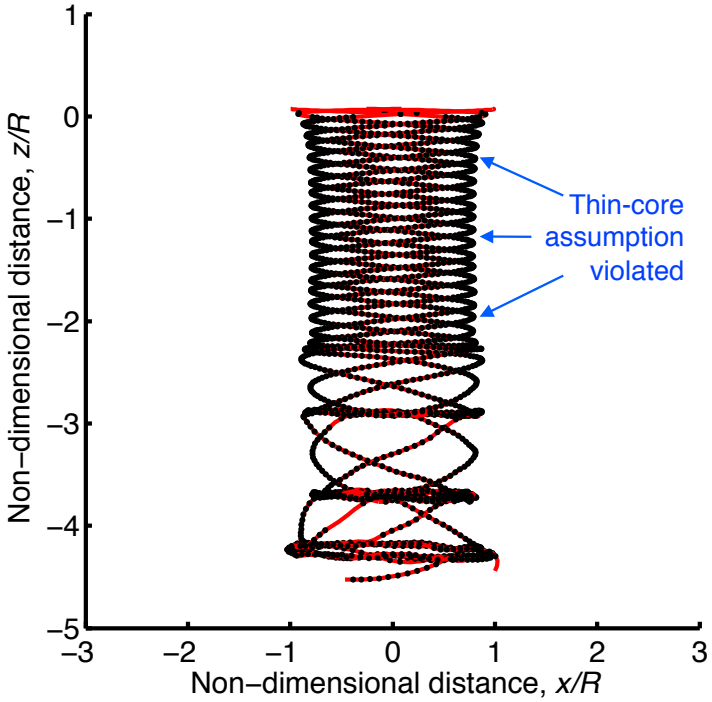

(b) $\Delta\psi = 5°$

Figure A.9: Side-view of the wake geometry for a rotor hovering with the inclusion of the curvature correction term for azimuthal discretizations of (a) 10°, and (b) 5°.

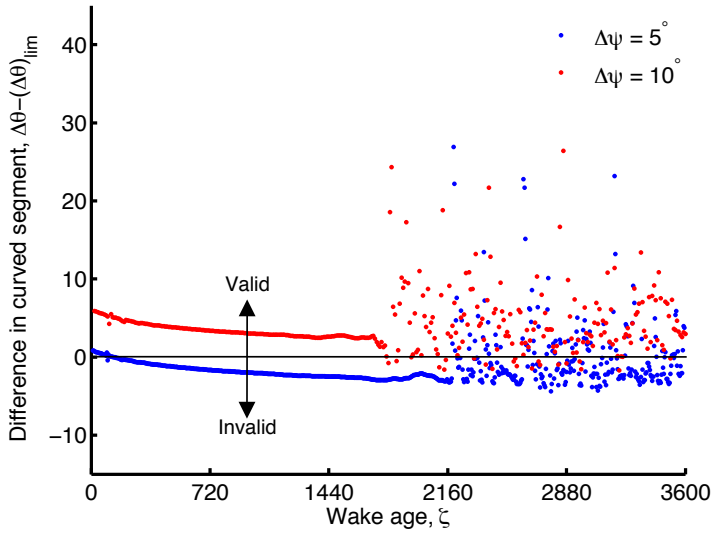

Figure A.10: Variation of $\Delta\theta - (\Delta\theta_c)_{\min}$ against wakeage for rotor azimuthal discretizations of (a) 10°, and (b) 5°.

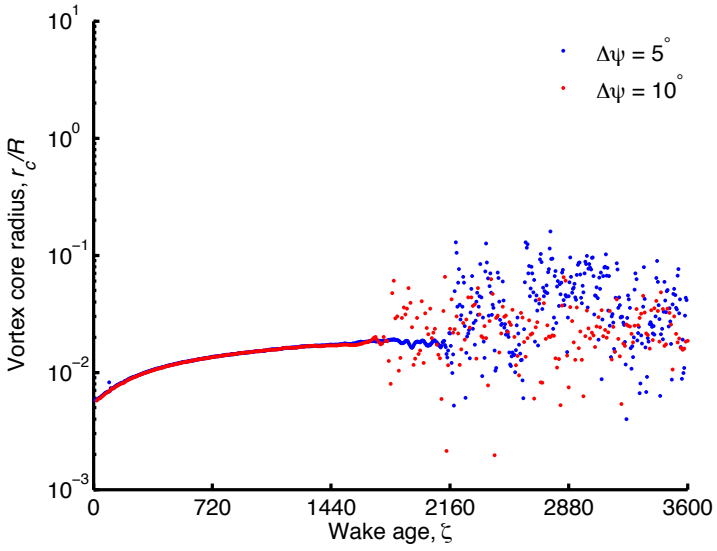

Figure A.11: Variation of r_c/R against wakeage for rotor azimuthal discretizations of (a) 10°, and (b) 5°.

cretizations of 5° and 10°. This quantity describes the difference between the local subtended angle and the minimum extent of the curved filament necessary to satisfy the thin-core condition (Eq. A.16), which is violated if $\Delta\theta < (\Delta\theta_c)_{\min}$ or $\Delta\theta - (\Delta\theta_c)_{\min}$ is negative. For an azimuthal discretization of 5°, most of the curved filaments violate the thin-core assumption, whereas for an azimuthal discretization of 10° most of the curved filaments satisfy the thin-core assumption, as shown in Fig. A.9. This outcome is obviously at variance with the the general notion of grid-convergence, where finer discretizations usually result in lower errors and, therefore, more accurate solutions.

The foregoing result can be better understood using the results in Fig. A.11, which shows that the value of r_c/R $(= (\Delta\theta_c)^2_{\min})$, is independent of the azimuthal discretization for earlier wake ages (i.e., $\zeta < 1,440°$). The subtended angle, $(\Delta\theta)$, decreases as the azimuthal discretization of the free-vortex solution decreases. Recall that as the subtended angle decreased for a given value of r_c/R, the correction term became invalid; see Fig. A.8(b). Therefore, while $(\Delta\theta_c)_{\min}$ has a constant between the two azimuthal discretizations, the value of $\Delta\theta$ decreased for $\Delta\psi = 5°$ compared to $\Delta\psi = 10°$, resulting in the curvature correction term violating the thin-core assumption at earlier wake ages, as shown in Fig. A.9(b).

Figure A.12 shows differences in the wake geometry, with and without the curvature correction terms, for $\Delta\psi = 10°$. When the correction terms are included, the wake convects axially somewhat faster. This occurs because without the use of curved filaments, the self-induced velocity from the segments on either side of the collocation point results in a zero velocity (from the evaluation of the Biot–Savart integral). However, for a curved filament, there will be a finite

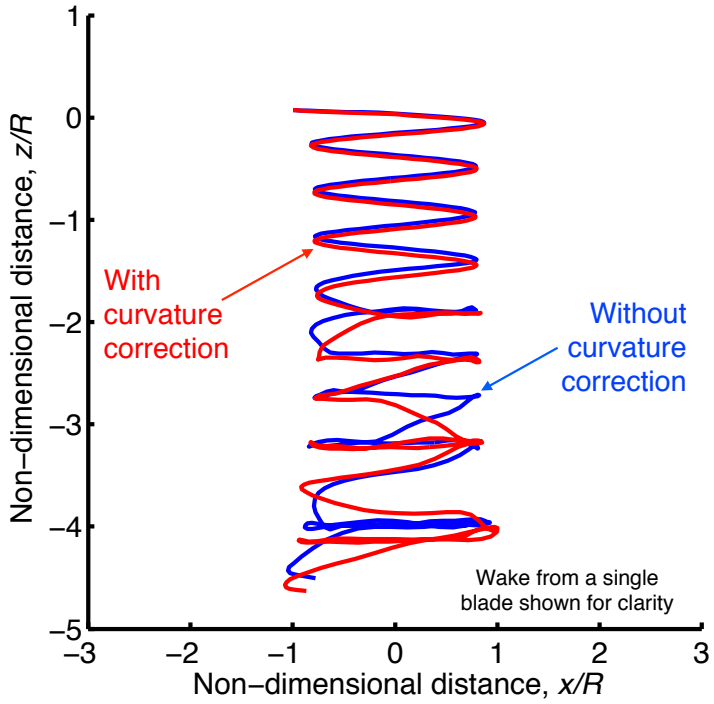

Figure A.12: Comparison of hover wake geometries with and without the curvature correction term. The wake geometry from a single blade is shown for clarity.

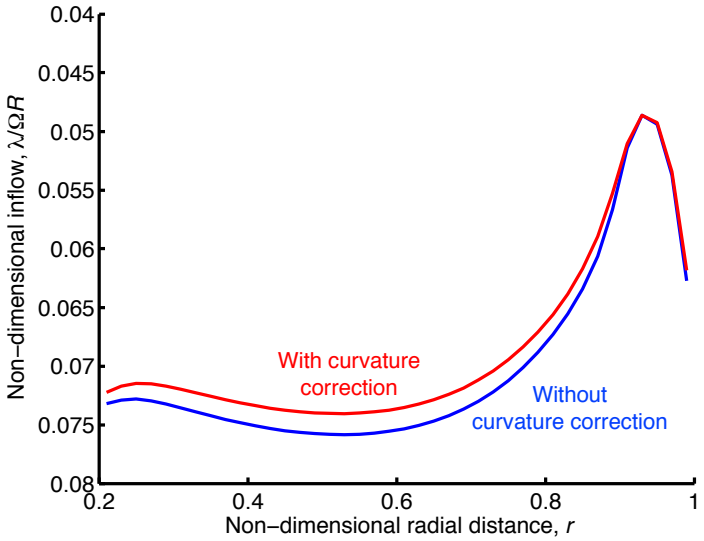

Figure A.13: Inflow distribution hover with and without the curvature correction term.

non-zero self-induced velocity from the adjacent filaments, which results in a higher rate of axial convection.

Figure A.13 shows the spanwise inflow with and without the use of the curvature correction term. The inflow with the curvature correction was noted to be slightly lower than the baseline without the correction. The axial position of the vortices with the inclusion of the correction term (Fig. A.12) produced a reduced value of induced velocity on the blade control points, which gave a lower inflow.

A.1.7.2 Forward Flight

Figure A.14 shows the side-view and top-view of the wake geometry of the rotor operating in forward flight condition at $\mu = 0.1$ with $\Delta\psi = 10^{\circ}$. The black circles indicate the collocation points where the thin-core condition was violated, which was predominantly in the vortex trailed from the advancing side of the rotor, where the vortices rolled up to form segments with a much smaller radius of curvature. As the value of was R decreased, the value of r_c/R increased, as shown in Fig. A.15(a), resulting in a filament with a "fat-core." Compared to the advancing side of the rotor, there were far fewer violations of the thin-core assumption on the retreating side, where the radius of curvature of the filaments are clearly much larger. Notice also that the tight filament loops on the advancing side result in values of r_c/R as high as 10, which violated the thin-core assumption (i.e., $r_c \ll R$) used to formulate the curvature correction term (Eq. A.3), as shown in Fig. A.14.

To quantify the effect of the curvature correction terms on the wake geometry, a comparison of the predicted wake geometries in was performed with and without the curvature correction term.

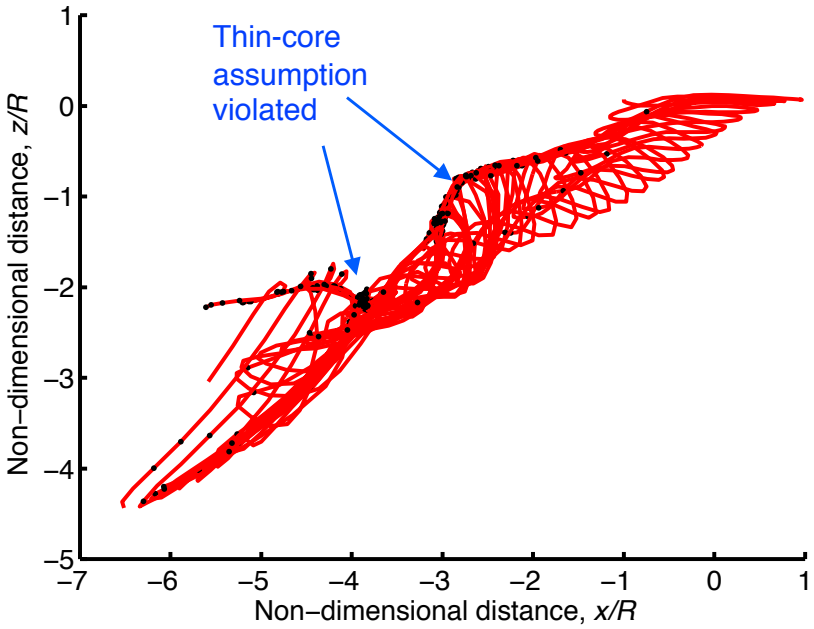

(a) Side-view

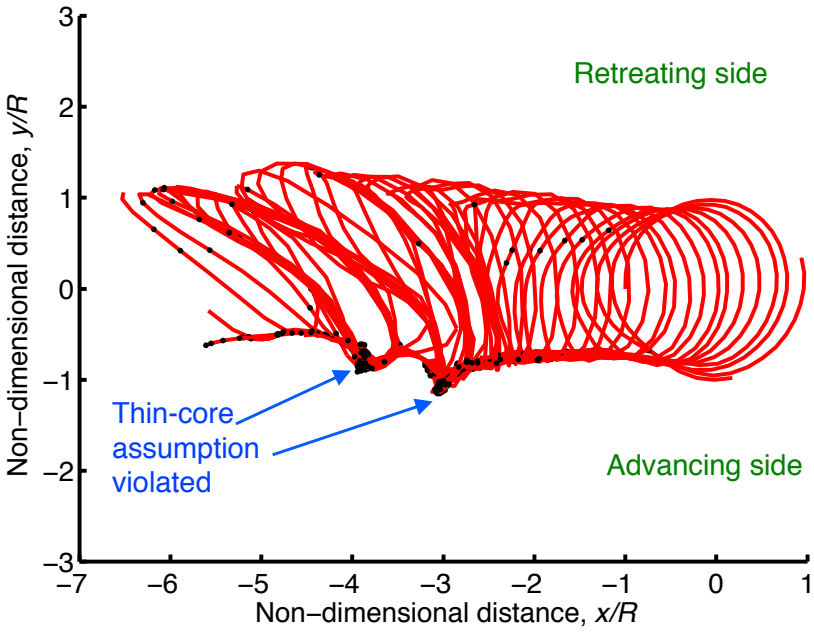

(b) Top-view

Figure A.14: Wake geometries for a rotor operating in forward flight with the inclusion of the curvature correction term.

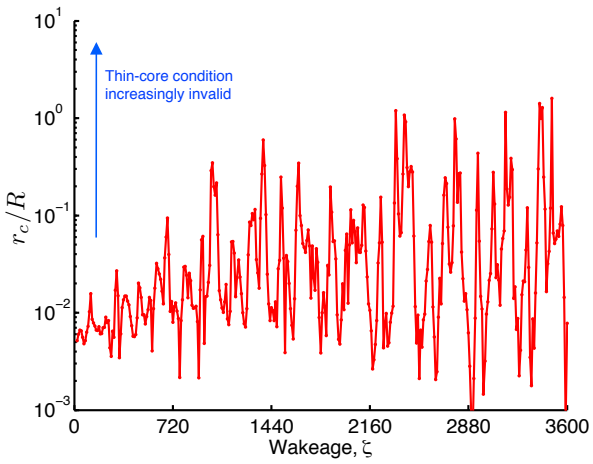

Figure A.15: Variation of r_c/R against wakeage for a rotor operating in forward flight.

The side-view and top-view of the resulting wake are shown in Fig. A.16, the geometry trailed by a single blade being shown here for clarity. The inclusion of the curvature correction term produced a substantial difference, which also affected the wake skew-angle, as shown in Fig. A.16(a). In fact, the wake geometry on the advancing side appeared as more tightly bundled vortices, as shown in Fig. A.16(b). This latter behavior is because the curvature correction term is inversely proportional to R (Eq. A.3) and, therefore, gives much higher values of the local induced velocities.

In summary, the accuracy of the induced velocity calculations augmented with a curved element correction were analyzed for application to a free-vortex wake simulation. While the inclusion of the correction term has been shown to accurately predict the self-induced velocity for a vortex ring, its application to actual rotor wake modeling requires more careful consideration because of the inherent thin-core assumption of the correction. Nevertheless, for certain classes of problems and for certain levels of wake discretization, the curvature correction can improve the fidelity of the solution with only small increases in computational cost.

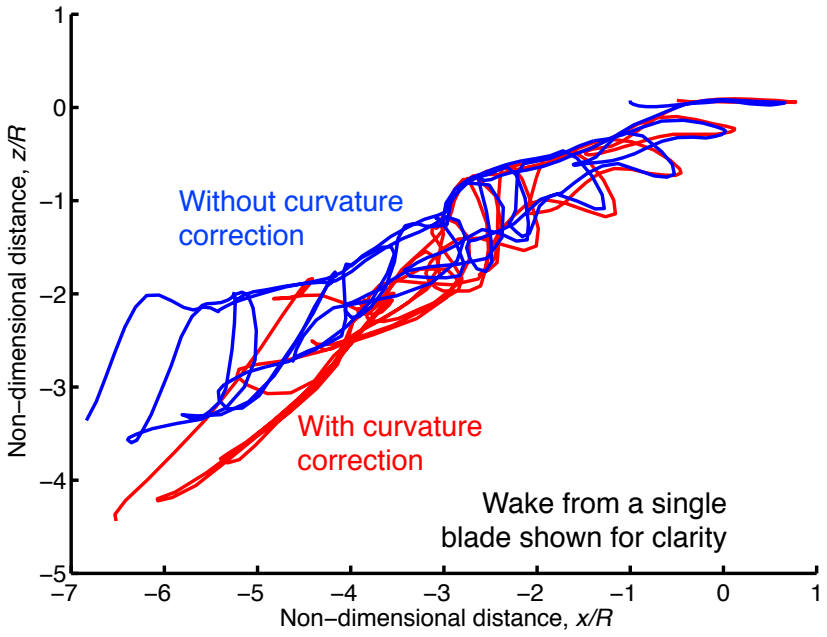

(a) Side-view

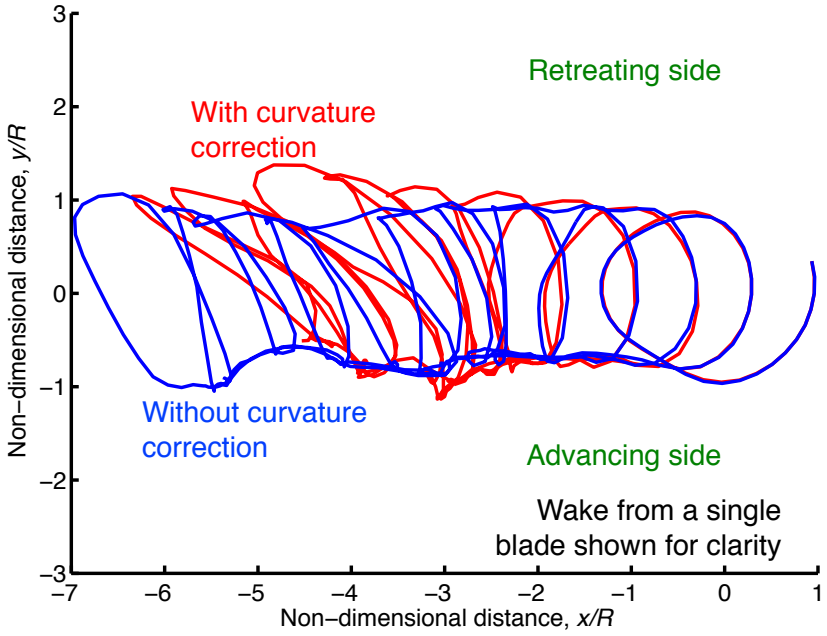

(b) Top-view

Figure A.16: Comparison of forward flight wake geometries with and without the curvature correction. The wake geometry from a single blade is shown for clarity.

Appendix B: Utilization of Graphics Processing Units

For several decades computer simulations have utilized the parallel capabilities offered by computing interfaces, such as the Message Passing Interface (MPI) for execution in parallel over a network of processors, or on multi-core CPUs when using OpenMP. The demand for real-time, high-definition, three dimensional graphics, primarily from the gaming industry, has resulted in the development of Graphics Processing Units (GPUs) into a highly parallel, multi-threaded, multi-core processors with large computational power and high memory bandwidth. GPUs are based on the single instruction multiple data (SIMD) architecture, which enables the multiple processing elements (threads) to perform the same operation on multiple data points simultaneously. Figure B.1 shows a comparison of the memory architecture of the CPU and the GPU. Notice the large number of transistors in the GPU that are devoted to data processing (Arithmetic and Logical Units, ALU) rather than to data caching and flow control as compared to that of the CPU.

In GPU computations, data is transfered back-and-forth from the CPU to the GPU and vice-versa during the computational procedure. These CPU-GPU memory communications are expensive when compared to the cost of GPU computations. Therefore, the philosophy of GPU programming is to minimize data transfer, while processing as much as data on the GPU as possible per data transfer. Programming on GPUs can be performed by using a general-purpose computing architecture called Compute Unified Device Architecture (CUDA, [17]), which was developed by NVIDIA. CUDA allows the programmer to easily manipulate the structure of the data passed to the GPU and use a large number of threads to execute them in parallel to each other. Tremendous performance gains can be obtained by using hundreds of cores of GPUs versus the limited number

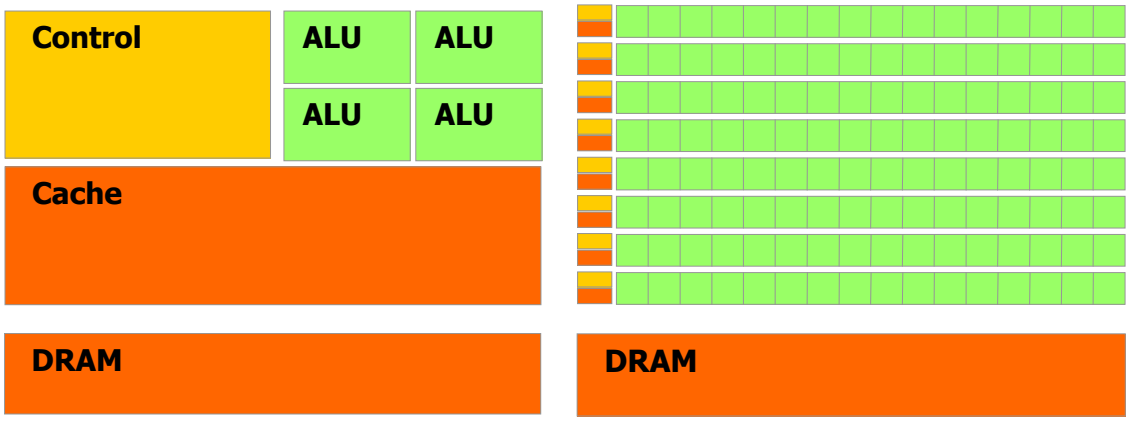

(a) CPU (b) GPU

Figure B.1: Internal memory architecture on a representative CPU and GPU.

of cores present on a multiprocessor CPU.

In the present work, GPUs were employed to expedite the calculation of the induced velocities in both the FVM and the sediment particle tracking algorithm. Specific portions of the induced velocity computed on the GPU include the: (a) self-induced effects of the vortex wake, (b) effects of far wake on to the blade control points, (c) effects of the panels on the vortex wake, and (b) the effect of the helicopter system (vortex wake and panels) on the sediment particles. Therefore, at each time step, the target positions were transferred from the CPU to the GPU, and the induced velocities were transferred from the GPU to the CPU. The parameters of the rotor wake solution, i.e., the wake geometries, vortex strengths, panel strengths, and core radii, were transferred only once from the CPU to the GPU and were stored in the constant memory of the GPU for use by all of the GPU threads. Because of the very high memory bandwidth of the GPUs ($\sim$ 200 GB s^{-1}), the CPU-GPU transfer can be limited to one per time step.

A study was undertaken to compare the accuracy of the rotor wake simulations on: (a) a parallel platform utilizing multiple cores of the CPU, and (b) a multi-core GPU architecture.

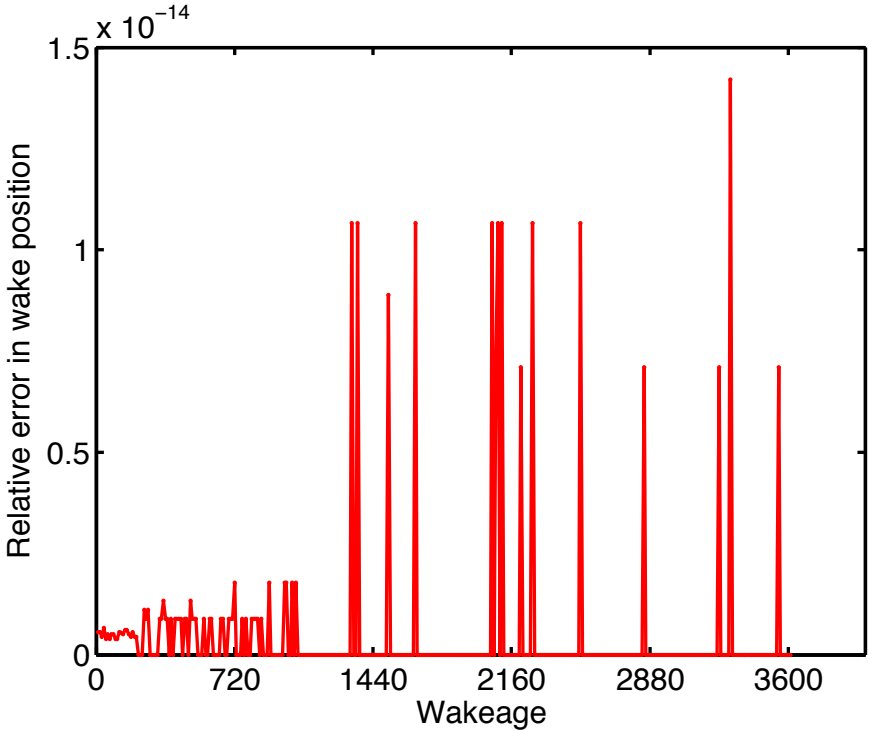

Figure B.2: L_2 norm of the error in the wake position after one time step between the CPU and GPU [17].

A representative 4-bladed rotor operating out of ground effect in hover and forward flight were considered as the test case. The vortical wake was truncated after 10 free turns. The induced velocity computations were performed using double-precision on the CPU and GPU. The GPU studies were performed on a Linux Ubuntu 12.10 operating system, using a GeForce GTX Titan GPU card.

Figure B.2 shows the L_2 norm in the wake position markers against the wake age along a vortex filament after one time step between the CPU and the GPU. The maximum difference between the two solutions is $O(10^{-14})$, which is the accuracy expected for a double-precision calculation and be attributed to machine truncation errors.

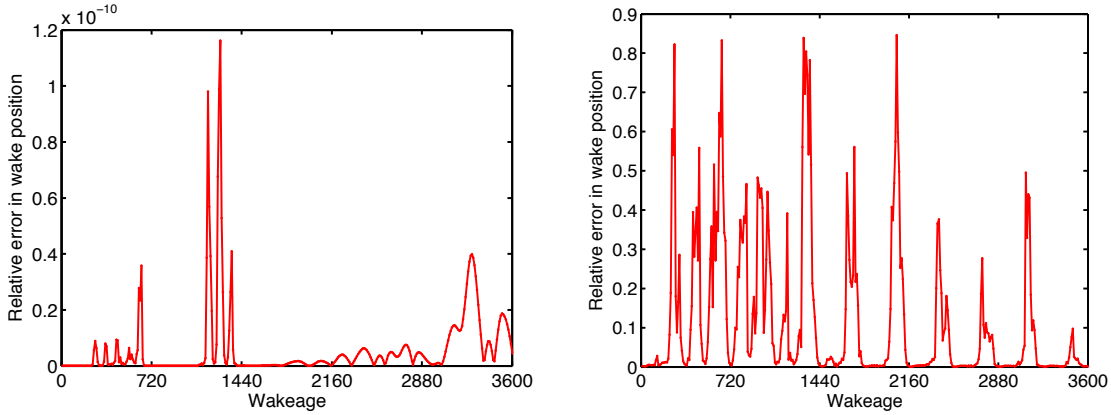

(a) Hover (b) Forward flight

Figure B.3: L_2 norm of the error in the wake position after 100 time step between the CPU and GPU for the case of (a) hover, and (b) forward flight.

Figures B.3(a) and B.3(b) shows the L_2 norm in the wake position makers against wake age after 100 time steps for the rotor in hover and forward flight, respectively. The value of L_2 norm for the hovering flight case is $O(10^{-10})$, while it is $O(10^{-1})$ for forward flight conditions. This error in the wake solution is a result of the accumulated precision error in the GPU computations over a single time step. The error in the computed induced velocity over a time step, which is $O(10^{-14})$ (see Fig. B.2), resulted in an error in the predicted filament positions compared to similar computations performed using the CPU. The error in the predicted wake positions introduced a further error in the induced velocity and so on.

Therefore, to use GPUs to perform the induced velocity computations in the FVM and sediment tracking algorithm, it is important to quantify the accuracy overall solution, i.e., the predicted dust clouds. Figure B.4 shows the predicted cloud at the end of a representative landing maneuver as computed using the CPU and GPU. Notice that while there are differences in the two solutions, the overall dimensions and structure of the dust cloud is largely similar.

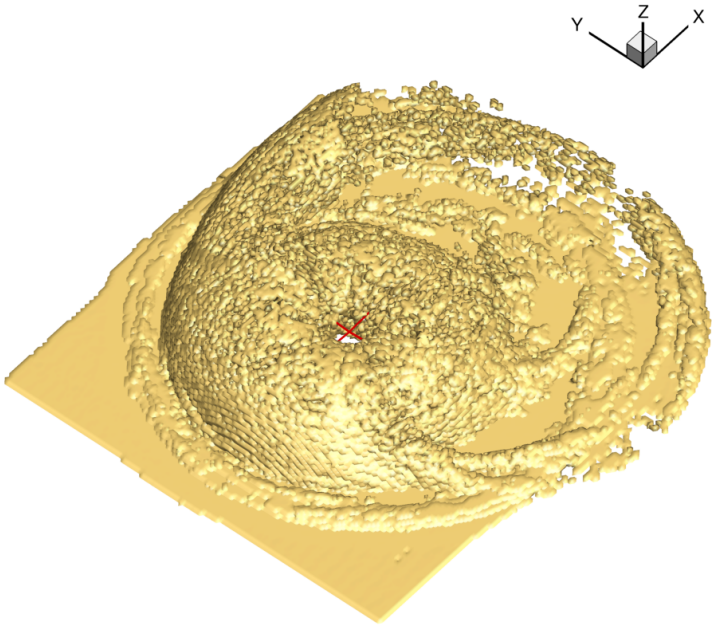

(a) CPU

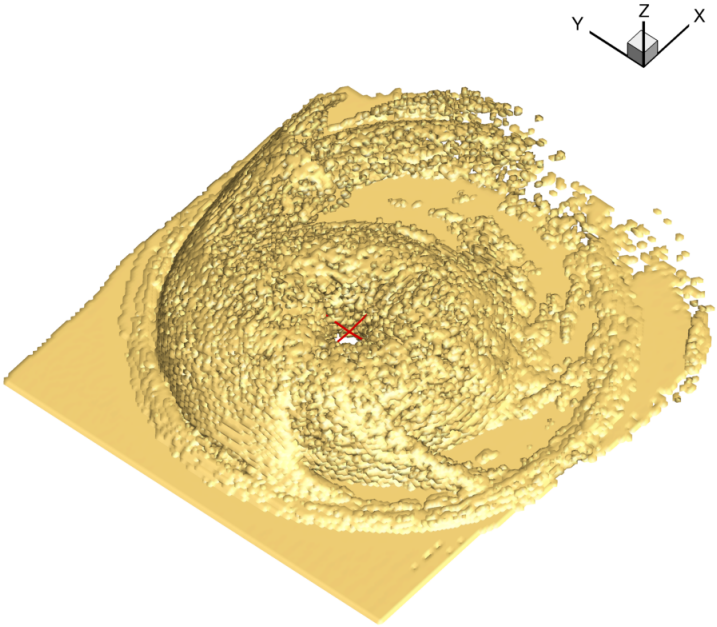

(b) GPU

Figure B.4: Isometric view of predicted brownout dust cloud at the end of a landing maneuver computed using (a) CPU, and (b) GPU.

	C_T	C_{P_i}	C_{P_p}	θ_0	β_0
CPU	8.00×10^{-3}	6.06×10^{-4}	7.87×10^{-5}	21.14°	4.19°
GPU	8.00×10^{-3}	6.06×10^{-4}	7.87×10^{-5}	21.14°	4.19°

Table B.1: Comparison of rotor performance parameters between CPU and GPU for a rotor operating in hover.

Studies were also conducted to compare the accuracy of certain metrics associated with rotor performance and control inputs when using the GPU. These metrics included the induced power, profile power, rotor control inputs, and blade flapping response. Tables B.1 and B.2 show the value of these metric for a rotor hover and forward flight conditions, respectively. The rotors were trimmed to a wind tunnel trim with a target $C_T = 8 \times 10^{-3}$. For the hovering flight condition, as shown in Table B.1 the predicted performance and rotor control parameters were identical to the third significant digit between the CPU and GPU computations. For the rotor operating in forward flight, the maximum percent error in the rotor metrics was less than 1%. Although induced velocity computations in forward flight using GPUs resulted in an error compared to the solution using the CPU (see Fig. B.3), the errors were bounded and did not lead to instabilities, as evident from the errors in the rotor performance metrics (Tables B.1 and B.2) and the similarities of the structures of the dust clouds between the CPU and GPU computations (Fig. B.4).

To consider even larger problems, algorithmic accelerations such as those provided by Fast Multipole Methods (FMM) may be utilized, which can reduce the computational cost to $O(N \log N)$. Hu et al. [148] showed that by using the FMM for such problems, and also by implementing the algorithm on GPUs, it can provide speedups of at least two orders of magnitude. This FMM

	C_T	C_{P_i}	C_{P_p}	θ_0	θ_{1c}	θ_{1s}	β_0
CPU	8.00×10^{-3}	5.27×10^{-4}	8.28×10^{-5}	20.49°	4.93°	-3.23°	4.14°
GPU	8.00×10^{-3}	5.30×10^{-4}	8.25×10^{-5}	20.50°	4.92°	-3.26°	4.14°
Percent error	-	0.56	-0.36	0.04	-0.20	0.92	-

Table B.2: Comparison of rotor performance parameters between CPU and GPU for a rotor operating in forward flight ($\mu = 0.1$).

technique, however, if beyond the scope of the present work.

Appendix C: Calculation of the Velocity Induced by a Quadrilateral Panel

The classic methodology of Hess and Smith [90] solves for the velocity induced by a planar quadrilateral panel. The formulation also assumes that the reference coordinate system contains the panel along the *x*-*y* plane, such that the third spatial coordinate is zero. This section presents the numerical implementation along with the equations for the induced velocity of a source and doublet quadrilateral panel.

C.1 Formation of a Plane Quadrilateral Surface Element

Let the four input coordinates in the reference (global) coordinate system be denoted by $\mathbf{p}_1, \mathbf{p}_2, \mathbf{p}_3$, and $\mathbf{p}_4$, respectively. Two unit diagonal vectors $\mathbf{t}_1$ and $\mathbf{t}_2$ can be formed, i.e.,

$$\mathbf{t}_1 = \frac{\mathbf{p}_3 - \mathbf{p}_1}{|\mathbf{p}_3 - \mathbf{p}_1|}, \quad \mathbf{t}_2 = \frac{\mathbf{p}_4 - \mathbf{p}_2}{|\mathbf{p}_4 - \mathbf{p}_2|} \tag{C.1}$$

In general, these vectors are not orthogonal, but a unit normal vector to the quadrilateral can be obtained by taking the cross-product of $\mathbf{t}_1$ and $\mathbf{t}_2$, i.e.,

$$\mathbf{n} = \mathbf{t}_2 \times \mathbf{t}_1 \tag{C.2}$$

The plane of the element is now completely determined if a point in this plane is specified. This point ($\mathbf{P}_{\text{avg}}$) is computed by using the average of the coordinates of the four input points, i.e.,

$$\mathbf{P}_{\text{avg}} = \frac{1}{4}(\mathbf{p}_1 + \mathbf{p}_2 + \mathbf{p}_3 + \mathbf{p}_4) \tag{C.3}$$

The element coordinate system is constructed based on three mutually perpendicular unit vectors ($\mathbf{t}_{1E}, \mathbf{t}_{2E}$, and $\mathbf{n}_E$), each one pointing along the coordinate axes of the system, and by specific the coordinate of the origin in the element coordinate system. The vector $\mathbf{t}_{1E}$ and $\mathbf{n}_E$ are chosen to be $\mathbf{t}_1$ (Eq. C.1) and $\mathbf{n}$ (Eq. C.2), respectively. Therefore, vector $\mathbf{t}_{2E}$ is defined by

$$\mathbf{t}_{2E} = \mathbf{n}_E \times \mathbf{t}_{1E} \tag{C.4}$$

To transform the coordinates of points and the components of vectors between the reference coordinate system and the element coordinate system, a transformation matrix is defined by using the components of the three basic unit vectors, i.e.,

$$\mathbf{A} = \begin{bmatrix} \mathbf{t}_{1E_x} & \mathbf{t}_{1E_y} & \mathbf{t}_{1E_z} \\ \mathbf{t}_{2E_x} & \mathbf{t}_{2E_y} & \mathbf{t}_{2E_z} \\ \mathbf{n}_{E_x} & \mathbf{n}_{E_y} & \mathbf{n}_{E_z} \end{bmatrix} \tag{C.5}$$

Therefore, if a point has coordinates (x', y', z') in the reference coordinate system and (x, y, z) in the element coordinate system, the transformation from the reference to element system is

$$\begin{aligned} x &= A_{11}(x' - x_0) + A_{12}(y' - y_0) + A_{13}(z' - z_0) \\ y &= A_{31}(x' - x_0) + A_{22}(y' - y_0) + A_{23}(z' - z_0) \\ z &= A_{21}(x' - x_0) + A_{32}(y' - y_0) + A_{33}(z' - z_0) \end{aligned} \tag{C.6}$$

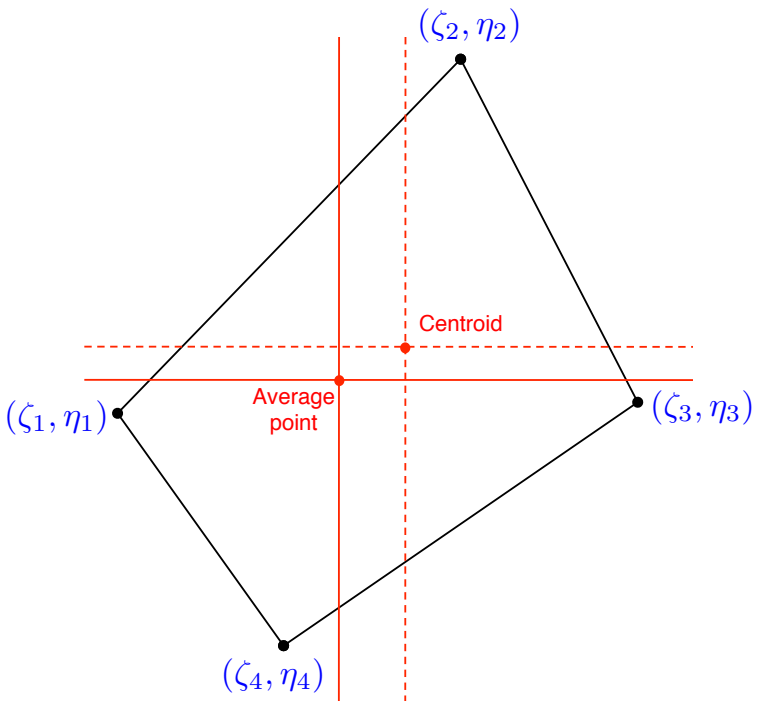

Figure C.1: Illustration of the transfer of origin from the average point to the centroid of a plane quadrilateral element.

while the transformation from the element to reference system is

$$\begin{aligned} x' &= x_0 + A_{11}x + A_{21}y + A_{31}z \\ y' &= y_0 + A_{12}x + A_{22}y + A_{32}z \\ z' &= z_0 + A_{13}x + A_{23}y + A_{33}z \end{aligned} \tag{C.7}$$

where (x_0, y_0, z_0) is the coordinate of the origin in the element coordinate system. The panel method enforces the flow tangency condition at a control point on the body surface (see Section 2.6), typically the centroid of the panel.

The corner points are transformed into the element coordinate system based on the average

point as the origin using Eq. C.6. Their coordinates in the element coordinate system are denoted by $(\zeta_k^*.\eta_k^*,0)$. The third coordinate is zero as the line in the plane of the element. The origin of the element coordinate system is now transferred to the centroid of the area of the quadrilateral, as shown in Fig. C.1. With the average point as origin the coordinates of the centroid in the element coordinate system can be expressed as [90]

$$\begin{aligned} \zeta_0 &= \frac{1}{3}\left(\frac{1}{\eta_2^*-\eta_4^*}\right)(\zeta_4^*(\eta_1^*-\eta_2^*)+\zeta_2^*(\eta_4^*-\eta_1^*)) \\ \eta_0 &= -\frac{1}{3}\eta_1^* \end{aligned} \tag{C.8}$$

The centroid given by Eq. C.8 are subtracted from the coordinates of the corner points in the element coordinate system based on the average point as origin to obtain the coordinates of the corner points in the element coordinate system based on the centroid as origin (see Fig. C.1), i.e.,

$$\zeta_k = \zeta_k^* - \zeta_0, \quad \eta_k = \eta_k^* - \eta_0 \qquad k = 1,2,3,4 \tag{C.9}$$

Using the centroid as the origin of the element coordinate system, its coordinate in the reference coordinate system (x_0, y_0, z_0) can be expressed by using Eq. C.7 as

$$\begin{aligned} x_0 &= \bar{x} + A_{11}\zeta_0 + A_{21}\eta_0 \\ y_0 &= \bar{y} + A_{12}\zeta_0 + A_{22}\eta_0 \\ z_0 &= \bar{z} + A_{13}\zeta_0 + A_{23}\eta_0 \end{aligned} \tag{C.10}$$

where $(\bar{x},\bar{y},\bar{z})$ are the coordinates of the averages of the four corner points of the panel in the reference coordinate system, as given by Eq. C.3.

C.2 Induced Velocity from a Quadrilateral Source

Figure C.2 shows a quadrilateral panel of constant strength source distribution, σ. The four corner points of the element are designated as $(\zeta_1,\eta_1,0)$, $(\zeta_2,\eta_2,0)$, $(\zeta_3,\eta_3,0)$, and $(\zeta_4,\eta_4,0)$ and the potential at a point $P(x,y,z)$ induced by this element is

$$\phi(x,y,z) = -\frac{\sigma}{4\pi}\int_S \frac{dS}{\sqrt{(x-\zeta_0)^2+(y-\eta_0^2)+z^2}} \tag{C.11}$$

The velocity components are obtained by differentiating the velocity potential, i.e.,

$$(u,v,w) = \left(\frac{\partial\phi}{\partial x},\frac{\partial\phi}{\partial y},\frac{\partial\phi}{\partial z}\right) \tag{C.12}$$

The detailed derivation of the equations for the velocity terms and the potential are given by Hess and Smith [90]. Using their results, the potential for a planar element is

$$\begin{aligned}\phi(x,y,z) &= -\frac{\sigma}{4\pi}\left\{\sum_{\substack{i=1\\j=i+1}}^{4}\frac{(x-\zeta_i)(\eta_j-\eta_i)-(y-\eta_i)(\zeta_j-\zeta_i)}{d_{ij}}\log\left(\frac{r_i+r_j+d_{ij}}{r_i+r_j-d_{ij}}\right)\right.\\ &- \left.|z|\left[\sum_{\substack{i=1\\j=i+1}}^{4}\tan^{-1}\left(\frac{m_{ij}e_i-h_i}{zr_i}\right)-\tan^{-1}\left(\frac{m_{ij}e_j-h_j}{zr_j}\right)\right]\right\}\end{aligned} \tag{C.13}$$

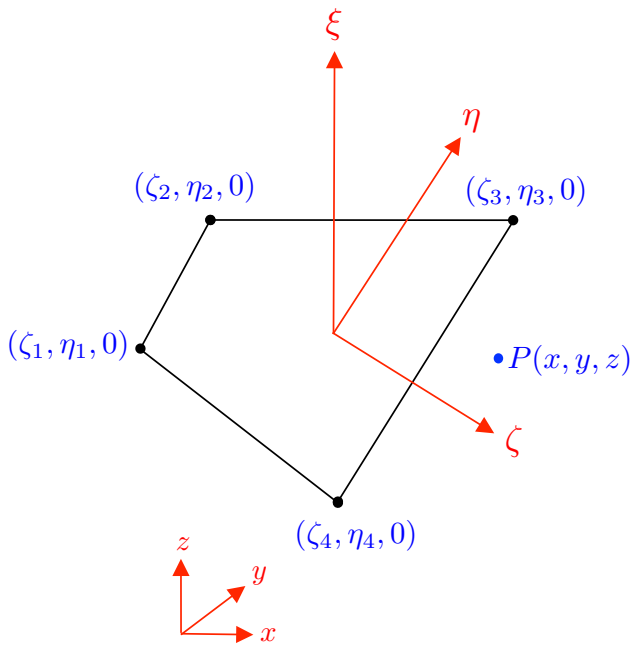

Figure C.2: Quadrilateral constant strength source element.

where

$$d_{ij} = \sqrt{(\zeta_j - \zeta_i)^2 + (\eta_j - \eta_i)^2} \tag{C.14}$$

$$m_{ij} = \frac{\eta_j - \eta_i}{\zeta_j - \zeta_i} \tag{C.15}$$

$$r_k = \sqrt{(x - \zeta_k)^2 + (y - \eta_k)^2 + z^2} \tag{C.16}$$

$$e_k = (x - \zeta_k)^2 + z^2 \tag{C.17}$$

$$h_k = (x - \zeta_k)(y - \eta_k) \tag{C.18}$$

and $i, j, k = 1, 2, 3, 4$. The velocities obtained using Eq. C.12 can be expressed as [90]

$$u = \frac{\sigma}{4\pi} \sum_{\substack{i=1 \\ j=i+1}}^{4} \frac{\eta_j - \eta_i}{d_{ij}} \log\left(\frac{r_i + r_j - d_{ij}}{r_i + r_j + d_{ij}}\right) \tag{C.19}$$

$$v = \frac{\sigma}{4\pi}\sum_{\substack{i=1\\ j=i+1}}^{4}\frac{\zeta_i-\zeta_j}{d_{ij}}\log\left(\frac{r_i+r_j-d_{ij}}{r_i+r_j+d_{ij}}\right) \tag{C.20}$$

$$w = \frac{\sigma}{4\pi}\sum_{\substack{i=1\\ j=i+1}}^{4}\left\{\tan^{-1}\left(\frac{m_{ij}e_i-h_i}{zr_i}\right)-\tan^{-1}\left(\frac{m_{ij}e_j-h_j}{zr_j}\right)\right\} \tag{C.21}$$

C.3 Induced Velocity from a Quadrilateral Doublet

Figure C.3 shows a quadrilateral panel of a doublet distribution, μ, along with its vortex ring representation. The potential of a doublet element at a point P is given by

$$\phi(x,y,z) = -\frac{\mu}{4\pi}\int_S \frac{z\,dS}{\left(\sqrt{(x-\zeta_0)^2+(y-\eta_0^2)+z^2}\right)^3} \tag{C.22}$$

The integral for the potential (Eq. C.22) is the same integral as the w velocity component of the quadrilateral source (Eq. C.21) and consequently

$$\phi(x,y,z) = \frac{\mu}{4\pi}\sum_{\substack{i=1\\ j=i+1}}^{4}\left\{\tan^{-1}\left(\frac{m_{ij}e_i-h_i}{zr_i}\right)-\tan^{-1}\left(\frac{m_{ij}e_j-h_j}{zr_j}\right)\right\} \tag{C.23}$$

$$\phi(x,y,z) = \mp\frac{\mu}{2} \quad \text{as} \quad z\to 0 \tag{C.24}$$

The velocity components are obtained by differentiating the velocity potential, similar to Eq. C.12, and are expressed as [90]

$$u = \frac{\mu}{4\pi}\sum_{\substack{i=1\\ j=i+1}}^{4}\frac{z(\eta_i-\eta_j)(r_i+r_j)}{r_ir_j\{r_ir_j-[(x-\zeta_i)(x-\zeta_j)+(y-\eta_i)(y-\eta_j)+z^2\}} \tag{C.25}$$

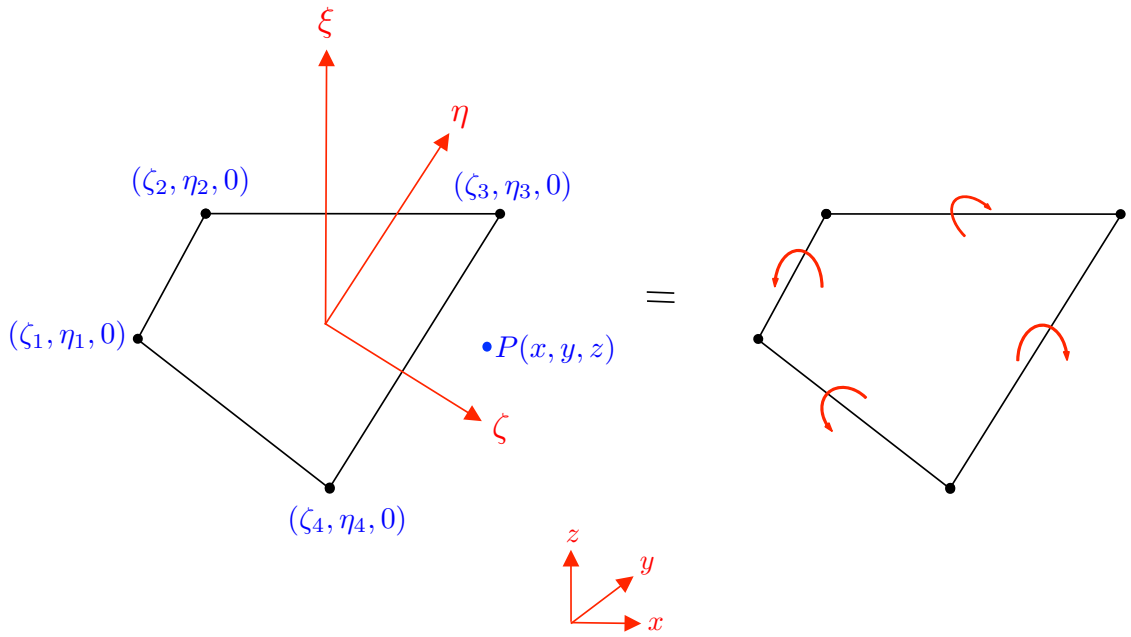

Figure C.3: Quadrilateral doublet element and its vortex ring equivalent.

$$v = \frac{\mu}{4\pi} \sum_{\substack{i=1 \\ j=i+1}}^{4} \frac{z(\zeta_j - \zeta_j)(r_i + r_j)}{r_i r_j \{r_i r_j - [(x-\zeta_i)(x-\zeta_j) + (y-\eta_i)(y-\eta_j) + z^2\}} \tag{C.26}$$

$$w = \frac{\mu}{4\pi} \sum_{\substack{i=1 \\ j=i+1}}^{4} \frac{[(x-\zeta_j)(y-\eta_i) - (x-\zeta_i)(y-\eta_j)](r_i + r_j)}{r_i r_j \{r_i r_j - [(x-\zeta_i)(x-\zeta_j) + (y-\eta_i)(y-\eta_j) + z^2\}} \tag{C.27}$$

Appendix D: Coordinate Transformations

While the wake collocation point positions for main and tail rotor are defined in a body fixed, wind axes coordinate system with its origin located at the rotor hub, the velocities encountered by the rotor blades at their control points must be referenced to a local, blade fixed coordinate system. The present analysis accounts for three transformation rotations from the fixed to the rotating frame, namely the rotor shaft angle α_s, the azimuthal location of the rotor blade ψ, and the blade flapping angle β. Figure D.1 shows a schematic of the coordinate systems used for each of the two rotors.

D.1 Main Rotor

The body fixed frame to rotating hub frame coordinate transformation matrix in the Cartesian space is given by

$$\{x\ y\ z\}^{\mathrm{T}}_{\mathrm{Rot}} = [\mathbf{A}]_{\mathrm{MR}}\ \{x\ y\ z\}^{\mathrm{T}}_{\mathrm{Fixed}} \tag{D.1}$$

where the matrix $\mathbf{A}_{\mathrm{MR}}$ is dependent on the rotor shaft angle, α_s (defined positive for forward shaft tilt), rotor coning, β, and the blade azimuthal position, ψ. The sequence of rotations are as follows

1. $(\bar{x},\bar{y},\bar{z}) = [T_{\alpha_s}](x,y,z)_{\mathrm{Fixed}}$ by α_s rotation about the y_{Fixed} axis

2. $(\hat{x},\hat{y},\hat{z}) = [T_{\psi}](\bar{x},\bar{y},\bar{z})$ by ψ rotation about the $\bar{z}$ axis

3. $(x,y,z)_{\mathrm{Rot}} = [T_{\beta}](\hat{x},\hat{y},\hat{z})$ by β rotation about the $\hat{y}$ axis

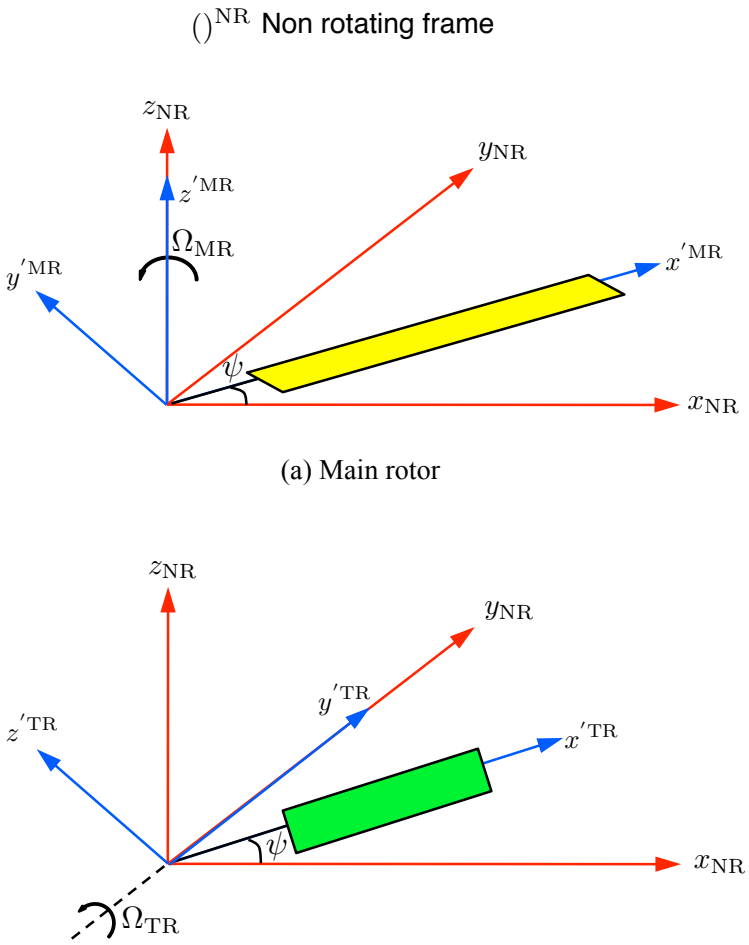

(a) Main rotor

(b) Tail rotor

Figure D.1: Schematic representationg of the fixed frame and hub rotating frame coordinate systems for the: (a) Main rotor, and (b) Tail rotor.

where the transformation matrices $[T_{\alpha_s}]$, $[T_{\psi}]$, and $[T_{\beta}]$ are given by

$$[T_{\alpha_s}] = \begin{bmatrix} \cos(\alpha_s) & 0 & -\sin(\alpha_s) \\ 0 & 1 & 0 \\ -\sin(\alpha_s) & 0 & \cos(\alpha_s) \end{bmatrix} \tag{D.2}$$

$$[T_{\psi}] = \begin{bmatrix} \cos\psi & -\sin\psi & 0 \\ -\sin\psi & \cos\psi & 0 \\ 0 & 0 & 1 \end{bmatrix} \tag{D.3}$$

$$[T_{\beta}] = \begin{bmatrix} \cos\beta & 0 & \sin\beta \\ 0 & 1 & 0 \\ -\sin\beta & 0 & \cos\beta \end{bmatrix} \tag{D.4}$$

Therefore, combining the three transformation matrices, $[A_{\mathrm{MR}}] = [T_{\alpha_s}][T_{\psi}][T_{\beta}]$,

$$\mathbf{A}_{\mathrm{MR}} = \begin{bmatrix} \cos\alpha_s\cos\psi\cos\beta \\ +\sin\alpha_s\sin\beta & \sin\psi\cos\beta & -\sin\alpha_s\cos\psi\cos\beta \\ & & +\cos\alpha_s\beta \\ -\cos\alpha_s\sin\psi & \cos\psi & \sin\alpha_s\sin\psi \\ -\cos\alpha_s\cos\psi\sin\beta & & \sin\alpha_s\cos\psi\sin\beta \\ +\sin\alpha_s\cos\beta & -\sin\psi\sin\beta & +\cos\alpha_s\cos\beta \end{bmatrix} \tag{D.5}$$

The conversion from hub rotating frame to fixed frame is obtained by inverting matrix $\mathbf{A}_{\mathrm{MR}}$ in Eq. D.1. Because $\mathbf{A}_{\mathrm{MR}}$ is an orthogonal matrix, $\mathbf{A}_{\mathrm{MR}}^{-1} = \mathbf{A}_{\mathrm{MR}}^{\mathrm{T}}$, therefore,

$$\{x\ y\ z\}_{\mathrm{Fixed}}^{\mathrm{T}} = [\mathbf{A}]_{\mathrm{MR}}^{\mathrm{T}}\ \{x\ y\ z\}_{\mathrm{Rot}}^{\mathrm{T}} \tag{D.6}$$

D.2 Tail Rotor

Similar to the transformation matrix from fixed to rotating hub frame discussed previously, the transformation matrix for the tail rotor is given by

$$\{x\ y\ z\}^{\mathrm{T}}_{\mathrm{Rot}} = [\mathbf{A}]_{\mathrm{TR}}\ \{x\ y\ z\}^{\mathrm{T}}_{\mathrm{Fixed}} \tag{D.7}$$

The sequence of rotations are as follows

1. $(\bar{x},\bar{y},\bar{z}) = [T_{\alpha_s}](x,y,z)_{\mathrm{Fixed}}$ by α_s rotation about the x_{Fixed} axis
2. $(\hat{x},\hat{y},\hat{z}) = [T_{\psi}](\bar{x},\bar{y},\bar{z})$ by ψ rotation about the $\bar{y}$ axis
3. $(x,y,z)_{\mathrm{Rot}} = [T_{\beta}](\hat{x},\hat{y},\hat{z})$ by β rotation about the $\hat{y}$ axis

where the transformation matrices $[T_{\alpha_s}]$, $[T_{\psi}]$, and $[T_{\beta}]$ are given by

$$[T_{\alpha_s}] = \begin{bmatrix} 1 & 0 & 0 \\ 0 & \cos(\alpha_s) & -\sin(\alpha_s) \\ 0 & -\sin(\alpha_s) & \cos(\alpha_s) \end{bmatrix} \tag{D.8}$$

$$[T_{\psi}] = \begin{bmatrix} \cos\psi & 0 & \sin\psi \\ 0 & 1 & 0 \\ -\sin\psi & 0 & \cos\psi \end{bmatrix} \tag{D.9}$$

$$[T_\beta] = \begin{bmatrix} \cos\beta & \sin\beta & 0 \\ -\sin\beta & \cos\beta & 0 \\ 0 & 0 & 1 \end{bmatrix} \tag{D.10}$$

Therefore, combining the three transformation matrices, $[A_{TR}] = [T_{\alpha_s}][T_\psi][T_\beta]$,

$$\mathbf{A}_{TR} = \begin{bmatrix} \cos\beta\cos\psi & \begin{matrix}\cos\alpha_s\sin\beta \\ -\sin\psi\cos\beta\sin\alpha_s\end{matrix} & \begin{matrix}\sin\alpha_s\sin\beta \\ +\sin\psi\cos\beta\cos\alpha_s\end{matrix} \\ -\sin\beta\cos\psi & \begin{matrix}\cos\alpha_s\cos\beta \\ +\sin\psi\sin\beta\sin\alpha_s\end{matrix} & \begin{matrix}\sin\alpha_s\cos\beta \\ -\sin\psi\sin\beta\cos\alpha_s\end{matrix} \\ -\sin\psi & -\cos\psi\sin\alpha_s & \cos\psi\cos\alpha_s \end{bmatrix} \tag{D.11}$$

The conversion from hub rotating frame to fixed frame is obtained by inverting matrix $\mathbf{A}_{TR}$ in Eq. D.7, similar to Eq. D.6, i.e.,

$$\{x\ y\ z\}^{\mathrm{T}}_{\mathrm{Fixed}} = [\mathbf{A}]^{\mathrm{T}}_{\mathrm{TR}}\ \{x\ y\ z\}^{\mathrm{T}}_{\mathrm{Rot}} \tag{D.12}$$

Appendix E: Particle Clustering Algorithms

The total number of particles in a typical brownout cloud can reach the order of billions, which makes the individual tracking of each particle computationally expensive and practically infeasible. Particle clustering is a technique that allows for the tracking of groups of particles in a brownout dust cloud. Particles are grouped into cluster based on prescribed rules, to which the EOMs are applied, the result being a significant savings in the computational costs. The effectiveness of clustering techniques depends on two conditions: (a) the number of clusters should be such that the computational benefit should far outweigh the overhead associated with the algorithm implementation, and (b) the accuracy of the clustering solution must be quantifiable and with the required solution tolerance. Only if these two conditions are satisfied can particle clustering techniques be used effectively for predicting the development of dust clouds.

The clustering algorithm used in the present study is based on the research conducted by Govindarajan and Leishman [124]. The applicability of three particle clustering algorithms to brownout simulations were studied in the foregoing research: (a) Gaussian-based clustering, (b) k-means, and (c) Osiptsov's method. The outcomes of this study suggested that each clustering technique has its advantages and disadvantages, and the outcomes from these methods must be analyzed thoroughly to account for any errors that might be incurred during the process of clustering. Among the methods studies, the Gaussian method, which was designed to preserve the actual computed solution even in regions of high velocity gradients, was shown to provide the most encouraging results when applied to the full brownout problem. Therefore, the Gaussian method is discussed in detail here.

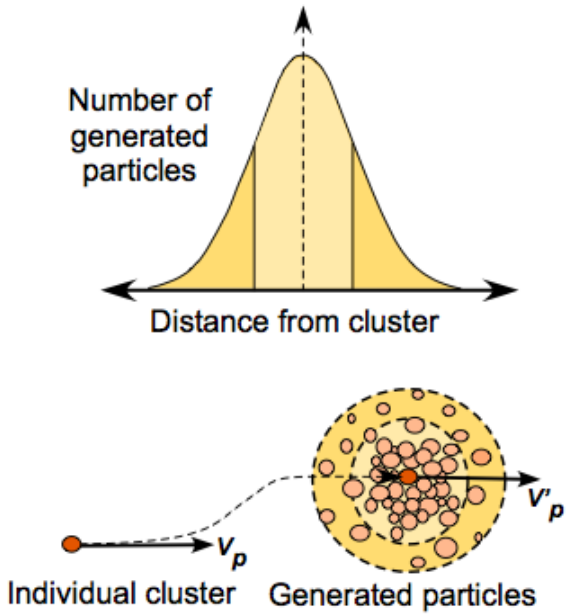

Figure E.1: Schematic showing the Gaussian method of particle clustering.

In the Gaussian-based clustering approach, the individual particles in the brownout simulation are treated as clusters, each representing a specific number of particles. The clusters are convected at each time using the EOMs. The positions of the individual particles associated with a cluster are calculated by using a multi-variate Gaussian distribution. The position of the particles within a specific cluster are recomputed at every time, and therefore, can be implemented as a post-processing step in the simulation framework.

In there are N_1 particle assumed in a brownout cloud simulation, then each of these particles can be treated as a cluster representing a further N_2 particles, giving a total of $N_1(N_2+1)$ particles. The N_2 particles around each N_1 particle are distributed in a Gaussian form, as shown in Fig. E.1.

Because the particles in the cluster are distributed in a Gaussian fashion, the mean vector, μ_c,

and covariance matrix, Σ_c, for each cluster can be defined as

$$\mu_c = [V_{px} V_{py} V_{pz}] \tag{E.1}$$

and

$$\Sigma_c = \frac{1}{E_c} \begin{bmatrix} k_1|V_{px}|^2 & k_2|V_{px}||V_{py}| & k_2|V_{px}||V_{pz}| \\ k_2|V_{py}||V_{px}| & k_1|V_{py}|^2 & k_2|V_{py}||V_{pz}| \\ k_2|V_{pz}||V_{px}| & k_2|V_{pz}||V_{py}| & k_2|V_{pz}|^2 \end{bmatrix} \tag{E.2}$$

where V_{px}, V_{py}, and V_{pz} are the instantaneous velocities of each cluster and E_c is a measure of the kinetic energy of the cluster. Ideally, the cluster spread should be proportional to E_c. This results, however, would lead to a large non-physical spread of the cluster in regions of high flow velocity. Scaling the covariance matrix by E_c^{-1} therefore would collapse the particles down to the location of the original particle where local velocities are large, preventing any non-physical error because of the clustering process.

One of the mathematical conditions on the covariance matrix is that is should be positive definite, i.e.,

$$k_1 > 0, \quad k_2 > 0, \quad (k_1 - k_2) > 0 \tag{E.3}$$

which is derived from Sylvester's condition for a positive definite matrix [149] and

$$\frac{k_2}{k_1} < \min \left[\frac{|V_{px}|}{|V_{py} + V_{pz}|} + \frac{|V_{py}|}{|V_{px} + V_{pz}|} + \frac{|V_{pz}|}{|V_{px} + V_{py}|} \right] \tag{E.4}$$

which is the condition on a matrix to be diagonally dominant. The parameter k_1 is a scalar that

dictates the spread in the each of the principal directions, i.e., x, y, z, and k_2 can be viewed as a cross-coupling coefficient. The positions of the N_2 particles are then calculated using the velocities obtained from the foregoing distribution matrix.

Estimation of errors incurred by the clustered solution is important to establish confidence in the clustering techniques. Metrics such as the root mean square and Pearson's coefficient were discussed by Govindarajan [18], but they are limited in its application for simpler problems. An application of the Gaussian clustering technique to a prototypical two dimensional problem (representing a train of vortices over a sediment bed) is shown in Fig. E.2. The details of this flow is given by Govindarajan [18], Chapter 2, pp. 41–45. Figure E.2 shows two solutions: one obtained using an exact computation, where all the particles are individually tracked, and the second one using the Gaussian-based clustering approach. The exact solution contained 5,625 particles while the clustered solution contained 1,125 cluster and each cluster represented 5 additional particles.

Figures E.2(a) and E.2(b) show an instantaneous rendition of the position of the particles for the exact and the clustered solution, respectively. Notice that the two solutions look similar but the cost of obtaining the clustered solution is approximately 5 times lower as compared to the exact solution. Figures E.2(c) and E.2(d) shows the particle concentration maps associated with the exact and clustered solution, respectively. The density maps looks very similar to each other and the error in the particle density were compared using Pearson's coefficient, with a 90% correlation, the details being given by Govindarajan [18].

Figure E.3 shows an example of the application of the Gaussian clustering technique to a three dimensional brownout cloud. A comparison of the solution was obtained with 10^6 clus-

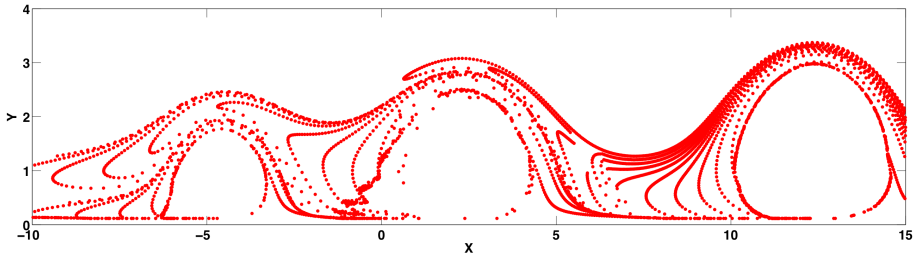

(a) Particle positions - Exact solution

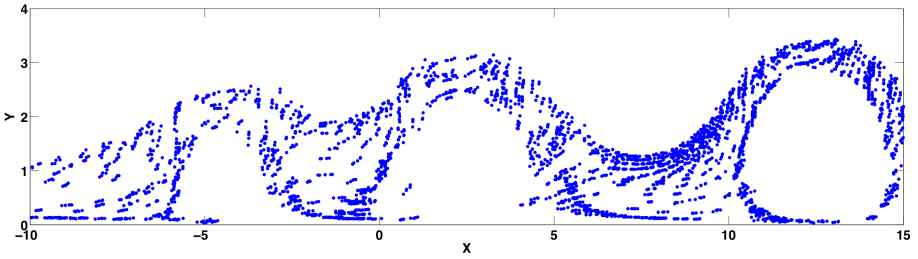

(b) Particle positions - Clustered solution: Gaussian

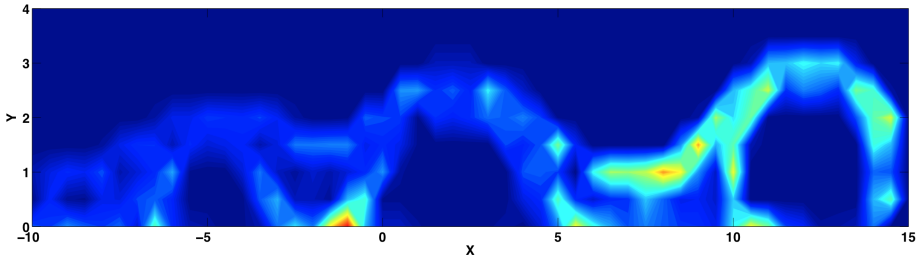

(c) Density contour plot - Exact solution

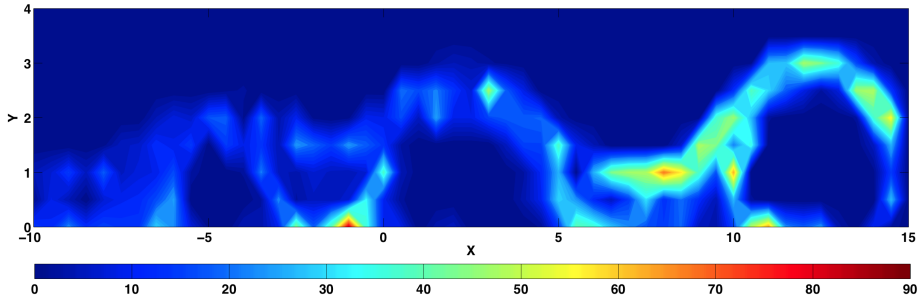

(d) Density contour plot - Clustered solution: Gaussian

Figure E.2: An example of Gaussian solution obtained from Govindarajan [18]: Total number of clusters cluster = 1,125, total number of particles per cluster = 5, i.e., total number of particles in the clustered solution = 5,625.

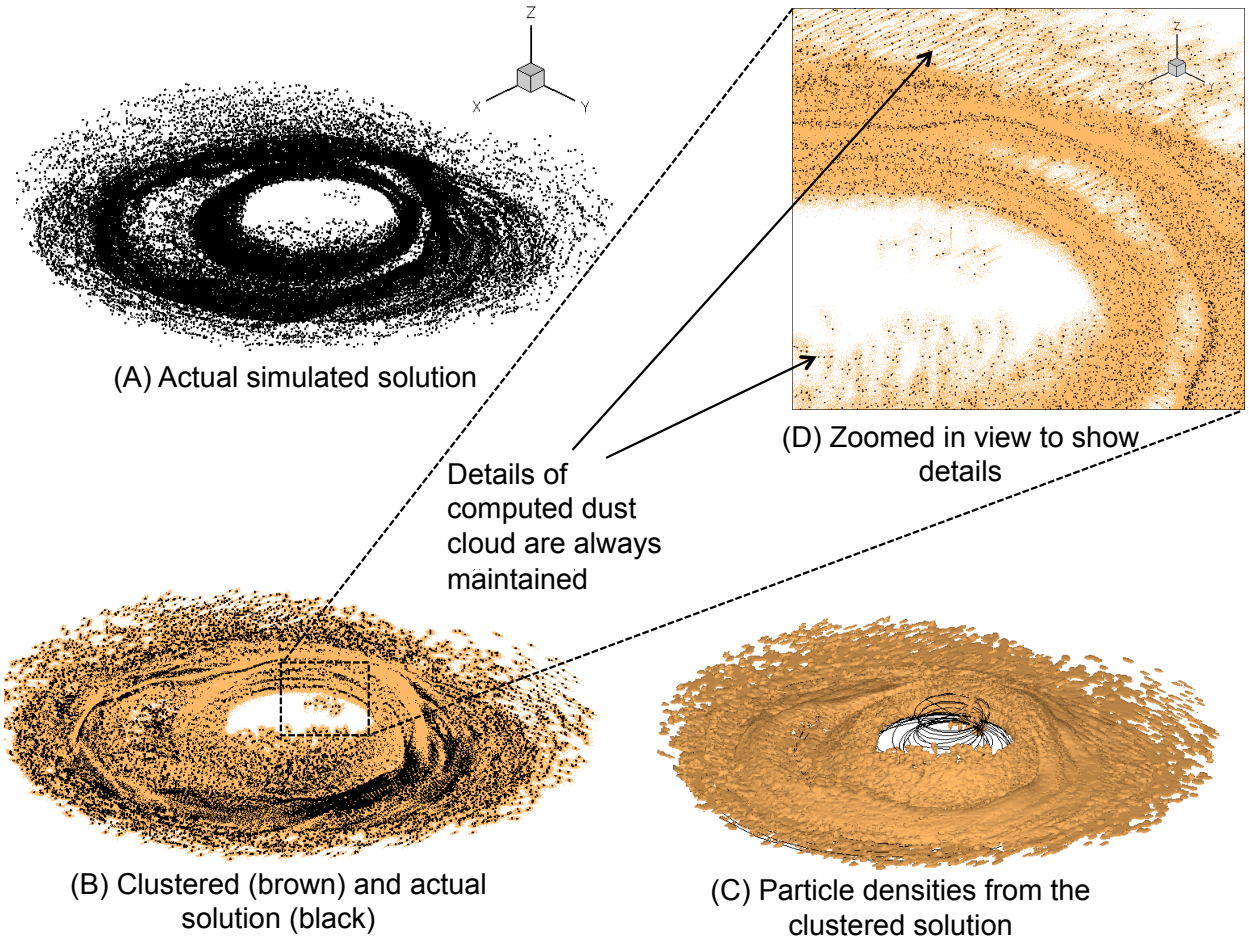

Figure E.3: A solution obtained from brownout dust field computations when using the Gaussian clustering method.

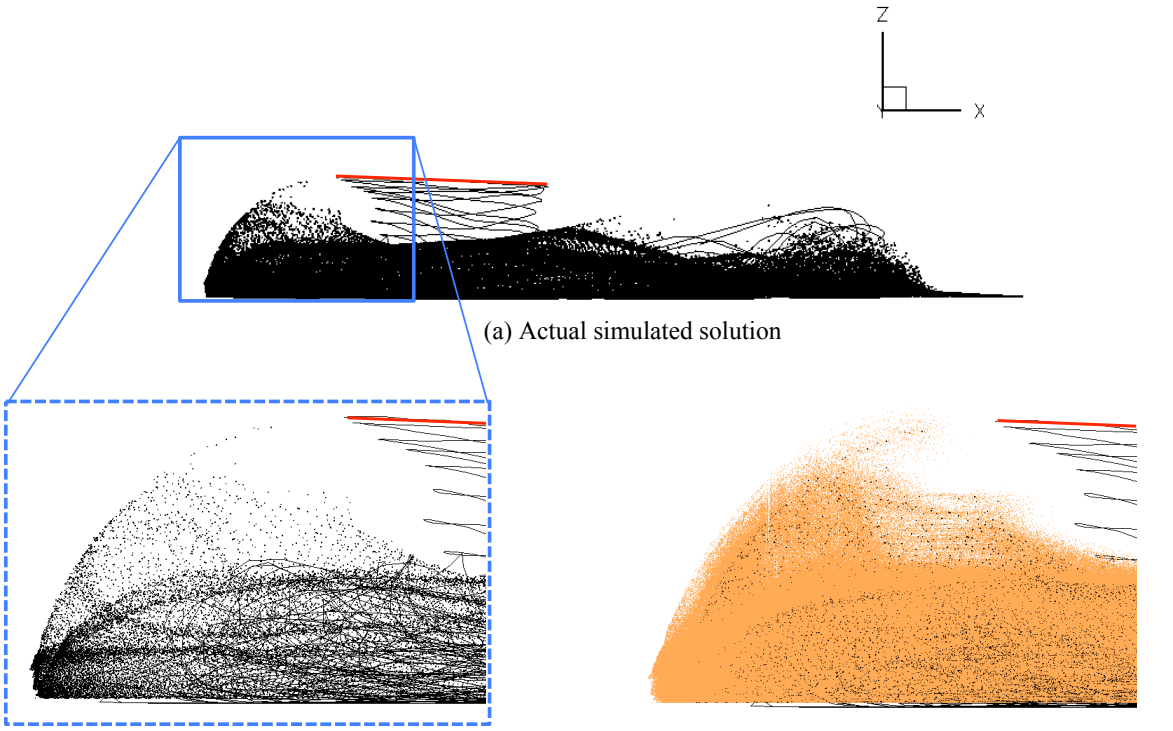

(a) Actual simulated solution

(b) Zoomed in view of the actual solution

(c) Zoomed in view of the Gaussian clustered solution

Figure E.4: Actual and clustered solution during a landing maneuver using the Gaussian distribution method. Source Govindarajan [18]

ter centers (denoted by the black dots in Fig. E.3(a)) and using the distributed particle clusters (Fig. E.3(b)) with a total of 100 particles per cluster, giving a total of 10^8 particles. Notice that the clustered solution, as shown by Fig. E.3(b), identifies the actually computed cluster centers as black dots, and the particles obtained through the Gaussian clustering technique as brown dots. The results clearly show that the clustered solution brings out the finer, structured details of the dust cloud. Figure E.3(c) shows the density of the dust cloud that is derived from the clustered solution, and Fig. E.3(d) shows some details of the dust cloud near the ground, the concentrations of which can be correlated to the positions of the tip vortices in the flow.

Figure E.4 shows the side views of an instantaneous rendition of the actual simulated and

clustered solution during a landing maneuver. Fig. E.4(a) shows a complete side view of the actual calculated brownout cloud, while Figs. E.4(b) and E.4(c) show the detailed views of the front of the rotor disk as obtained from the actual simulation as well as the clustered solution, respectively. Notice that the dimensions of the brownout dust cloud obtained using the clustering technique are nearly the same as the dimensions from the exact solution. It has been pointed earlier that the Gaussian clustering technique does not adversely impact the accuracy of the cluster centers. In fact, in the regions of high velocity gradients where other clustering techniques can cause errors, the Gaussian clustered solution will be the same as the actually computed solution and will not cause any additional errors in the simulation. Overall, these results show that the Gaussian clustering method can be reliably used to bring out the finer details of the dust cloud without adding substantially to the computational cost. Therefore, this method was used in the present work to simulate brownout dust clouds.

Appendix F: Helicopter Rotor Specifications

This appendix provides the specifications of the different helicopter rotors that were used for analysis in the present work. These specifications include the rotor geometry, configuration, and operational parameters.

Parameter	Value
Number of rotors, N_r	1
Number of blades, N_b	2
Rotor radius, R	0.086 m
Blade chord, c	0.019 m
Rotor solidity, σ	0.14
Total blade twist, θ_{tw}	0°
Rotational frequency, Ω	314.15 rad s^{-1}

Table F.1: Specifications of laboratory scale Rotor 1.

Parameter	Value
Number of rotors, N_r	1
Number of blades, N_b	2
Rotor radius, R	0.408 m
Blade chord, c	0.04445 m
Rotor solidity, σ	0.0694
Total blade twist, θ_{tw}	0°
Rotational frequency, Ω	194.78 rad s^{-1}

Table F.2: Specifications of laboratory scale Rotor 2.

Parameter	Value
Number of rotors, N_r	1
Number of blades, N_b	4
Rotor radius, R	0.8255 m
Blade chord, c	0.0635 m
Rotor solidity, σ	0.0979
Total blade twist, θ_{tw}	13° linear nose down
Rotational frequency, Ω	198.77 rad s^{-1}

Table F.3: Specifications of AGARD rotor.

Parameter	Value
Number of rotors, N_r	1
Number of blades, N_b	6
Rotor radius, R	11.0 m
Blade chord, c	0.66 m
Rotor solidity, σ	0.115
Total blade twist, θ_{tw}	6° linear nose down
Rotational frequency, Ω	19.37 rad s^{-1}

Table F.4: Specifications of the CH-54 helicopter rotor.

Parameter	Value
Number of rotors, N_r	1
Number of blades, N_b	2
Rotor radius, R	7.32 m
Blade chord, c	0.53 m
Rotor solidity, σ	0.138
Total blade twist, θ_{tw}	10.9° linear nose down
Rotational frequency, Ω	33.5 rad s^{-1}

Table F.5: Specifications of the UH-1 helicopter rotor.

Parameter	Upper rotor	Lower rotor
Number of blades, N_b	2	2
Rotor radius, R	3.81 m	3.81 m
Blade chord, c	0.287 m	0.457 m
Rotor solidity, σ	0.027	0.076
Total blade twist, θ_{tw}	0°	0°
Rotational frequency, Ω	40.0 rad s^{-1}	40.0 rad s^{-1}

Table F.6: Specifications of the Harrington coaxial rotor.

Parameter	Value
Number of rotors, N_r	1
Number of blades, N_b	4
Rotor radius, R	8.17 m
Blade chord, c	0.53 m
Rotor solidity, σ	0.083
Total blade twist, θ_{tw}	18° linear nose down
Rotational frequency, Ω	27.00 rad s^{-1}

Table F.7: Specifications of full-scale isolated single main rotor.

Parameter	Value
Number of rotors, N_r	1
Number of blades, N_b	4
Rotor radius, R	1.67 m
Blade chord, c	0.27 m
Rotor solidity, σ	0.21
Total blade twist, θ_{tw}	0° linear nose down
Rotational frequency, Ω	135.00 rad s^{-1}

Table F.8: Specifications of full-scale tail rotor.

Parameter	Value
Number of rotors, N_r	2
Number of blades, N_b	3
Rotor radius, R	7.25 m
Blade chord, c	0.48 m
Rotor solidity, σ	0.063
Total blade twist, θ_{tw}	10° linear nose down
Rotational frequency, Ω	30.30 rad s^{-1}
Rotor horizontal spacing	-
Rotor vertical spacing	$0.22R$

Table F.9: Specifications of a representative coaxial rotor configurations.

Parameter	Value
Number of rotors, N_r	2
Number of blades, N_b	3
Rotor radius, R	9.14 m
Blade chord, c	0.64 m
Rotor solidity, σ	0.067
Total blade twist, θ_{tw}	10° linear nose down
Rotational frequency, Ω	24.1 rad s^{-1}
Rotor horizontal spacing	$1.31R$
Rotor vertical spacing	$0.18R$

Table F.10: Specifications of a representative tandem rotor configurations.

Parameter	Value
Number of rotors, N_r	2
Number of blades, N_b	3
Rotor radius, R	6.46 m
Blade chord, c	0.58 m
Rotor solidity, σ	0.086
Total blade twist, θ_{tw}	15° linear nose down
Rotational frequency, Ω	37.1 rad s^{-1}
Rotor horizontal spacing	2.50R
Rotor vertical spacing	-

Table F.11: Specifications of a representative side-by-side rotor configuration.

Parameter	Value
Number of rotors, N_r	1
Number of blades, N_b	5
Rotor radius, R	9.3 m
Blade chord, c	0.45 m
Rotor solidity, σ	0.077
Total blade twist, θ_{tw}	16° linear nose down
Rotational frequency, Ω	23.7 rad s^{-1}

Table F.12: Specifications of the AW-101 helicopter rotor.

Bibliography

[1] Warren, T., Hong, S. C., Yu, C. J., and Rosenzweig, E. L., "Enhanced Erosion Protection for Rotor Blades," 65th Annual Forum Proceedings of the American Helicopter Society, Grapevine, TX, May 27–29, 2009.

[2] Milluzzo, J., and Leishman, J. G., "Assessment of Rotorcraft Brownout Severity in Terms of Rotor Design Parameters," *Journal of the American Helicopter Society*, Vol. 55, (3), October 2010, pp. 032009–1–9.

[3] Sydney, A., Baharani, A., and Leishman, J. G., "Understanding Brownout using Near-Wall Dual-Phase Flow Measurements," 67th Annual Forum Proceedings of the American Helicopter Society, Virginia Beach, VA, May 3–5, 2011.

[4] Leishman, J. G., *Principles of Helicopter Aerodynamics*, Cambridge University Press, New York, NY, 2006.

[5] Sydney, A., and Leishman, J. G., "Measurements of Rotor/Airframe Interactions in Ground Effect Over a Sediment Bed," 69th Annual Forum Proceedings of the American Helicopter Society, Phoenix, AZ, May 21–23, 2013.

[6] "Sandblaster 2 Support of See-Through Technologies for Particulate Brownout," Technical report, Task 1 Technical Report, Sponsored by Defense Advanced Research Projects Agency (DOD) Strategic Technology Office, Issued by U.S. Army Aviation and Missile Command under Contract No. W31P4Q-07-C-0215, MRI Project No. 110565, October 31, 2007.

[7] "Sandblaster 2 Support of See-Through Technologies for Particulate Brownout," Technical report, Task 5 Final Technical Report, Sponsored by Defense Advanced Research Projects Agency (DOD) Strategic Technology Office, Issued by U.S. Army Aviation and Missile Command under Contract No. W31P4Q-07-C-0215, MRI Project No. 110565, October 31, 2007.

[8] Sydney, A., and Leishman, J. G., "Time-Resolved Measurements of Rotor-Induced Particle Flows Produced by a Hovering Rotor," *Journal of the American Helicopter Society*, 2014, To appear.

[9] Milluzzo, J., Sydney, A., Rauleder, J., and Leishman, J. G., "In-Ground-Effect Aerodynamics of Rotors with Different Blade Tips," 66th Annual Forum Proceedings of the American Helicopter Society, Phoenix, AZ, May 10–13, 2010.

[10] Tanner, P. E., "Photogrammetric Characterization of a Brownout Cloud," 67th Annual Forum Proceedings of the American Helicopter Society, Virginia Beach, VA, May 3–5, 2011.

[11] Bagai, A., and Leishman, J. G., "A Study of Rotor Wake Development and Wake/Body Interactions in Hover using Wide-Field Shadowgraphy," *Journal of the American Helicopter Society*, Vol. 37, (4), October, 1992, pp. 48–57.

[12] Hance, B. T., *Effects of Body Shapes on Rotor In-Ground-Effect Aerodynamics*, M.S. thesis, Department of Aerospace Engineering, University of Maryland, College Park, MD, 2012.

[13] Tritschler, J., *Contributions to the Characterization and Mitigation of Rotorcraft Brownout*, Doctor of philosophy, Department of Aerospace Engineering, University of Maryland, College Park, MD, 2012.

[14] Stack, J., Lindsey, W. F., and Littell, R. E., "The Compressibility Bubble and the Effect of Compressibility on Pressures and Forces Acting on an Airfoil," Technical Report 646, NACA, 1988.

[15] Bhagwat, M. J., and Leishman, J. G., "Accuracy of Straight-Line Segmentation Applied to Curvilinear Vortex Filaments," *Journal of the American Helicopter Society*, Vol. 46, (2), April 2001, pp. 166–169.

[16] Bhagwat, M. J., and Leishman, J. G., "Self-Induced Velocity of a Vortex Ring Using Straight-Line Segmentation," *Journal of the American Helicopter Society*, Vol. 59, (1), January 2014, pp. 1–7.

[17] NVIDIA, *CUDA C Programming Guide*, www.nvidia.com, , July, 2013.

[18] Govindarajan, B. M., *Evaluation of Particle Clustering Algorithms in the Prediction of Brownout Dust Clouds*, M.S. thesis, Department of Aerospace Engineering, University of Maryland, College Park, MD, 2011.

[19] Mapes, P., Kent, R., and Wood, R., "DoD Helicopter Mishaps FY85-05: Findings and Recommendations," Technical report, U.S. Air Force, Washington, D. C., 2008.

[20] Technical report, National Transportation Safety Board, NTSB Accident Briefs: LAX01LA283, LAX01LA304, LAX04LA285, SEA05CA173.

[21] Jansen, C., Wennemers, A., and Groen, E., "FlyTact: A Tactile Display Improves a Helicopter Pilots Landing Performance in Degraded Visual Environments," *Haptics: Perception, Devices and Scenarios*, Vol. 502, (4), 2008, pp. 867–875.

[22] Johnson, B., Leishman, J. G., and Sydney, A., "Investigation of Sediment Entrainment Using Dual-Phase, High-Speed Particle Image Velocimetry," *Journal of the American Helicopter Society*, Vol. 55, (4), 2010, pp. 42003.

[23] Cheeseman, I. C., and Bennett, W. E., "The Effect of the Ground on a Helicopter Rotor in Forward Flight," Technical Report 3021, ARC RM, 1955.

[24] Fradenburgh, E. A., "The Helicopter and the Ground Effect Machine," *Journal of the American Helicopter Society*, Vol. 5, (4), 1960, pp. 26–28.

[25] Knight, M., and Hefner, R. A., "Analysis of Ground Effect on the Lifting Airscrew," Technical Report 835, NACA TN, 1941.

[26] Hayden, J.S., "The Effect of the Ground on Helicopter Hovering Power Required," American Helicopter Society 32th Annual National V/STOL Forum Proceedings, Washington D.C., May 10–12, 1976.

[27] Curtiss, H. C., Sun, M., Putman, W. F., and Hanker, E. J., "Rotor Aerodynamics in Ground Effect at Low Advance Ratios," *Journal of the American Helicopter Society*, Vol. 29, (1), 1984, pp. 48–55.

[28] Prouty, R. W., "Ground Effect and the Helicopter," AIAA Paper 85-4034, AIAA/AHS/ASEE Aircraft Design Systems and Operations Meeting, Colorado Springs, CO, October 14–16, 1985.

[29] Light, J. S., and Norman, T., "Tip Vortex Geometry of a Hovering Helicopter Rotor in Ground Effect," 45th Annual Forum Proceedings of the American Helicopter Society, Boston, MA, May 22–24, 1989.

[30] Lee, T. E., Leishman, J. G., and Ramasamy, M., "Fluid Dynamics of Interacting Blade Tip Vortices With a Ground Plane," *Journal of the American Helicopter Society*, Vol. 55, (2), April 2010, pp. 1–16.

[31] Nathan, N. D., and Green, R. B., "Measurements of a Rotor Flow in Ground Effect and Visualisation of the Brown-out Phenomenon," 64th Annual Forum Proceedings of the American Helicopter Society, Montréal, Canada, April 29–May 1, 2008.

[32] Phillips, C., and Brown, R.E., "Eulerian Simulation of the Fluid Dynamics of Helicopter Brownout," *AIAA Journal of Aircraft*, Vol. 46, (4), July 2009, pp. 1416–1429.

[33] Rauleder, J., and Leishman, J. G., "Flow Environment and Organized Turbulence Structures Near a Plane Below a Rotor," *AIAA Journal*, Vol. 52, (1), 2014, pp. 146–161.

[34] Shao, Y., *Physics and Modelling of Wind Erosion*, Springer, 2nd Edition, , 2008.

[35] Shao, Y., Raupach, M. R., and Findlater, P. A., "Effect of Saltation Bombardment on the Entrainment of Dust by the Wind," *Journal of Geophysical Research*, Vol. 98, (D7), February 1993, pp. 12,719–12,726.

[36] Rodgers, S. J., "Evaluation of the Dust Cloud Generated by Helicopter Rotor Downwash," Technical Report under Contract DA 44-177-AMC-289(T), USA AV LABS Technical Report, Issued by U.S. Army Aviation Material Laboratories, Fort Eustis, VA, March 1968.

[37] Gillies, J. A., Etyemezian, V., Kuhns, H., McAlpine, J. D., King, J., Uppapalli, S., Nikolich, G., and Engelbrecht, J., "Dust Emissions Created by Low-Level Rotary-Winged Aircraft Flight Over Desert Surfaces," *Atmospheric Environment*, Vol. 44, (8), 2010, pp. 1,043–1,053.

[38] Wong, O. D., and Tanner, P. E., "Photogrammetric Measurements of an EH-60L Brownout Cloud," 67th Annual Forum Proceedings of the American Helicopter Society, Phoenix, AZ, May 10–13, 2010.

[39] Taylor, M. K., "A Balsa-Dust Technique for Air-Flow Visualization and its Applications to Flow Through Model Helicopter Rotors in Static Thrust," Technical Report NACA TN 2220, Langley Aeronautical Laboratory, Langley Air Force Base, VA, November 1950.

[40] Lee, T. E., Leishman, J. G., and Ramasamy, M., "Fluid Dynamics of Interacting Blade Tip Vortices With a Ground Plane," 64th Annual Forum Proceedings of the American Helicopter Society, Montréal, Canada, April 20–May 1, 2008.

[41] Reel, J. L., *Mechanisms of Vortex-Induced Particle Transport from a Mobile Bed Below a Hovering Rotor*, M.S. thesis, Department of Aerospace Engineering, University of Maryland, College Park, MD, 2014.

[42] Rauleder, J., and Leishman, J. G., "Particle–Fluid Interactions in Rotor-Generated Vortex Flows," *Experiments in Fluids*, Vol. 55, (3), 2014, pp. 1–15.

[43] Mulinti, R., and Kiger, K., "Two-Phase PIV Measurements of Particle Suspension in a Forced Impinging Jet," 63rd Annual Meeting of the APS Division of Fluid Dynamics, Long Beach, CA, November 21–23, 2010.

[44] Geiser, J., and Kiger, K., "A Simplified Analog for a Rotorcraft-in-Ground-Effect Flow Using a Forced Impinging Jet," 63rd Annual Meeting of the APS Division of Fluid Dynamics, Long Beach, CA, November 21–23, 2010.

[45] Haehnel, R., and Dade, W. B., "Physics of Particle Entrainment Under the Influence of an Impinging Jet," Army Science Conference Proceedings, Orlando, FL, 2008.

[46] Wilson, J. C., and Mineck, R. E., "Wind-Tunnel Investigation of Helicopter Rotor Wake Effects on Three Helicopter Fuselage Models," Technical Report TM X-3185, NASA, 1975.

[47] Sheridan, P. F., and Smith, R. P., "Interactional Aerodynamics — A New Challenge to Helicopter Technology," *Journal of the American Helicopter Society*, Vol. 25, (1), 1979, pp. 3–21.

[48] Smith, C. A., and Betzina, M. D., "Aerodynamic Loads Induced by a Rotor on a Body of Revolution," *Journal of the American Helicopter Society*, Vol. 31, (1), 1986, pp. 29–36.

[49] Brand, A., G., McMahon, H., M., and Komerath, N., M., "Surface Pressure Measurements on a Body Subject to Vortex Wake Interaction," *AIAA Journal*, Vol. 27, (5), 1989, pp. 569–574.

[50] Bi, Nai-pei, and Leishman, J. G., "Experimental Study of Rotor/Body Aerodynamic Interactions," *Journal of Aircraft*, Vol. 27, (9), September 1990, pp. 779–788.

[51] Bi, Nai-pei, Leishman, J. G., and Crouse, G. L., "Investigation of Rotor Tip Vortex Interactions with a Body," *Journal of Aircraft*, Vol. 30, (6), Nov.–Dec. 1993, pp. 879–888.

[52] Weisner, W., and Kohler, G., "Tail Rotor Performance in Presence of Main Rotor, Ground, and Winds," *Journal of the American Helicopter Society*, Vol. 19, (3), July 1974, pp. 2–9.

[53] Balch, D. T., "Experimental Study of Main Rotor/Tail Rotor/Airframe Interaction in Hover," *Journal of the American Helicopter Society*, Vol. 30, (2), April 1985, pp. 49–56.

[54] Early, J. M., Green, R. B., and Coton, F. N., "Flow Visualization of the Orthogonal Blade–Vortex Interaction Using Particle Image Velocimetry," *Aeronautical Journal*, Vol. 106, (1,057), 2002, pp. 37–145.

[55] Betz, A., "The Ground Effect on Lifting Propellers," Technical Report TM-836, NACA, 1937.

[56] Kalra, T., Lakshminarayan, V., and Baeder, J., "CFD Validation of Micro Hovering Rotor in Ground Effect," AHS International Specialists Conference Proceedings on Aeromechanics, San Francisco, CA, January, 2010.

[57] Lakshminarayan, V. K., *Computational Investigation of Micro-Scale Coaxial Ro- tor Aerodynamics in Hover*, Doctor of philosophy, Department of Aerospace Engineering, University of Maryland, College Park, MD, 2009.

[58] Lakshminarayan, V. K., and Baeder, J. D., "Computational Investigation of Micro Hovering Rotor Aerodynamics," *Journal of the American Helicopter Society*, Vol. 55, (1), 2010, pp. 14–29.

[59] Rajagopalan, R. G., and Fanucci, J. B., "Finite Difference Model for Vertical Axis Wind Turbines," *Journal of Propulsion and Power*, Vol. 1, (6), 1985, pp. 432–436.

[60] Phillips, C., and Brown, R., "The Effect of Helicopter Configuration on the Fluid Dynamics of Brownout," 34th European Rotorcraft Forum Proceedings, Liverpool, UK, September 16–19, 2008.

[61] Phillips, C., Kim, H. W., and Brown, R.E., "The Flow Physics of Helicopter Brownout," 66th Annual Forum Proceedings of the American Helicopter Society, Phoenix, AZ, May 10–13, 2010.

[62] Wenren, Y., Steinhoff, J., and Caradonna, F., "Application of Vorticity Confinement to Rotorcraft Flows," 31st European Rotorcraft Forum, Florence, Italy, September 12–16, 2005.

[63] Morales, F., and Squires, K. D., "Numerical Analysis of Unsteady Vortical Flows Generated by a Rotorcraft Operating on Ground: A First Assessment of Helicopter Brownout," Proceedings of the 29th AIAA Applied Aerodynamics Conference, Honolulu, HI, June 27–30, 2011.

[64] Syal, M., Govindarajan, B., and Leishman, J. G., "Mesoscale Sediment Tracking Methodology to Analyze Brownout Cloud Developments," 66th Annual Forum Proceedings of the American Helicopter Society, Phoenix, AZ, May 10–13, 2010.

[65] Syal, M., Rauleder, J., Tritschler, J. K., and Leishman, J. G., "On the Possibilities of Brownout Mitigation Using a Slotted-Tip Rotor Blade," AIAA 2011-3183, 29th AIAA Applied Aerodynamics Conference, Honolulu, Hawaii, June 27–30, 2011.

[66] Syal, M., and Leishman, J. G., "Modeling of Bombardment Ejection in the Rotorcraft Brownout Problem," *AIAA Journal*, Vol. 51, (4), April 2013, pp. 549–566.

[67] Syal, M., and Leishman, J. G., "Predictions of Brownout Dust Clouds Compared to Photogrammetric Measurements," *Journal of the American Helicopter Society*, Vol. 58, (1), 2013, pp. 1–18.

[68] Wachspress, D. A., Quackenbush, T. R., and Boschitsch, A. H., "First-Principles Free-Vortex Wake Analysis for Helicopters and Tiltrotors," 59th Annual Forum Proceedings of the American Helicopter Society, Phoenix, Arizona, May 6–8, 2003.

[69] Wachspress, D. A., Keller, J. D., Quackenbush, T. R., Whitehouse, G. R., and Yu, K., "High Fidelity Rotor Aerodynamic Module for Real-Time Rotorcraft Flight Simulation," 64th Annual Forum Proceedings of the American Helicopter Society, Montreal, Canada, April 29–May 1, 2008.

[70] Fletcher, T. M., and Brown, R. E., "Main Rotor-Tail Rotor Interaction and Its Implications for Helicopter Directional Control," *Journal of the American Helicopter Society*, Vol. 53, (2), April 2008, pp. 125–138.

[71] Ghosh, S., Lohry, M. W., and Rajagopalan, R. G., "Rotor Configurational Effect on Rotorcraft Brownout," 28th AIAA Applied Aerodynamics Conference, Chicago, Illinois, June 28–July 1, 2010.

[72] Thomas, S., *A GPU-Accelerated, Hybrid FVM-RANS Methodology for Modeling Rotorcraft Brownout*, Doctor of philosophy, Department of Aerospace Engineering, University of Maryland, College Park, MD, 2013.

[73] Ryerson, C. C., Haehnel, R. B., Koenig, G. G., and Moulton, M. A., "Visibility Enhancement in Rotorwash Clouds," Paper AIAA-2005-263, 43rd AIAA Aerospace Sciences Meeting and Exhibit, Reno, Nevada, January 10–13, 2005.

[74] Pomeroy, J. W., and Gray, D. M., "Saltation of Snow," *Water Resources Research*, Vol. 26, (7), 1990, pp. 1,583–1,594.

[75] Wenren, Y, Walter, J., Fan, M., and Steinhoff, J., "Vorticity Confinement and Advanced Rendering to Compute and Visualize Complex Flows," Paper AIAA-2006-945, 44th AIAA Aerospace Sciences Meeting and Exhibit, Reno, Nevada, January 9–12, 2006.

[76] Steinhoff, J., and Wenren, Y., "An Efficient Vorticity Confinement Based Lifting Surface Method for Rotor Wake Computations," 32nd European Rotorcraft Forum, Maastricht, The Netherlands, September 12–14, 2006.

[77] White, B. R., "Soil Transport by Winds on Mars," *Journal of Geophysical Research*, Vol. 84, (B9), August 1979, pp. 4,643–4,651.

[78] Shao, Y., and Lu, H., "A Simple Expression for Wind Erosion Threshold Friction Velocity," *Journal of Geophysical Research*, Vol. 105, (D17), 2000, pp. 22,437–22,443.

[79] Wachspress, D., A., Whitehouse, G., R., Keller, J., D., and Yu, H., "A High Fidelity Brownout Model for Real-Time Flight Simulations and Trainers," 65th Annual Forum Proceedings of the American Helicopter Society, Grapevine, TX, May 27–29, 2009.

[80] D'Andrea, A., "Numerical Analysis of Unsteady Vortical Flows Generated by a Rotorcraft Operating on Ground: A First Assessment of Helicopter Brownout," 65th Annual Forum Proceedings of the American Helicopter Society, Grapevine, Texas, May 27–29, 2009.

[81] D'Andrea, A., "Unsteady Numerical Simulations of Helicopters and Tiltrotors Operating in Sandy-Desert Environments," Proceedings of the American Helicopter Society Specialists Conference on Aeromechanics, San Francisco, CA, January 20–22, 2010.

[82] D'Andrea, A., "Development and Application of a Physics-Based Computational Tool to Simulate Helicopter Brownout," Proceedings of the 37th European Rotorcraft Forum, Gallarate (VA), Italy, September 13–15, 2011.

[83] Syal, M., *Development of a Lagrangian-Lagrangian Methodology to Predict Brownout Dust Clouds*, Doctor of philosophy, Department of Aerospace Engineering, University of Maryland, College Park, MD, 2012.

[84] Tritschler, J., Syal, M., Celi, R., and Leishman, J. G., "A Methodology for Rotor Design Optimization for Rotorcraft Brownout Mitigation," 66th Annual Forum Proceedings of the American Helicopter Society, Phoenix, AZ, May 10–13, 2010.

[85] Tritschler, J., Syal, M., Celi, R., and Leishman, J. G., "The Effect of Number of Blades on Optimum Rotor Design for Brownout Mitigation," Future Vertical Lift Aircraft Design Conference, San Francisco, CA, January 18–20, 2012.

[86] Tritschler, J. K., and Celi, R., "Brownout Cloud Characterization Using the Modulation Transfer Function," *Journal of the American Helicopter Society*, Vol. 58, (1), 2013, pp. 1–13.

[87] Whitehouse, G. R., Wachspress, D. A., Quackenbush, T. R., and Keller, J. D., "Exploring Aerodynamic Methods for Mitigating Brownout," 65th Annual Forum Proceedings of the American Helicopter Society, Grapevine, TX, May 27–29, 2009.

[88] Bhagwat, M. J., and Leishman, J. G., "Time-Accurate Modeling of Rotor Wakes Using A Free-Vortex Wake Method," AIAA 2000-4120, 18th AIAA Applied Aerodynamics Conference Proceedings, Denver, CO, August 2000.

[89] Griffiths, D. A., Ananthan, S., and Leishman, J. G., "Predictions of Rotor Performance in Ground Effect Using a Free-Vortex Wake Model," 58th Annual Forum Proceedings of the American Helicopter Society, Montréal, Canada, June 11–13, 2002.

[90] Hess, J. L., and Smith, A. M. O., "Calculation of Nonlifting Potential Flow About Arbitrary Three-Dimensional Bodies," Technical Report ES40622, Douglas Aircraft Report, 1962.

[91] Weissinger, J., "The Lift Distribution of Swept-Back Wings," Technical Report TM-1120, NACA, 1947.

[92] Krishnamurthy, K., *Principles of Ideal-Fluid Aerodynamics*, Wiley, New York, NY, 1966.

[93] Saffman, P. G., *Vortex Dynamics*, Cambridge University Press, Cambridge, UK, 1992.

[94] Bagai, A., *Contributions to the Mathematical Modeling of Rotor Flow-Fields using a Pseudo-Implicit Free-Wake Analysis*, Doctor of philosophy, Department of Aerospace Engineering, University of Maryland, College Park, MD, 1995.

[95] Leishman, J. G., and Beddoes, T. S., "A Semi-Emperical Model for Dynamic Stall," *Journal of the American Helicopter Society*, Vol. 34, (3), 1989, pp. 3–17.

[96] Beddoes, T.S., "Representation of Airfoil Behavior," *Vertica*, Vol. 7, (2), 1983, pp. 183–197.

[97] Batchelor, G. K., *An Introduction to Fluid Dynamics*, Cambridge University Press, Cambridge, UK, 1967.

[98] Gupta, S., and Leishman, J. G., "Accuracy of the Induced Velocity of Wind Turbine Wakes Using Vortex Segmentation," 23rd ASME Wind Energy Symposium and the 42nd AIAA Aerospace Sciences Meeting, Reno, NV, January 5–8, 2004.

[99] Bhagwat, M. J., and Leishman, J. G., "Stability, Consistency and Convergence of Time-Marching Free-Vortex Rotor Wake Algorithms," *Journal of the American Helicopter Society*, Vol. 46, (1), January 2001, pp. 59–71.

[100] Crouse, G.L., Leishman, J.G., and Bi Nai-pei, "Theoretical and Experimental Study of Unsteady Rotor/Body Aerodynamic Interactions," *Journal of the American Helicopter Society*, Vol. 37, (1), January 1992, pp. 55–65.

[101] Bhagwat, M. J., *Mathematical Modeling of the Transient Dynamics of Helicopter Rotor Wakes Using a Time-Accurate Free-Vortex Method*, Doctor of philosophy, Department of Aerospace Engineering, University of Maryland, College Park, MD, 2001.

[102] Vatistas, G. H., Kozel, V., and Mih, W. C., "A Simpler Model for Concentrated Vortices," *Experiments in Fluids*, Vol. 11, (1), 1991, pp. 73–76.

[103] Bagai, A., and Leishman, J. G., "Flow Visualization of Compressible Vortex Structures Using Density Gradient Techniques," *Experiments in Fluids*, Vol. 15, (6), October 1993, pp. 431–442.

[104] Squire, H. B., "The Growth of a Vortex in Turbulent Flow," *Aeronautical Quaterly*, Vol. 16, (3), August 1965, pp. 302–306.

[105] Bhagwat, M. J., and Leishman, J. G., "Generalized Viscous Vortex Core Models for Application to Free-Vortex Wake and Aeroacoustic Calculations," 58th Annual Forum Proceedings of the American Helicopter Society, Montréal, Canada, June 11–13, 2002.

[106] Ramasamy, M., and Leishman, J. G., "A Generalized Model for Transitional Blade Tip Vortices," *Journal of the American Helicopter Society*, Vol. 51, (1), January 2006, pp. 92–103.

[107] Ananthan, S., and Leishman, J. G., "Role of Filament Strain in the Free-Vortex Modeling of Rotor Wakes," *Journal of the American Helicopter Society*, Vol. 49, (2), April, 2004, pp. 176–191.

[108] Ananthan, S., *Analysis of Rotor Wake Aerodynamics During Maneuvering Flight Using a Free-Vortex Wake Methodology*, Doctor of philosophy, Department of Aerospace Engineering, University of Maryland, College Park, MD, 2006.

[109] Katz, J., and Plotkin, A., *Low Speed Aerodynamics*, Cambridge University Press, New York, NY, 2001.

[110] Rankine, W. J. M., "Calculation of Potential Flow About Arbitrary Bodies," *Transactions of the Institute for Naval Architecture*, Vol. 6, (13), 1865, pp. 012007.

[111] Glauret, H., *The Elements of Aerofoil and Airscrew Theory*, Cambridge University Press, London, 1926.

[112] Anderson, J. D., *Fundamentals of Aerodynamics*, McGraw-Hill, New York, 1984.

[113] Lorber, P. F., and Egolf, T. A., "An Unsteady Helicopter Rotor-Fuselage Aerodynamic Interaction Analysis," *Journal of the American Helicopter Society*, Vol. 35, (1), 1990, pp. 32–42.

[114] Quackenbush, T. R., Lam, C.-M. G., and Bliss, D. B., "Vortex Methods for the Computational Analysis of Rotor/Body Interaction," *Journal of the American Helicopter Society*, Vol. 39, (4), 1994, pp. 14–24.

[115] Alfred, J., Celi, R., and Leishman, J. G., "Flight Path Optimization for Brownout Mitigation using a High Fidelity Simulation Model," 69th Annual Forum Proceedings of the American Helicopter Society, Phoenix, AZ, May 21–23, 2013.

[116] Bagnold, R. A., *The Physics of Blown Sand and Desert Dunes*, Dover Publications, Inc., Mineola, NY, 1941.

[117] Baharani, A., *Investigation into the Effects of Aeolian Scaling Parameters on Sediment Mobilization Below a Hovering Rotor*, M.s. thesis, Department of Aerospace Engineering, University of Maryland, College Park, MD, 2011.

[118] Greeley, R., and Iversen, J. D., *Wind as a Geological Process on Earth, Mars, Venus and Titan*, Cambridge University Press, New York, NY, 1985.

[119] Crowe, C., Sommerfeld, M., and, Tsuji, Y., *Multiphase Flows with Particles and Droplets*, CRC Press, Washington DC, 1998.

[120] Schlichting, H., *Boundary-Layer Theory*, McGraw-Hill Book Company, New York, 1979.

[121] Lomax, H., Pullilam, T. H., and Zingg, D. W., *Fundamentals of Computational Fluid Dynamics*, Springers, , 2001.

[122] Lu, H., and Shao, Y., "A New Model for Dust Emission by Saltation Bombardment," *Journal of Geophysical Research*, Vol. 104, (D14), July 1999, pp. 16,827–16,842.

[123] Poppe, T., Blum, J., and Henning, T., "Analogous Experiments on the Stickiness of Micron-Sized Preplanetary Dust," *The Astrophysical Journal*, Vol. 533, (1), April 2000, pp. 454–471.

[124] Govindarajan, B., Leishman, J. G., and Gumerov, N. A., "Particle-Clustering Algorithms for the Prediction of Brownout Dust Clouds," *AIAA Journal*, Vol. 51, (5), 2013, pp. 1080–1094.

[125] Thomas, S., Lakshminarayan, V. K., Kalra, T. S., and Baeder, J. D., "Eulerian-Lagrangian Analysis of Cloud Evolution using CFD Coupled with a Sediment Tracking Algorithm," 67th Annual Forum Proceedings of the American Helicopter Society, Virginia Beach, VA, May 3–5, 2011.

[126] Coleman, C. P., "A Survey of Theoretical and Experimental Coaxial Rotor Aerodynamic Research," Technical Report TP 3,675, NASA, 1997.

[127] Harrington, R. D., "Full-Scale-Tunnel Investigation of the Static-Thrust Performance of a Coaxial Helicopter Rotor," Technical Report TN 2,318, NACA, 1951.

[128] Leese, G. W., and Knight, I. T., "Helicopter Downwash Data," Technical Report 754, AD-780, June 1974.

[129] "A Selection of Experimental Test Cases for the Validation of CFD Codes," Technical Report AR-303, Volume 2, AGARD, 1994.

[130] Cook, C. V., "Tail Rotor Design and Performance," *Vertica*, Vol. 2, (1), 1978, pp. 163–181.

[131] Bhagwat, M. J., and Leishman, J. G., "Stability Analysis of Helicopter Rotor Wakes in Axial Flight," *Journal of the American Helicopter Society*, Vol. 45, (3), July 2000, pp. 165–178.

[132] Moen, C. G., DiCarlo, D. J., and Yenni, K. R., "A Parametric Analysis of Visual Approaches for Helicopters," Technical Report TN-D-8275, NASA, December 27, 1976.

[133] Hong, S. C., O'Connor, T., Duhaine, G., and Kopchik, J., "Review of U.S. Army's One Year Field Trial of Hontek Coatings on Black Hawk Helicopters in Iraq," 11th Joint NASA/FAA/DoD Conference on Aging Aircraft, Phoenix, AZ, April 23, 2008.

[134] Abbott, I. H., and von Doenhoff, A., *Theory of Wing Sections*, McGraw-Hill, New York, 1959.

[135] Scully, M. P., "Computation of Helicopter Rotor Wake Geometry and Its Influence on Rotor Harmonic Airloads," Technical Report TR 178-1, ASRL, March 1975.

[136] Johnson, W., "A General Free Wake Geometry Calculation for Wings and Rotors," 51st Annual Forum Proceedings of the American Helicopter Society, Fort Worth, TX, May 9–11, 1995.

[137] Bagai, A., and Leishman, J. G., "Rotor Free-Wake Modeling using a Pseudoimplicit Relaxation Algorithm," *Journal of Aircraft*, Vol. 32, (6), November–December, 1995, pp. 1276–1285.

[138] Bliss, D. B., Teske, M. E., and Quackenbush, T. R., "A New Methodology for Free-Wake Analysis using Curved Vortex Elements," Technical report, CR-3958, December 1987.

[139] Zhao, J., and He, C., "A Viscous Vortex Particle Model for Rotor Wake and Interference Analysis," *Journal of the American Helicopter Society*, Vol. 55, (1), 2010, pp. 1–14.

[140] Bir, G. S., and Chopra, I., "Status of the University of Maryland Advanced Rotorcraft Code (UMARC)," American Helicopter Society Aeromechanics Specialist Conference Proceedings, San Francisco, CA, January 19–21, 1994.

[141] Gupta, S. and Leishman, J. G., "Accuracy of the Induced Velocity from Helicoidal Wake Vortices Using Straight-line Segmentation," *AIAA Journal*, Vol. 23, (1), January 2005, pp. 29–40.

[142] Lamb, H., *Hydrodynamics*, 3rd Edition, Cambridge University Press, Cambridge, UK, 1993.

[143] Saffman, P. G., "Lift on a Small Sphere in a Slow Shear Flow," *Journal of Fluid Mechanics*, Vol. 22, (2), 1965, pp. 385–400.

[144] Oseen, C. W., "Über Wirbelbewegung in Einer Reibenden Flüssigkeit," *Arkiv for Matematik Astronomi och Fysik*, Vol. 7, (1), 1912, pp. 14–21.

[145] Rankine, W. J. M., *Manual of Applied Mechanics*, C. Griffen Company, London, UK, 1858.

[146] Scully, M. P., and Sullivan, J. P., "Helicopter Rotor Wake Geometry and Airloads and Development of Laser Doppler Velocimeter for Use in Helicopter Rotor Wakes," Technical Report 183, MIT DSR No. 73032, Massachusetts Institute of Technology Aerophysics Labratory, August 1972.

[147] Sterbenz, P. H., *Floating-Point Computation*, Prentice Hall, Englewood Cliffs, NJ, 1973.

[148] Hu, Q., Gumerov, N. A., Duraiswami, R., Syal, M., and Leishman, J. G., "Toward Improved Aeromechanics Simulations Using Recent Advancements in Scientific Computing," 67th Annual Forum Proceedings of the American Helicopter Society, Virginia Beach, VA, May 3–5, 2011.

[149] Li, W., "Practical Criteria for Positive-Definite Matrix, M-Matrix and Hurwitz Matrix," *Applied Mathematics and Computation*, Vol. 185, (1), 2007, pp. 397–401.